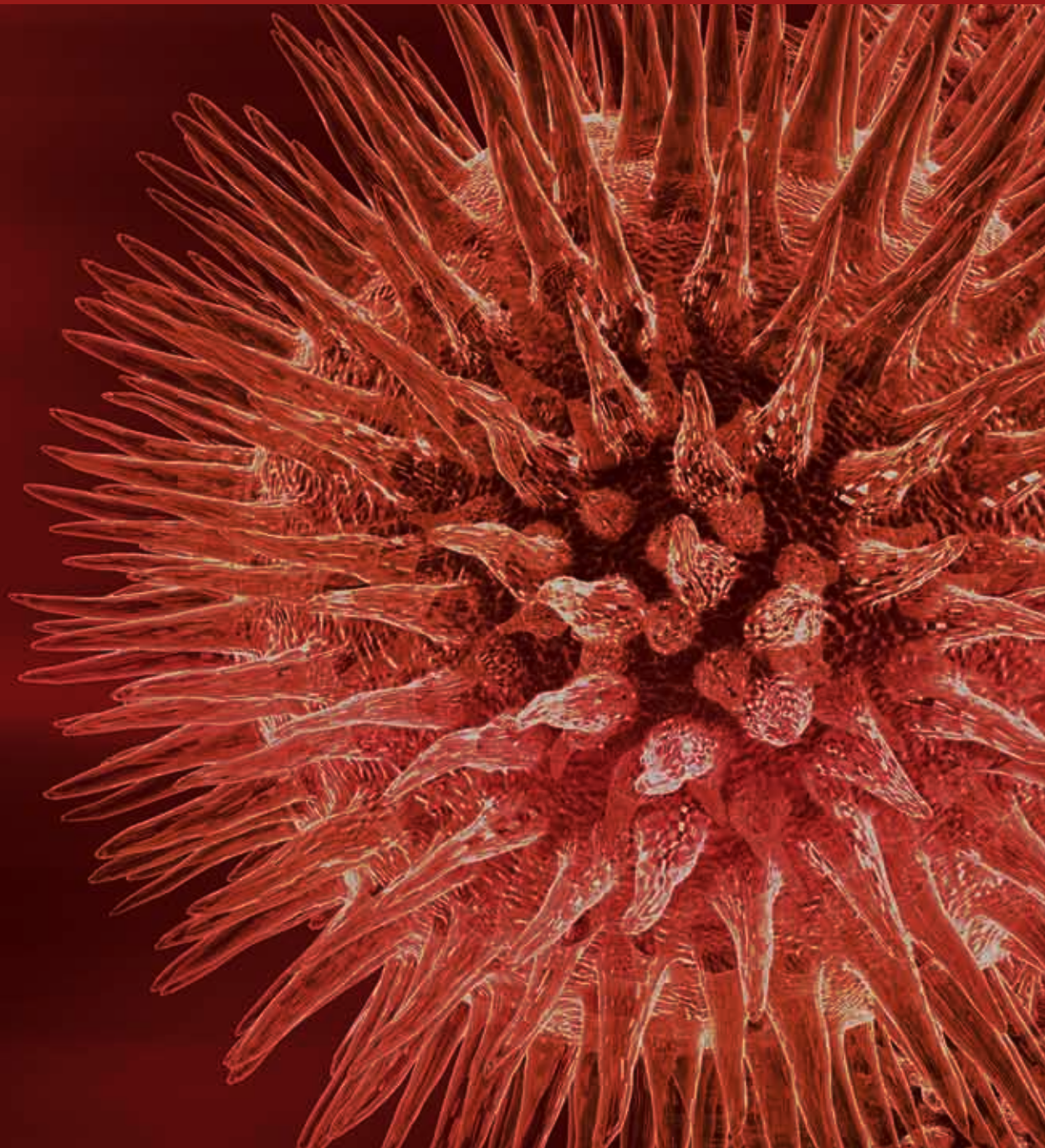


Molecular Imaging-Guided Theranostics and Personalized Medicine

Guest Editors: David J. Yang, Fong Y. Tsai, Tomio Inoue, Mei-Hsiu Liao, Fan-Lin Kong, and Shaoli Song





Molecular Imaging-Guided Theranostics and Personalized Medicine

Molecular Imaging-Guided Theranostics and Personalized Medicine

Guest Editors: David J. Yang, Fong Y. Tsai, Tomio Inoue, Mei-Hsiu Liao, Fan-Lin Kong, and Shaoli Song



Copyright © 2013 Hindawi Publishing Corporation. All rights reserved.

This is a special issue published in "BioMed Research International." All articles are open access articles distributed under the Creative Commons Attribution License, which permits unrestricted use, distribution, and reproduction in any medium, provided the original work is properly cited.

Contents

Molecular Imaging-Guided Theranostics and Personalized Medicine, David J. Yang, Fong Y. Tsai, Tomio Inoue, Mei-Hsiu Liao, Fan-Lin Kong, and Shaoli Song
Volume 2013, Article ID 859453, 2 pages

In Vivo Evidence of Increased nNOS Activity in Acute MPTP Neurotoxicity: A Functional Pharmacological MRI Study, Tiing Yee Siow, Chiao-Chi V. Chen, Nina Wan, Kai-Ping N. Chow, and Chen Chang
Volume 2013, Article ID 964034, 7 pages

Molecular Imaging of Nonsmall Cell Lung Carcinomas Expressing Active Mutant EGFR Kinase Using PET with [¹²⁴I]-Morpholino-IPQA, Skye Hsin-Hsien Yeh, Chien-Feng Lin, Fan-Lin Kong, Hsin-Ell Wang, Ya-Ju Hsieh, Juri G. Gelovani, and Ren-Shyan Liu
Volume 2013, Article ID 549359, 10 pages

Synthesis and Biological Evaluation of O-[3-¹⁸F-fluoropropyl]- α -methyl Tyrosine in Mesothelioma-Bearing Rodents, I-Hong Shih, Fan-Lin Kong, Mohammad S. Ali, Yinhan Zhang, Dong-Fang Yu, Xudong Duan, and David J. Yang
Volume 2013, Article ID 460619, 9 pages

Affinity Labeling of Membrane Receptors Using Tissue-Penetrating Radiations, Franklin C. Wong, John Boja, Beng Ho, Michael J. Kuhar, and Dean F. Wong
Volume 2013, Article ID 503095, 7 pages

Kidney Dosimetry in ¹⁷⁷Lu and ⁹⁰Y Peptide Receptor Radionuclide Therapy: Influence of Image Timing, Time-Activity Integration Method, and Risk Factors, F. Guerriero, M. E. Ferrari, F. Botta, F. Fioroni, E. Grassi, A. Versari, A. Sarnelli, M. Pacilio, E. Amato, L. Strigari, L. Bodei, G. Paganelli, M. Iori, G. Pedroli, and M. Cremonesi
Volume 2013, Article ID 935351, 12 pages

The Adjunctive Digital Breast Tomosynthesis in Diagnosis of Breast Cancer, Tsung-Lung Yang, Huei-Lung Liang, Chen-Pin Chou, Jer-Shyung Huang, and Huay-Ben Pan
Volume 2013, Article ID 597253, 7 pages

Managing Lymphoma with Non-FDG Radiotracers: Current Clinical and Preclinical Applications, Fan-Lin Kong, Richard J. Ford, and David J. Yang
Volume 2013, Article ID 626910, 12 pages

Clinical Application of Magnetic Resonance Imaging in Management of Breast Cancer Patients Receiving Neoadjuvant Chemotherapy, Jeon-Hor Chen and Min-Ying Su
Volume 2013, Article ID 348167, 14 pages

Advanced MR Imaging of Gliomas: An Update, Hung-Wen Kao, Shih-Wei Chiang, Hsiao-Wen Chung, Fong Y. Tsai, and Cheng-Yu Chen
Volume 2013, Article ID 970586, 14 pages

The Potential Roles of ¹⁸F-FDG-PET in Management of Acute Stroke Patients, Adomas Bunevicius, Hong Yuan, and Weili Lin
Volume 2013, Article ID 634598, 14 pages

Toward the Era of a One-Stop Imaging Service Using an Angiography Suite for Neurovascular Disorders, Sheng-Che Hung, Chung-Jung Lin, Wan-Yuo Guo, Feng-Chi Chang, Chao-Bao Luo, Michael Mu-Huo Teng, and Cheng-Yen Chang
Volume 2013, Article ID 873614, 7 pages

Pharmacodynamic Analysis of Magnetic Resonance Imaging-Monitored Focused Ultrasound-Induced Blood-Brain Barrier Opening for Drug Delivery to Brain Tumors, Po-Chun Chu, Wen-Yen Chai, Han-Yi Hsieh, Jiun-Jie Wang, Shiaw-Pyng Wey, Chiung-Yin Huang, Kuo-Chen Wei, and Hao-Li Liu
Volume 2013, Article ID 627496, 13 pages

Significance of Coronary Calcification for Prediction of Coronary Artery Disease and Cardiac Events Based on 64-Slice Coronary Computed Tomography Angiography, Yuan-Chang Liu, Zhonghua Sun, Pei-Kwei Tsay, Tiffany Chan, I-Chang Hsieh, Chun-Chi Chen, Ming-Shien Wen, and Yung-Liang Wan
Volume 2013, Article ID 472347, 9 pages

Editorial

Molecular Imaging-Guided Theranostics and Personalized Medicine

David J. Yang,¹ Fong Y. Tsai,^{2,3} Tomio Inoue,⁴ Mei-Hsiu Liao,⁵ Fan-Lin Kong,⁶ and Shaoli Song⁷

¹ Diagnostic Imaging, The University of Texas MD Anderson Cancer Center, Houston, TX 77030, USA

² Taipei Medical University, Taipei 11031, Taiwan

³ University of California at Irvine, Orange, CA 92868, USA

⁴ Department of Radiology, Yokohama City University School of Medicine, 3-9 Fukuura Kanazawa-ku, Yokohama 236-0004, Japan

⁵ Radiopharmaceuticals Production and Marketing Center, Institute of Nuclear Energy Research, Atomic Energy Council, Taoyuan 32546, Taiwan

⁶ Department of Cancer Systems Imaging, The University of Texas MD Anderson Cancer Center, Houston, TX 77030, USA

⁷ Renji Hospital, School of Medicine, Shanghai Jiao Tong University, Shanghai 200127, China

Correspondence should be addressed to David J. Yang; dyang@mdanderson.org

Received 22 September 2013; Accepted 22 September 2013

Copyright © 2013 David J. Yang et al. This is an open access article distributed under the Creative Commons Attribution License, which permits unrestricted use, distribution, and reproduction in any medium, provided the original work is properly cited.

Molecular imaging science has been focused on imaging guidance in the areas of targeting epigenetic abnormalities and tumor microenvironment in overcoming resistance in cancers. The use of image-guided technologies to select patient for personalized therapy and to monitor therapeutic outcomes is the focus of this special issue. For instance, mutations in the kinase domain of epidermal growth factor receptor (EGFR) have been associated with clinical responsiveness using tyrosine kinase inhibitors for nonsmall cell lung cancer (NSCLC). S. H.-H. Yeh et al. reported the feasibility of using morpholino-[I-124]IPQA as an in vivo PET imaging probe for the expression of different EGFR mutants in NSCLC. Their micro-PET imaging along with biologic validation indicated that [I-124]IPQA derivative might be a useful probe in selecting the patients with NSCLC for tyrosine kinase inhibitor therapy.

Molecular imaging enables the comprehensive characterization of therapeutic intervention and can be used in preclinical studies, pharmacokinetic (microdosing) studies, dose-finding studies, and proof-of-concept studies. F. Guerriero et al. reported the most adequate timing for imaging and kidney dosimetry in Lu-177 and Y-90 labeled DOTATATE and DOTATOC by SPECT in 1-2 scans.

Fluorodeoxyglucose (FDG) is a gold standard glycolytic agent in nuclear imaging. For instance, A. Bunevicius et al.

suggested that FDG PET might serve as an alternative and noninvasive tool to MRI and CT for the management of acute stroke patients. However, FDG has poor differentiation between inflammation/infection and tumor recurrence. To characterize cancers, new tracers have been focused on target expressions, pathway directed therapies, and cell functions in the intact organism. F.-L. Kong et al. reported promising theranostic radiotracers beyond FDG that are currently under preclinical development and clinic management in lymphoma. I.-H. Shih et al. also reported the alternative of using F-18 labeled alpha-methyltyrosine to assess amino acid transporter systems in mesothelioma models.

Topics covered in this special issue are advances in molecular imaging both in radioactive and nonradioactive applications in preclinical drug discovery, drug development, drug delivery, pharmacokinetics and pharmacodynamics, and differential diagnosis. For nonradioactive molecular imaging technology, F. C. Wong et al. reported photo affinity labeling using tissue-penetrating radiation (X-ray or gamma rays), which could overcome the tissue attenuation and irreversibly label membrane receptor proteins. They described that X-ray and gamma rays could induce affinity labeling of membrane receptors in a manner similar to UV with photo reactive ligands of the dopamine transporters, D2 dopamine receptors, and peripheral benzodiazepine receptors. P.-C. Chu et al.

reported that the brain tumor conditions on the distribution and dynamics of small molecule leakage into targeted regions of the brain could be influenced by focused ultrasound (FUS)-BBB opening. Their findings indicated that FUS-BBB opening might have the most significant permeability-enhancing effect on tumor peripheral. Their report provides useful information toward designing an optimized FUS-BBB opening strategy to deliver small-molecule therapeutic agents into brain tumors.

MRI has been proven to be a valuable tool to provide important information facilitating individualized image-guided treatment and personalized management for cancers. J.-H. Chen and M.-Y. Su reviewed the use of different MR imaging methods, including dynamic contrast-enhanced MRI proton MR spectroscopy, and diffusion-weighted MRI, to monitor and evaluate the treatment response. They also described how the changes of parameters measured at an early time after initiation of a drug regimen could predict final treatment outcome. H.-W. Kao et al. also reviewed advanced MR imaging techniques including cellularity, invasiveness, mitotic activity, angiogenesis, and necrosis in gliomas. Molecular imaging with MRI also permits mapping and measuring the rate of physiological, biochemical, and molecular process with the use of appropriate kinetic models. For instance, T. Y. Siow et al. described their MRI findings with increased nNOS activity in brain cortex and striatum after l-methyl-4-phenyl-1,2,3,6-tetrahydropyridine (MPTP) treatment. They concluded that the transient changes in hyperperfusion state in cerebral blood flow in the cortex and striatum might be an early indicator of neuronal inflammation.

T.-L. Yang et al. compared the diagnostic performance of digital breast tomosynthesis (DBT) and digital mammography (DM) for breast cancers. They concluded that adjunctive DBT provided exquisite information for mass lesion, focal asymmetry, and/or architecture distortion which could improve the diagnostic performance in mammography. Y.-C. Liu et al. reported the validation of the clinical significance of coronary artery calcium score (CACS) in predicting coronary artery disease (CAD) and cardiac events using a 64-slice coronary CT angiography. They concluded that CACS was significantly correlated with CAD and cardiac events.

The emergence of flat-detector X-ray angiography in conjunction with contrast medium injection and specialized reconstruction algorithms can provide not only high-quality and high-resolution CT-like images but also functional information. This improvement in imaging technology allows quantitative assessment of intracranial hemodynamics and subsequently in the same imaging session. S.-C. Hung et al. described the recent developments in the field of flat-detector imaging and shared their experience of applying this technology in neurovascular disorders such as acute ischemic stroke, cerebral aneurysm, and steno occlusive carotid diseases.

*David J. Yang
Fong Y. Tsai
Tomio Inoue
Mei-Hsiu Liao
Fan-Lin Kong
Shaoli Song*

Research Article

In Vivo Evidence of Increased nNOS Activity in Acute MPTP Neurotoxicity: A Functional Pharmacological MRI Study

Tiing Yee Siew,^{1,2} Chiao-Chi V. Chen,¹ Nina Wan,³ Kai-Ping N. Chow,⁴ and Chen Chang¹

¹ Institute of Biomedical Sciences, Academia Sinica, 128 Section 2, Academia Road, Nankang, Taipei 11529, Taiwan

² Department of Medical Imaging and Intervention, Chang-Gung Memorial Hospital, Chang-Gung University College of Medicine, Taoyuan 33302, Taiwan

³ School of Nursing, Queen's University, Kingston, ON, Canada K7L 3N6

⁴ Department of Microbiology and Immunology, Chang-Gung University, Taoyuan 33302, Taiwan

Correspondence should be addressed to Chen Chang: bmcchen@ibms.sinica.edu.tw

Received 13 January 2013; Revised 21 July 2013; Accepted 1 August 2013

Academic Editor: Tomio Inoue

Copyright © 2013 Tiing Yee Siew et al. This is an open access article distributed under the Creative Commons Attribution License, which permits unrestricted use, distribution, and reproduction in any medium, provided the original work is properly cited.

1-Methyl-4-phenyl-1,2,3,6-tetrahydropyridine (MPTP) is a neurotoxin commonly used to produce an animal model of Parkinson's disease. Previous studies have suggested a critical role for neuronal nitric oxide (NO) synthase- (nNOS-) derived NO in the pathogenesis of MPTP. However, NO activity is difficult to assess *in vivo* due to its extremely short biological half-life, and so *in vivo* evidence of NO involvement in MPTP neurotoxicity remains scarce. In the present study, we utilized flow-sensitive alternating inversion recovery sequences, *in vivo* localized proton magnetic resonance spectroscopy, and diffusion-weighted imaging to, respectively, assess the hemodynamics, metabolism, and cytotoxicity induced by MPTP. The role of NO in MPTP toxicity was clarified further by administering a selective nNOS inhibitor, 7-nitroindazole (7-NI), intraperitoneally to some of the experimental animals prior to MPTP challenge. The transient increase in cerebral blood flow (CBF) in the cortex and striatum induced by systemic injection of MPTP was completely prevented by pretreatment with 7-NI. We provide the first *in vivo* evidence of increased nNOS activity in acute MPTP-induced neurotoxicity. Although the observed CBF change may be independent of the toxicogenesis of MPTP, this transient hyperperfusion state may serve as an early indicator of neuroinflammation.

1. Introduction

Parkinson's disease (PD) is a neurodegenerative disorder that is caused by the progressive loss of dopaminergic (DAergic) neurons in the substantia nigra pars compacta (SNpc). The cardinal manifestations of this debilitating disease include muscle rigidity, uncontrolled tremor, and bradykinesia. Much of the insight into PD has come from the animal model, in which the condition is induced by administration of the toxin 1-methyl-4-phenyl-1,2,3,6-tetrahydropyridine (MPTP), which faithfully reproduces the pathological hallmarks of PD. MPTP is initially converted to its toxic metabolic form, 1-methyl-4-phenylpyridinium ion (MPP^+), *in vivo* by monoamine oxidase- (MAO)-B (MAO-B) [1]. MPP^+ subsequently accumulates in DAergic neurons through high-affinity dopamine transporters [2]. Once inside neurons, MPP^+ disrupts oxidative phosphorylation by inhibiting mitochondrial complex I of the electron transport chain [3–8]. It is

hypothesized that interference with the cellular respiratory machinery leads to rapid depletion of adenosine triphosphate (ATP) and eventually cell death. However, it appears that complex I activity requires reduction of more than 70% to cause significant energy depletion in nonsynaptic brain mitochondria [9] and an *in vivo* study has shown that MPTP causes only a transient 20% reduction in ATP level in the mouse striatum and midbrain [10]. Together these data argue that ATP deficit is the sole factor underlying MPTP-induced neuron loss.

In addition to the ATP-depletion hypothesis, it has been postulated that increased production of nitric oxide (NO) also contributes to MPTP-induced neurotoxicity [11–15]. The impaired oxidative phosphorylation after administrating MPTP causes activation of *N*-methyl-D-aspartate receptors with subsequent increase in the intracellular Ca^{2+} concentration. This leads to the activation of neuronal NO synthase

(nNOS), which is a calmodulin-dependent enzyme [16]. The subsequently produced NO combines with superoxide to form the free radical peroxynitrite [17], which in turn degrades into a more noxious hydroxyl radical to cause cell injury. Nevertheless, NO activity is difficult to assess *in vivo* due to its extremely short biological half-life of only a few seconds [18]. *In vivo* evidence of NO involvement in MPTP neurotoxicity remains scarce.

As well as playing a part in neuroinflammation, NO is known to play a pivotal role in the regulation of vascular tone [19, 20]. The central effect of NO in hemodynamic homeostasis provides a rationale for the present study, which examined the role of NO in the MPTP-induced neurotoxic cascade by monitoring alterations in CBF.

Over the past few decades, magnetic resonance imaging (MRI) has evolved into a powerful imaging modality that offers functional imaging in addition to anatomical information. Flow-sensitive alternating inversion recovery (FAIR) [21], a commonly used magnetic-resonance-based perfusion imaging technique, utilizes tissue water as an endogenous contrast agent to obtain tissue perfusion information. In addition to FAIR, functional imaging modalities such as diffusion-weighted imaging (DWI) and magnetic resonance spectroscopy (MRS) could provide useful information on cytotoxicity and metabolic changes. The noninvasiveness of these techniques enables repeated *in vivo* measurements with high temporal and spatial resolutions.

Combining these MRI techniques with pharmacological inquiries, termed pharmacological MRI (phMRI) [22–24], has provided a platform for investigating drug effects *in vivo*. The present study used phMRI to investigate the acute effects of MPTP on the rodent central nervous system (CNS). FAIR, DWI, and *in vivo* localized proton magnetic resonance spectroscopy (¹H-MRS) were used to, respectively, assess MPTP-induced hemodynamic perturbations, cytotoxicity, and metabolic changes. To further clarify the role of NO in MPTP toxicity, a selective nNOS inhibitor, 7-nitroindazole (7-NI) [25], was administered intraperitoneally (i.p.) to experimental animals prior to an MPTP challenge.

2. Materials and Methods

2.1. Animal Preparations. All experimental procedures were approved by the Institute of Animal Care and Utilization Committee at Academia Sinica, Taipei, Taiwan. Male Sprague-Dawley rats (4–5 months old) weighing 450–550 g were anesthetized i.p. with a mixture of urethane (800 mg/kg; Sigma, MO, USA) in normal saline and α -chloralose (40 mg/kg, Sigma) in polyethylene glycol (Merck, Darmstadt, Germany). Each rat was placed in the prone position and fitted with a custom-designed head-holder. The rats were set up as described previously [26]. Briefly, one femoral vein was cannulated with PE-50 tubing for drug/test solution administration, and an endotracheal tube (PE-280) was inserted for artificial ventilation with an animal ventilator (Model 683, Harvard Instruments, South Natick, MA, USA). The expiratory CO₂ concentration, which was monitored with the aid of a capnograph (Normocap 200, Datex, Helsinki, Finland), was maintained at 3.5–4.5% by adjusting the tidal

volume and ventilation rate. An intravenous (i.v.) injection of a muscle relaxant, gallamine (Sigma), was used to prevent spontaneous ventilation and movement during the image-acquisition period. The initial dose of gallamine was 12 mgs and the maintenance dosage was 6 mg/h. Body temperature was detected by an optical fiber thermoprobe (Model SFF-5, Luxtron, Santa Clara, CA, USA) connected to a Fluoroptic thermometer (Model 790, Luxtron) and was maintained at 37°C by a ceramic heater (Model TH-8105, Tashin, Taipei, Taiwan) throughout the MRI measurements.

The rats were divided into three groups, with six rats in each group. In the first group, the rats received a single, i.v. injection of MPTP (15 mg/kg, Sigma), while the age-matched control group received an i.v. injection of normal saline. The third group of rats received a single dose of 7-NI (50 mg/kg i.p., Sigma) 30 min prior to the i.v. administration of 15 mg/kg MPTP. As shown previously [27], maximal NOS inhibition in the rat brain is manifested within 30 min following the injection of 7-NI i.p.

2.2. MRI Protocols. All magnetic resonance experiments were performed on a 4.7-T Biospec 47/40 spectrometer with an active shielding gradient (5.6 G/cm in 500 μ s). A 20 cm birdcage coil was used for radiofrequency (RF) excitation, and a 2 cm diameter surface coil was used for signal reception.

Conventional DWI was employed using a pulsed-gradient spin-echo diffusion method, with a repetition time (TR) of 2000 ms, an echo time (TE) of 59 ms, a gradient pulse duration of 20 ms, a time interval between diffusion gradient pulses of 27 ms, and a *b* value of 1300 s/mm². Images were obtained using a 5 cm field of view (FOV), a slice thickness of 2 mm, a 256 × 128 matrix size that was zero filled to 256 × 256, and a total imaging time of 4 min 17 s. The diffusion-sensitive gradients were applied in the read (*x*) direction before and after the refocusing pulse. Hermite-shaped RF pulses with durations of 3 and 1.86 ms were used for the excitation and refocusing pulses, respectively.

The FAIR experiment was implemented with inversion recovery fast spin-echo (IR-FSE) sequences with and without a slice-selective gradient during an inversion pulse. Slice-selective IR-FSE (ssIR-FSE) and non-slice-selective IR-FSE (nsIR-FSE) images were collected using a TR of 3 s, a TE of 20 ms, and an effective TE of 50 ms with an echo train length of 4, a slice thickness of 2 mm, an FOV of 4 cm, an inversion time (TI) of 1.5 s, and a matrix size of 256 × 128. A slab thickness of 5 mm was inverted for the ssIR-FSE images and a hyperbolic secant pulse was used for inversion with a pulse length of 8 ms. The *T*₁ was measured from nsIR-FSE with TI values of 0.5, 0.9, 1.1, 1.3, 1.5, and 1.9 s.

A point-resolved spectroscopy (PRESS) sequence was used for localized spectroscopy with the following parameters: 5 × 5 × 5 mm³ voxel located at the striatal region, spectral width = 4000 Hz, TR = 2 s, TE = 136 ms, number of average = 256, and total scanning time = 8 min 32 s. Water suppression was achieved by chemical-shift-selective saturation, whereby three consecutive Hermite-shaped RF pulses, each of 15 ms duration, are applied followed by spoiling gradients preceding the PRESS sequence. Spectral assignments of the

resonance lines *in vivo* were based on the results from *in vitro* ^1H -MRS.

2.3. Data Analysis. All data were processed using commercially available image-analysis software MRVision (MRVision Co., Menlo Park, CA, USA). The T_1 maps were produced using a nonlinear, three-parameter fitting procedure on a pixel-by-pixel basis. The FAIR images were generated by the subtraction of nsIR-FSE images from their corresponding ssIR-FSE images. The resulting images (ΔM) were used to generate CBF maps according to the following:

$$f = \frac{\lambda \cdot \Delta M}{2M_0 \text{TI} \exp(-\text{TI}/T_1)}, \quad (1)$$

where λ is the tissue-blood partition coefficient (0.9 mL/g) [28], M_0 is the thermal equilibrium magnetization, and f is the calculated CBF (expressed as mL/min/100 g of tissue, or mL/min/100 g). The M_0 maps were calculated based on the T_1 maps and nsIR-FSE images using the following:

$$M_{\text{ns}}(\text{TI}) = M_0 \left(1 - 2 \exp \left(\frac{\text{TI}}{T_1} \right) \right), \quad (2)$$

where M_{ns} is the magnetization in nonselective inversion.

Two regions of interest (ROIs) were analyzed in all cases: the entire cerebral cortex and the striatum. The average CBF was calculated within each ROI. All results are expressed as mean \pm SD values. Student's *t*-test was used for statistical evaluations, with the level of statistical significance set at $P < 0.05$.

3. Results

Administration of MPTP did not significantly change either the signal intensity or metabolite concentrations on DWI and *in vivo* ^1H -MRS, respectively, throughout the 6 h experimental period (data not shown). However, FAIR revealed significant alterations in regional CBF. Figure 1 shows representative temporal CBF profiles from an MPTP-treated rat, a 7-NI-pretreated and MPTP-treated rat, and a saline-treated (control) rat. The basal CBFs in the cortex and striatum were 109 ± 22 and 102 ± 17 mL/min/100 g, respectively; these values are consistent with those reported previously [21, 29]. There were no significant changes in CBF in brain region over time in the control rats injected with saline alone. However, in rats treated with MPTP alone, there were progressive elevations of CBFs in both the cortex and striatum. In both regions, the changes in CBF became significant at 29 min post-MPTP injection ($P < 0.05$ for the striatum and $P < 0.001$ for the cortex). The CBF was significantly higher in the cortex than in the striatum until 63 min after MPTP injection ($P < 0.05$).

As shown in Figure 2, the cortical CBF of MPTP-injected rats was significantly increased at 29 min after injection (267 ± 51 mL/min/100 g, $P < 0.001$) reached its peak at 63 min (329 ± 27 mL/min/100 g, $P < 0.001$) but subsequently returned gradually to the control level at 165 min (147 ± 51 mL/min/100 g), where it remained until the end of the experiment at 369 min after injection. The CBF increased less in the striatum than in the cortex at 29 min

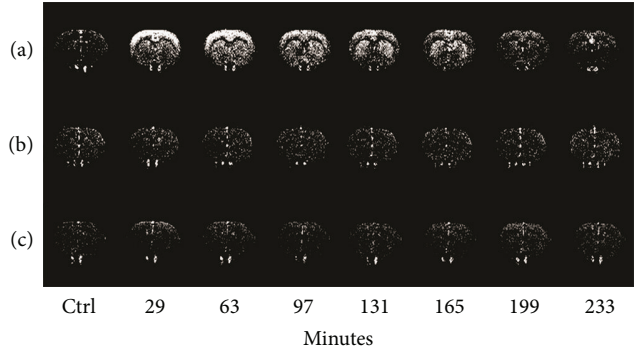


FIGURE 1: Temporal FAIR images. Representative temporal FAIR images from (a) an MPTP-treated rat, (b) a 7-NI-pretreated and MPTP-treated rat, and (c) a saline-treated (control) rat at baseline (ctrl) and various times postinjection. Progressive elevations of CBF were observed in the cortex and striatum of rats treated with MPTP alone. These elevations were prevented by pretreatment with 7-NI. There were essentially no changes in CBF in either brain region over time in the control rats.

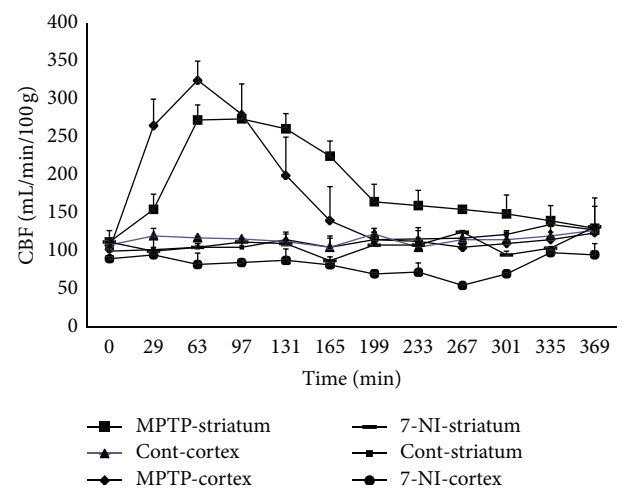


FIGURE 2: CBF changes over time. Temporal changes in CBF in the cortical and striatal regions of saline-treated (control (Cont)) and MPTP-treated rats. Pretreatment with 7-NI prevented the elevation of CBF induced by MPTP. Data are mean and SD values.

(158 ± 46 mL/min/100 g, $P < 0.05$) and then reached its maximum at 97 min after injection (273 ± 42 mL/min/100 g, $P < 0.001$) but subsequently returned gradually to the control level at 335 min (140 ± 21 mL/min/100 g). The increase in CBF lasted longer in the striatum than in the cortex.

Pretreatment with 7-NI did not change basal striatal CBF, but it significantly attenuated the basal cortical CBF before MPTP treatment ($P < 0.01$). 7-NI completely blocked the MPTP-induced increase in CBF over time in both the cerebral cortex and the striatum. There was no significant MPTP-induced change in CBF in either the cerebral cortex or the striatum throughout the 6 h experimental period following pretreatment with 7-NI.

4. Discussion

A possible role of NO in the pathogenic mechanism underlying the actions of MPTP has received considerable attention. There are several lines of evidence that implicated that neuronally derived NO at least partly mediates MPTP-induced SNpc neuronal death. It was previously shown that MPTP neurotoxicity in mice results in an increase in striatal 3-nitrotyrosine (a product of NO and superoxide), which can be attenuated by the administration of 7-NI [30]. In addition, 7-NI can significantly prevent MPTP-related neurotoxicity, as evidenced by the greater number of tyrosine-hydroxylase-immunostained neurons in 7-NI-pretreated mice [15]. Moreover, this protective effect occurred in a dose-dependent manner, indicating that MPTP-induced toxicity is directly proportional to nNOS activity. Further evidence comes from the observation that nNOS-deficient mice are twofold less affected by MPTP than wild-type and heterozygous mice [31]. Together these findings suggest that nNOS-derived NO plays a critical role in the neurotoxicity of MPTP. Although previous studies also suggested that inducible nitric oxide synthase (iNOS) activity was increased after MPTP exposure [31, 32]; due to the relative selectivity of 7-NI, we thus concluded that the transient cerebral hyperperfusion as showed in our study was a result of increased nNOS activity rather than the iNOS.

FAIR is recognized as a completely noninvasive means of visualizing tissue perfusion. Secondary to its noninvasiveness, this technique allows multiple repeated measurements of CBF at sufficiently high temporal and spatial resolutions. Our results obtained using FAIR-phMRI are the first to provide *in vivo* evidence of increased nNOS activity in acute MPTP-induced neurotoxicity. Although FAIR revealed remarkable changes in CBF following MPTP administration, this alteration was not accompanied by metabolic or structural lesions, as evaluated by MRS and DWI. This suggests that FAIR remains a superior tool for detecting early changes in MPTP-induced neurotoxicity.

Apparent diffusion coefficient (ADC) is a DWI-derived quantitative parameter that reflects the degree of tissue water diffusivity restriction. The reduction of ADC has been related to various biological conditions, particularly in the processes that involve cytotoxic edema or increased cellularity (such as inflammation). It has been reported [33] that there was no significant difference of regional ADC values in various brain regions between the PD patients and control group. This is consistent with the result in the present study of rodent PD model. On the other hand, *in vivo* ¹H-MRS detects low concentration neuronal metabolites to provide surrogate markers for neuronal damage. Previous *in vivo* ¹H-MRS studies [34–36] showed decreased N-acetylaspartate/creatinine ratio in the lentiform nuclei and striatum of PD patients. However, in the present study, *in vivo* ¹H-MRS revealed no significant signal change in rat brain after acute MPTP exposure; only CBF change was observed. It could be largely due to the fact that NO is an obligatory regulator of cerebral hemodynamics, where CBF is highly sensitive to the alterations of NO level. Whereas under current dosing regimen, the produced NO level may not be sufficiently high to cause neuronal damage that can be detected by ¹H-MRS.

The increase in CBF revealed in our study is probably due to an NO-cyclic guanosine monophosphate (cGMP)-mediated vasodilatory effect [19, 37], which might be independent of the toxicogenesis of MPTP. However, given the strong oxidative power of NO, it is likely that it is at least partly involved in the neurotoxicity of MPTP. The main aim of this study was to demonstrate the spatial-temporal distribution of NO in MPTP-induced toxicity. We believe that our findings will facilitate future studies on the role of NO.

Perfusion neuroimaging studies, either by single-photon emission computed tomography [38] or MRI [39], have generally confirmed the presence of a hypoperfusion state in the gray matter of PD patients. These studies have demonstrated that several cerebral regions, including the posterior parieto-occipital cortex, precuneus, cuneus, and middle frontal gyri, experience decreases in regional perfusion. Paradoxically, the present study revealed a transient hyperperfusion in the cerebral cortex and striatum in the MPTP animal model, which may be related to overproduction of NO. This finding suggests that a similar hyperperfusion state is present in human PD, and this may represent an early neuroinflammation in the brain. Further research should be conducted to examine the existence of this early hemodynamic alteration in human PD.

We found that MPTP injection caused a persistent elevation in regional CBF in the striatum, suggesting that this brain area is a major source of the neurotoxic NO. Consistent with this notion, the striatum contains a rich density of nNOS-positive neurons and fibers [40]. In contrast, there is no evidence for nNOS immunoreactivity in neurons or fibers in the vicinity of the SNpc [40]. Hypothetically, dopamine nerve terminals in the striatum become the primary target for NO, followed by a secondary retrodegeneration of dopamine cell bodies in the SNpc [41]. Consistent with this hypothesis is the observation that MPP⁺ accumulates primarily in the striatal dopamine terminals, but not in SNpc DAergic neuronal cell bodies [42].

While the cerebral cortex exhibits less nNOS activity, there is one possible explanation for the more-prominent increase in the MPTP-induced CBF increase in this region: in addition to the NO-cGMP-mediated direct relaxation of the vascular smooth muscle, the vasodilation effect of NO may also arise from its counteraction to endogenous vasoconstrictors [20]. The observed change in CBF is hence a complex interplay between NO and other vasoactive substances (e.g., angiotensin). Therefore, variations in CBF increases across different brain regions do not necessarily reflect the proportional nNOS activities, since it is likely that there are distinct basal regulation mechanisms in these regions.

It is known that NO plays an important role in the normal regulation of cerebral vascular tone [19]. Our findings also show that 7-NI attenuated the basal cortical CBF prior to MPTP administration. This is consistent with previous reports that 7-NI injection results in a decrease in local CBF in the rat brain [43, 44]. It is worth noting that basal striatal CBF was unaffected by 7-NI injection in the present study, which might have been due to the much lower dosage of 7-NI used.

A major drawback of the present study is the lack of perfusion measurements in the SNpc, which is thought to be a site of PD lesions. This was mainly due to technical

limitations associated with the use of the single-slice FAIR technique in this work. Multislice FAIR [45] could be implemented to include measurement of SNpc by increasing the slab thickness of slice-selective inversion such that several slices were contained within it. However, multislice FAIR imaging presents two major problems: (1) the integrity of selective inversion across all slices is questionable (i.e., the imperfect inversion pulse profile across slices causes significant errors) [46], and (2) the multislice FAIR approach introduces an increased transit time delay for those slices farther from the edge of the inversion slice [47]. Together, these limitations hinder accurate measurements using multislice FAIR. Nevertheless, the present results warrant further study of the hemodynamics of the SNpc in acute MPTP toxicity.

It has been reported that rats are less susceptible to systemic MPTP toxicity than mice and primates [48], which might be due to systemic MPTP being extensively metabolized by MAO-B in the rat blood-brain barrier, thereby converting MPTP into MPP⁺ [49]. MPP⁺ is a polar molecule that does not readily cross biological membranes, hence preventing it from reaching sites of injury in sufficient concentrations. This view is supported by the direct infusion of MPTP into the rat SNpc causing a selective 50–70% loss of DAergic neurons, without affecting other neurons or glia at the injection site [50]. Therefore, the differences in susceptibility between species probably arise from their distinct pharmacokinetic profiles. Such differences may have a relatively minimal impact on pharmacodynamic investigations, as in the present research.

As discussed above, several previous studies have shown that 7-NI reduces MPTP-induced neurotoxicity in several animal models, presumably through the inhibition of nNOS. However, Castagnoli et al. demonstrated that 7-NI can also inhibit the MAO-B-catalyzed oxidation of MPTP to MPP⁺ [51]. In sharp contrast, Schulz et al. reported no effect of 7-NI on MAO-B activity [30]. Hence, the exact mechanism underlying the neuroprotective effect of 7-NI against MPTP toxicity remains to be established. Recent data from an *in vitro* study suggested that 7-NI has only a mild MAO-B-inhibitory effect [52]. It is unlikely that such inhibition could affect the interpretation of the results in the present study.

5. Conclusion

In summary, this study has demonstrated that systemic administration of MPTP leads to prominent changes in CBF in striatal and cortical regions of the rodent CNS. Such increases can be prevented by pretreatment with the selective nNOS inhibitor, 7-NI. Thus, our results provide the first *in vivo* evidence of NO production in the acute neurotoxicity of MPTP. Given the similarity between the MPTP model and human parkinsonism, this cascade of events may also occur in PD.

Abbreviations

- 7-NI: 7-Nitroindazole
- ADC: Apparent diffusion coefficient
- ATP: Adenosine triphosphate

CBF:	Cerebral blood flow
cGMP:	Cyclic guanosine monophosphate
CNS:	Central nervous system
DAergic:	Dopaminergic
DWI:	Diffusion-weighted imaging
FAIR:	Flow-sensitive alternating inversion recovery
FOV:	Field of view
i.p.:	Intraperitoneally
IR-FSE:	Inversion recovery fast spin-echo
i.v.:	Intravenous
MAO:	Monoamine oxidase
MPP ⁺ :	1-Methyl-4-phenylpyridinium ion
MPTP:	1-Methyl-4-phenyl-1,2,3,6-tetrahydropyridine
MRI:	Magnetic resonance imaging
MRS:	Magnetic resonance spectroscopy
iNOS:	Inducible nitric oxide synthase
nNOS:	Neuronal nitric oxide synthase
NO:	Nitric oxide
nsIR-FSE:	Non-slice-selective IR-FSE
PD:	Parkinson's disease
phMRI:	Pharmacological MRI
PRESS:	Point-resolved spectroscopy
RF:	Radiofrequency
ROI:	Region-of-interest
SD:	Standard deviation
SNpc:	Substantia nigra pars compacta
ssIR-FSE:	Slice-selective IR-FSE
TE:	Echo time
TI:	Inversion time
TR:	Repetition time.

Conflict of Interests

The authors declare no conflict financial of interests.

Acknowledgments

The authors acknowledge technical support from the Functional and Micro-Magnetic Resonance Imaging Center supported by the National Research Program for Genomic Medicine, National Science Council, Taiwan, ROC. The authors thank Mr. Y. L. Pan for providing technological support of MRI.

References

- [1] J. W. Langston, I. Irwin, E. B. Langston, and L. S. Forno, “1-Methyl-4-phenylpyridinium ion (MPP⁺): identification of a metabolite of MPTP, a toxin selective to the substantia nigra,” *Neuroscience Letters*, vol. 48, no. 1, pp. 87–92, 1984.
- [2] J. A. Javitch and S. H. Snyder, “Uptake of MPP(+) by dopamine neurons explains selectivity of Parkinsonism-inducing neurotoxin, MPTP,” *European Journal of Pharmacology*, vol. 106, no. 2, pp. 455–456, 1984.
- [3] V. G. Desai, R. J. Feuers, R. W. Hart, and S. F. Ali, “MPP+-induced neurotoxicity in mouse is age-dependent: evidenced by the selective inhibition of complexes of electron transport,” *Brain Research*, vol. 715, no. 1-2, pp. 1–8, 1996.

- [4] J. B. Schulz, D. R. Henshaw, R. T. Matthews, and M. F. Beal, "Coenzyme Q10 and nicotinamide and a free radical spin trap protect against MPTP neurotoxicity," *Experimental Neurology*, vol. 132, no. 2, pp. 279–283, 1995.
- [5] R. R. Ramsay, J. I. Salach, and T. P. Singer, "Uptake of the neurotoxin 1-methyl-4-phenylpyridine (MPP⁺) by mitochondria and its relation to the inhibition of the mitochondrial oxidation of NAD⁺-linked substrates by MPP⁺," *Biochemical and Biophysical Research Communications*, vol. 134, no. 2, pp. 743–748, 1986.
- [6] R. R. Ramsay, J. Dadgar, A. Trevor, and T. P. Singer, "Energy-driven uptake of N-methyl-4-phenylpyridine by brain mitochondria mediates the neurotoxicity of MPTP," *Life Sciences*, vol. 39, no. 7, pp. 581–588, 1986.
- [7] W. J. Nicklas, S. K. Youngster, M. V. Kindt, and R. E. Heikkila, "MPTP, MPP⁺ and mitochondrial function," *Life Sciences*, vol. 40, no. 8, pp. 721–729, 1987.
- [8] Y. Mizuno, N. Sone, and T. Saitoh, "Effects of 1-methyl-4-phenyl-1,2,3,6-tetrahydropyridine and 1-methyl-4-phenylpyridinium ion on activities of the enzymes in the electron transport system in mouse brain," *Journal of Neurochemistry*, vol. 48, no. 6, pp. 1787–1793, 1987.
- [9] G. P. Davey and J. B. Clark, "Threshold effects and control of oxidative phosphorylation in nonsynaptic rat brain mitochondria," *Journal of Neurochemistry*, vol. 66, no. 4, pp. 1617–1624, 1996.
- [10] P. Chan, L. E. DeLaney, I. Irwin, J. W. Langston, and D. di Monte, "Rapid ATP loss caused by 1-methyl-4-phenyl-1,2,3,6-tetrahydropyridine in mouse brain," *Journal of Neurochemistry*, vol. 57, no. 1, pp. 348–351, 1991.
- [11] J. B. Schulz, R. T. Matthews, B. G. Jenkins et al., "Blockade of neuronal nitric oxide synthase protects against excitotoxicity in vivo," *Journal of Neuroscience*, vol. 15, no. 12, pp. 8419–8429, 1995.
- [12] J. B. Schulz, R. T. Matthews, T. Klockgether, J. Dichgans, and M. F. Beal, "The role of mitochondrial dysfunction and neuronal nitric oxide in animal models of neurodegenerative diseases," *Molecular and Cellular Biochemistry*, vol. 174, no. 1-2, pp. 193–197, 1997.
- [13] J. Ara, S. Przedborski, A. B. Naini et al., "Inactivation of tyrosine hydroxylase by nitration following exposure to peroxynitrite and 1-methyl-4-phenyl-1,2,3,6-tetrahydropyridine (MPTP)," *Proceedings of the National Academy of Sciences of the United States of America*, vol. 95, no. 13, pp. 7659–7663, 1998.
- [14] T. Spencer Smith, R. H. Swerdlow, W. Davis Parker Jr., and J. P. Bennett Jr., "Reduction of MPP⁺-induced hydroxyl radical formation and nigrostriatal MPTP toxicity by inhibiting nitric oxide synthase," *NeuroReport*, vol. 5, no. 18, pp. 2598–2600, 1994.
- [15] S. Przedborski, V. Jackson-Lewis, R. Yokoyama, T. Shibata, V. L. Dawson, and T. M. Dawson, "Role of neuronal nitric oxide in 1-methyl-4-phenyl-1,2,3,6-tetrahydropyridine (MPTP)-induced dopaminergic neurotoxicity," *Proceedings of the National Academy of Sciences of the United States of America*, vol. 93, no. 10, pp. 4565–4571, 1996.
- [16] J. Garthwaite, S. L. Charles, and R. Chess-Williams, "Endothelium-derived relaxing factor release on activation of NMDA receptors suggests role as intercellular messenger in the brain," *Nature*, vol. 336, no. 6197, pp. 385–388, 1988.
- [17] N. Hogg, V. M. Darley-Usmar, M. T. Wilson, and S. Moncada, "Production of hydroxyl radicals from the simultaneous generation of superoxide and nitric oxide," *Biochemical Journal*, vol. 281, no. 2, pp. 419–424, 1992.
- [18] T. S. Hakim, K. Sugimori, E. M. Camporesi, and G. Andersen, "Half-life of nitric oxide in aqueous solutions with and without haemoglobin," *Physiological Measurement*, vol. 17, no. 4, pp. 267–277, 1996.
- [19] S. Moncada, R. M. J. Palmer, and E. A. Higgs, "Nitric oxide: physiology, pathophysiology, and pharmacology," *Pharmacological Reviews*, vol. 43, no. 2, pp. 109–142, 1991.
- [20] V. Bauer and R. Sotníková, "Nitric oxide: the endothelium-derived relaxing factor and its role in endothelial functions," *General Physiology and Biophysics*, vol. 29, no. 4, pp. 319–340, 2010.
- [21] S.-G. Kim, "Quantification of relative cerebral blood flow change by flow-sensitive alternating inversion recovery (FAIR) technique: application to functional mapping," *Magnetic Resonance in Medicine*, vol. 34, no. 3, pp. 293–301, 1995.
- [22] R. A. Leslie and M. F. James, "Pharmacological magnetic resonance imaging: a new application for functional MRI," *Trends in Pharmacological Sciences*, vol. 21, no. 8, pp. 314–318, 2000.
- [23] N. Easton, F. H. Marshall, C. A. Marsden, and K. C. F. Fone, "Mapping the central effects of methylphenidate in the rat using pharmacological MRI BOLD contrast," *Neuropharmacology*, vol. 57, no. 7-8, pp. 653–664, 2009.
- [24] C. Martin and N. R. Sibson, "Pharmacological MRI in animal models: a useful tool for 5-HT research?" *Neuropharmacology*, vol. 55, no. 6, pp. 1038–1047, 2008.
- [25] G. J. Southan and C. Szabó, "Selective pharmacological inhibition of distinct nitric oxide synthase isoforms," *Biochemical Pharmacology*, vol. 51, no. 4, pp. 383–394, 1996.
- [26] W. T. Lee, H. S. Yin, and Y. Z. Shen, "The mechanisms of neuronal death produced by mitochondrial toxin 3-nitropropionic acid: the roles of N-methyl-D-aspartate glutamate receptors and mitochondrial calcium overload," *Neuroscience*, vol. 112, no. 3, pp. 707–716, 2002.
- [27] G. M. Mackenzie, M. J. Jackson, P. Jenner, and C. D. Marsden, "Nitric oxide synthase inhibition and MPTP-induced toxicity in the common marmoset," *Synapse*, vol. 26, pp. 301–316, 1997.
- [28] P. Herscovitch and M. E. Raichle, "What is the correct value for the brain-blood partition coefficient for water?" *Journal of Cerebral Blood Flow and Metabolism*, vol. 5, no. 1, pp. 65–69, 1985.
- [29] N. V. Tsekos, F. Zhang, H. Merkle, M. Nagayama, C. Iadecola, and S.-G. Kim, "Quantitative measurements of cerebral blood flow in rats using the FAIR technique: correlation with previous iodoantipyrine autoradiographic studies," *Magnetic Resonance in Medicine*, vol. 39, no. 4, pp. 564–573, 1998.
- [30] J. B. Schulz, R. T. Matthews, M. M. K. Muqit, S. E. Browne, and M. F. Beal, "Inhibition of neuronal nitric oxide synthase by 7-nitroindazole protects against MPTP-induced neurotoxicity in mice," *Journal of Neurochemistry*, vol. 64, no. 2, pp. 936–939, 1995.
- [31] T. Dehmer, J. Lindenau, S. Haid, J. Dichgans, and J. B. Schulz, "Deficiency of inducible nitric oxide synthase protects against MPTP toxicity in vivo," *Journal of Neurochemistry*, vol. 74, no. 5, pp. 2213–2216, 2000.
- [32] G. T. Liberatore, V. Jackson-Lewis, S. Vukosavic et al., "Inducible nitric oxide synthase stimulates dopaminergic neurodegeneration in the MPTP model of Parkinson disease," *Nature Medicine*, vol. 5, no. 12, pp. 1403–1409, 1999.
- [33] B. Degirmenci, M. Yaman, A. Haktanir, R. Albayrak, M. Acar, and G. Caliskan, "The effects of levodopa use on diffusion coefficients in various brain regions in Parkinson's disease," *Neuroscience Letters*, vol. 416, no. 3, pp. 294–298, 2007.

- [34] F. Federico, I. L. Simone, V. Lucivero et al., "Proton magnetic resonance spectroscopy in Parkinson's disease and atypical parkinsonian disorders," *Movement Disorders*, vol. 12, no. 6, pp. 903–909, 1997.
- [35] F. Federico, I. L. Simone, V. Lucivero et al., "Proton magnetic resonance spectroscopy in Parkinson's disease and progressive supranuclear palsy," *Journal of Neurology Neurosurgery and Psychiatry*, vol. 62, no. 3, pp. 239–242, 1997.
- [36] C. E. Clarke and M. Lowry, "Systematic review of proton magnetic resonance spectroscopy of the striatum in parkinsonian syndromes," *European Journal of Neurology*, vol. 8, no. 6, pp. 573–577, 2001.
- [37] F. Murad, "Cyclic guanosine monophosphate as a mediator of vasodilation," *Journal of Clinical Investigation*, vol. 78, no. 1, pp. 1–5, 1986.
- [38] J.-L. Hsu, T.-P. Jung, C.-Y. Hsu et al., "Regional CBF changes in Parkinson's disease: a correlation with motor dysfunction," *European Journal of Nuclear Medicine and Molecular Imaging*, vol. 34, no. 9, pp. 1458–1466, 2007.
- [39] T. R. Melzer, R. Watts, M. R. MacAskill et al., "Arterial spin labelling reveals an abnormal cerebral perfusion pattern in Parkinson's disease," *Brain*, vol. 134, no. 3, pp. 845–855, 2011.
- [40] D. S. Bredt, C. E. Glatt, P. M. Hwang, M. Fotuhi, T. M. Dawson, and S. H. Snyder, "Nitric oxide synthase protein and mRNA are discretely localized in neuronal populations of the mammalian CNS together with NADPH diaphorase," *Neuron*, vol. 7, no. 4, pp. 615–624, 1991.
- [41] S. Przedborski, M. Levivier, H. Jiang et al., "Dose-dependent lesions of the dopaminergic nigrostriatal pathway induced by intrastriatal injection of 6-hydroxydopamine," *Neuroscience*, vol. 67, no. 3, pp. 631–647, 1995.
- [42] M. Herkenham, M. D. Little, K. Bankiewicz, S.-C. Yang, S. P. Markey, and J. N. Johannessen, "Selective retention of MPP+ within the monoaminergic systems of the primate brain following MPTP administration: an in vivo autoradiographic study," *Neuroscience*, vol. 40, no. 1, pp. 133–158, 1991.
- [43] K. Tanaka, Y. Fukuuchi, S. Gomi et al., "Inhibition of nitric oxide synthesis impairs autoregulation of local cerebral blood flow in the rat," *NeuroReport*, vol. 4, no. 3, pp. 267–270, 1993.
- [44] P. A. T. Kelly, I. M. Ritchie, and G. W. Arbuthnott, "Inhibition of neuronal nitric oxide synthase by 7-nitroindazole: effects upon local cerebral blood flow and glucose use in the rat," *Journal of Cerebral Blood Flow and Metabolism*, vol. 15, no. 5, pp. 766–773, 1995.
- [45] S.-G. Kim, N. V. Tsekos, and J. Ashe, "Multi-slice perfusion-based functional MRI using the FAIR technique: comparison of CBF and BOLD effects," *NMR in Biomedicine*, vol. 10, no. 4–5, pp. 191–196, 1997.
- [46] L. R. Frank, E. C. Wong, and R. B. Buxton, "Slice profile effects in adiabatic inversion: application to multislice perfusion imaging," *Magnetic Resonance in Medicine*, vol. 38, no. 4, pp. 558–564, 1997.
- [47] F. Calamante, D. L. Thomas, G. S. Pell, J. Wiersma, and R. Turner, "Measuring cerebral blood flow using magnetic resonance imaging techniques," *Journal of Cerebral Blood Flow and Metabolism*, vol. 19, no. 7, pp. 701–735, 1999.
- [48] A. Giovanni, B.-A. Sieber, R. E. Heikkila, and P. K. Sonsalla, "Studies on species sensitivity to the dopaminergic neurotoxin 1-methyl-4-phenyl-1,2,3,6-tetrahydropyridine. Part 1: systemic administration," *Journal of Pharmacology and Experimental Therapeutics*, vol. 270, no. 3, pp. 1000–1007, 1994.
- [49] R. N. Kalaria, M. J. Mitchell, and S. I. Harik, "Correlation of 1-methyl-4-phenyl-1,2,3,6-tetrahydropyridine neurotoxicity with blood-brain barrier monoamine oxidase activity," *Proceedings of the National Academy of Sciences of the United States of America*, vol. 84, no. 10, pp. 3521–3525, 1987.
- [50] L. M. Sayre, P. K. Arora, L. A. Iacofano, and S. I. Harik, "Comparative toxicity of MPTP, MPP+ and 3,3-dimethyl-MPD⁺ to dopaminergic neurons of the rat substantia nigra," *European Journal of Pharmacology*, vol. 124, no. 1–2, pp. 171–174, 1986.
- [51] K. Castagnoli, S. Palmer, A. Anderson, T. Bueters, and N. Castagnoli Jr., "The neuronal nitric oxide synthase inhibitor 7-nitroindazole also inhibits the monoamine oxidase-B-catalyzed oxidation of 1-methyl-4-phenyl-1,2,3,6-tetrahydropyridine," *Chemical Research in Toxicology*, vol. 10, no. 4, pp. 364–368, 1997.
- [52] B. Thomas, K. S. Saravanan, and K. P. Mohanakumar, "In vitro and in vivo evidences that antioxidant action contributes to the neuroprotective effects of the neuronal nitric oxide synthase and monoamine oxidase-B inhibitor, 7-nitroindazole," *Neurochemistry International*, vol. 52, no. 6, pp. 990–1001, 2008.

Research Article

Molecular Imaging of Nonsmall Cell Lung Carcinomas Expressing Active Mutant EGFR Kinase Using PET with [¹²⁴I]-Morpholino-IPQA

Skye Hsin-Hsien Yeh,^{1,2,3,4} Chien-Feng Lin,¹ Fan-Lin Kong,⁵ Hsin-Ell Wang,² Ya-Ju Hsieh,⁶ Juri G. Gelovani,⁷ and Ren-Shyan Liu^{1,4,8}

¹ National PET/Cyclotron Center, Department of Nuclear Medicine, Taipei Veterans General Hospital, Taiwan

² Department of Biomedical Imaging and Radiological Sciences, National Yang-Ming University, Taipei, Taiwan

³ Biophotonic and Molecular Imaging Research Center, National Yang-Ming University, Taipei, Taiwan

⁴ Taiwan Mouse Clinic, National Comprehensive Mouse Phenotyping and Drug Testing Center, Taiwan

⁵ Department of Experimental Diagnostic Imaging, The University of Texas MD Anderson Cancer Center, TX, USA

⁶ Department of Medicinal Imaging and Radiological Sciences, College of Health Sciences, Kaohsiung Medical University, Kaohsiung, Taiwan

⁷ Department of Biomedical Engineering, Wayne State University, MI, USA

⁸ Department of Nuclear Medicine, National Yang-Ming University School of Medicine, Taiwan

Correspondence should be addressed to Ren-Shyan Liu; rsliu@vghtpe.gov.tw

Received 25 April 2013; Revised 11 June 2013; Accepted 14 June 2013

Academic Editor: Shaoli Song

Copyright © 2013 Skye Hsin-Hsien Yeh et al. This is an open access article distributed under the Creative Commons Attribution License, which permits unrestricted use, distribution, and reproduction in any medium, provided the original work is properly cited.

Mutations in the kinase domain of epidermal growth factor receptor (EGFR) have high levels of basal receptor phosphorylation and are associated with clinical responsiveness to Iressa in patients with nonsmall cell lung cancer (NSCLC). This study aimed to assess the feasibility of morpholino-[¹²⁴I]IPQA derivative as an *in vivo* PET imaging tool for the expression of different EGFR mutants in NSCLC. *In vitro* radiotracer accumulation and washout studies demonstrated a rapid accumulation and progressive retention after washout of morpholino-[¹³¹I]IPQA derivative in high EGFR-expressing H1299 NSCLC derivative cell lines (L858R and E746-A750 del cell lines), but not in EGFR-transfected H1299 cell line and vector-transfected H1299 cell line. Using the morpholino-[¹²⁴I]IPQA derivative, we obtained noninvasive microPET images of EGFR activity in L858R and E746-A750 del subcutaneous tumor xenografts, but not in subcutaneous tumor xenografts grown from control cell line. Different EGFR mutant (activity) tumors have a different morpholino-[¹²⁴I]IPQA derivative uptake. However, it still needs to modify the structure of IPQA to increase its water solubility and reduce hepatobiliary clearance. Morpholino-[¹²⁴I]IPQA derivative may be a potential probe for selection of the candidate patients suffering from NSCLC for the small molecule tyrosine kinase inhibitor therapy (e.g., Iressa) in the future.

1. Introduction

Nonsmall cell lung cancer (NSCLC) represents the majority of lung cancers [1]. Lung cancer treatment depends on several factors including tumor type, size, and patient's health. Surgery, radiation therapy, and chemotherapy using tumor specific targeted agents such as vascular endothelial growth factor (VEGF) inhibitor bevacizumab and epidermal growth

factor receptor-tyrosine kinase inhibitors (EGFR TKIs) are the primary tools for treating lung cancer. These targeted agents are initially effective in certain small subpopulations of patients, but eventually nearly all patients turn out to be resistant to the further treatments [2]. The limitations in efficacy and safety associated with the existing treatments for NSCLC underscore the need for novel biomarkers and imaging approaches for identification of patients who may

benefit from particular therapeutic agents and approaches with improved efficacy and safety profiles.

The importance of EGFR signaling pathway in the development and progression of NSCLC has been widely recognized [3, 4]. EGFR overexpression is observed in tumors of more than 60% of patients with metastatic NSCLC and correlates with poor prognosis [5]. These observations have provided a rationale for the development of novel anticancer agents that target EGFR. Two classes of EGFR-targeted agents are currently being tested in clinical trials: antibodies that bind to the extracellular domain of EGFR (i.e., cetuximab, panitumumab, matuzumab, nimotuzumab, etc.) and small molecular inhibitors that bind to the ATP-binding site of the EGFR tyrosine kinase (i.e., gefitinib, erlotinib, lapatinib, canertinib, etc.) [6]. Clinical trials have revealed significant variability in response to EGFR TKI gefitinib (Iressa), with approximately 10% of Caucasian patients, 25–30% of Japanese patients, and 57% of Taiwanese patients [5, 7–13]. Sequencing test of the *EGFR* gene is associated with a majority of tumors responding to EGFR kinase inhibitors harbor mutations in the kinase domain of EGFR [9, 14, 15]. The response rate to gefitinib and erlotinib in patients with tumors exhibiting activating mutations of EGFR is approximately 75%, suggesting that these mutations, at least in part, may have caused malignant transformation and contribute in large to the tumor maintenance pathway [16, 17]. Two subtypes of activating EGFR mutations have been described: tyrosine kinase domain mutation (45%–50%) in EGFR exons 18–24 and truncating mutations involving exon 2 to 7. The most frequently detected alterations are small deletions in exon 19 (35%–45%) that eliminate amino acids 747–750 (Leu-Arg-Glu-Ala), located around the active site of the tyrosine kinase, and point mutations in exon 21 that result in the amino acid substitution Leu858 → Arg, a residue located in the activation loop [9]. Mutations are most frequently detected in a subpopulation of NSCLC patients with characteristics associated with a better treatment outcome: women, nonsmokers, patients of southeast Asian and Japanese origins, and patients with adenocarcinoma histology and, in particular, bronchioalveolar carcinoma [18, 19]. The mutational status of EGFR kinase could be considered as a positive predictive biomarker of response to NSCLC [20, 21].

Considerable efforts have been made over the past decade to develop radiolabeled agents for noninvasive imaging of EGFR expression and activity. These agents include radiolabeled antibodies to EGFR and radiolabeled small molecular compounds based on structures of known EGFR TKIs [22]. Most of the radiolabeled agents for molecular imaging with positron emission tomography (PET) are derived from 4-(anilino)quinazoline pharmacophore [23, 24], which includes ML series [21, 22, 25–27], as well as [4-(3-[¹²⁴I]iodoani-lino)-quinazolin-6-yl]-amide-(3-morpholin-4-yl-propyl)-amide ([¹²⁴I]IPQA) [28], [¹⁸F]gefitinib [29], [¹¹C]PD153035 [30], and [¹¹C]erlotinib [31]. Recently, clinical studies with [¹¹C]PD153035 have demonstrated some promise for imaging EGFR expression in NSCLC patients [32]; however, none of these imaging agents exhibits selectivity for detection of NSCLC expressing

active mutant EGFR kinases or EGFR kinase mutations that confer resistance to inhibitors that are currently used in clinical practice. Therefore, we have been developing a PET radiotracer with preferential binding to active mutant EGFR kinases, not to EGFR kinase mutants conferring resistance to current small molecular inhibitors (i.e., gefitinib). PET imaging using such a selective radiolabeled agent should allow for visualization of primary and metastatic tumor lesions driven by activating mutations in EGFR kinase and selection of patients who may benefit from therapy with EGFR kinase inhibitors. Also, after the initial course of treatment with EGFR inhibitors, repetitive imaging with such a selective radiotracer could be used for monitoring the development of tumor lesions with acquired mutations (i.e., T790 M) conferring resistance to EGFR inhibitors.

Here, we describe the [4-(3-[¹²⁴I]iodoani-lino)-quinazolin-6-yl]-amide-(3-morpholin-4-yl-propyl)-amide ([¹²⁴I]morpholino-IPQA) as a PET imaging agent with increased selectivity and irreversible binding to active mutant L858R and E746-A750 del EGFR kinase, which allows for noninvasive detection of NSCLC in mouse xenografts harboring this mutation.

2. Materials and Methods

2.1. Radiosynthesis of Morpholino-[¹²⁴I]IPQA Derivative. Morpholino-[¹²⁴I]IPQA derivative was synthesized from but-2-enedioic acid(3-morpholin-4-propyl)-amide[4-(3-triethylstannyl-phenyl-amino)-quinazolin-6-yl]-amide (morpholino-IPQA derivative), as described previously [28]. The radiosynthesis of morpholino-[¹²⁴I]IPQA derivative was modified according to the earlier study [33]. The tin precursor (100 µg; from MD Anderson Cancer Center, Houston, TX, USA) was dissolved in 0.02 mL of methanol, and then the [¹²⁴I]NaI (37~55 MBq) was added to the solution of precursor and vortexed followed by the addition of a 0.018 mL mixture of 30% hydrogen peroxide/acetic acid (1:3). The reaction mixture was vortexed for 1 min and then allowed to stand for 5 min. Saturated sodium bicarbonate (0.2 mL) and 2N sodium thiosulphate (0.12 mL) were added to quench the reaction, and the reaction mixture was then loaded to a plus C-18 Sep-Pak cartridge system. The C-18 cartridge system (preconditioned with 10 mL of ethanol, then 10 mL of water) was eluted with water (30 mL), followed by 20% ethanol/water (25 mL), 40% ethanol/water (25 mL), and 60% ethanol/water (25 mL). The majority of the product was isolated during the elution with 60% ethanol/water. Each fraction was collected and assayed for radioactivity measurement, and the fractions that contain the final product were assayed by radio-thin-layer chromatography (radio-TLC). The radiochemical purity was determined by radio-TLC (silica gel 60 F254; eluent: chloroform/methanol = 6/1). The collected products with sufficient purity were combined and evaporated.

2.2. Radiosynthesis of Morpholino-[¹³¹I]IPQA Derivative. No carrier-added morpholino-[¹³¹I]IPQA derivative was

prepared using the same procedure as that of morpholino-[¹²⁴I]IPQA (50 µg of the tin precursor was used). The radiolabeled product was isolated in 65% radiochemical yield (decay corrected) with a radiochemical purity of 92.3%.

2.3. Tumor Cell Lines. Human NSCLC cell line H1299 with 4 different levels of wild-type (WT) or mutant EGFR expression was selected: (a) L858R EGFR (point mutation in exon 21); (b) E746-A750 del EGFR (in frame deletion); (c) EGFR-transfected (wild-type); (d) vector-transfected (study control).

Cells were grown in flasks with RPMI 1640 with 10% FBS and antibiotics at 37°C in humidified atmosphere with 5% CO₂. Cells were kept in the log phase of proliferative activity. The L858R, E746-A750del, EGFR-transfected, and vector-transfected H1299 cells were kind gifts from Drs. Shih-Feng Tsai and Yi-Rong Chen (The National Health Research Institutes, Miaoli, Taiwan).

2.4. Irreversible Binding of Morpholino-[¹²⁴I]IPQA to Active Mutant EGFR Kinase Domain. The irreversible and covalent bindings of morpholino-[¹³¹I]IPQA to the EGFR kinase domain were evaluated in H1299 derivatives cells. The cells were grown in a 15 cm culture dish until 60–70% confluence and then incubated for one hour in fresh culture medium supplemented with 20% FBS and morpholino-[¹³¹I]IPQA at 0.37 MBq/mL. Thereafter, the cells were harvested by scraping, pelleted by centrifugation at 1,000 rpm for 5 minutes, and lysed in 0.5 mL of buffer containing protein extraction reagent (Cytobuster, Novagen, USA) and aprotinin, leupeptin, pepstatin (1 µg/mL for each), Na₃VO₄, NaF, and PMSF (1 mM for each; Sigma-Aldrich, CA, USA). The cell lysate was cleared by 14,000 × g centrifugation at 4°C for 15 minutes. The cell lysate supernatant was denatured by boiling with 4x Laemmli sample buffer and separated by sodium dodecyl sulfate polyacrylamide gel electrophoresis using precast 8% Tris HCl gel cassettes (BioRad, CA, USA). After transferring proteins into a minitank electroblotter device, the membrane was exposed to AX film (Konica, Japan) for seven days at room temperature to produce an autoradiogram of ¹³¹I-labeled protein bands. Thereafter, the nitrocellulose transfer membrane was immunostained with a rabbit polyclonal EGFR (1005)-sc-03 antibody (Santa Cruz, CA, USA) and visualized using the ECL kit (Amersham Biosciences, UK). The colocalization of ¹³¹I-labeled proteins in the autoradiogram with protein bands stained with anti-EGFR antibody was assessed.

2.5. In Vitro Radiotracer Uptake and Washout Assay. Radiotracer uptake and washout studies were performed in monolayer cultures of four NSCLC cell lines as described previously [28]. Briefly, tumor cells were grown in 15 cm culture dishes until 60~70% confluent, at which point the cells were exposed to the culture medium without FCS to induce serum starvation (to inhibit EGFR kinase activity). The radiotracer morpholino-[¹³¹I]IPQA at 0.18 MBq/mL was then added to fresh cell culture medium without FCS (serum-starved), and

tumor cell monolayers were exposed to the radioactivity-containing medium for 5, 10, 20, 30, and 60 minutes. In the first part of the experiment, the cells were harvested by gentle scraping at different time intervals, pelleted by centrifugation (3,500 rpm for 2 minutes). The cell pellet and 0.1 mL of radioactive supernatant were weighed and assessed for radioactivity using a Packard 5500 gamma counter (Perkin-Elmer, CA, USA); the radioactivity concentration was expressed as cpm/g cells and cpm/mL medium, respectively. In the second part of the experiment, tumor cells exposed to the morpholino-[¹³¹I]IPQA containing medium for a given time interval (5, 10, 20, and 60 minutes) were washed with fresh (nonradioactive) medium for different time intervals before subsequent harvesting for measurement of retained radioactivity, as described above. Cells-to-medium radioactivity concentration ratios were calculated and plotted versus time to evaluate the radiotracer accumulation and washout kinetics.

2.6. Subcutaneous Tumor Xenografts and PET Image Acquisition and Data Analysis. NOD/SCID mice weighing about 25~30 g (*N* = 3) were injected subcutaneously into the left shoulder region with L858R, E746-A750 del, or wild-type EGFR-transfected H1299 cells (5 × 10⁶ cells/mouse). In the right shoulder region of each mouse, 5 × 10⁶ of vector-transfected H1299 cells were inoculated as a control tumor. The tumors grew to about 8~10 mm in diameter after 4 weeks. At this point, the mice were anesthetized (2% isoflurane/98% oxygen mixture) and injected intravenously with morpholino-[¹²⁴I]IPQA (2.6 MBq/mouse). One-hour dynamic PET imaging was performed on MicroPET R4 system (Siemens, TN, USA) and followed with a 30-minute static imaging at 24 hours after i.v. administration of radiotracer. PET images were reconstructed using the ordered subsets expectation maximization iterative reconstruction algorithm. Regions of interest were drawn over tumors and other tissues of interest.

2.7. Biodistribution of Morpholino-[¹³¹I]IPQA Derivative in Mice. NOD/SCID mice (*n* = 3/time point) were injected subcutaneously into shoulders and limbs with L858R (8 × 10⁶ cells/mouse), E746-A750 del (8 × 10⁶ cells/mouse), wild-type EGFR-transfected (8 × 10⁶ cells/mouse), and vector-transfected H1299 cells (5 × 10⁶ cells/mouse). Three weeks later, each mouse was injected with 0.1 mL of a saline solution containing 2.6 MBq of morpholino-[¹³¹I]IPQA through the caudal vein. Animals were sacrificed by chloroform (Nacalai Tesque Inc., Japan) at different time points after i.v. administration of radiotracer. Organs of interest were collected and weighed, and the radioactivity was counted. The percent injected dose per gram of tissue (% ID/g) was calculated and recorded.

2.8. Statistical Analysis. Group data were expressed as average ± SE and compared using analysis of variance, regression analysis, and group and paired Student's *t* tests; a *P* value of < 0.05 was considered statistically significant.

TABLE 1: Pharmacokinetics of morpholino-[¹³¹I]IPQA accumulation and washout in different tumor cells *in vitro*.

Tumor cells	L858R	E746-A750 del	EGFR	Vector
Plateau level at 60 minutes ¹	3.12 ± 0.304	1.57 ± 0.17	1.47 ± 0.001	1.47 ± 0.001
Washout at 60 minutes ²	1.78 ± 0.147*	1.10 ± 0.16	1.17 ± 0.001	1.17 ± 0.001
Washout at 21 minutes	1.09 ± 0.124*	1.16 ± 0.20	0.55 ± 0.000*	0.55 ± 0.000*

¹Volume of distribution at equilibrium expressed as cell-to-medium accumulation ratio (average ± standard error). ²Coefficient B (slope) of the exponential washout = $A \times \exp^{(-BX)}$.

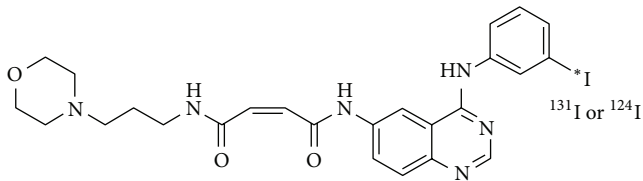


FIGURE 1: The chemical structure of the (E)-But2-enedioic acid [4-(3-[¹²⁴I]iodoanilino)-quinazolin-6-yl]-amide-(3-morpholin-4-ylpropyl)-amide, termed as morpholino-[¹²⁴I]IPQA.

3. Results

3.1. Radiochemistry. The final product of morpholino-[¹²⁴I]IPQA derivative (Figure 1) was dissolved in saline (with 10% ethanol added). Radio-TLC showed the Rf value of morpholino-[¹³¹/¹²⁴I]IPQA derivative to be 0.5. The radiochemical yield was 50%, and the radiochemical purity was ≥90% (decay-corrected). Radio-high-performance liquid chromatography (radio-HPLC) using an Alltech Alltima C18LL column (250 × 4.6 mm; Fisher Scientific, USA) and a mobile phase consisting of 0.1 M acetate buffer (acetate/acetonitrile = 55/45) at a flow rate of 1.0 mL/min exhibited the product as a peak at about 10 minutes.

3.2. Irreversible and Specific Bindings of Morpholino-[¹³¹I]IPQA to the L858R and E746-A750 Del EGFR Mutations. The autoradiographic and western blot analysis was used to demonstrate the irreversible and covalent bindings of morpholino-[¹³¹I]IPQA in four types of NSCLC cells. The autographic electropherogram of protein extracts from these NSCLC cell lines that were pretreated with morpholino-[¹³¹I]IPQA demonstrated the preferential covalent binding of morpholino-[¹³¹I]IPQA to the cells with L858R and E746-A750 del EGFR mutations (Figure 2(a)). These bands were correspondent with the 172 kDa protein band stained with anti-EGFR antibody (Figure 2(b)). The above observations collectively suggest that in EGFR-transfected cells (cells with wild-type EGFR overexpression) the lower radioactive intensity of morpholino-[¹³¹I]IPQA (Figure 2(a)) corresponds to a higher level of anti-EGFR immunoblotting (Figure 2(b)) compared to EGFR mutation cells.

The covalent binding of morpholino-[¹³¹I]IPQA to the H1299 vector-transfected and MB-435S (EGFR negative cells) was barely detected by autographic electropherogram (Figures 2(a) and 2(b)).

3.3. Preferential Accumulation of Morpholino-[¹³¹I]IPQA in NSCLC Cells with L858R and E746-A750 Del EGFR Mutations. All four types of cells showed a rapid accumulation of morpholino-[¹³¹I]IPQA at the initial 10 minutes and thereafter reached a plateau at 60 minutes (Figures 3(a)-3(d)). In L858R and E746-A750 del cells, the cell-to-medium ratio (CMR) of morpholino-[¹³¹I]IPQA was about 60–65 at 60 minutes, which was ~1.6-fold higher than that of wild-type EGFR-transfected H1299 cells (Table 1).

In L858R and E746-A750 del cells, the loss of morpholino-[¹³¹I]IPQA accumulation could be characterized by a rapid washout, followed by a plateau, with a slow but slightly decreased (L858R cells, Figure 3(e)) (E746-A750 del cells, Figure 3(f)) CMR over time. In contrast, wild-type EGFR-transfected H1299 cells showed consistent decrease of CMR with time (Figure 3(g)). At 120 min, the washout studies showed the higher retention of morpholino-[¹³¹I]IPQA in L858R (8.9 ± 0.2 CMR, Figure 3(e) red dot line) and E746-A750 del cells (12.6 ± 3.2 CMR, Figure 3(f) red dot line) than that in EGFR-transfected H1299 (5.7 ± 0.4 CMR, Figure 3(g) red dot line) and vector-transfected H1299 (6.6 ± 0.3 CMR, data not shown). The results of *in vitro* radiotracer uptake and washout studies of morpholino-[¹³¹I]IPQA are summarized in Table 1.

3.4. In Vivo PET Imaging of Morpholino-[¹²⁴I]IPQA Exhibits Differentials of Accumulation in NSCLC Tumors with Different EGFR Expressions. *In vivo* PET imaging was performed in 18 mice (6 per tumor pair) before and after treatment with Iressa. MicroPET images demonstrated that highest accumulation level of morpholino-[¹²⁴I]IPQA was observed in L858R tumor xenograft at 24 hours after radiotracer administration. The accumulation was 1.23-, 2.36-, and 3.08-folds higher than that of E746-A750 del, wild-type EGFR-transfected, and vector-transfected tumor xenograft in baseline group, respectively (Figures 4(a)-4(c), left panel, Figure 5). Pretreatment with Iressa (100 mg/kg 1 h before administration of morpholino-[¹²⁴I]IPQA) results in 53% and 38% decrease in the accumulation of radiotracer in L858R and E746-A750 del tumors, respectively (Figures 4(a)-4(b) right panels, Figure 5). There was a similar accumulation of radiotracer in wild-type EGFR-transfected and vector-transfected tumor xenografts before and after Iressa treatment (Figures 4(a)-4(c); Figure 5). The results of tumor-to-vector ratio at 24 hours after administration of morpholino-[¹²⁴I]IPQA was summarized in Table 5.

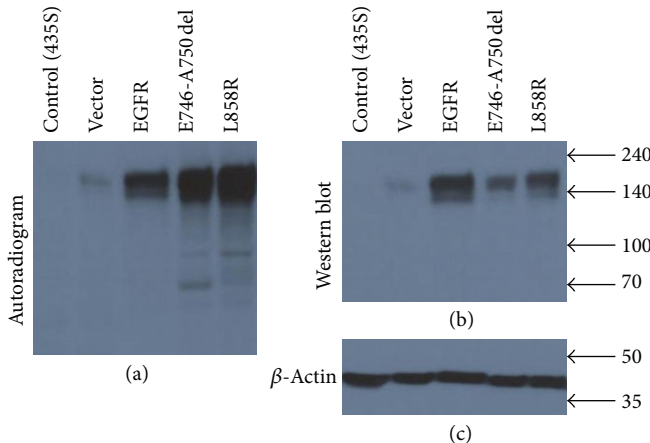


FIGURE 2: Assessment of irreversible binding of morpholino-[¹³¹I]IPQA to wild-type and mutant EGFR kinase in four types of human nonsmall cell lung carcinoma cell lines. (a) The autoradiography demonstrates the irreversible and covalent bindings of morpholino-[¹³¹I]IPQA to the EGFR kinase domain in different cell lines. (b) The same membrane was stained with anti-EGFR kinase antibody. A single band of radiolabeled protein corresponds to the predominant band of ~170 kDa.

TABLE 2: Biodistribution of accumulated radioactivity (%ID/g) in different tissues at the designed time points after administration of morpholino-[¹³¹I]IPQA.

Tissue	1 hr	4 hr	24 hr	48 hr
Blood	0.124 ± 0.000	0.076 ± 0.000	0.030 ± 0.000	0.009 ± 0.000
Lung	1.319 ± 0.001	0.776 ± 0.001	0.239 ± 0.000	0.119 ± 0.000
Heart	0.240 ± 0.002	0.191 ± 0.001	0.076 ± 0.000	0.676 ± 0.001
Stomach	1.330 ± 0.001	1.302 ± 0.002	1.407 ± 0.012	0.299 ± 0.000
Liver	1.241 ± 0.002	0.500 ± 0.000	0.424 ± 0.000	1.063 ± 0.001
Spleen	0.560 ± 0.009	0.303 ± 0.000	0.225 ± 0.001	0.486 ± 0.001
Pancreas	5.443 ± 0.002	5.334 ± 0.002	3.232 ± 0.004	0.389 ± 0.002
Small intestine	0.858 ± 0.001	0.774 ± 0.004	0.135 ± 0.000	0.044 ± 0.000
Large intestine	0.807 ± 0.002	0.289 ± 0.000	0.301 ± 0.000	0.021 ± 0.000
Kidney	4.785 ± 0.001	3.772 ± 0.008	1.431 ± 0.001	0.523 ± 0.000
Bone	0.190 ± 0.002	0.109 ± 0.000	0.062 ± 0.000	0.04 ± 0.000
Muscle	0.034 ± 0.000	0.025 ± 0.000	0.009 ± 0.000	0.009 ± 0.000
Brain	0.010 ± 0.000	0.008 ± 0.000	0.003 ± 0.000	0.002 ± 0.000
L858R	0.280 ± 0.000	0.251 ± 0.001	0.125 ± 0.000	0.037 ± 0.000
E746-A750 del	0.304 ± 0.000	0.195 ± 0.000	0.100 ± 0.000	0.052 ± 0.000
EGFR	0.347 ± 0.000	0.208 ± 0.000	0.047 ± 0.000	0.036 ± 0.000
Vector	0.222 ± 0.000	0.143 ± 0.000	0.085 ± 0.001	0.123 ± 0.002

Data shown as average ± standard deviation ($n = 3$ per tumor pair).

3.5. Biodistribution of Morpholino-[¹³¹I]IPQA Derivative in NSCLC Tumor-Bearing Mice. In the first hour, high % ID/g was observed in pancreas, kidney, stomach, lung, liver, and small and large intestines (Table 2). Four tumors expressing different levels of EGFR activity/expression had the peak radioactivity concentration in the first hour and then showed a gradual decrease over time; however, blood, heart, liver, and spleen showed a redistribution 24 hours after administration of morpholino-[¹³¹I]IPQA. The levels of radioactivity in blood or heart rapidly dropped to 0.1~0.2% ID/g one hour after radiotracer injection and progressively decreased during 4 to 48 hours. We also observed a rapid excretion of

radiotracer by liver. This pattern of hepatobiliary clearance was followed by a fast increased radioactivity in blood and liver and subsequent clearance by kidneys.

All four tumor xenografts had similar accumulations of morpholino-[¹³¹I]IPQA at the first hour after injection of radiotracer. The L858R tumor xenograft had a longer retention time of morpholino-[¹³¹I]IPQA when compared to other 3 xenografts.

Up to 24 hours after injection of radiotracer, the tumor-to-blood (TBR) and tumor-to-muscle concentration ratios (TMR) were not distinguishable among four tumor xenografts (Tables 3 and 4; all other three cell lines

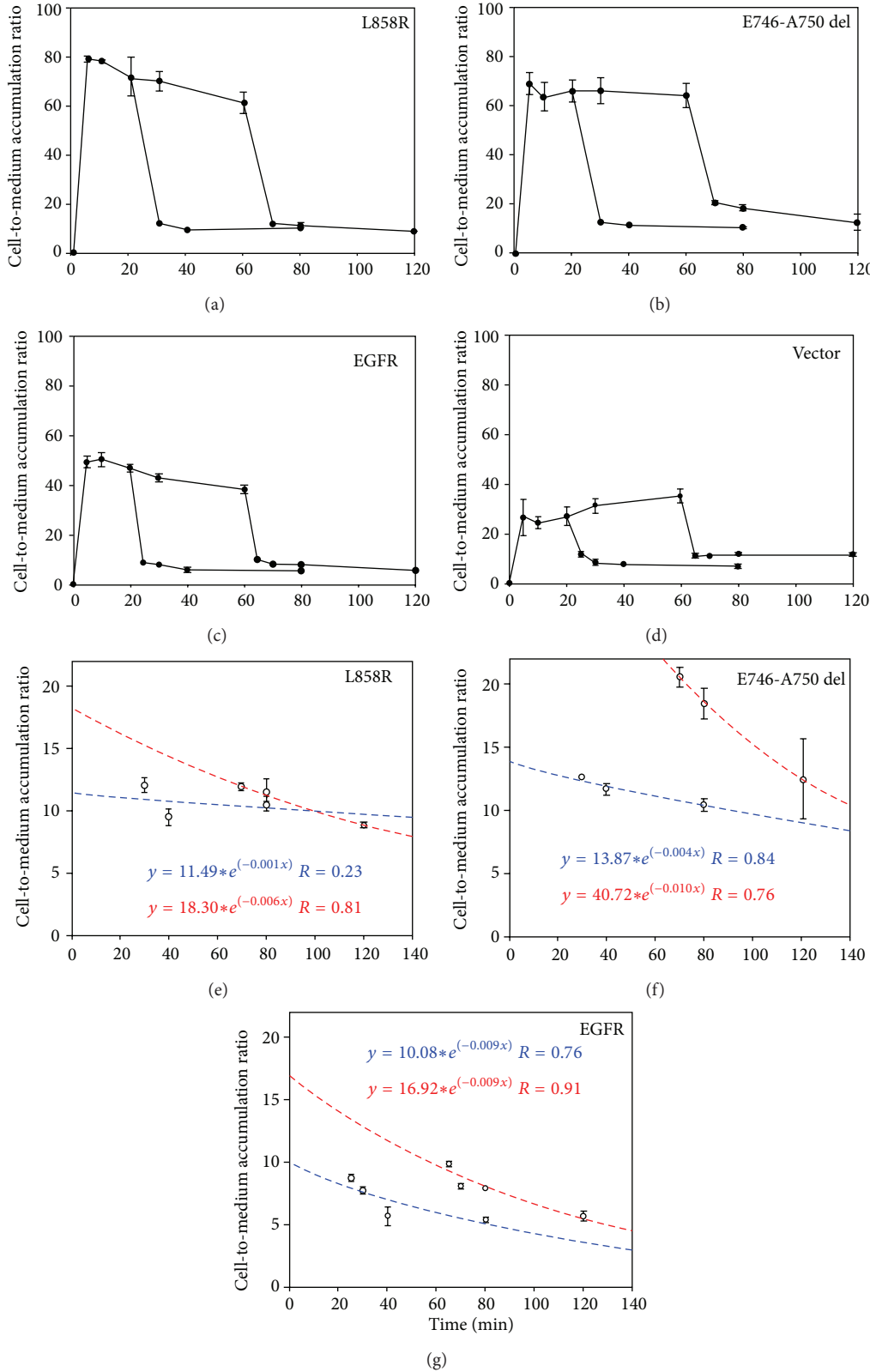


FIGURE 3: *In vitro* uptake and washout phases of morpholino-[¹³¹I]IPQA in L858R (a), E746-A750 del (b), wild-type EGFR-transfected (c), and EGFR-vector (d). Linear fits of radioactivity accumulation time points show the washout rate at short duration (20–80 minutes, blue dot line) and long duration (60–120 minutes, red dot line) after initial accumulation (from (e) to (g)). Coefficient *B* (slope) of the exponential washout = $A \times \exp(-BX)$. Panels (a)–(d) are shown in full scale, and panels (e)–(g) are from the same data in panels (a)–(c) but are shown in smaller scale to visualize differences in washout results.

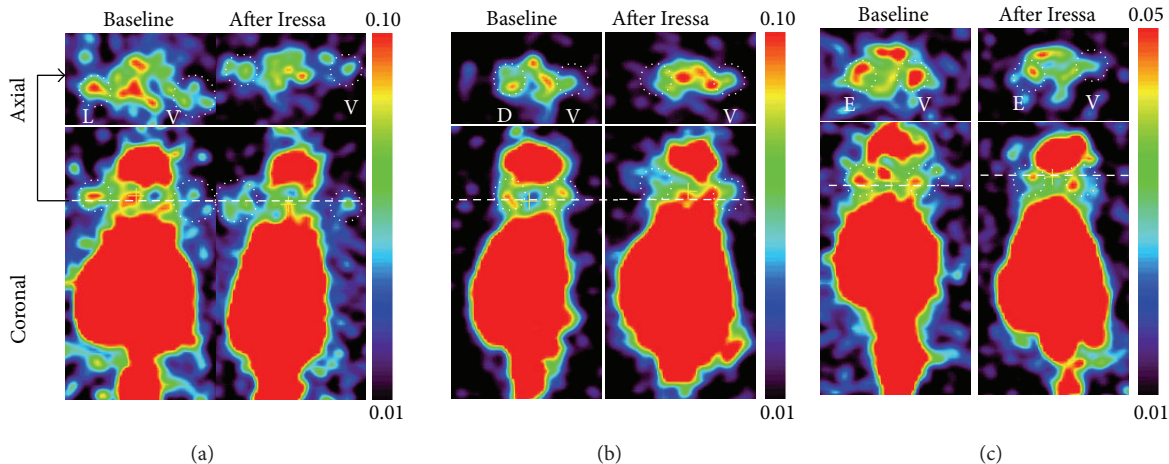


FIGURE 4: Reprehensive coronal and axial PET images obtained 24 hours after morpholino-[¹²⁴I]IPQA administration in mice bearing L858R EGFR (a), E746-A750 del (b), wild-type EGFR-transfected (c), and EGFR-vector ((a)–(c)) subcutaneous tumor xenografts (dot circle). Color coding in the image is set to maximize the visualization of tumor in each projection. The different scale was used in (c). L: L858R EGFR; V: vector; D: E746-A750 del; E: EGFR-vector.

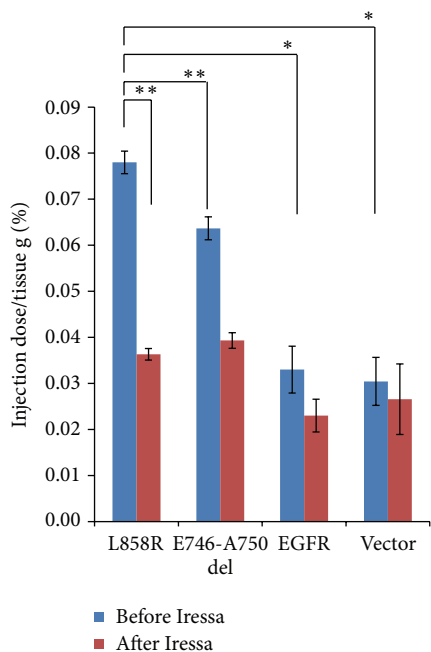


FIGURE 5: Quantification of accumulation of [¹²⁴I]IPQA in different tumor xenografts at baseline (blue) and pretreated with Iressa (red), respectively. Error bars represent standard deviation; statically significant difference is indicated by an asterisk (* $P < 0.05$) or double asterisks (** $P < 0.01$).

were compared to L858R tumor cells at the same time point). The TBR and TMR in L858R tumor xenograft 24 hours after injection of radiotracer were 2.64 and 13.89, respectively (Tables 3 and 4). The E746-A750 del tumor xenograft had similar TBR and TMR compared to those of L858R group. The L858R tumor xenograft also had a better tumor-to-vector ratio 24 hours after administration of

radiotracer when compared to those of other 2 xenografts (Table 5).

4. Discussion

Predicting the expression of EGFR mutation through noninvasive PET imaging with a specific EGFR kinase radiotracer would provide an assessment for the NSCLC patients who may benefit from EGFR inhibitors therapeutic regimen. Previously, our collaborator reported that the PET imaging with morpholino-[¹²⁴I]IPQA, which could irreversibly and specifically bind to active form of EGFR kinase, allowed for identification of tumors with high EGFR kinase signaling activity (i.e., A431 highly expressing EGFR in NSCLC and U87 del EGFR cells expressing EGFRvIII mutants in brain gliomas) [28].

In the current study, by using morpholino-[¹²⁴I]IPQA with PET, we demonstrated that L858R and E746-A750 del EGFR mutated cells, which are the most frequent mutation in NSCLC [9], showed significant increased accumulation of radiotracer when compared to the wild-type EGFR-transfected and vector-transfected cells *in vitro* and *in vivo*. The locations of the L858R missense mutations are shown within the activating loop of the tyrosine kinase, whereas the in-frame deletion, E746-A750 del, is present within another loop which flanks the ATP cleft [14]. Those mutations are predicted to alter the position of these amino acids relative to that of phosphorylation status of the cells and the sensitivity of inhibitor (i.e., gefitinib).

The expression levels of phosphorylated EGFR in L858R and E746-A750 del EGFR mutated cells were similar, whereas wild-type EGFR-transfected cells showed the highest expression of total EGFR. Nevertheless, the mutation in active site of tyrosine kinase domain results in the enhanced EGFR signaling (phosphorylation status), which explains the increased accumulation of morpholino-[¹³¹I]IPQA in L858R and E746-A750 del EGFR mutated cells. Similar interpretation can also

TABLE 3: Tumor-to-blood ratio in different tumor cells in *in vitro* study.

	1hr	4 hr	24 hr	48 hr
L858R/blood	2.25 ± 0.001	3.75 ± 0.001	2.64 ± 0.000	3.98 ± 0.000*
E746-A750 del/blood	2.45 ± 0.000	2.96 ± 0.001	2.68 ± 0.000	5.55 ± 0.002*
Wild-type EGFR/blood	2.79 ± 0.001*	2.91 ± 0.000	1.22 ± 0.000	3.87 ± 0.001*
Vector/blood	1.79 ± 0.001	1.97 ± 0.000	2.37 ± 0.001	13.12 ± 0.000

Data shown as average ± standard deviation ($n = 3$ for each tumor pair). All other three cell lines were compared to L858R tumor cells at the same time point, and statistically significant difference (* $P < 0.05$) is indicated by an asterisk.

TABLE 4: Tumor-to-muscle ratio in different tumor cells in *in vitro* study.

	1hr	4 hr	24 hr	48 hr
L858R/muscle	8.24 ± 0.001	10.04 ± 0.001*	13.99 ± 0.001*	4.11 ± 0.000*
E746-A750 del/muscle	8.94 ± 0.001*	7.80 ± 0.001	11.11 ± 0.001*	5.78 ± 0.001*
Wild-type EGFR/muscle	10.21 ± 0.00*	8.32 ± 0.002*	5.22 ± 0.002*	4.00 ± 0.001*
Vector/muscle	6.53 ± 0.001	5.36 ± 0.000	9.44 ± 0.001	13.67 ± 0.001*

Data shown as average ± standard deviation ($n = 3$ for each tumor pair). All other three cell lines were compared to L858R tumor cells at the same time point, and statistically significant difference (* $P < 0.05$) is indicated by an asterisk.

TABLE 5: Tumor-to-vector ratio in different tumor cells in *in vitro* study of morpholino-[¹³¹I]IPQA and *in vivo* study of morpholino-[¹²⁴I]IPQA.

	PET		Biodistribution
	Baseline	Iressa	Baseline
L858R/vector	3.12 ± 0.304	1.57 ± 0.17	1.47 ± 0.001
E746-A750 del/vector	1.78 ± 0.147*	1.10 ± 0.16	1.17 ± 0.001
EGFR/vector	1.09 ± 0.124*	1.16 ± 0.20	0.55 ± 0.000*

Data shown as average ± standard deviation ($n = 3$ for each tumor pair). All other three cell lines were compared to L858R tumor, and statistically significant difference (* $P < 0.05$) is indicated by an asterisk.

be applied to the preferential accumulation and retention of morpholino-[¹²⁴I]IPQA in these mutant EGFR cells in *in vivo* PET imaging.

In comparison with previous reports of EGFR imaging agents [22, 25, 26, 34, 35], the results of our *in vivo* PET imaging studies with morpholino-[¹²⁴I]IPQA in mice bearing four tumor xenografts expressing different levels of phosphorylated EGFR are more selective. Predominant accumulations of morpholino-[¹²⁴I]IPQA in EGFR-expressing L858R and E746-A750 del carcinoma tumor xenografts reflect the high level of phosphorylated EGFR expression and activity in those tumor cells, which are known to be responsive to therapy with small molecular inhibitors of EGFR (e.g., Gefitinib) [14]. The H1299 EGFR tumor xenograft expressing EGFR represented a model of therapy-resistant tumors. H1299 EGFR tumor had lower morpholino-[¹²⁴I]IPQA accumulation and produced similar images before and after treatment with EGFR inhibitor, Gefitinib (Iressa).

Our results also provided more information of tissue distributions at later time points (24 and 48 hours after radiotracer administration). Selective accumulations of radiotracer in the L858R and E746-A750 del EGFR mutants were observed when compared to the tumors with wild-type EGFR or vector-transfected cells. Similar to the results

from dynamic PET imaging obtained from 0 to 70 minutes after administration of morpholino-[¹²⁴I]IPQA [28], the biodistribution data obtained from 1, 4, 24, and 48 hours after administration of morpholino-[¹³¹I]IPQA showed a rapid clearance of radiotracer from blood and other major tissues such as heart, brain, liver, intestines, and kidney. The results demonstrated that the nonspecific binding of the radiotracer was washed out rapidly and caused increased tumor-to-background ratio due to the irreversible and selective bindings to active state of EGFR kinase.

We also observed an unexpected high accumulation (3.2% ID/g at 24-hour time point) in pancreas at all time points. Mohammed et al. reported that gefitinib blocks EGFR signaling pathway in progression of pancreatic intraepithelial neoplasms (PanINs) to PDAC in conditional LSL-Kras^{G12D/+} transgenic mice model [36]. Kelley and Ko reported a significant survival benefit with the addition of the EGFR tyrosine kinase inhibitor erlotinib to gemcitabine chemotherapy for the first-line treatment of patients with advanced pancreatic cancer [37]. These results demonstrated that morpholino-[¹³¹I]IPQA was entrapped in normal pancreatic cell (i.e., ductal cells and the islets of Langerhans) [38].

However, despite the lower lipophilicity of morpholino-[¹²⁴I]IPQA compared to previously reported EGFR imaging compounds such as the N-{4-[(4,5-dichloro-2-fluorophenyl)amino]quinazolin-6-yl}-acrylamide, 4-[(3,4-dichloro-6-fluorophenyl)amino]-6,7-dimethoxyquinazoline, and 4-(3-bromoanilino)-6,7-dimethoxyquinazoline [22, 25, 26, 34, 35], the morpholino-[¹²⁴I]IPQA still exhibited a significant hepatobiliary clearance. Also, high accumulation of the radiotracer in abdomen area over time would decrease the possibility of using this radiotracer for imaging primary site of NSCLC in animal model or for colorectal metastases. The further improvement could focus on the optimization of its pharmacokinetic properties by additional chemical derivatization (i.e., decrease lipophilicity and extraction by the liver, increase the half-life in plasma and accumulation amount/retention time in tumor tissue, and increase water

solubility0 and renal clearance for a better background-to-target ratio).

The relatively low resolution of microPET system (spatial resolution ~1.8 mm) may not allow for assessing the heterogeneity of morpholino-[¹²⁴I]IPQA radioactivity accumulation. Therefore, micro-PET/CT and autoradiography (with 10–30 μM in plane resolution) are suitable to study the heterogeneity of morpholino-[¹²⁴I]IPQA-derived radioactivity accumulation and to compare it with the immunohistochemically stained (adjacent) tissue sections for the total EGFR or phosphorylated EGFR (Tyrosine 1068).

As a breakthrough of NSCLC treatment management in 2004, Lynch et al. [14] first reported that specific mutations in EGFR gene in NSCLC patients were correlated with clinical responsiveness to the tyrosine kinase inhibitor gefitinib. These findings were confirmed by Pao et al. in the tumor cells from the patients with L858R mutation but not for L747-S752 del EGFR mutant [14]. The study results from Sordella et al. also supported that EGF-independent autophosphorylation in these mutations caused high sensitivity to gefitinib and selectively activated downstream pathways [39]. Tracy et al. also proved that gefitinib-induced apoptosis in the L858R mutant lead dramatic response to gefitinib [40]. The authors also concluded that the affinity for the L858R mutant to gefitinib was 20-fold higher than that for wild type, which could be explained by its tighter binding to active conformation of the tyrosine kinase domain. Also, it could be expected to predict the efficacy in the treatment of the subgroup with gefitinib. Tracy et al. suggested that targeted agents developed to inhibit AKT pathway may be therapeutically more effective than those designed to inhibit the ERK 1/2 pathway in patients whose tumors contain EGFR L858R if the AKT pathway is consistently active [40]. Moreover, Brognard et al. reported that constitutive AKT activation has also been associated with resistance to chemotherapy and radiation in NSCLC cell lines [41]. Further study could be the mono/combinations of chemotherapy with gefitinib or inhibitors of the AKT pathway which should be tested *in vitro* in cell lines and *in vivo* in tumor xenografts with EGFR L858R mutations to determine whether these may be additive or synergistic.

In conclusion, an enhanced binding of morpholino-[^{124/131}I]IPQA derivatives to the ATP binding site of mutant kinase of L858R or E746-A750 del EGFR mutant warrants that PET imaging with morpholino-[¹²⁴I]IPQA has a potential for identification of tumors with high EGFR kinase activity in NSCLC and for the monitoring or selection of individual therapies with EGFR inhibitors. Further optimization of this class of radio compound would be necessary in order to lower lipophilicity and reduce hepatobiliary clearance.

Conflict of Interests

The authors declare that there is no conflict of interests.

Acknowledgments

The authors would like to thank Drs. Shih-Feng Tsai and Yi-Rong Chen for the cell lines as kind gifts. This research

was supported by the grants NSC101-2314-B-010-046 (the National Science Council, Taiwan), DOH101-TD-C-111-007, DOH102-TD-C-111-007 (the Department of Health), and V101C-127 (Taipei Veterans General Hospital). The authors thank the technical support from Molecular and Genetic Imaging Core, Taiwan Mouse Clinic, which is funded by the National Research Program for Biopharmaceuticals (NRPB) at the National Science Council (NSC) of Taiwan.

References

- [1] ACS, 2012, <http://www.cancer.org/cancer/lungcancer-non-smallcell/detailedguide/non-small-cell-lung-cancer-key-statistics>.
- [2] H. A. Burris III, "Shortcomings of current therapies for non-small-cell lung cancer: unmet medical needs," *Oncogene*, vol. 28, no. 1, pp. S4–S13, 2009.
- [3] Y. Yarden, "The EGFR family and its ligands in human cancer: signalling mechanisms and therapeutic opportunities," *European Journal of Cancer*, vol. 37, no. 4, pp. S3–S8, 2001.
- [4] A. F. Gazdar, "Activating and resistance mutations of EGFR in non-small-cell lung cancer: role in clinical response to EGFR tyrosine kinase inhibitors," *Oncogene*, vol. 28, no. 1, pp. S24–S31, 2009.
- [5] S. V. Sharma, D. W. Bell, J. Settleman, and D. A. Haber, "Epidermal growth factor receptor mutations in lung cancer," *Nature Reviews Cancer*, vol. 7, no. 3, pp. 169–181, 2007.
- [6] C. A. Reade and A. K. Ganti, "EGFR targeted therapy in non-small cell lung cancer: potential role of cetuximab," *Biologics*, vol. 3, pp. 215–224, 2009.
- [7] F. Fukuoka, "Multi-institutional randomized phase II trial of gefitinib for previously treated patients with advanced non-small-cell lung cancer (The IDEAL 1 Trial)," *Journal of Clinical Oncology*, vol. 21, no. 12, pp. 2237–2246, 2003.
- [8] M. G. Kris, R. B. Natale, R. S. Herbst et al., "Efficacy of gefitinib, an inhibitor of the epidermal growth factor receptor tyrosine kinase, in symptomatic patients with non-small cell lung cancer: a randomized trial," *Journal of the American Medical Association*, vol. 290, no. 16, pp. 2149–2158, 2003.
- [9] J. G. Paez, P. A. Jänne, J. C. Lee et al., "EGFR mutations in lung cancer: correlation with clinical response to gefitinib therapy," *Science*, vol. 304, no. 5676, pp. 1497–1500, 2004.
- [10] S.-F. Huang, H.-P. Liu, L.-H. Li et al., "High frequency of epidermal growth factor receptor mutations with complex patterns in non-small cell lung cancers related to gefitinib responsiveness in Taiwan," *Clinical Cancer Research*, vol. 10, no. 24, pp. 8195–8203, 2004.
- [11] N. Thatcher, A. Chang, P. Parikh et al., "Gefitinib plus best supportive care in previously treated patients with refractory advanced non-small-cell lung cancer: results from a randomised, placebo-controlled, multicentre study (Iressa Survival Evaluation in Lung Cancer)," *The Lancet*, vol. 366, no. 9496, pp. 1527–1537, 2005.
- [12] F. A. Shepherd and M.-S. Tsao, "Unraveling the mystery of prognostic and predictive factors in epidermal growth factor receptor therapy," *Journal of Clinical Oncology*, vol. 24, no. 7, pp. 1219–1220, 2006.
- [13] G. J. Riely, W. Pao, D. Pham et al., "Clinical course of patients with non-small cell lung cancer and epidermal growth factor receptor exon 19 and exon 21 mutations treated with gefitinib

- or erlotinib," *Clinical Cancer Research*, vol. 12, no. 3, part 1, pp. 839–844, 2006.
- [14] T. J. Lynch, D. W. Bell, R. Sordella et al., "Activating mutations in the epidermal growth factor receptor underlying responsiveness of non-small-cell lung cancer to gefitinib," *The New England Journal of Medicine*, vol. 350, no. 21, pp. 2129–2139, 2004.
- [15] W. Pao, V. A. Miller, K. A. Politi et al., "Acquired resistance of lung adenocarcinomas to gefitinib or erlotinib is associated with a second mutation in the EGFR kinase domain," *PLoS Medicine*, vol. 2, no. 3, article e73, 2005.
- [16] D. M. Jackman, B. Y. Yeap, L. V. Sequist et al., "Exon 19 deletion mutations of epidermal growth factor receptor are associated with prolonged survival in non-small cell lung cancer patients treated with gefitinib or erlotinib," *Clinical Cancer Research*, vol. 12, no. 13, pp. 3908–3914, 2006.
- [17] G. J. Riely, K. A. Politi, V. A. Miller, and W. Pao, "Update on epidermal growth factor receptor mutations in non-small cell lung cancer," *Clinical Cancer Research*, vol. 12, no. 24, pp. 7232–7241, 2006.
- [18] G. Giaccone, "Epidermal growth factor receptor inhibitors in the treatment of non-small-cell lung cancer," *Journal of Clinical Oncology*, vol. 23, no. 14, pp. 3235–3242, 2005.
- [19] P. A. Jänne, "Ongoing first-line studies of epidermal growth factor receptor tyrosine kinase inhibitors in select patient populations," *Seminars in Oncology*, vol. 32, no. 6, supplement 10, pp. S9–e15, 2005.
- [20] J. G. Gelovani, "Molecular imaging of epidermal growth factor receptor expression-activity at the kinase level in tumors with positron emission tomography," *Cancer and Metastasis Reviews*, vol. 27, no. 4, pp. 645–653, 2008.
- [21] S. Dissoki, Y. Aviv, D. Laky, G. Abourbeh, A. Levitzki, and E. Mishani, "The effect of the [¹⁸F]-PEG group on tracer qualification of [4-(phenylamino)-quinazoline-6-YL]-amide moiety: An EGFR putative irreversible inhibitor," *Applied Radiation and Isotopes*, vol. 65, no. 10, pp. 1140–1151, 2007.
- [22] E. Mishani, G. Abourbeh, Y. Rozen et al., "Novel carbon-11 labeled 4-dimethylamino-but-2-enoic acid [4-(phenylamino)-quinazoline-6-yl]-amides: potential PET bioprobes for molecular imaging of EGFR-positive tumors," *Nuclear Medicine and Biology*, vol. 31, no. 4, pp. 469–476, 2004.
- [23] E. Mishani and G. Abourbeh, "Cancer molecular imaging: radionuclide-based biomarkers of the epidermal growth factor receptor (EGFR)," *Current Topics in Medicinal Chemistry*, vol. 7, no. 18, pp. 1755–1772, 2007.
- [24] E. Mishani and A. Hagooly, "Strategies for molecular imaging of epidermal growth factor receptor tyrosine kinase in cancer," *Journal of Nuclear Medicine*, vol. 50, no. 8, pp. 1199–1202, 2009.
- [25] T. A. Bonasera, G. Ortú, Y. Rozen et al., "Potential ¹⁸F-labeled biomarkers for epidermal growth factor receptor tyrosine kinase," *Nuclear Medicine and Biology*, vol. 28, no. 4, pp. 359–374, 2001.
- [26] G. Ortú, I. Ben-David, Y. Rozen et al., "Labeled EGFr-TK irreversible inhibitor (ML03): *in vitro* and *in vivo* properties, potential as pet biomarker for cancer and feasibility as anti-cancer drug," *International Journal of Cancer*, vol. 101, no. 4, pp. 360–370, 2002.
- [27] G. Abourbeh, S. Dissoki, O. Jacobson et al., "Evaluation of radiolabeled ML04, a putative irreversible inhibitor of epidermal growth factor receptor, as a bioprobe for PET imaging of EGFR-overexpressing tumors," *Nuclear Medicine and Biology*, vol. 34, no. 1, pp. 55–70, 2007.
- [28] A. Pal, A. Glekas, M. Doubrovin et al., "Molecular imaging of EGFR kinase activity in tumors with ¹²⁴I-labeled small molecular tracer and positron emission tomography," *Molecular Imaging and Biology*, vol. 8, no. 5, pp. 262–277, 2006.
- [29] H. Su, Y. Seimbille, G. Z. Ferl et al., "Evaluation of [¹⁸F]gefitinib as a molecular imaging probe for the assessment of the epidermal growth factor receptor status in malignant tumors," *European Journal of Nuclear Medicine and Molecular Imaging*, vol. 35, no. 6, pp. 1089–1099, 2008.
- [30] H. Wang, J.-M. Yu, G.-R. Yang et al., "Further characterization of the epidermal growth factor receptor ligand ¹¹C-PD153035," *Chinese Medical Journal*, vol. 120, no. 11, pp. 960–964, 2007.
- [31] A. A. Memon, S. Jakobsen, F. Dagnaes-Hansen, B. S. Sorensen, S. Keiding, and E. Nexo, "Positron emission tomography (PET) imaging with [¹¹C]-labeled erlotinib: a micro-PET study on mice with lung tumor xenografts," *Cancer Research*, vol. 69, no. 3, pp. 873–878, 2009.
- [32] N. Liu, M. Li, X. Li et al., "PET-based biodistribution and radiation dosimetry of epidermal growth factor receptor-selective tracer ¹¹C-PD153035 in humans," *Journal of Nuclear Medicine*, vol. 50, no. 2, pp. 303–308, 2009.
- [33] W.-P. Deng, W. K. Yang, W.-F. Lai et al., "Non-invasive *in vivo* imaging with radiolabelled FIAU for monitoring cancer gene therapy using herpes simplex virus type 1 thymidine kinase and ganciclovir," *European Journal of Nuclear Medicine and Molecular Imaging*, vol. 31, no. 1, pp. 99–109, 2004.
- [34] A. Fredriksson, P. Johnström, J.-O. Thorell et al., "In vivo evaluation of the biodistribution of ¹¹C-labeled PD153035 in rats without and with neuroblastoma implants," *Life Sciences*, vol. 65, no. 2, pp. 165–174, 1999.
- [35] M. Shaul, G. Abourbeh, O. Jacobson et al., "Novel iodine-124 labeled EGFR inhibitors as potential PET agents for molecular imaging in cancer," *Bioorganic and Medicinal Chemistry*, vol. 12, no. 13, pp. 3421–3429, 2004.
- [36] A. Mohammed, N. B. Janakiram, Q. Li et al., "The epidermal growth factor receptor inhibitor gefitinib prevents the progression of pancreatic lesions to carcinoma in a conditional LSL-Kras^{G12D/+} transgenic mouse model," *Cancer Prevention Research*, vol. 3, no. 11, pp. 1417–1426, 2010.
- [37] R. K. Kelley and A. H. Ko, "Erlotinib in the treatment of advanced pancreatic cancer," *Biologics*, vol. 2, no. 1, pp. 83–95, 2008.
- [38] S. Ueda, S. Ogata, H. Tsuda et al., "The correlation between cytoplasmic overexpression of epidermal growth factor receptor and tumor aggressiveness: poor prognosis in patients with pancreatic ductal adenocarcinoma," *Pancreas*, vol. 29, no. 1, pp. e1–e8, 2004.
- [39] R. Sordella, D. W. Bell, D. A. Haber, and J. Settleman, "Gefitinib-sensitizing EGFR mutations in lung cancer activate anti-apoptotic pathways," *Science*, vol. 305, no. 5687, pp. 1163–1167, 2004.
- [40] S. Tracy, T. Mukohara, M. Hansen, M. Meyerson, B. E. Johnson, and P. A. Jänne, "Gefitinib induces apoptosis in the EGFR-L858R non-small-cell lung cancer cell line H3255," *Cancer Research*, vol. 64, no. 20, pp. 7241–7244, 2004.
- [41] J. Brognard, A. S. Clark, Y. Ni, and P. A. Dennis, "Akt/pbotein kinase B is constitutively active in non-small cell lung cancer cells and promotes cellular survival and resistance to chemotherapy and radiation," *Cancer Research*, vol. 61, no. 10, pp. 3986–3997, 2001.

Research Article

Synthesis and Biological Evaluation of O-[3-¹⁸F-fluoropropyl]- α -methyl Tyrosine in Mesothelioma-Bearing Rodents

I-Hong Shih, Fan-Lin Kong, Mohammad S. Ali, Yinhan Zhang, Dong-Fang Yu, Xudong Duan, and David J. Yang

Department of Experimental Diagnosis Imaging, Unit 59, The University of Texas MD Anderson Cancer Center, 1515 Holcombe Boulevard, Houston, TX 77030, USA

Correspondence should be addressed to David J. Yang; dyang@mdanderson.org

Received 12 April 2013; Accepted 6 June 2013

Academic Editor: Tomio Inoue

Copyright © 2013 I-Hong Shih et al. This is an open access article distributed under the Creative Commons Attribution License, which permits unrestricted use, distribution, and reproduction in any medium, provided the original work is properly cited.

Radiolabeled tyrosine analogs enter cancer cells via upregulated amino acid transporter system and have been shown to be superior to ¹⁸F-fluoro-2-deoxy-D-glucose (¹⁸F-FDG) in differential diagnosis in cancers. In this study, we synthesized O-[3-¹⁹F-fluoropropyl]- α -methyl tyrosine (¹⁹F-FPAMT) and used manual and automated methods to synthesize O-[3-¹⁸F-fluoropropyl]- α -methyl tyrosine (¹⁸F-FPAMT) in three steps: nucleophilic substitution, deprotection of butoxycarbonyl, and deesterification. Manual and automated synthesis methods produced ¹⁸F-FPAMT with a radiochemical purity >96%. The decay-corrected yield of ¹⁸F-FPAMT by manual synthesis was 34% at end-of-synthesis (88 min). The decay-corrected yield of ¹⁸F-FPAMT by automated synthesis was 15% at end-of-synthesis (110 min). ¹⁸F-FDG and ¹⁸F-FPAMT were used for *in vitro* and *in vivo* studies to evaluate the feasibility of ¹⁸F-FPAMT for imaging rat mesothelioma (IL-45). *In vitro* studies comparing ¹⁸F-FPAMT with ¹⁸F-FDG revealed that ¹⁸F-FDG had higher uptake than that of ¹⁸F-FPAMT, and the uptake ratio of ¹⁸F-FPAMT reached the plateau after being incubated for 60 min. Biodistribution studies revealed that the accumulation of ¹⁸F-FPAMT in the heart, lungs, thyroid, spleen, and brain was significantly lower than that of ¹⁸F-FDG. There was poor bone uptake in ¹⁸F-FPAMT for up to 3 hrs suggesting its *in vivo* stability. The imaging studies showed good visualization of tumors with ¹⁸F-FPAMT. Together, these results suggest that ¹⁸F-FPAMT can be successfully synthesized and has great potential in mesothelioma imaging.

1. Introduction

Numerous studies have demonstrated that growing cancer cells have higher metabolism of glucose and amino acids than other cells in the body. One well-known modality for imaging the metabolic activity of cancers is positron emission tomography (PET) using ¹⁸F-2-fluoro-2-deoxy-D-glucose (¹⁸F-FDG), the current gold standard for cancer diagnosis [1]. However, ¹⁸F-FDG has limitations such as poor differentiation between low-grade tumor and normal tissues in brain [2] and between tumor and inflamed or infected tissues [3]. Radiolabeled amino acids offer higher specificity in characterizing tumors than ¹⁸F-FDG does. In particular, radiolabeled aromatic amino acids are attractive alternatives to ¹⁸F-FDG because of easier chemistry alteration

and their ability of detection of upregulated amino acid transporters [4], which indirectly reveal cell proliferation. Therefore, ¹¹C- and ¹⁸F-labeled amino acid analogs were developed as alternative metabolic imaging tracers for PET.

¹¹C-methyl methionine (¹¹C-MET) and L-1-¹¹C tyrosine (¹¹C-TYR) have been commonly used for clinical research and practices. Unfortunately, the half-life of ¹¹C is only 20 min, and, therefore, ¹¹C-labeled amino acid analogs require an inconvenient on-site synthesis which reduces their broad clinical usages. ¹⁸F has a half-life of 110 min, and it can be used at a centralized remote facility to synthesize radiolabeled compounds which can then be delivered to different hospitals simultaneously. Moreover, low β^+ -energy of ¹⁸F causes a short positron linear range in tissue, thereby providing high resolution in PET images. A number of ¹⁸F-labeled amino

acid analogs in PET have been investigated, including L-2-¹⁸F-fluorotyrosine (¹⁸F-TYR) [5], O-2-¹⁸F-fluoroethyl-L-tyrosine (¹⁸F-FET) [6], and L-3-¹⁸F-fluoro- α -methyl tyrosine (¹⁸F-FAMT). Recently, Wiriayasermkul et al. found that, unlike ¹⁸F-TYR, ¹⁸F-FET, and other ¹⁸F-labeled amino acids, ¹⁸F-FAMT is transported into cells through L-type amino transporter 1, which contributes to its highly tumor-specific accumulation [4]. ¹⁸F-FAMT was first studied as a brain-imaging probe [7]; later, its use in detecting oral squamous cell carcinoma [8], nonsmall cell lung cancer [9], and esophageal squamous cell carcinoma [10] was investigated. However, the yield of ¹⁸F-labeled amino acids by an electrophilic fluorination reaction is low (17% for ¹⁸F-TYR [5]; 20% ± 5.1% for ¹⁸F-FAMT [11]). Wester et al. synthesized O-2-¹⁸F-fluoroethyl-L-tyrosine (¹⁸F-FET) by a nucleophilic fluorination reaction in about 50 min with an overall radiochemical yield of 40% and evaluated it as a PET tracer for cerebral and peripheral tumors [6]. Hamacher and Coenen synthesized ¹⁸F-FET using one-pot reaction, and the radiochemical yield obtained within 80 min was about 60% [12]. However, both methods require high-performance liquid chromatography (HPLC) for purification, which limits the possibility of automated synthesis. Wang et al. obtained ¹⁸F-FET by direct nucleophilic fluorination reaction of the protected precursor N-butoxycarbonyl-(O-(2-tosyloxyethyl))-L-tyrosine methyl ester, followed by a rapid removal of the protecting group, and a labeled intermediate was separated out with Sep-Pak silica plus cartridge [13]. The radiochemical yield was about 40% at the end of synthesis (50 min). Bourdier et al. used this method for automated radiosynthesis of ¹⁸F-FET, and the yield was about 35% within 63 min [14]. ¹⁸F-FET was widely used in clinical studies in patients with high-grade or low-grade glioma [15, 16].

Despite the very promising clinical results of ¹⁸F-FAMT, existing methods for synthesizing ¹⁸F-FAMT produce a low chemical yield, which limits the availability of the compound for clinical use, and they require high-performance liquid chromatography (HPLC) for purification, which precludes the use of an automated module to synthesize ¹⁸F-FAMT. Therefore, it is desirable to develop an ¹⁸F-FAMT analog with high chemical yield that can be applied clinically in most major medical facilities. In the present study, we synthesized unlabeled O-[3-¹⁹F-fluoropropyl]- α -methyl tyrosine (¹⁹F-FPAMT) and ¹⁸F-labeled O-[3-¹⁸F-fluoropropyl]- α -methyl tyrosine (¹⁸F-FPAMT) by using nucleophilic substitution to place a fluorine atom on the aliphatic chain of α -methyl tyrosine and solid-phase extraction (SPE) column to purify the products. We then used our customized, fully automated synthesis module to synthesize ¹⁸F-FPAMT. Finally, we used a rat mesothelioma model to investigate the feasibility of using ¹⁸F-FPAMT as a tumor-seeking imaging agent.

2. Materials and Methods

2.1. General. All chemicals and solvents were obtained from Sigma-Aldrich (St. Louis, MO, USA). Nuclear magnetic resonance (NMR) spectra were obtained using a Bruker 300 MHz

Spectrometer (Bruker BioSpin Corporation, Billerica, MA, USA), and mass spectra were recorded on a Waters Q-TOF Ultima mass spectrometer (Waters, Milford, MA, USA) at the Chemistry Core Facility at The University of Texas MD Anderson Cancer Center (Houston, TX, USA). An HPLC system (Waters) was integrated with an ultraviolet detector and a flow-count radio-HPLC detector (BioScan Inc., Washington, DC, USA). The analyses of radio-thin layer chromatography (TLC) were performed on radio-TLC Imaging Scanner (BioScan, Inc.). The scintigraphic imaging studies were processed on microPET (Siemens Medical Systems, Inc., Malvern, PA, USA).

2.2. Synthesis of N-t-butoxycarbonyl-O-[3-tosylpropyl]- α -methyl Tyrosine Ethyl Ester. N-t-butoxycarbonyl-O-[3-hydroxypropyl]- α -methyl tyrosine ethyl ester, which we used as the precursor compound for synthesis of ¹⁹F-FPAMT and ¹⁸F-FPAMT, was prepared as described previously [17]. Briefly, N-t-butoxycarbonyl-O-[3-hydroxypropyl]- α -methyl tyrosine ethyl ester (490 mg; 1.28 mmol) in anhydrous pyridine (32 mL) was cooled to 0°C. Paratoluenesulfonyl chloride (1015 mg; 5.32 mmol) was added to this solution, and the solution was stirred for 30 min. The reaction mixture was then stored in a refrigerator overnight. The mixture was filtered, and the filtrate was poured into an ice and water mixture and extracted with diethyl ether. The ethereal solvent was washed with 30 mL of hydrochloric acid and water (1:1, v/v) to remove pyridine, and the solvent was dried over anhydrous MgSO₄. After filtration and solvent evaporation, N-t-butoxycarbonyl-O-[3-tosylpropyl]- α -methyl tyrosine ethyl ester was purified by column chromatography using a silica gel column and eluted with hexane and ethyl acetate (2:1, v/v) to yield 430 mg (62.5%). NMR and mass spectrometry were performed to confirm the structures.

2.3. Synthesis of ¹⁹F-FPAMT. We used a three-step procedure to synthesize ¹⁹F-FPAMT (Figure 1). The first step was a displacement reaction. Kryptofix 222 (253.9 mg; 0.67 mmol) and K¹⁹F (40.5 mg; 0.69 mmol) were added to a vial containing N-t-butoxycarbonyl-O-[3-tosylpropyl]- α -methyl tyrosine ethyl ester (compound 1; 390 mg; 0.75 mmol) in acetonitrile (1 mL). The reaction vial was heated under reflux at 90°C for 40 min. After heating, the solution was evaporated to dryness. The mixture was reconstituted in 0.5 mL of ethyl acetate. N-t-butoxycarbonyl-O-[3-¹⁹F-fluoropropyl]- α -methyl tyrosine ethyl ester (compound 2) was purified by column chromatography using a silica gel column and eluted with hexane and ethyl acetate (4:1, v/v) to yield 120.0 mg of the compound. The second step was to deprotect butoxycarbonyl (BOC), and the third step was to remove ethyl ester groups. O-[3-¹⁹F-fluoropropyl]- α -methyl tyrosine ethyl ester (compound 3) was synthesized by reacting N-t-butoxycarbonyl-O-[3-¹⁹F-fluoropropyl]- α -methyl tyrosine ethyl ester (compound 2; 82.3 mg; 0.30 mmol) with trifluoroacetate (0.7 mL) in dichloromethane (2.0 mL) at room temperature for 50 min. After the solvent was evaporated to dryness, sodium hydroxide (1N; 1.0 mL) in methanol (1.0 mL) was added, and

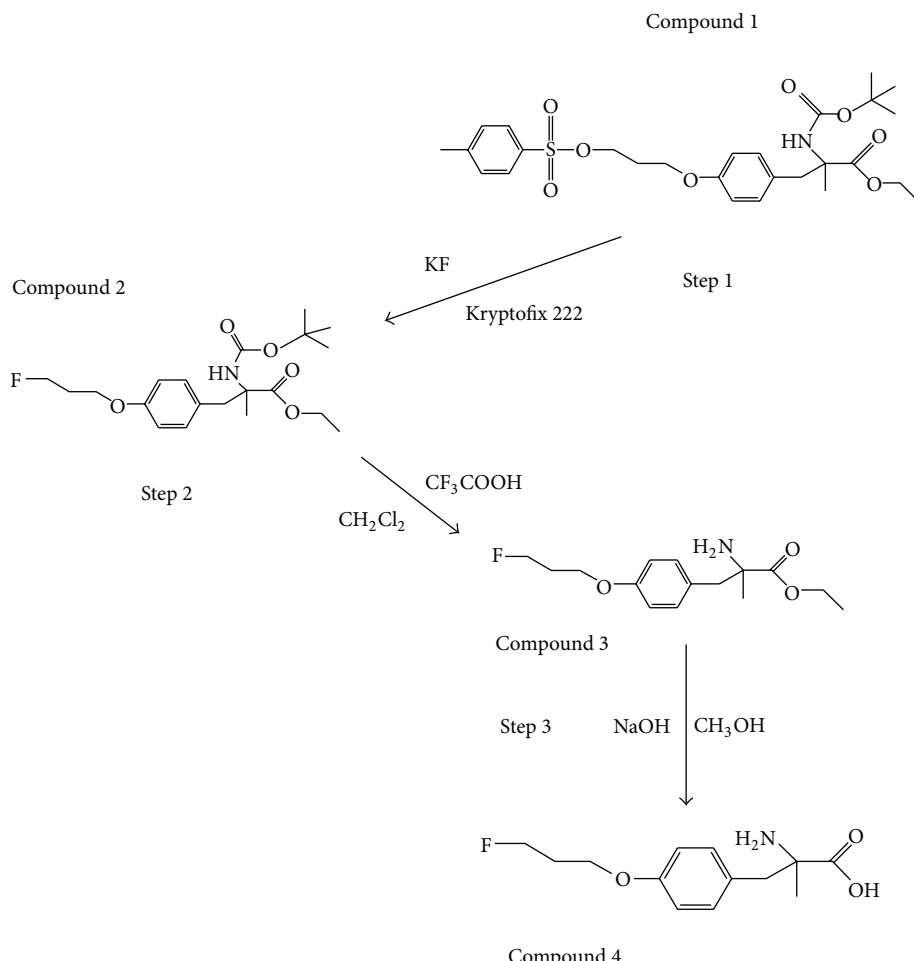


FIGURE 1: Synthetic scheme of FPAMT. The KF and kryptofix complex were incubated with N-t-butoxycarbonyl-O-[3-tosylpropyl]- α -methyl tyrosine ethyl ester (compound 1) in acetonitrile for synthesis of N-t-butoxycarbonyl-O-[3-¹⁹F-fluoropropyl]- α -methyl tyrosine ethyl ester (compound 2). After deprotection of butoxycarbonyl (BOC) of compound 2, O-[3-¹⁹F-fluoropropyl]- α -methyl tyrosine ethyl ester (compound 3) was synthesized. The final step is to yield FPAMT (compound 4) by deesterification of compound 3.

the mixture was heated at 90°C for 15 min to remove ethyl ester group. The mixture was passed through a 0.22 μ M filter to yield ¹⁹F-FPAMT (compound 4). NMR and mass spectrometry were used to confirm the structure of this compound.

2.4. Manual Radiosynthesis of ¹⁸F-FPAMT. [¹⁸F]Fluoride in kryptofix complex (100 mCi in 0.3 mL acetonitrile) was purchased from the cyclotron facility of Cyclotope (Houston, TX, USA). N-t-butoxycarbonyl-O-[3-tosylpropyl]- α -methyl tyrosine ethyl ester (2 mg; 3.83 μ mol) dissolved in acetonitrile (0.1 mL) was added to the [¹⁸F]fluoride-kryptofix complex (51.5 mCi). The reaction mixture was heated at 90°C for 15 min to allow the displacement to occur. After the reaction mixture cooled, it was passed through a 500 mg silica gel packed SPE column (Whatman Lab., Clifton, NJ, USA) and eluted with acetonitrile (2 mL). The acetonitrile was then evaporated *in vacuo* at 85°C. The resulting mixture was hydrolyzed with trifluoroacetate (0.2 mL) in dichloromethane (0.2 mL) at room temperature for 10 min

to deprotect BOC. After the solvent was evaporated to dryness *in vacuo*, sodium hydroxide (1 N; 0.2 mL) in methanol (0.2 mL) was added and heated at 90°C for 15 min to remove ethyl ester group. After methanol evaporated, hydrochloric acid (0.1 N; 0.2 mL) was used to adjust the pH of the final product to 6.5. Radio-TLC and HPLC were performed to assure the purity and identity of the product.

2.5. Automated Radiosynthesis of ¹⁸F-FPAMT. The automated radiosynthesis of ¹⁸F-FPAMT was achieved by our customized automated module. The diagram of this automated module is shown in Figure 2. The automated radiosynthesis consisted of three steps: nucleophilic substitution, deprotection of BOC, and deesterification. Before radiosynthesis was completed, the reaction vial 1 (RV1) was preloaded with N-t-butoxycarbonyl-O-[3-tosylpropyl]- α -methyl tyrosine ethyl ester (6.2 mg; 11.8 μ mol), and three syringes were loaded with different solutions: acetonitrile (3.0 mL), trifluoroacetate in dichloromethane (2.5 mL; 1:1, v/v), and sodium hydroxide in ethyl alcohol (1 N; 3.0 mL; 1:2, v/v).

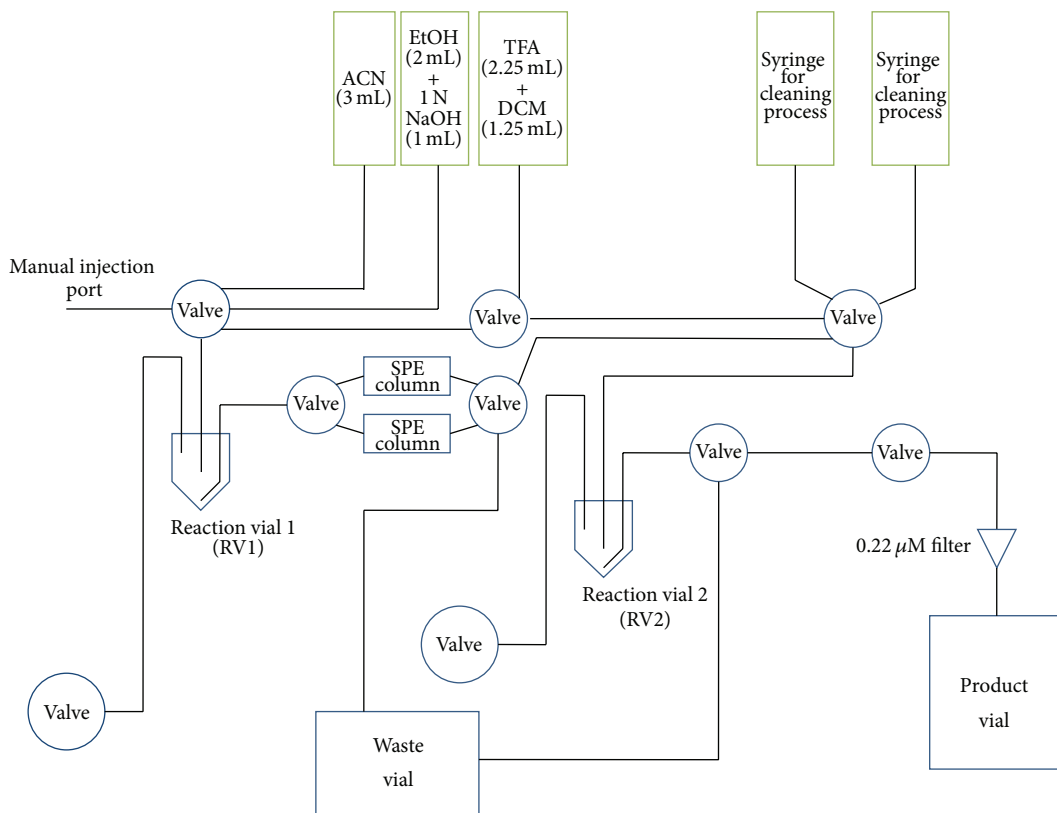


FIGURE 2: Diagram of this customized automated synthesis device. Radioisotope can be manually injected into reaction vial 1 (RV1) through the manual injection port. The upper five green blocks are syringes which were loaded with different chemicals for synthesis or cleaning process. Other blue blocks are fixed parts, such as valves, vials, and columns.

For the nucleophilic substitution, [¹⁸F]fluoride-kryptofix complex (0.2 mL; 29.36 mCi) was manually injected into the RV1 through the injection hole, and additional acetonitrile (0.35 mL) was manually injected into the RV1 to flush the residual [¹⁸F]fluoride-kryptofix complex inside the flow channel. Following this step, the infrared (IR) heater automatically heated the RV1 at 90°C for 15 min. For free fluoride separation, the mixture in the RV1 was automatically passed through a silica gel packed column (SPE 500 mg; Whatman Lab., Clifton, NJ, USA) to the reaction vial 2 (RV2) via nitrogen flow. Additional acetonitrile (2.0 mL) was then added to RV1, and the residual mixture was filtered through a SPE column to remove the free fluoride. The solution inside RV2 was evaporated *in vacuo* at 90°C for 15 min before deprotection of BOC was performed. Trifluoroacetate in dichloromethane (0.4 mL) was loaded into RV2, and the solution was set under room temperature for 10 min to allow the reaction to finish. The solvent was then evaporated to dryness *in vacuo* for 15 min. For deesterification, sodium hydroxide in methanol (0.6 mL) was loaded into RV2. The reaction mixture in RV2 was heated at 90°C for 15 min. Once deesterification was completed, the solvent in RV2 was evaporated *in vacuo*, and the radioactivities of the solvent in the column, RV1, and RV2 were measured upon the completion of ¹⁸F-FPAMT. Radio-TLC and HPLC were performed to assure the purity and identity of the final product.

2.6. In Vitro Cellular Uptake Studies. Rat mesothelioma IL-45 cells were maintained in the mixtures of Dulbecco's modification of Eagle's medium, F-12 (GIBCO, Grand Island, NY, USA), and 10% phosphate-buffered saline at 37°C in a humidified atmosphere containing 5% CO₂. Cells were plated onto 6-well tissue culture plates (2×10^5 cells/well) and incubated with ¹⁸F-FPAMT (8 μCi/well) or ¹⁸F-FDG (Cyclotope, Houston, TX, USA; 8 μCi/well) for 0–2 h. After incubation, the cells were collected, and their radioactivity was measured using a gamma counter. Data were expressed as the mean percent ± the standard deviation of the cellular uptake of ¹⁸F-FPAMT or ¹⁸F-FDG.

2.7. Biodistribution of ¹⁸F-FPAMT and ¹⁸F-FDG in Mesothelioma-Bearing Rats. Three hundred forty-four female Fischer rats (140–185 g) were obtained from Harlan, Inc. (Indianapolis, IN, USA). The rats were housed in an animal facility at The University of Texas MD Anderson Cancer Center. All protocols involving animals were approved by the Animal Use and Care Committee at MD Anderson Cancer Center. Nine rats were inoculated with mesothelioma IL-45 cells (1×10^5 cells/rat) at the hinged leg. Twelve days after being inoculated with the mesothelioma cells, the rats were anesthetized with ketamine (10–15 mg/rat). ¹⁸F-FPAMT dissolved in saline (0.5 mCi/5 mL) was injected intravenously into 9 rats ($n = 3$ rats/group, 30 μCi/rat.). For comparison, the clinical

standard, ^{18}F -FDG (Cyclotope), was injected intravenously into 9 rats ($n = 3$ rats/group; 30 $\mu\text{Ci}/\text{rat}$). The distribution of ^{18}F -FPAMT or ^{18}F -FDG in various tissues was assessed at 30 min, 1.5 hrs, and 3 hrs after injection by COBRA. Percent of injected dose per tissue type was then calculated, and the data were expressed as the mean percent \pm the standard deviation of the injected dose.

2.8. Dosimetry of ^{18}F -FPAMT and ^{18}F -FDG. Dosimetric calculations were performed from 30 to 180 min after the administration of ^{18}F -FPAMT and ^{18}F -FDG, and time-activity curves were generated for each organ. Analytic integration of the curves was used to determine the area under the curve (AUC), which was divided by the injected dose to yield the residence times of ^{18}F -FPAMT and ^{18}F -FDG in each organ. Residence times were then used to calculate target organ absorbed radiation doses based on the medical internal radiation dosimetry methodology for the normal adult male using the Olinda software package (Oak Ridge, TN, USA).

2.9. PET Imaging of Mesothelioma-Bearing Rats. Mesothelioma-bearing rats cells were imaged when their tumors were 1-2 cm in diameter. The rats were anesthetized with 2% isoflurane and administered with 500 μCi of ^{18}F -FDG or 500 μCi of ^{18}F -FPAMT. Four serial 15-minute transaxial PET images of each rat were obtained using microPET (Siemens Medical Systems, Inc., IL, USA).

3. Results

3.1. Chemistry. The synthetic schemes of ^{18}F -FPAMT and ^{19}F -FPAMT are shown in Figure 1. The structure of precursor N-t-butoxycarbonyl-O-[3-tosylpropyl]- α -methyl tyrosine ethyl ester (compound 1) was confirmed using $^1\text{H-NMR}$ and mass spectrometry. The $^1\text{H-NMR}$ (CDCl_3) result was the following: $\delta = 7.76$ (d, 2 H, $J = 8.1$ Hz), 7.26 (d, 2 H, $J = 8.1$ Hz), 6.97 (d, 2 H, $J = 8.4$ Hz), 6.67 (d, 2 H, $J = 8.7$ Hz), 4.23 (t, 2 H, $J = 12.0$ Hz), 4.12 (q, 2 H, $J = 7.2$ Hz, $J = 7.2$ Hz), 3.92 (t, 2 H, $J = 11.7$ Hz), 3.22 (q, 2 H, $J = 13.5$ Hz, $J = 12.9$ Hz), 2.40 (s, 3 H), 2.12 (m, 2 H), 1.54 (s, 3 H), 1.47 (s, 9 H), and 1.29 (t, 3 H, $J = 12.3$ Hz) ppm; M/Z: 558.29 ($\text{M}+\text{Na}^+$).

^{19}F -FPAMT was obtained after subjecting compound 1 to nucleophilic substitution, free fluoride separation, deprotection of BOC, and deesterification. The structure of ^{19}F -FPAMT (compound 4) was confirmed using $^1\text{H-NMR}$ and mass spectrometry. The $^1\text{H-NMR}$ (D_2O) result the following result was: $\delta = 7.17$ (d, 2 H, $J = 8.4$ Hz), 6.93 (d, 2 H, $J = 8.7$ Hz), 4.75 (t, 1 H, $J = 11.7$ Hz), 4.59 (t, 1 H, $J = 11.7$ Hz), 4.13 (t, 2 H, $J = 12.3$ Hz), 2.84 (dd, $J = 13.2$ Hz, $J = 13.5$ Hz), 2.14 (m, 2 H), and 1.29 (s, 3 H) ppm. $^{19}\text{F-NMR}$ $\delta = 220.33$; M/Z: 406.38 ($\text{M}+\text{Na}^+$).

3.2. Radiochemistry. The ^{18}F -displacement reaction produced 35.4 mCi (yield: 78%, decay corrected) of N-t-butoxycarbonyl-O-[3- ^{18}F -fluoropropyl]- α -methyl tyrosine ethyl ester, and the residual in the column was 3.77 mCi

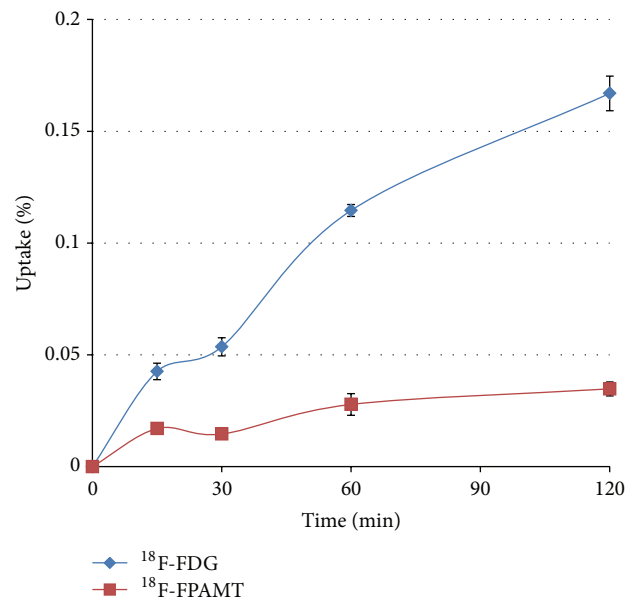


FIGURE 3: *In vitro* cellular uptake of ^{18}F -FPAMT and ^{18}F -FDG in mesothelioma cells (IL-45). Data are expressed as mean percent of cellular uptake \pm standard deviation (%uptake \pm SD) measured at 15, 30, 60, and 120 min.

(8.3%, decay corrected). The no-carrier-added displacement product corresponded to the unlabeled N-t-butoxycarbonyl-O-[3-fluoropropyl]- α -methyl tyrosine ethyl ester under the same TLC system (hexane: ethyl acetate; 10:3, v/v) and HPLC system (20 μL loop, 210 nm, Bondapak CN-RP column, Waters, eluted with methanol:water, 3:2, v/v; flow rate 1.0 mL/min). The retention factor (R_f) of N-t-butoxycarbonyl-O-[3- ^{18}F -fluoropropyl]- α -methyl tyrosine ethyl ester was 0.46 with purity >99%. Under the same conditions, the R_f value for [^{18}F]fluoride in kryptofix complex was 0.1. After hydrolysis, ^{18}F -FPAMT stayed at origin ($R_f = 0.1$). The retention times for N-BOC and the ethyl ester form of tosylpropyl-, fluoropropyl-, and ^{18}F -fluoropropyl- α -ethyltyrosine were 16.13, 8.37, and 8.79 min, respectively. The decay-corrected yield for hydrolysis (deprotection of BOC and deesterification) was 89%. At the end-of-synthesis (88 min), 10 mCi of ^{18}F -FPAMT was obtained, and the decay-corrected yield was 34%. The specific activity of this compound was 0.32 Ci/ μmol . For the automated synthesis of ^{18}F -FPAMT, the decay-corrected yield was 15%, the end-of-synthesis time was 110 min, and the specific activity was 0.16 Ci/ μmol .

3.3. In Vitro Cellular Uptake Studies. The uptake of ^{18}F -FPAMT reached saturation at 60 min (Figure 3). ^{18}F -FDG uptake continued to increase throughout the period, and the percentage uptake of ^{18}F -FDG was higher than that of ^{18}F -FPAMT at each time point.

3.4. Biodistribution of ^{18}F -FPAMT and ^{18}F -FDG in Mesothelioma-Bearing Rats. The distributions of ^{18}F -FPAMT and

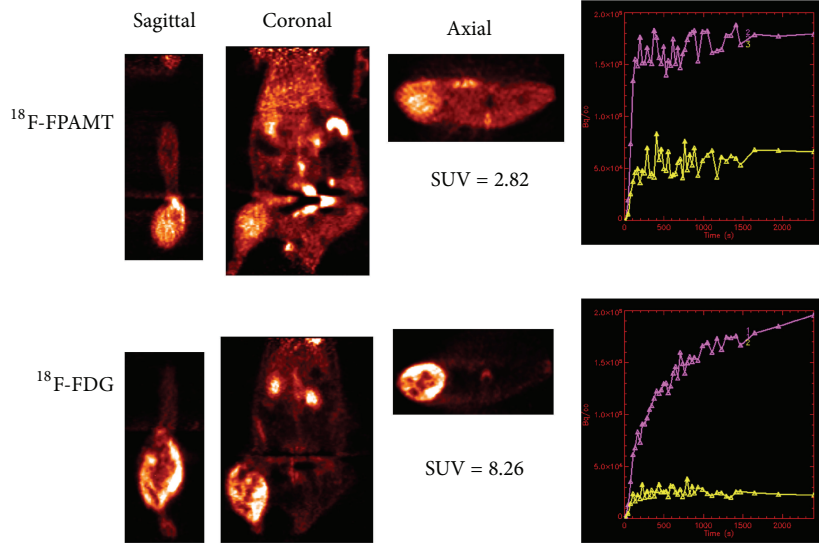


FIGURE 4: μ PET images of ¹⁸F-FPAMT and ¹⁸F-FDG in mesothelioma-bearing rats (lower body: IL-45, at 45 min). The SUV ratios of tumor to muscle for ¹⁸F-FPAMT and ¹⁸F-FDG were 2.82 and 8.26, respectively. Computer-outlined regions of interest (ROI) (counts per pixel) for tumor and muscle at the corresponding time interval were used to generate a dynamic plot. Dynamic plot was from 0 to 45 minutes.

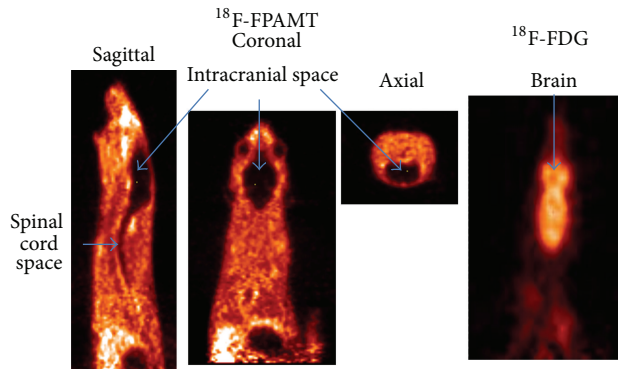


FIGURE 5: μ PET images of ¹⁸F-FPAMT and ¹⁸F-FDG in mesothelioma-bearing rats (upper body: IL-45, at 45 min). There was extremely low uptake of ¹⁸F-FPAMT in the brain and spinal cord when compared with ¹⁸F-FDG.

¹⁸F-FDG in various tissues in mesothelioma-bearing rats are shown in Tables 1 and 2, respectively. Both compounds showed no marked increase in bone uptake, representing their *in vivo* stability. High kidney and pancreas uptake of ¹⁸F-FPAMT was observed, and this phenomenon was also observed from other tyrosine-based radiotracers [18]. Unlike ¹⁸F-FDG, ¹⁸F-FPAMT had poor uptake in brain tissue.

3.5. Dosimetry of ¹⁸F-FPAMT in Rats. The estimated absorbed radiation dose of ¹⁸F-FPAMT is shown in Table 3. According to the US Food and Drug Administration Regulations, human exposure to radiation from the use of “radioactive research drugs” should be limited to 3 rem per single administration and 3 rem per year to the whole body, blood-forming organs (red marrow, osteogenic cells, and spleen), the lens of the eye, and gonads (testes and uterus);

the limit for other organs is 5 rem per single administration and 15 rem annually. The total rem of ¹⁸F-FPAMT absorbed by each organ was below these limits at the proposed injection of 30 mCi per patient.

3.6. Imaging of Mesothelioma-Bearing Rats. Scintigraphic images of mesothelioma-bearing rats administrated ¹⁸F-FPAMT or ¹⁸F-FDG showed that tumors could be clearly detected, and bone uptake was low (Figure 4). The standardized uptake value (SUV) curve of ¹⁸F-FPAMT for tumor and muscle reached the plateau at 30 min after injection, but the SUV curve of ¹⁸F-FDG for tumor continued increasing during the imaging. The SUV ratios of tumor to muscle for ¹⁸F-FPAMT and ¹⁸F-FDG were 2.82 and 8.26, respectively. There was extremely low uptake of ¹⁸F-FPAMT in the brain and spinal cord when compared with ¹⁸F-FDG (Figure 5).

TABLE 1: Biodistribution of ¹⁸F-FPAMT in rats.

	% of injected dose per gram of tissue weight (n = 3/time, interval (iv))		
	30 min	90 min	180 min
Blood	0.37 ± 0.07	0.11 ± 0.01	0.04 ± 0.00
Heart	0.32 ± 0.04	0.12 ± 0.01	0.04 ± 0.00
Lungs	0.31 ± 0.06	0.09 ± 0.01	0.03 ± 0.00
Thyroid	0.28 ± 0.01	0.14 ± 0.01	0.09 ± 0.01
Pancreas	0.84 ± 0.11	0.19 ± 0.03	0.07 ± 0.01
Liver	0.49 ± 0.06	0.14 ± 0.01	0.05 ± 0.00
Spleen	0.34 ± 0.05	0.09 ± 0.01	0.03 ± 0.00
Kidneys	3.86 ± 0.74	0.90 ± 0.13	0.40 ± 0.02
Stomach	0.27 ± 0.03	0.09 ± 0.01	0.03 ± 0.00
Intestines	0.37 ± 0.04	0.15 ± 0.05	0.04 ± 0.00
Uterus	0.27 ± 0.03	0.07 ± 0.01	0.03 ± 0.00
Muscle	0.27 ± 0.03	0.15 ± 0.01	0.07 ± 0.01
Bone	0.11 ± 0.01	0.10 ± 0.02	0.19 ± 0.05
Brain	0.02 ± 0.00	0.01 ± 0.00	0.01 ± 0.00

Values shown represent the mean ± standard deviation of data from 3 animals.

TABLE 2: Biodistribution of ¹⁸F-FDG in rats.

	% of injected dose per gram of tissue weight (n = 3/time, interval (iv))		
	30 min	90 min	180 min
Blood	0.45 ± 0.07	0.15 ± 0.01	0.07 ± 0.01
Heart	3.42 ± 1.14	1.95 ± 0.40	1.94 ± 0.45
Lungs	0.60 ± 0.07	0.53 ± 0.03	0.46 ± 0.06
Thyroid	0.65 ± 0.04	0.47 ± 0.05	0.54 ± 0.04
Pancreas	0.22 ± 0.02	0.21 ± 0.02	0.21 ± 0.03
Liver	0.51 ± 0.08	0.33 ± 0.03	0.23 ± 0.03
Spleen	0.88 ± 0.08	0.87 ± 0.06	0.98 ± 0.10
Kidneys	0.85 ± 0.13	0.43 ± 0.04	0.23 ± 0.01
Stomach	0.55 ± 0.03	0.40 ± 0.03	0.38 ± 0.02
Intestines	0.94 ± 0.16	1.00 ± 0.22	0.62 ± 0.07
Uterus	0.52 ± 0.06	0.57 ± 0.08	0.39 ± 0.09
Muscle	0.45 ± 0.14	0.23 ± 0.03	0.42 ± 0.06
Bone	0.21 ± 0.09	0.14 ± 0.07	0.24 ± 0.06
Brain	2.36 ± 0.10	2.24 ± 0.20	1.89 ± 0.35

Values shown represent the mean ± standard deviation of data from 3 animals.

4. Discussion

Mesothelioma is an asbestos-related neoplasm generating from mesothelial cells in the pleural, peritoneal, and pericardial cavities, and its incidence increased in several countries [19]. The diagnostic tools and treatment regimens for these tumors are disappointing, and median survival time is 12 months after initial diagnosis [20]. The initial diagnoses of mesothelioma are based on patient's medical history and physical examination. After that, computed tomography

TABLE 3: Radiation dose estimates of reference adult for ¹⁸F-FPAMT.

Target organ	rad/mCi	human dose (mCi)	rad
Organs (5 rem annually/15 rem total)			
Adrenals	2.98E - 03	30	0.089
Brain	9.27E - 04	30	0.028
Breasts	1.95E - 03	30	0.059
Gall bladder wall	2.88E - 03	30	0.086
Lli wall	3.16E - 03	30	0.095
Small int.	3.54E - 03	30	0.106
Stomach	2.79E - 03	30	0.084
Uli wall	3.21E - 03	30	0.096
Heart wall	2.94E - 03	30	0.088
Kidneys	6.19E - 03	30	0.186
Liver	1.51E - 03	30	0.045
Lungs	2.40E - 03	30	0.072
Muscle	1.63E - 03	30	0.049
Pancreas	3.38E - 03	30	0.101
Bone surfaces	6.88E - 03	30	0.206
Skin	1.55E - 03	30	0.047
Testes	2.29E - 03	30	0.069
Thymus	2.43E - 03	30	0.073
Thyroid	2.47E - 03	30	0.074
Urine bladder wall	3.01E - 03	30	0.090
Uterus	3.36E - 03	30	0.101
Eff dose	2.61E - 03	30	0.078
Blood-forming organs (3 rem annually/5 rem total)			
Ovaries	3.24E - 03	30	0.097
Red marrow	2.29E - 03	30	0.069
Spleen	3.42E - 03	30	0.103
Eff dose eq.	3.14E - 03	30	0.094
Total body	2.35E - 03	30	0.071

scans and magnetic resonance imaging are used to screen patients, and then biopsy test is needed to confirm the incidence of mesothelioma. ¹⁸F-FDG/PET scan is the tool to determine whether a suspicious area is malignant mesothelioma or a benign condition such as pleural scarring, and the result can identify the best area for an accurate biopsy. PET scans are also effective for highlighting mesothelioma metastases that may not appear on other conventional imaging scans. However, ¹⁸F-FDG/PET scans have limitations in differential diagnosis between cancerous cells and inflammation tissues which metabolize glucose with abnormally high rates. In this case, radiolabeled amino acids are the alternative methods to detect malignant pleural mesothelial and other cancerous cells which overexpress unregulated amino acid transporters [21–23]. Mesothelioma rat model was then selected because rat model provided better anatomical differentiation than mouse model in imaging studies. It is more accurate to determine radiation dosimetry from biodistribution data.

¹⁸F-FET and ¹⁸F-FAMT are radiolabeled amino acids, and they are useful in imaging cancers. However, existing

methods for synthesizing these compounds result in low yields, thus limiting the availability of ¹⁸F-FET and ¹⁸F-FAMT in the clinic. In the present study, we synthesized ¹⁸F-FPAMT, an ¹⁸F-FAMT analog, and used a mesothelioma rat model to preliminarily evaluate it as a tumor-imaging compound. We used NMR and mass spectrometry to confirm the structure of ¹⁹F-FPAMT. The yield of ¹⁹F-FPAMT was 46.71%. N-t-butoxycarbonyl-O-[3-tosylpropyl]- α -methyl tyrosine ethyl ester was used as the starting material for manual and automated syntheses of ¹⁸F-FPAMT. The quality control of ¹⁸F-FPAMT was evaluated by radio-TLC and HPLC. Manual synthesis of ¹⁸F-FPAMT resulted in the decay-corrected yield of 34%, radiochemical purity of >95%, the specific activity of 0.32 Ci/ μ mol, and pH value of 5 to 6; the manual synthesis time was 88 min. Automated synthesis of ¹⁸F-FPAMT resulted in the decay-corrected yield of 15%, radiochemical purity of >95%, the specific activity of 0.16 Ci/ μ mol, and pH value of 5 to 6; the manual synthesis time was 110 min.

The traditional method of radiosynthesizing ¹⁸F-labeled tyrosine analogs such as ¹⁸F-FET and ¹⁸F-FAMT was through electrophilic substitution reaction which has low synthetic yield. Besides, the reaction uses ¹⁸F-F₂ gas, and HPLC separation makes it even difficult to use this method in automated modules. Although a nucleophilic reaction could result in a high yield of ¹⁸F-FET (40%), this method still requires HPLC for purification, and, thus, it is not ideal to use this synthesis method in automated synthesis modules. In the present study, we obtained ¹⁸F-FPAMT by a nucleophilic reaction, but we completed the purification process without HPLC. Therefore, our method of synthesizing ¹⁸F-FPAMT can be applied to the customized automated synthesis module.

For the *in vitro* studies, although the result showed that ¹⁸F-FPAMT had lower cellular uptake than that of ¹⁸F-FDG, the uptake mechanism of these two compounds is different. Malignant cells utilize ¹⁸F-FDG as glucose for upregulated aerobic glycolysis and ¹⁸F-FPAMT as an amino acid for proliferation. The results indicate that ¹⁸F-FPAMT has the potential to become a tumor detecting tracer. Biodistribution studies showed that ¹⁸F-FPAMT and ¹⁸F-FDG were rapidly cleared from blood and distributed in other tissues. Compared with ¹⁸F-FDG, the accumulation of ¹⁸F-FPAMT was significantly lower in heart, lungs, thyroid, spleen, and brain. High accumulation of ¹⁸F-FPAMT was observed in the kidneys and pancreas after administration. This could be due to the high expression of the amino acid transporters in the kidneys and pancreas [4]. These results were consistent with those of other radiolabeled amino acid analogs such as ¹⁸F-FAMT [24] and ⁷⁷Br-BAMT [18], although ¹⁸F-FET showed only higher uptake in kidneys [25]. The bone uptakes of ¹⁸F-FPAMT and ¹⁸F-FDG at 180 min after administration increased slightly, suggesting defluorination of both compounds. In the microPET studies of ¹⁸F-FDG and ¹⁸F-FPAMT, the lesions could be observed clearly at 45 min after administration (Figure 4), and the accumulation of ¹⁸F-FPAMT in the brain and spinal cord was significantly less than that of ¹⁸F-FDG (Figure 5), suggesting that ¹⁸F-FPAMT has great potential in imaging brain tumors.

5. Conclusion

In this study, we manually synthesized ¹⁸F-FPAMT with high yielding and radiochemical purity, and we used the customized automated synthesizer for the proof of concept of automated manufacturing of ¹⁸F-FPAMT. Both *in vitro* and *in vivo* studies suggested that ¹⁸F-FPAMT can be a good PET agent for detecting mesothelioma, and it might have great potential in brain tumor imaging. In the future, we will focus on optimization of the automated processes for a better yield and a higher specific activity.

Conflict of Interests

All authors have no commercial associations that might pose a conflict of interests in connection with the submitted paper.

Acknowledgments

This paper was supported in part by the John S. Dunn Foundation and the Sponsored Research Agreement (LS01-212) made by Cell > Point L.L.C. at the MD Anderson Cancer Center. The NMR, mass spectrometry, and animal research were supported by the MD Anderson Cancer Center Support Grant.

References

- [1] L. Kostakoglu, H. Agress Jr., and S. J. Goldsmith, "Clinical role of FDG PET in evaluation of cancer patients," *Radiographics*, vol. 23, no. 2, pp. 315–340, 2003.
- [2] W. Chen, T. Cloughesy, N. Kamdar et al., "Imaging proliferation in brain tumors with ¹⁸F-FLT PET: comparison with ¹⁸F-FDG," *Journal of Nuclear Medicine*, vol. 46, no. 6, pp. 945–952, 2005.
- [3] C. Love, M. B. Tomas, G. G. Tronco, and C. J. Palestro, "FDG PET of infection and inflammation," *Radiographics*, vol. 25, no. 5, pp. 1357–1368, 2005.
- [4] P. Wiriyasermkul, S. Nagamori, H. Tominaga et al., "Transport of 3-fluoro-L- α -methyl-tyrosine by tumor-upregulated L-type amino acid transporter 1: a cause of the tumor uptake in PET," *Journal of Nuclear Medicine*, vol. 53, no. 8, pp. 1253–1261, 2012.
- [5] H. H. Coenen, P. Kling, and G. Stocklin, "Cerebral metabolism of L-[2-¹⁸F]fluorotyrosine, a new PET tracer of protein synthesis," *Journal of Nuclear Medicine*, vol. 30, no. 8, pp. 1367–1372, 1989.
- [6] H. J. Wester, M. Herz, W. Weber et al., "Synthesis and radio-pharmacology of O-(2-[¹⁸F]fluoroethyl)-L-tyrosine for tumor imaging," *Journal of Nuclear Medicine*, vol. 40, no. 1, pp. 205–212, 1999.
- [7] T. Inoue, K. Koyama, N. Oriuchi et al., "Detection of malignant tumors: whole-body PET with fluorine 18 α -methyl tyrosine versus FDG—preliminary study," *Radiology*, vol. 220, no. 1, pp. 54–62, 2001.
- [8] G. Miyashita, T. Higuchi, N. Oriuchi et al., "¹⁸F-FAMT uptake correlates with tumor proliferative activity in oral squamous cell carcinoma: comparative study with ¹⁸F-FDG PET and immunohistochemistry," *Annals of Nuclear Medicine*, vol. 24, no. 8, pp. 579–584, 2010.
- [9] K. Kaira, N. Oriuchi, K. Shimizu et al., "Comparison of l-type amino acid transporter 1 expression and L-[3-¹⁸F]- α -methyl

- tyrosine uptake in outcome of non-small cell lung cancer," *Nuclear Medicine and Biology*, vol. 37, no. 8, pp. 911–916, 2010.
- [10] M. Sohda, H. Kato, S. Suzuki et al., "“¹⁸F-FAMT-PET is useful for the diagnosis of lymph node metastasis in operable esophageal squamous cell carcinoma," *Annals of Surgical Oncology*, vol. 17, no. 12, pp. 3181–3186, 2010.
- [11] K. Tomiyoshi, K. Amed, S. Muhammad et al., "Synthesis of isomers of ¹⁸F-labelled amino acid radiopharmaceutical: position 2- and 3-L-¹⁸F- α -methyltyrosine using a separation and purification system," *Nuclear Medicine Communications*, vol. 18, no. 2, pp. 169–175, 1997.
- [12] K. Hamacher and H. H. Coenen, "Efficient routine production of the ¹⁸F-labelled amino acid O-(2-[¹⁸F]fluoroethyl)-L-tyrosine," *Applied Radiation and Isotopes*, vol. 57, no. 6, pp. 853–856, 2002.
- [13] M. Wang, D. Yin, S. Li, and Y. Wang, "Synthesis of O-(2-[¹⁸F]fluoroethyl)-L-tyrosine and its biological evaluation in B16 melanoma-bearing mice as PET tracer for tumor imaging," *Science in China Series B*, vol. 50, no. 2, pp. 276–283, 2007.
- [14] T. Bourdier, I. Greguric, P. Roselt, T. Jackson, J. Faragalla, and A. Katsifis, "Fully automated one-pot radiosynthesis of O-(2-[¹⁸F]fluoroethyl)-l-tyrosine on the TracerLab FXFN module," *Nuclear Medicine and Biology*, vol. 38, no. 5, pp. 645–651, 2011.
- [15] N. Galldiks, M. Rapp, G. Stoffels et al., "Response assessment of bevacizumab in patients with recurrent malignant glioma using [¹⁸F]Fluoroethyl-L-tyrosine PET in comparison to MRI," *European Journal of Nuclear Medicine and Molecular Imaging*, vol. 40, pp. 22–33, 2012.
- [16] E. W. F. Lau, K. J. Drummond, R. E. Ware et al., "Comparative PET study using F-18 FET and F-18 FDG for the evaluation of patients with suspected brain tumour," *Journal of Clinical Neuroscience*, vol. 17, no. 1, pp. 43–49, 2010.
- [17] F.-L. Kong, M. S. Ali, Y. Zhang et al., "Synthesis and evaluation of amino acid-based radiotracer ^{99m}Tc-N4-AMT for breast cancer imaging," *Journal of Biomedicine and Biotechnology*, vol. 2011, Article ID 276907, 7 pages, 2011.
- [18] Y. Ohshima, H. Hanaoka, S. Watanabe et al., "Preparation and biological evaluation of 3-[⁷⁶Br]bromo- α -methyl-l-tyrosine, a novel tyrosine analog for positron emission tomography imaging of tumors," *Nuclear Medicine and Biology*, vol. 38, no. 6, pp. 857–865, 2011.
- [19] V. Delgermaa, K. Takahashi, E.-K. Park, G. V. Le, T. Hara, and T. Sorahan, "Global mesothelioma deaths reported to the World Health Organization between 1994 and 2008," *Bulletin of the World Health Organization*, vol. 89, no. 10, pp. 716–724, 2011.
- [20] B. W. S. Robinson, A. W. Musk, and R. A. Lake, "Malignant mesothelioma," *Lancet*, vol. 366, no. 9483, pp. 397–408, 2005.
- [21] K. Kaira, N. Oriuchi, T. Takahashi et al., "L-Type amino acid transporter 1 (LAT1) expression in malignant pleural mesothelioma," *Anticancer Research*, vol. 31, no. 12, pp. 4075–4082, 2011.
- [22] H. Kobayashi, Y. Ishii, and T. Takayama, "Expression of L-type amino acid transporter 1 (LAT1) in esophageal carcinoma," *Journal of Surgical Oncology*, vol. 90, no. 4, pp. 233–238, 2005.
- [23] D. K. Kim, I. J. Kim, S. Hwang et al., "System L-amino acid transporters are differently expressed in rat astrocyte and C6 glioma cells," *Neuroscience Research*, vol. 50, no. 4, pp. 437–446, 2004.
- [24] T. Inoue, K. Tomiyoshi, T. Higuichi et al., "Biodistribution studies on L-3-[Fluorine-18]Fluoro- α -methyl tyrosine: a potential tumor-detecting agent," *Journal of Nuclear Medicine*, vol. 39, no. 4, pp. 663–667, 1998.
- [25] T. S. Lee, S. H. Ahn, B. S. Moon et al., "Comparison of ¹⁸F-FDG, ¹⁸F-FET and ¹⁸F-FLT for differentiation between tumor and inflammation in rats," *Nuclear Medicine and Biology*, vol. 36, no. 6, pp. 681–686, 2009.

Research Article

Affinity Labeling of Membrane Receptors Using Tissue-Penetrating Radiations

Franklin C. Wong,^{1,2,3,4} John Boja,^{5,6} Beng Ho,² Michael J. Kuhar,^{5,7} and Dean F. Wong^{3,8}

¹ Nuclear Medicine, University of Texas MD Anderson Cancer Center, Houston, TX 77030-4009, USA

² Neuro-Oncology, University of Texas MD Anderson Cancer Center, Houston, TX 77030-4009, USA

³ Department of Radiology, Johns Hopkins Medical Institutions, Baltimore, MD 21205, USA

⁴ University of Texas MD Anderson Cancer Center, 1400 Pressler, Unit 1483, Houston, TX 77030-4009, USA

⁵ Addiction Research Center, National Institute of Drug Abuse, Baltimore, MD 21224, USA

⁶ U.S. Consumer Product Safety Commission, Bethesda, MD 20814, USA

⁷ Neuropharmacology, Yerkes National Primate Research Center of Emory University, Atlanta, GA 30322, USA

⁸ Radiology, Psychiatry, Neuroscience, Environmental Health Science, and Carey Business School,

Johns Hopkins Medical Institutions, Baltimore, MD 21205, USA

Correspondence should be addressed to Franklin C. Wong; fwong@mdanderson.org

Received 15 April 2013; Revised 6 June 2013; Accepted 13 June 2013

Academic Editor: Mei-Hsiu Liao

Copyright © 2013 Franklin C. Wong et al. This is an open access article distributed under the Creative Commons Attribution License, which permits unrestricted use, distribution, and reproduction in any medium, provided the original work is properly cited.

Photoaffinity labeling, a useful *in vivo* biochemical tool, is limited when applied *in vivo* because of the poor tissue penetration by ultraviolet (UV) photons. This study investigates affinity labeling using tissue-penetrating radiation to overcome the tissue attenuation and irreversibly label membrane receptor proteins. Using X-ray (115 kVp) at low doses (<50 cGy or Rad), specific and irreversible binding was found on striatal dopamine transporters with 3 photoaffinity ligands for dopamine transporters, to different extents. Upon X-ray exposure (115 kVp), RTI-38 and RTI-78 ligands showed irreversible and specific binding to the dopamine transporter similar to those seen with UV exposure under other conditions. Similarly, gamma rays at higher energy (662 keV) also affect irreversible binding of photoreactive ligands to peripheral benzodiazepine receptors (by PK14105) and to the dopamine (D2) membrane receptors (by azidoclebopride), respectively. This study reports that X-ray and gamma rays induced affinity labeling of membrane receptors in a manner similar to UV with photoreactive ligands of the dopamine transporter, D2 dopamine receptor (D2R), and peripheral benzodiazepine receptor (PBDZR). It may provide specific noninvasive irreversible block or stimulation of a receptor using tissue-penetrating radiation targeting selected anatomic sites.

1. Introduction

Photoaffinity labeling utilizes UV photons to convert reversible binding between a photoreactive ligand and a receptor/protein into irreversible binding [1]. This biochemical technique has provided useful tools to characterize receptors and biologically important proteins, mostly *in vitro*, because the irreversible binding enhances the signal-to-noise ratio upon washout of the unbound ligand. The classic study of affinity labeling is the use of radiolabeled affinity ligand to bind membrane protein receptor followed by UV irradiation, washing, and radioactivity counts. The alternative is

binding of nonradioactive photoaffinity ligand to membrane receptors, followed by UV irradiation, washing, and assay of residual available receptors. Free-radical formation is also the mechanism through which X-ray and gamma rays interact in biologic systems. In fact, interactions between low-dose of X-ray (20–100 cGy) and photoreactive substrates have been reported to result in >80% enzyme inhibition in a dose-related manner similar to the effects of UV [2].

Due to the poor tissue penetration of the UV photon, *in vivo* application of affinity labeling is limited. Although the exact mechanism of photoaffinity labeling is not clear, free-radical formation is inevitably involved. Therefore, if

the photoreactive ligand can be activated and converted into an irreversible bound label by tissue-penetrating radiation, it may prove useful in *in vivo* studies. The translation from *in vitro* to *in vivo* studies could be started with established membrane neuroreceptor systems. When established, neuroreceptor and other affinity labeling systems can be measured *in vivo* by advanced tomography including PET and SPECT.

Striatal dopamine transporter (SDT), which mediates the actions of many drugs, has been investigated using PET for diseases including drug abuse. These studies have utilized high-affinity reversible ligands. Several photoreactive ligands (including the three studied in this project) have been developed as well [3].

In baboon and human brains, striatal dopamine-2 receptors (D2R) can be imaged and quantified by PET using ^{11}C -N-methylspiperone, NMSP [4]. The density of D2R is found to be elevated in the prolactin secreting human pituitary adenomas [5] and nonsecreting macroadenoma [6]. The D2R photoaffinity labeling agent, azidoclebopride, is commercially available and has been used to irreversibly label the D2R [7, 8]. Since PET studies of human D2R are well-established, it may be interesting to study these compounds before and after irradiation.

Most abundantly found in the kidneys, peripheral benzodiazepine receptors (PBDZR) localize in the mitochondrial membranes with porphyrins as the endogenous ligand. It is involved in the depression of the respiration ratio and oxidative phosphorylation; *in vitro* studies show that PBDZR ligands stimulate proliferation of the neoplastic cells and inhibit reproduction of the normal immune cell [9]. The levels of PBDZR are shown to be markedly elevated (3–20-folds) in animal gliomas, human gliomas, and colonic and ovarian carcinomas. Positron emission tomography using ^{11}C -PK11195, a PBDZR ligand, was able to distinguish gliomas from normal brain tissue in *in vivo* human studies [10, 11]. The potential of PBDZR photoaffinity labeling is best illustrated with PK14105 which if unbound has a favorable rapid dissociation feature [12]. This feature is desirable because the difference between the irreversible ligand bond and reversibly bound residual ligand may be maximized by subsequent washout of the free ligand over time. PK14105 has also been found to serve a good potential tracer to evaluate brain lesions [11] as well as immune tissues in rats [13].

X-ray and gamma rays are identical forms of higher energy photon radiations differing only by their origins. X-ray is produced by machine while gamma rays are produced by radionuclides. Direct inactivation of enzymes by ionizing radiations such as target-site analysis occurs at higher doses ($>1000\text{ Gy}$). On the other hand, radiochemical reactions in biologic systems are predominantly mediated by free-radicals formation at lower radiation doses (e.g., $<10\text{ Gy}$). Therefore, the plausibility of specific and irreversible affinity labeling is studied using these tissue-penetrating radiations, X-ray, and gamma rays which are ionizing radiation. Besides conventional ionizing radiations, higher doses of ultrasounds at therapeutic range have been observed to alter *in vitro* enzyme kinetics [14] and affect cell damages [15]. Synergistic

damaging effects have been reported with high-dose ultrasounds when hematoporphyrins were used to treat sarcomas [16]. Plausible mechanisms involve free-radical formation [17] and/or singlet oxygen formation [18]. The potential common mechanism of free-radical formation in photoaffinity labeling, X-ray/gamma ray, and ultrasounds should be further investigated.

The present *in vitro* study investigates the effects of X-ray on the irreversible binding to the striatal dopamine transporter (SDT) using three different photoreactive affinity ligands, RTI-38, RTI-63, and RTI-78. In a parallel set of *in vitro* experiments, we study the irreversible binding to the peripheral benzodiazepine receptors (PBDZR) and dopamine-2 receptors (D2R) with two photoreactive affinity ligands, respectively. The characterization of affinity labeling of receptors using tissue-penetrating radiation will provide a foundation for the development of receptor-specific or tissue-specific delivery of extrinsic diagnostic or therapeutic agents.

2. Materials

The three RTI compounds, p-azidobenzoylecgonine methyl ester tartrate (RTI-38), 3- β -benzoyloxy-8-methyl-8-azabicyclo [3.2.1] octan-2-carboxylic acid p-azidophenyl ester hydrochloride (RTI-63), and 3- β -(p-chlorophenyl) tropan-2- β -carboxylic acid p-azidophenylethyl ester hydrochloride (RTI-78), were supplied by Carroll [3, 19]. [^3H]-CFT, [^3H]-NMSP, [^3H]-N-methyl-PK 11195 (NET885), and nonlabeled PK11195 were supplied by New England Nuclear (Boston, MA). The nonradioactive PK14105 was a gift from Rhone-Poulenc Rorer (France).

3. Methods

3.1. Membrane Receptor Preparation for D2R and PBDZR Binding. Male rats weighing from 200 to 250 g were used for D2R experiments. The animals were decapitated, the brains were immediately removed, and the striatum was excised and stored at -70°C until used. Dog kidney membranes were similarly prepared for PBDZR experiments and stored. Tissue preparation was carried out as described by Kleven et al. [20]. The tissue was homogenized briefly in 20 volumes (w/v) of 50 mM Tris-HCl, pH 7.4, with 5 mM Na-EDTA and 50 mM NaCl at 4°C . The homogenate was centrifuged at 48,000 $\times g$ for 15 min at 4°C . The resultant pellet was rehomogenized in Tris-HCl buffer (with 50 mM NaCl) and centrifuged again. The final pellet was resuspended in 50 mM Tris-HCl buffer with 100 mM NaCl, pH 7.4, to a final concentration of 5–10 mg tissue/mL or 2.5 to 3.0 mg protein/mL.

3.2. Irradiation. Using UV irradiation, aliquots of tissue suspension were incubated in the dark with the photoaffinity ligand azidoclebopride (1 mM final concentration) for D2R and PK14105 for PBDZR for 90 minutes at room temperature. A 15-mL tissue suspension in an uncovered plastic petri dish (100 \times 13 mM) (fluid depth, 3–4 mM) was irradiated 11 cm away from a light source (ultraviolet lamp) for 30 seconds.

For X-ray irradiation, a Dynamax 42–40 rotating-anode X-ray tube unit (Machlett Laboratories, Inc., Stamford, CT, USA) set at 115 kVp and 180 mAs was used to treat receptor preparations in test tubes with repeated exposures; the radiation dose was calibrated by thermoluminescent dosimeters.

For gamma ray irradiation, a NASATRON (F0103) irradiator (US Nuclear Co.) (662 keV) from Cesium 137 source was applied to receptor preparations in test tubes covered with aluminum foil. The calibrated dose rate range was from 1 to 10 Gy/minute. The total radiation dose was determined from the dose rate and the exposure time.

Ultrasound irradiation experiments were briefly conducted and involved the use of a calibrated sonicator (Sonicator II, Model ME702, 10 cm crystal, 1 MHz, Mettler Electronics, Anaheim, CA, USA) with the applicator immersed in ice-cold water irradiating the test tube (1 cm in diameter) containing PK14105 and dog kidney membrane preparation (prepared and stored in similar manners as with the rats membranes). It was turned on at a single intensity setting of 1 MHz at 2 Watt per sq. cm for 2 and 10 minutes, respectively.

3.3. Binding Assays and Data Analyses. For SDT binding, striatal membranes were first incubated with (50–100 uM) of photoreactive ligands (RTI-38 and RTI-63) in the presence or absence of 25 uM cocaine. Higher dose of cocaine (50 uM) was used with the higher affinity agent RTI-78. The IC₅₀ for RTI-38, RTI-63, RTI-78, and cocaine has been determined to be 475, 227, 6, and 102 nM, respectively. They were then irradiated with UV or X-ray. After 5 cycles of wash with buffer and centrifugation, the SDT was assayed as described above. The concentration of the radioactive ligand ³H-CFT was 50 pM.

For dopamine D2R binding assays, samples (1.0 mL) containing striatal membrane suspension (0.05–0.12 mg protein/mL) in 50 mM Tris-HCl buffer were incubated for 45 minutes (37°C) with [³H]spiperone (from 0.08 to 0.1 nM) in the presence or absence of (+)butaclamol (10 mM) for nonspecific binding [21]. For peripheral PBDZR binding assays, kidney homogenate (0.05–0.2 mg protein in 0.5 mL) was incubated with [³H]-PK11195 (1 nM). Nonspecific binding was determined by the addition of PK11195 (1000 nM) [22]. Membrane-bound striatal ligands were separated by filtration through Whatman GF/B filters followed by two washes with 5 mL of cold incubation buffer. The radioactivity on the filters was assayed by liquid scintillation spectrometry.

The extent of irreversible binding of the nonradioactive affinity labels to the receptors was calculated as the decrease in the subsequent binding with [³H]-labeled ligand. Fractions of bound radioactive ligand were tabulated and analyzed using one-way ANOVA and two-way ANOVA from SigmaStat (version 3.5, Systat software, Point Richmond, CA, USA). Data and standard errors are plotted with Microsoft Excel 2003 graphics options (Microsoft Inc., Redmond, WA, USA) in Figures 1–5. The Holm-Sidak pairwise-comparison option was adopted to obtain *t*-test scores.

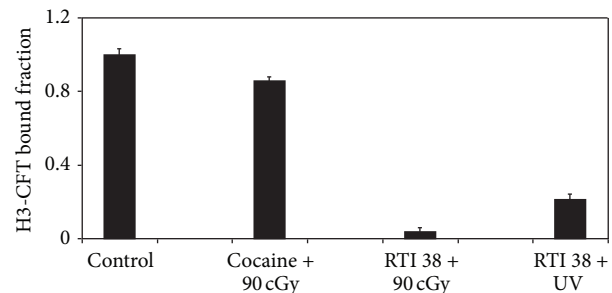


FIGURE 1: Affinity labeling of SDT with 50 uM of RTI-38 using UV or X-ray. Irreversible and specific binding of RTI-38 to SDT is noted with 90 cGy of X-ray or with UV ($F = 840$, $P < 0.001$). *t*-tests and one-way ANOVA indicate statistically significant difference from the control group ($t = 39.5$, $P = 0.010$) or the cocaine group treated with X-ray ($t = 45.7$, $P = 0.009$).

4. Results

4.1. X-Ray Affinity Binding of RTI-38, RTI-78, or RTI-63 to SDT (Figures 1, 2, and 3). Striatal membranes prepared as described in Section 3 were incubated with 0.05 mM of RTI-38, 20–200 nM of RTI-78, or from 100 nM to 2000 nM of RTI-63 for 30 minutes on ice. The mixture was irradiated with total doses from 1 to 500 cGy X-ray. Binding experiments using 90 cGy were able to achieve 96% binding with RTI-38 while a concurrent UV experiment achieved 79% inhibition of binding, both of which are different from the control group or cocaine under X-ray without RTI-38 (Figure 1). One-way ANOVA confirmed statistical significance with $F = 840.3$ and $P < 0.001$ and all treatment groups. Although the small but significant control group of cocaine with 90 cGy X-ray might need to be further explored, these RTI-38 experiments at high reactant concentration (>1000 nM) were not further pursued because the limited supply was exhausted.

Although RTI-63 in combination with UV significantly decreased subsequent CFT binding (two-way ANOVA with $F = 10.4$ and $P = 0.009$ for UV and $F = 6.7$ and $P = 0.009$ for RTI-63), no dose-related response is noted (Figure 2). Large variations are noted in the baseline binding under X-ray without RTI-63 and may be related to technical variance, in light of subsequent similar baseline binding of CFT close to unity with X-ray up to 111 cGy in Figure 3. Although significant binding is noted with 100 nM of RTI-63 ($T = 7.0$, $P = 0.009$), the lack of dose-related responses to RTI-63 levels or to X-ray doses indeed brings into doubt the utility and efficiency of RTI-63 as X-ray affinity labels.

Initial experiments indicated that reversible inhibition of SDT occurs with RTI compounds at nM range and the initial experiment with RTI-38 used concentrations that were supersaturating to the SDT. Subsequent experiments were carried out at lower concentrations. RTI-78 at 20 nM inhibited specific binding (36%–43%) with X-ray, but no dose-response relationship was identified. With the higher dose of RTI-78 at 200 nM, dose-related specific irreversible binding (85%–99%) is demonstrated with increasing radiation dose from 1 cGy to 211 cGy (Figure 3). While one-way ANOVA indicates significance ($F = 208.6$ and $P < 0.001$) for UV for

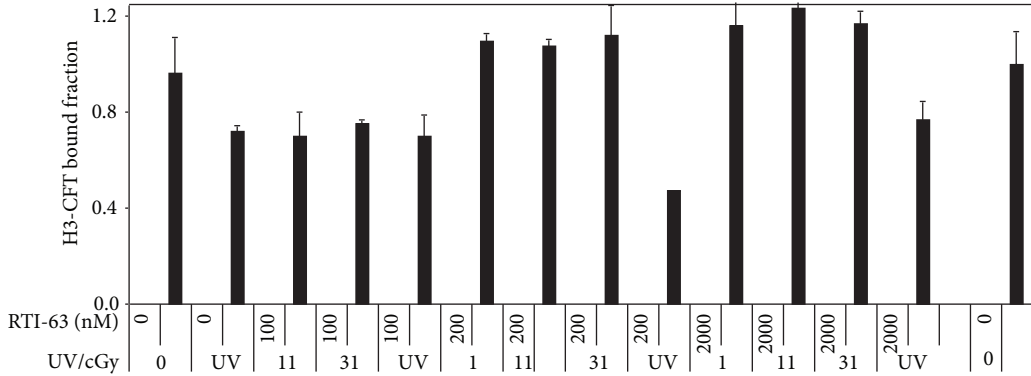


FIGURE 2: Affinity labeling of SDT with RTI-63 using UV or X-rays. While UV affects affinity labeling of SDT ($F = 10.4$, $P = 0.009$) in a manner related to RTI-63 concentration ($F = 6.7$, $P = 0.009$), no significant dose-related binding is identified with respect to X-ray dose (11–31 cGy) or to RTI-63 concentrations (100–2000 nM). The largest magnitude of gamma-rays-induced binding occurs with RTI-63 at 100 nM ($t = 7.0$, $P < 0.001$).

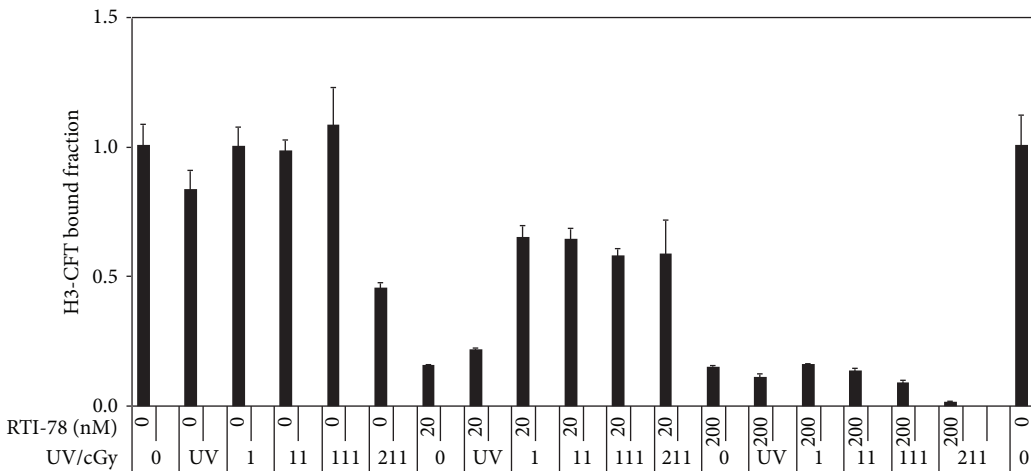


FIGURE 3: Affinity labeling of SDT with RTI-78 using UV or X-ray. Binding data suggest possible dose-related binding with respect to radiation doses as well as RTI-78 concentration. While one-way ANOVA indicates significance ($F = 208.6$ and $P < 0.001$) for UV for both 20 nM and 200 nM RTI-78, two-way ANOVA indicates significance for both doses of X-ray ($F = 32.8$ and $P < 0.001$) and concentration of RTI-78 ($F = 535.7$ and $P < 0.001$) with interaction ($F = 28.0$ and $P < 0.001$).

both 20 nM and 200 nM RTI-78, two-way ANOVA indicates significance for both doses of X-ray ($F = 32.8$ and $P < 0.001$) and concentration of RTI-78 ($F = 535.7$ and $P < 0.001$). Interaction between X-ray and RTI-78 was also noted preventing identification of the main effect ($F = 28.0$ and $P < 0.001$).

4.2. Gamma Ray Affinity Labeling of D2 Receptor (Figure 4). When using 1000 nM of azidoclebopride (N3), specific and irreversible D2R binding was induced by gamma rays in a dose-related manner. In spite of moderate variations in the bound fractions of baseline groups and the baseline group with N3, two-way ANOVA found significant correlation of specific binding with gamma ray doses ($F = 4.3$ and $P = 0.042$) and with N3 ($F = 27.3$ and $P < 0.001$). Gamma rays of 20 cGy were able to affect significant binding above baseline ($T = 2.9$ and $P = 0.019$). UV irradiation induced 34% specific

binding (one-way ANOVA, $F = 11.6$ and $P = 0.009$). This latter figure is similar to previously published results [7, 8].

4.3. Affinity Labeling of PBDZR Using Gamma Rays (Figure 5). While the effects of UV on binding are not different than those of control, UV in combination with PK14105 is significantly different from UV alone or control (one-way ANOVA findings of $F = 566.7$ and $P < 0.001$; $T = 29.3$ and 29.0 , resp.). Irreversible and specific binding is noted at 60.8%, 72.3%, and 76.2% using 20 cGy, 100 cGy, and 500 cGy of gamma rays, respectively. Two-way ANOVA found significant data for gamma rays doses ($F = 4.1$, $P = 0.011$) and PK14105 ($F = 482.0$ and $P < 0.001$), respectively. A weak dose-related response was also noted with PK14105 between 50 and 500 cGy ($T = 3.9$ and 3.6 , resp., for 50 cGy versus 100 cGy and 500 cGy, resp.).

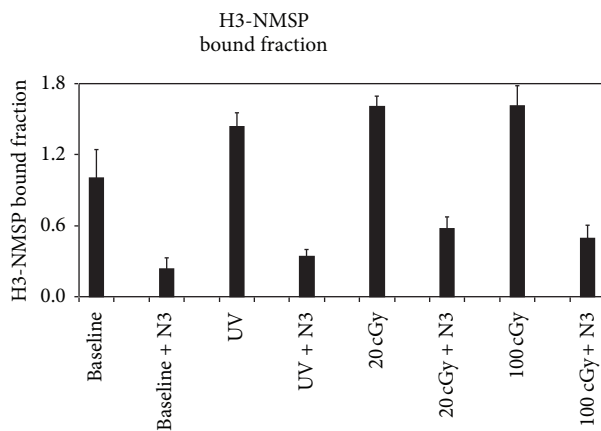


FIGURE 4: Affinity labeling of D2R with azidocleopride (N3) using UV or gamma rays. Irreversible and specific binding to peripheral benzodiazepine receptor, D2R, is noted after exposure of the mixture of D2R and 1uM N3 under UV or gamma rays. Statistically significant correlations of binding to N3 ($F = 27.3, P < 0.001$) and gamma rays doses ($F = 4.3, P = 0.04$) are revealed by two-way ANOVA.

5. Discussion

We have demonstrated that photoaffinity labeling of photoreactive ligands using UV may be selectively extended to using tissue-penetrating radiations including X-ray, gamma ray, and possibly ultrasound. However, even with the same receptor system (e.g., SDT), this extension is not observed to the same degree with all photoaffinity labels (e.g., not with RTI-63) and needs to be confirmed for each compound individually. Although no direct mechanism is proposed to explain radiation-affinity labeling, the most likely common underlying process would be free-radical formation to affect covalent binding of photoreactive moieties in the affinity label to the neighboring receptor/protein. Therefore, in the selection of compounds for radiation-affinity labeling experiments, photoaffinity labels will serve as good starting points.

Low-dose (<100 cGy) X-ray (250 kVp) irradiation of photoreactive substrate to cause enzyme inhibition has been reported by a single study [2]. The end point of this latter study is inhibition of enzyme activity, which is a functional measure and subjected to other regulatory factors (cofactors or other substrates) that may also be altered by X-ray. In this affinity binding study, radiation of higher energy (e.g., X-ray and gamma ray) as well as lower energy radiation (e.g., ultrasound) achieves immediate and direct labeling. Therefore, arguably, affinity labeling is a more direct and more efficient method to evaluate the effects of the radiation. Furthermore, this affinity labeling mechanism may allow selective and locoregional delivery of photoreactive drugs to stimulate or block receptors.

Affinity labeling using UV has been used to study “*in vitro*” chemistry. Affinity labeling using X-ray, gamma ray, or ultrasounds may allow study of “*in vivo*” chemistry. Further investigations of radiation-affinity labeling may provide new ways to produce better molecular imaging or drug delivery.

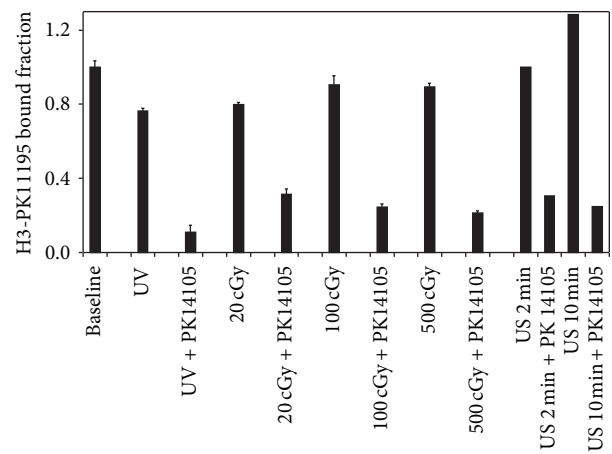


FIGURE 5: Affinity labeling to PBDZR with PK14105 using UV, gamma rays, or ultrasounds. Affinity binding of PK14105 to PBDZR under UV, gamma rays, and ultrasounds is confirmed. Two-way ANOVA was used to analyze all data found significant for gamma rays doses ($F = 4.1$ and $P = 0.011$) and PK14105 (with $F = 482.0$ and $P < 0.001$). Ultrasonic exposure (2 Watts/sq. cm at 1 MHz) of the reactants on ice in the dark for 2 and 10 minutes affects binding of 69% and 80%, respectively, in single-point experiments.

For instance, if nonradioactive PK14105 is injected during brain radiotherapy, the concurrent binding of this drug to the brain cortices may be visualized by subsequent PET imaging using ^{11}C -PK11195 according to established procedures in humans as by Junck et al. [10]. Alternatively, ^{18}F labeled-PK14105 may be synthesized as described [21] and directly injected before or during scheduled radiotherapy of organs rich in PBDZR (such as brain lesions or kidney); the paths and amounts of radiation absorbed may be visualized. The PBDZR has been identified to a translocation protein (TSPO) which further pinpoints functional roles of PBDZR pathways and have gained increasing interest in molecular biology [23, 24].

^{11}C -NMSP may be similarly used to study binding of photoreactive D2R drugs such as azidocleopride during or before radiotherapy to evaluate radiation effects. The baseline variation with azidocleopride alone (Figure 4) in the dark showed irreversible binding that is different from those in the literature [7, 8] and needs to be further studied. The rising binding with UV and increasing gamma ray doses above baseline fraction of 1.0 also needs further investigation. Plausible mechanisms include destruction of internal bound ligands releasing or unfolding receptor to be bound by subsequent ligands. In spite of these variations, there is statistical significance of UV and gamma ray to affect irreversible-specific receptor binding between azidocleopride and D2R.

Ultrasounds at higher intensity (0.5 W for 10 minutes) have been found to produce free-radicals and affect radical-related therapeutic effects [15, 16]. To test the ability of ultrasound to affect affinity labeling with PBDZR, ultrasound exposure (2 Watts/sq. cm at 1 MHz) of reactants on ice in the dark for 2 and 10 minutes affects irreversible binding of 69% and 80% in two experiments of single data point (Figure 5).

The radionuclide supply and membrane preparations were exhausted during these experiments, and preliminary findings with ultrasounds need to be verified. If confirmed, may be found wider *in vivo* applications because of the wide availability of ultrasound instruments and no ionizing radiation is involved.

This *in vitro* qualitative study is a survey of performing irreversible affinity labeling of readily available receptor systems (rat SDT, rat D2R, and dog kidney PBDZR) using available irradiation sources (X-ray, gamma, and ultrasound) for proof of concepts. It has illustrated the possibilities of radiation-affinity labeling. The concentration of study compounds is in the nano- to micromolar range and is within pharmacologic range following systemic administration. The current study examines the interaction of photoaffinity labels with radiation at dose ranges feasible in the clinical setting. The gamma ray radiation doses (1–200 cGy) are within ranges of external beam radiotherapy for cancers (total 2000–6000 cGy or fractionated doses of 100–300 cGy daily). Ultrasound (2 W/min for 2 to 10 minutes) strength is within range of routine therapeutic use in rehabilitation medicine. Therefore, large fractions/quantities of photoreactive chemicals may be delivered to target tissues at selected time using switchable external irradiation commonly used in humans with cancer or ultrasounds. When further *in vitro* and animal experiments verify this concept, tissue-penetrating radiation-affinity labeling may be translated to the clinics.

Conflict of Interests

None of the authors has any financial interest with any commercial vendor or supplier of material for the conduct of experiments and presentation of work related to this study.

Acknowledgments

The authors acknowledge the logistic support of gamma rays irradiation from Raymond Meyn, Ph.D., of the Division of Radiation Oncology, University of Texas MD Anderson Cancer Center. The report work was partially supported by a research Grant RR00165 from the National Institutes of Health to Dr. Michael Kuhar.

References

- [1] H. Bayley and J. R. Knowles, "Photogenerated, hydrophobic reagents for intrinsic membrane proteins," *Annals of the New York Academy of Sciences*, vol. 346, pp. 45–58, 1980.
- [2] W. Cohen, S. V. Chau, P. R. Kastl, and D. R. Caldwell, "X-ray affinity and photoaffinity inhibitor of aldose reductase," *Journal of Ocular Pharmacology*, vol. 2, no. 2, pp. 151–158, 1986.
- [3] F. I. Carroll, A. Philip, and A. H. Lewing, "Cocaine receptor. Design of ligands," *NIDA Research Monograph Series*, no. 96, pp. 112–121, 1990.
- [4] D. F. Wong, E. P. Broussolle, G. Wand et al., "*In vivo* measurement of dopamine receptors in human brain by positron emission tomography. Age and sex differences," *Annals of the New York Academy of Sciences*, vol. 515, pp. 203–214, 1987.
- [5] C. Muhr, M. Bergstrom, and P. O. Lundberg, "Dopamine receptors in pituitary adenomas: PET visualization with ¹¹C-N-methylspiperone," *Journal of Computer Assisted Tomography*, vol. 10, no. 2, pp. 175–180, 1986.
- [6] B. C. K. Yung, G. S. Wand, L. Blevins et al., "*In vivo* assessment of dopamine receptor density in pituitary macroadenoma and correlation with *in vitro* assay," *Journal of Nuclear Medicine*, vol. 34, p. 133, 1993.
- [7] H. B. Niznik, J. H. Guan, J. L. Neumeyer, and P. Seeman, "A photoaffinity ligand for dopamine D2 receptors: azidoclebopride," *Molecular Pharmacology*, vol. 27, no. 2, pp. 193–199, 1985.
- [8] H. B. Niznik, A. Dumbrille-Ross, and J. H. Guan, "Dopamine D2 receptors photolabeled by iodo-acido-clebopride," *Neuroscience Letters*, vol. 55, no. 3, pp. 267–272, 1985.
- [9] M. Gavish, Y. Katz, S. Bar-Ami, and R. Weizman, "Biochemical, physiological, and pathological aspects of the peripheral benzodiazepine receptor," *Journal of Neurochemistry*, vol. 58, no. 5, pp. 1589–1601, 1992.
- [10] L. Junck, J. M. M. Olson, B. J. Ciliax et al., "PET imaging of human gliomas with ligands for the peripheral benzodiazepine binding site," *Annals of Neurology*, vol. 26, no. 6, pp. 752–758, 1989.
- [11] S. Pappata, P. Cornu, Y. Samson et al., "PET study of carbon-11-PK 11195 binding to peripheral type benzodiazepine sites in glioblastoma: a case report," *Journal of Nuclear Medicine*, vol. 32, no. 8, pp. 1608–1610, 1991.
- [12] J. Benavides, A. Dubois, T. Dennis, E. Hamel, and B. Scattton, "Omega3 (peripheral type benzodiazepine binding) site distribution in the rat immune system: an autoradiographic study with the photoaffinity ligand [³H]PK 14105," *Journal of Pharmacology and Experimental Therapeutics*, vol. 249, no. 1, pp. 333–339, 1989.
- [13] R. Skowronski, D. D. Fanestil, and K. Beaumont, "Photoaffinity labeling of peripheral-type benzodiazepine receptors in rat kidney mitochondria with [³H]PK 14105," *European Journal of Pharmacology*, vol. 148, no. 2, pp. 187–193, 1988.
- [14] F. I. Braginskaya and O. M. Zorina, "Comparative study on the therapeutic ultrasound effects on erythrocyte membrane-bound and free acetylcholinesterase," *Radiation and Environmental Biophysics*, vol. 26, no. 3, pp. 239–249, 1987.
- [15] S. Umemura, N. Yumita, and R. Nishigaki, "Enhancement of ultrasonically induced cell damage by a gallium-porphyrin complex, ATX-70," *Japanese Journal of Cancer Research*, vol. 84, no. 5, pp. 582–588, 1993.
- [16] N. Yumita, R. Nishigaki, K. Umemura, and S. Umemura, "Synergistic effect of ultrasound and hematoporphyrin on sarcoma 180," *Japanese Journal of Cancer Research*, vol. 81, no. 3, pp. 304–308, 1990.
- [17] P. Riesz and T. Kondo, "Free radical formation induced by ultrasound and its biological implications," *Free Radical Biology and Medicine*, vol. 13, no. 3, pp. 247–270, 1992.
- [18] S. Umemura, N. Yumita, R. Nishigaki, and K. Umemura, "Mechanism of cell damage by ultrasound in combination with hematoporphyrin," *Japanese Journal of Cancer Research*, vol. 81, no. 9, pp. 962–966, 1990.
- [19] F. I. Carroll, M. Abdur Rahman, A. Philip, A. H. Lewin, J. W. Boja, and M. J. Kuhar, "Synthesis and receptor binding of cocaine analogs," *NIDA Research Monograph Series*, no. 105, pp. 147–153, 1990.
- [20] M. S. Kleven, B. D. Perry, W. L. Woolverton, and L. S. Seiden, "Effects of repeated injections of cocaine on D1 and D2

- dopamine receptors in rat brain," *Brain Research*, vol. 532, no. 1-2, pp. 265–270, 1990.
- [21] G. W. Price, R. G. Ahier, S. P. Hume et al., "In vivo binding to peripheral benzodiazepine binding sites in lesioned rat brain: comparison between [³H]PK11195 and [¹⁸F]PK14105 as markers for neuronal damage," *Journal of Neurochemistry*, vol. 55, no. 1, pp. 175–185, 1990.
- [22] A. Doble, O. Ferris, and M. C. Burgevin, "Photoaffinity labeling of peripheral-type benzodiazepine-binding sites," *Molecular Pharmacology*, vol. 31, no. 1, pp. 42–49, 1987.
- [23] A. Zulian, J. Sileikyte, V. Petronilli et al., "The translocator protein (peripheral benzodiazepine receptor) mediates rat-selective activation of the mitochondrial permeability transition by norbormide," *Biochimica et Biophysica Acta*, vol. 1807, no. 12, pp. 1600–1605, 2011.
- [24] S. Murail, J. C. Robert, Y. M. Coic et al., "Secondary and tertiary structures of the transmembrane domains of the translocator protein TSPO determined by NMR. Stabilization of the TSPO tertiary fold upon ligand binding," *Biochimica et Biophysica Acta*, vol. 1778, no. 6, pp. 1375–1381, 2008.

Clinical Study

Kidney Dosimetry in ^{177}Lu and ^{90}Y Peptide Receptor Radionuclide Therapy: Influence of Image Timing, Time-Activity Integration Method, and Risk Factors

F. Guerriero,¹ M. E. Ferrari,¹ F. Botta,¹ F. Fioroni,² E. Grassi,² A. Versari,³ A. Sarnelli,⁴ M. Pacilio,⁵ E. Amato,⁶ L. Strigari,⁷ L. Bodei,⁸ G. Paganelli,⁸ M. Iori,² G. Pedroli,¹ and M. Cremonesi¹

¹ Medical Physics Department, European Institute of Oncology, 20141 Milan, Italy

² Medical Physics Department, IRCCS Arcispedale Santa Maria Nuova, 42123 Reggio Emilia, Italy

³ Nuclear Medicine Department, IRCCS Arcispedale Santa Maria Nuova, 42123 Reggio Emilia, Italy

⁴ Medical Physics Department, IRCCS Istituto Scientifico Romagnolo per lo Studio e la Cura dei Tumori, 47014 Meldola, Italy

⁵ Medical Physics Department, Azienda Ospedaliera S. Camillo Forlanini, 00151 Rome, Italy

⁶ Section of Radiological Sciences, Department of Biomedical Sciences and Morphologic and Functional Imaging, University of Messina, 98125 Messina, Italy

⁷ Laboratory of Medical Physics and Expert Systems, National Cancer Institute Regina Elena, 00144 Rome, Italy

⁸ Nuclear Medicine Department, European Institute of Oncology, 20141 Milan, Italy

Correspondence should be addressed to M. Cremonesi; marta.cremonesi@ieo.it

Received 30 April 2013; Accepted 31 May 2013

Academic Editor: David J. Yang

Copyright © 2013 F. Guerriero et al. This is an open access article distributed under the Creative Commons Attribution License, which permits unrestricted use, distribution, and reproduction in any medium, provided the original work is properly cited.

Kidney dosimetry in ^{177}Lu and ^{90}Y PRRT requires 3 to 6 whole-body/SPECT scans to extrapolate the peptide kinetics, and it is considered time and resource consuming. We investigated the most adequate timing for imaging and time-activity interpolating curve, as well as the performance of a simplified dosimetry, by means of just 1-2 scans. Finally the influence of risk factors and of the peptide (DOTATOC versus DOTATATE) is considered. 28 patients treated at first cycle with ^{177}Lu DOTATATE and 30 with ^{177}Lu DOTATOC underwent SPECT scans at 2 and 6 hours, 1, 2, and 3 days after the radiopharmaceutical injection. Dose was calculated with our simplified method, as well as the ones most used in the clinic, that is, trapezoids, monoexponential, and biexponential functions. The same was done skipping the 6 h and the 3 d points. We found that data should be collected until 100 h for ^{177}Lu therapy and 70 h for ^{90}Y therapy, otherwise the dose calculation is strongly influenced by the curve interpolating the data and should be carefully chosen. Risk factors (hypertension, diabetes) cause a rather statistically significant 20% increase in dose (*t*-test, $P < 0.10$), with DOTATATE affecting an increase of 25% compared to DOTATOC (*t*-test, $P < 0.05$).

1. Introduction

PRRT is an important option for the treatment of neuroendocrine tumors (NETs) and other somatostatin receptor expressing neoplasms. Overall, the response rate of complete, partial, and minor response reaches 50% for Lu DOTATATE [1]. The cumulative absorbed dose to the tumor is limited by the irradiation of the organs at risk, the kidney, and the red marrow. In particular, specific and nonspecific radionuclide

accumulation in the kidneys is of major concern, and considerable variation has been found in patients' maximal kidney uptake and biological washout.

In general, the biological processes are assumed to follow a first-order kinetics [2], which can be described by the sum of exponential functions.

Renal peptide clearance is characterized by a single- or two-step phase, the first lasting about 24 hours after injection. In order to best extrapolate the renal time-activity curve,

calculate the time-integrated activity \tilde{a} , and have a reliable estimate of the absorbed dose, several experimental data need to be collected, requiring several planar and/or 3D scans.

When ^{177}Lu is used for therapy, its gamma decay branch allows imaging at the same time: 3 to 5 whole-body/SPECT scans are taken from 2 to 7 days after the infusion. When ^{90}Y is the radiopharmaceutical, either ^{111}In - or ^{86}Y -labeled peptides are used as a surrogate and 2 to 5 scans are collected up to 2–3 days p.i. [3]. These activity data are usually fitted by means of monoexponential functions [4–6], biexponential [3], or trapezoids [7].

The great value of dosimetry is an established tenet, nonetheless each experimental point requires time-consuming acquisitions. In this respect, an optimal choice of the number of scans and of their temporal location is warranted to balance feasibility, resources, and adequate dosimetric information.

In recent years, much effort has been made to improve the accuracy of image analysis and quantification [5]. However, the step from a set of activity data to absorbed dose passes through time points integration: if data are few and do not properly span the radionuclide renal clearance time, most of the time-activity curve is obtained by extrapolation, and, as a consequence, this can dramatically affect the results.

The issue of experimental-point fitting has been addressed by Glatting and coll in blood serum dosimetry [2], where collecting several data (generally three) for each kinetic phase is feasible from the cost point of view. The aforementioned reasons (expense of data gathering, slow renal clearance) make this more critical for the renal curves in peptide therapy. This question has also been raised by Konijnenberg [8] and Sandström et al. [5]. A dedicated analysis was presented only in a different scenario, that is, when having whole-body scans at 1 h, 1, 2, 7 d for ^{177}Lu therapy only, demonstrating a high impact of the 7th day point [9].

The aim of the present study was to compare the dosimetric results obtained in 58 patients undergoing ^{177}Lu therapy when considering (a) SPECT scans at $2(\pm 1)$, $6(\pm 3)$, $20(\pm 3)$, $44(\pm 3)$, $67(\pm 2)$ h, (b) when neglecting the 6 h point, (c) and when neglecting the 67 h point. The possibility of a simplified Injected Activity clearance $\text{IA}(t) = \text{IA}_{\text{OPT}} \cdot \exp^{-\langle \lambda \rangle \cdot t}$, $\langle \lambda \rangle$ obtained fitting all sets of data together and the patient-specific IA_{OPT} (IA at $t = 0$) was also investigated. The impact of time-activity interpolation method (trapezoids, sum of exponentials) on dose and BED estimate was also highlighted, as well as the possible influence of risk factors and of the peptide (DOTATOC versus DOTATATE). The analysis was also extended to ^{90}Y , *mutatis mutandis*.

2. Materials and Methods

2.1. Patients and Radiopharmaceutical Administration. The cohort included 28 patients (age 46–82, mean 65 yrs.) undergoing $^{177}\text{Lu}/^{90}\text{Y}$ -DOTATATE therapy and 30 patients (age 31–77, mean 58 yrs.) $^{177}\text{Lu}/^{90}\text{Y}$ DOTATOC therapy. During the first cycle patients were evaluated for dosimetry with ^{177}Lu DOTATATE (median [range]: 5.0 [3.5–5.7] GBq) and ^{177}Lu

DOTATOC (5.7 [3.7–7.8] GBq), respectively. All patients received the therapeutic administration of radiolabeled peptides with an infusion of aminoacid solution for renal protection. Details on the synthesis and the administration procedures are described elsewhere [10, 11].

Patients had been diagnosed with metastatic neuroendocrine tumors (primary site: 11 pancreas, 14 gastrointestinal tract, 7 lung, and 3 of unknown origin). The remaining were mainly affected by iodine negative thyroid carcinomas.

The therapy schedule alternated cycles of ^{177}Lu (5.3 GBq/cycle on average) and ^{90}Y (2.50 GBq/cycle on average) radiolabelled peptides, for a total of 5 cycles at maximum, 8–10 weeks apart. The physician determined the specific activity to be administered, according to the dosimetric results, patient's clinical conditions, and presence of risk factors for the kidneys (blood hypertension, diabetes) [12]. Toxicity was recorded throughout all the study and up to 6 months after completion. A comprehensive description of this clinical study and patients is reported in a companion paper [13].

2.2. Imaging

2.2.1. SPECT-CT Patient Acquisitions. In order to determine the absorbed dose to the kidneys, all patients performed a series of SPECT-CT scans of the abdomen (Symbia T2, Siemens, Germany), at Arcispedale S. Maria Nuova, Reggio Emilia, taken at $2(\pm 1)$, $6(\pm 3)$, $20(\pm 3)$, $44(\pm 3)$, $67(\pm 2)$ h after injection. For the sake of simplicity we will refer to these times as 2 h, 6 h, 1 d, 2 d, 3 d in the following.

Acquisitions were performed with a 128×128 matrix, zoom = 1.32×2 views, 30 s time/view, medium-energy general-purpose collimators. The energy windows were centered over ^{177}Lu photon peaks (208 keV and 113 keV, width 15%) while scatter fraction was evaluated with the triple energy window method, through three scatter windows next to the peaks, defined as lower scatter windows (width 10% and 15%) and upper scatter window (width 8%). The SPECT projections were reconstructed by an iterative algorithm with compensations for attenuation, scatter, and full collimator-detector response (Flash 3D iterative algorithm: 10 iterations; 8 subsets; 4.8 mm cubic voxel).

2.2.2. SPECT-CT Calibration and Activity Quantification. To convert counts/s into activity in volumes of interest, the scanner was calibrated by means of a hollow anthropomorphic Torso phantom (Data Spectrum Corporation, Hillsborough, USA) with a set of hollow spheres (volume: 1.5, 0.6, 0.3 mL) and other home-made inserts (two Eppendorf microtubes of 1.5 mL, two conical tubes of 50 mL). Phantom background, liver, and inserts were filled with different activity concentrations of ^{177}Lu (conical tubes: 0.8 and 1.2 MBq/mL; spheres with volume of 1.5, 0.6, 0.3 mL: 0.6, 0.75, and 2.5 MBq/mL, resp.; both microtubes: 7 MBq/mL, liver = 0.047 MBq/mL, and phantom background = 0.011 MBq/mL). One microtube and the 0.6 mL sphere were fixed inside the liver region. The acquisition setting and reconstruction algorithm were as described previously (for patients).

The objects were contoured on the CT image, and for each region of interest (ROI), the total counts were divided by the activity, the number of voxels, and the duration of SPECT-CT acquisition to obtain the calibration factor.

The experimental data representing counts/s/voxel/MBq versus volume (cm^3) were fitted by the equation $y = a_1 - a_2 \cdot \exp(-k \cdot x)$. This curve was used to account also for the partial volume effect when converting counts/s into activity in volumes of interest differently sized. Regards patient kidney volumes, the partial volume effect correction was considered negligible, as from our recovery curves (not shown). Kidney volumes were manually measured on CT scan, and the counts inside each ROI averaged over the number of renal voxels.

The activity quantified in kidneys was corrected for physical decay to have biological time-activity curves expressed by means of $\%IA(t)$, the fraction of the total injected activity versus time.

2.2.3. Calculation of Kidney Time-Integrated Activity and Dose. For each patient, time-integrated activity per unit activity (\tilde{a} -expressed in h) for the kidneys was computed from experimental $\%IA(t)$ by means of seven different methods:

- (1) trapezoidal method up to the last experimental data plus physical decay after the 3 d point (hereafter called TR_{ph});
- (2) trapezoidal method up to the last experimental data plus monoexponential decay after the 3 d point obtained passing through the last two points (TR_{exp});
- (3) biexponential fit of the experimental data (BI): $y(t) = a_1 \cdot \exp(-\lambda_{1,BI} \cdot t) + a_2 \cdot \exp(-\lambda_{2,BI} \cdot t)$;
- (4) monoexponential fit of the experimental data (MN): $y(t) = a \cdot \exp(-\lambda_{MN} \cdot t)$;
- (5) monoexponential model deriving a unique fit for all the data sets for each radiopeptide (MNfix): $y(t) = a_{pt} \cdot \exp(-\lambda_{MNfix, TOC} \cdot t)$; $y(t) = a_{pt} \cdot \exp(-\lambda_{MNfix, TATE} \cdot t)$. This was done in order to evaluate the feasibility of a simplified method for dosimetry in PRRT, based on the best shared fit parameter (λ_{MNfix}) specific for the peptide (i.e., DOTATOC and DOTATATE) and the patient-specific initial uptake a_{pt} ;
- (6) the best fitting function among the analytical functions (3), (4), and (5) according to *F*-test (hereafter called FT) (see next section, point (b));
- (7) the best fitting function among the analytical functions (3), (4), and (5) according to the visual choice of trained physician/physicists (VIS) (see next section, point (c)).

All fits for (3), (4), (5) were performed using Matlab 7.7.0, Statistics Toolbox.

Once \tilde{a} was computed, the absorbed dose per unit of injected activity $A_o(D/A_o)$ of ^{177}Lu was obtained as $D/A_o = S \cdot \tilde{a}$, where S is the self-absorbed dose per nuclear transformation in the kidneys for ^{177}Lu .

Similar biodistribution and kinetics for peptides labeled with ^{177}Lu and ^{90}Y are generally assumed [14], therefore the results obtained with ^{177}Lu were extrapolated to ^{90}Y , simply

substituting physical decay constant λ and S factor in the computation of \tilde{a} and D/A_o .

The standard S values for the kidney of the OLINDA/EXM software (^{177}Lu : 0.29 Gy/GBq/h; ^{90}Y : 1.76 Gy/GBq/h) were rescaled for the actual patient kidney mass [15].

2.3. Comparison of Methods and Statistical Analysis. Different criteria were considered to identify the method providing the most accurate estimate of kidney \tilde{a} .

The two trapezoidal methods (1) and (2) cannot be analyzed from a statistical point of view. Their results were simply compared with the best fit identified by a statistical test and the visual criterion.

(a) Considering the three methods using analytical functions (3), (4), and (5), the coefficient of determination [16] R^2 given by $R^2 = 1 - \text{SSE}/\text{TSS}$ was computed for each fit, where SSE is the sum of the squared residuals $\text{SEE} = \sum_i (y_i - y_{i,\text{fit}})^2$; $\text{TSS} = \sum_i (y_i - \langle y \rangle)^2$; y_i is the experimental IA% at time i ; $y_{i,\text{fit}}$ is the fitting-extrapolated IA% at each time i ; and $\langle y \rangle$ is the mean value of the experimental data.

Although most frequently used within pharmacological and dosimetry papers, indeed this criterion just says how a model fits the data better than a constant function equal to the mean value $\langle y \rangle$ (see Discussion). For this reason R^2 is not be a very helpful indicator in assessing nonlinear fit quality, as in our case [16].

(b) To properly identify the best method, the one-tailed *F*-test was used, which is indicated for nested functions [2]. This is the case of BI, MN, and MNfix, MN being a particular case of BI and MNfix, a particular case of MN.

Given a pair of fitting functions, one with “reduced” and the other with “full” parameters, with the corresponding sum of squared residuals $\text{SSE}_{\text{reduced}}$ and SSE_{full} and the number of Degrees of Freedom as $\text{DF}_{\text{reduced}}$, DF_{full} , the *F* value was obtained by the equation:

$$\begin{aligned} F & (\text{DF}_{\text{reduced}} - \text{DF}_{\text{full}}, \text{DF}_{\text{full}}) \\ &= \frac{(\text{SSE}_{\text{reduced}} - \text{SSE}_{\text{full}}) / \text{SSE}_{\text{full}}}{(\text{DF}_{\text{reduced}} - \text{DF}_{\text{full}}) / \text{DF}_{\text{full}}} \end{aligned} \quad (1)$$

The *P* value of the *F*-test selects which of the two models is better, the null hypothesis being that the simpler (i.e., the one with lower parameters) model is better. The level of significance was set as $\alpha = 0.10$, so if $P < 0.1$ the simpler model was rejected. Although $\alpha = 0.05$ is more often quoted in the literature, its value is more or less arbitrary [2]; our choice was required to increase the statistical power in this case of quite small sample size (5 points).

(c) Besides, the statistical criteria, the best function among BI, MN, MNfix describing the experimental data was also chosen visually. This was done by three expert physicians/physicists to give more weight to the clinical evidence about the peptide kinetics in the kidneys especially long after the experimental points.

In addition, all the interpolating functions (except MNfix) were computed skipping either the 6 h or the 3 d point to discern their relevance on the determination of \tilde{a} values.

Both the $\tilde{\alpha}$ values, determined by the F test ($\tilde{\alpha}_{FT}$) and visually ($\tilde{\alpha}_{VIS}$), were only evaluated in the five-point case.

Finally, the equal-variance one-tailed t -test was applied to the two peptide data sets, in order to assess whether the mean time-integrated activity for DOTATOC and DOTATATE was significantly different, despite the interpatient variability, as previously derived in an intrapatient study of 7 patients [4]. To this, a P value <0.05 was considered significant, and a P value <0.1 rather statistically significant. Similarly, the possible influence of risk factors on $\tilde{\alpha}$ was investigated.

2.4. BED. For radionuclide therapy with an absorbed dose per cycle D given in N cycles, assuming complete decay and full repair of sublethal damage between cycles, the BED takes the following form [17]:

$$\text{BED} = \text{RE} \cdot D_{\text{TOT}} = \left(1 + \frac{G(\infty) \cdot D}{\alpha/\beta} \right) \cdot ND, \quad (2)$$

where $D_{\text{TOT}} = ND$ and RE is the Relative Effectiveness factor, expressed using the Lea-Catcheside factor in the last term, which reduces to

$$\begin{aligned} G(\infty) &= (a_1^2 / \lambda_1 (\mu + \lambda_1) + 2a_1 a_2 / (\lambda_1 + \lambda_2) (\mu + \lambda_1) \\ &\quad + 2a_1 a_2 / (\lambda_1 + \lambda_2) (\mu + \lambda_2) + a_2^2 / \lambda_2 (\mu + \lambda_2)) \\ &\quad \times ((a_1 / \lambda_1 + a_2 / \lambda_2)^2)^{-1}, \end{aligned} \quad (3)$$

for a biexponential clearance $\text{IA}(t)/A_o = a_1 \cdot e^{-\lambda_1 t} + a_2 \cdot e^{-\lambda_2 t}$ (either a_1 or a_2 could be <0 , if an accumulation phase is present (Figure 1)) and to

$$G(\infty) = \frac{\lambda}{\lambda + \mu_{\text{rep}}}, \quad (4)$$

for a monoexponential clearance $A(t)/A_o = a_1 \cdot e^{-\lambda t}$, μ_{rep} being the normal tissue repair constant. Following Wessels and coll [18] we set $\mu_{\text{rep}} = 0.24 \text{ h}^{-1}$ and $\alpha/\beta = 2.5 \text{ Gy}$ for the kidneys. The amount of administered radiopharmaceutical activity varied among patients according to their clinical situation, nonetheless in the following we considered, irrespective of the patient, 4 cycles, 7.4 GBq each for ^{177}Lu peptides and 2 cycles, 3.7 GBq each for ^{90}Y peptides. This choice allowed interpatient comparison and also comparison with the typical schedules used in the clinic.

BED was only computed for the analytical time-activity fits (methods MNfix, MN, BI), even though a recent work [19] illustrated a procedure for BED computation for piecewise defined fits as well.

For a same patient, relative absorbed dose differences found using diverse fitting functions could result in an amplified difference in BED, which is the dosimetric parameter used, together with absorbed dose, for clinical implementation of treatment planning in PRRT.

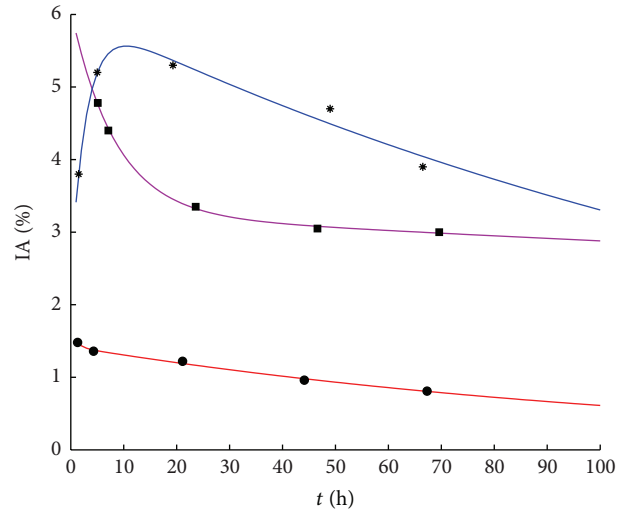


FIGURE 1: Examples of observed pharmacokinetic behaviour: with-accumulation (blue line, pt no. 45), single-slope clearance (red line, pt no. 43), two-slope clearance (violet line, pt no. 38).

3. Results

3.1. SPECT-CT Calibration. Exponential fit $y = a_1 - a_2 \cdot \exp(-k \cdot x)$ of scanner counts as a function of the source volume x gave the following sensitivity parameters: $a_1 = 11.4 \pm 0.7 \text{ counts/s/voxel/MBq}$, $a_2 = 16.5 \pm 5.1 \text{ counts/s/voxel/MBq}$, $k = 0.2 \pm 0.1 \text{ cm}^{-3}$.

3.2. Time-Activity Trends. In the majority of cases (41 out of 58 pts, 71%), the experimental data had a maximum value in the first time point and subsequent values depictable with exponential decrease. A single-slope clearance was observed in 29 pts, while in 12 patients a faster elimination phase followed by a slower one after about 24 h. Conversely, 17 patients showed an accumulation trend until 24 hours after injection. Accumulation was associated with DOTATATE in ten patients and with DOTATOC in seven.

Figure 1 offers three biological curves which are representative of the three observed pharmacokinetic behaviours.

In all but six cases (90% of pts), the elimination persisted even after 2 d, although at a slower rate as compared to the first day after injection. In particular, the mean ($\pm SD$) value of the kidney activity fraction at 3 d showed, on average, a further 20–25% decrease as compared to the 2 d renal uptake (namely for DOTATATE $\% \text{IA}_{3d} = (0.80 \pm 0.15) \cdot \% \text{IA}_{2d}$, and $\% \text{IA}_{3d} = (0.60 \pm 0.20) \cdot \% \text{IA}_{6h}$; for DOTATOC $\% \text{IA}_{3d} = (0.75 \pm 0.10) \cdot \% \text{IA}_{2d}$, and $\% \text{IA}_{3d} = (0.50 \pm 0.20) \cdot \% \text{IA}_{6h}$).

Table 1 reports the results concerning the biological pharmacokinetic parameters λ , obtained by using methods MN, BI, and MNfix. Results are provided separately for DOTATOC and DOTATATE and, with the exception of MNfix, with distinction between cases with accumulation and with clearance only. In 12 cases (21%) biexponential fittings gave $\lambda_1 = \lambda_2$, that is, a monoexponential function in the inspected time interval. Six times a negative R^2 was found when fitting with accumulation cases with MNfix, meaning that a constant

TABLE 1: Statistical results (R^2 and SSE) and λ_s computed by means of different fitting functions, with distinction between DOTATOC and DOTATATE peptides, with and without accumulation behaviour. Concerning λ_{MNfix} , a single value for each peptide was computed, irrespective of the kinetic behaviour. A negative R^2 (obtained in 6 MNfix fits) means that a constant function equal to the mean value of the data would fit better; that is, the fit is of very poor quality.

	Biological constants λ					
	Cases with accumulation			Clearance only cases		
	Mean \pm 1SD $\cdot 10^{-3}$ (range) (h $^{-1}$)	R^2 median (range)	SEE median (range)	Mean \pm 1SD $\cdot 10^{-3}$ (range) (h $^{-1}$)	R^2 median (range)	SEE median (range)
DOTATATE						
λ_{MNfix}	8.6	0.71 (-1.6–0.99)	0.89 (0.07–5.30)	8.6	0.81 (0.40–0.99)	0.58 (0.004–4.04)
λ_{MN}	7 \pm 3 (2–13)	0.82 (0.08–0.98)	0.59 (0.007–1.83)	10 \pm 4 (5–21)	0.94 (0.57–0.99)	0.25 (0.002–1.07)
λ_{IBI}	207 \pm 147 (42–427)	0.99 (0.75–1)	0.017 (0.001–0.147)	47 \pm 9 (9–311)	0.98 (0.75–0.99)	0.092 (0–1.057)
λ_{2BI}	11 \pm 5 (6–21)			16 \pm 37 (0–162)		
DOTATOC						
λ_{MNfix}	11.04	-0.71 (-1.47–0.60)	2.32 (1.05–11.24)	11.04	0.82 (0.36–0.98)	0.49 (0.05–9.09)
λ_{MN}	4 \pm 2 (1–7)	0.57 (0.01–0.93)	0.34 (0.13–4.71)	13 \pm 5 (7–24)	0.97 (0.66–1.00)	0.17 (0.002–5.26)
λ_{IBI}	191 \pm 114 (28–308)	1 (0.89–1)	0.01 (0–0.02)	143 \pm 155 (9–443)	0.99 (0.80–1)	0.025 (0–0.364)
λ_{2BI}	12 \pm 5 (6–22)			10 \pm 5 (0–22)		

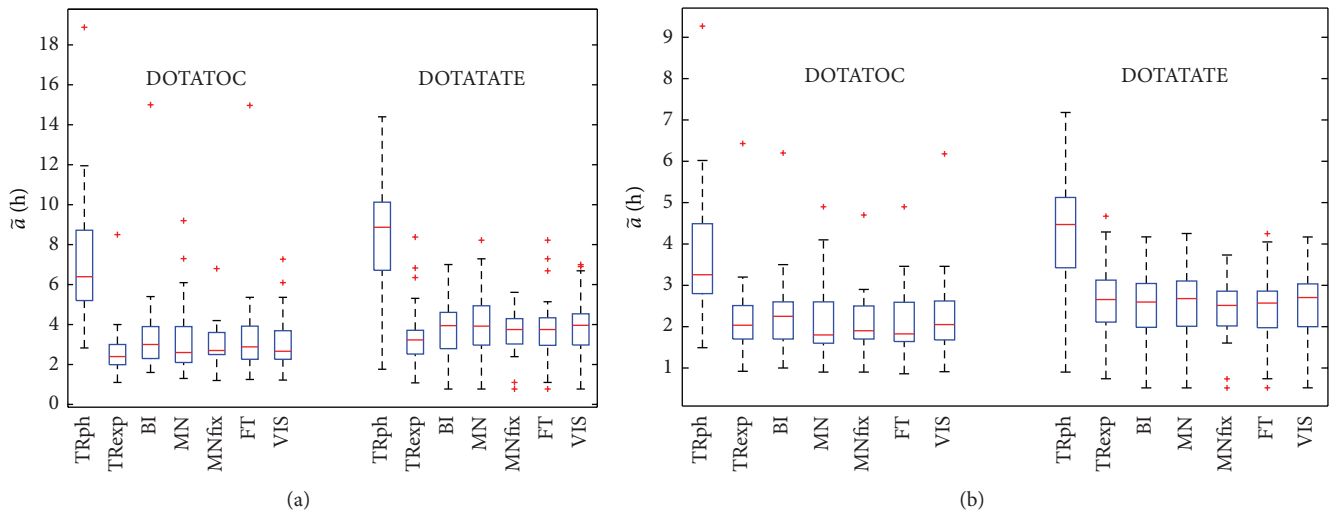


FIGURE 2: ^{177}Lu (a) and ^{90}Y (b) time-integrated activities \bar{a} in hours for methods TRph, TRexp, BI, MN, MNfix, VIS, FT. Boxes draw the 25th percentile (lower box bound, indicating 25th of data fall below it), 50th percentile (i.e., median value), and 75th percentile (upper box bound). Crosses indicate outliers defined as observations out of $1.5 \cdot (75\text{th percentile value} - 25\text{th percentile value})$. Whiskers extend to the most extreme values that are not outliers.

function equal to the mean data value would better fit the data.

Concerning MNfix, the biological half time ($t_{1/2}$) was 81 h for DOTATATE and 63 h for DOTATOC; these results are in the middle of the mean MN results: for DOTATATE $t_{1/2} = 99$ h and 69 h patients with and without accumulation, respectively, for DOTATOC $t_{1/2} = 173$ h and 53 h. Concerning the other methods (TRph, TRexp, BI), comparisons are more easily made referring to time-integrated activity \bar{a} .

3.3. \bar{a} Values. Box and whisker plots in Figure 2 illustrate the \bar{a} values for all the methods applied to ^{177}Lu peptides (Figure 2(a)) and ^{90}Y peptides (Figure 2(b)), with distinction made between DOTATOC and DOTATATE.

The graph emphasizes that ^{177}Lu time-integrated activities are consistently overestimated by TRph and slightly underestimated by TRexp as compared to BI, MN, and MNfix. Smaller differences concern ^{90}Y because of the minor influence from the curve tail in consequence of the smaller physical half-time $T_{1/2}$ (64.1 h for ^{90}Y versus 164.2 h for ^{177}Lu). The mean ratio between the tail contribution to \bar{a} (\bar{a}_{tail}) (i.e., the area under the time-activity curve from last experimental data point on) and the whole \bar{a} is reported in Table 2, for all the different methods. These ratios point out that the curve after the last experimental point takes about 40% of the total \bar{a} for ^{177}Lu peptides and 25–30% for ^{90}Y peptides, while for TRph the \bar{a}_{tail} accounts for ~70% (Lu) and ~55% (Y) of the total \bar{a} .

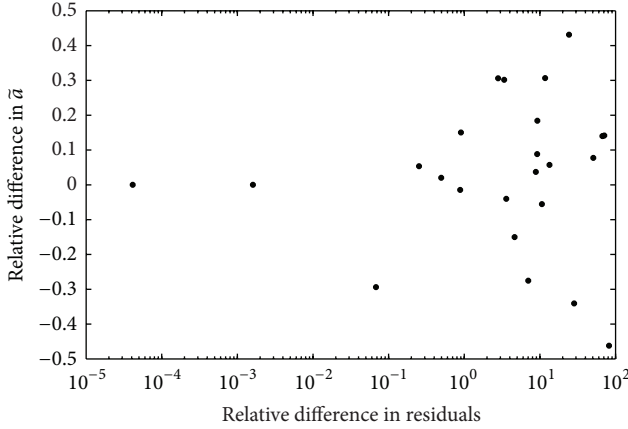


FIGURE 3: Relative difference of $\tilde{\alpha}$ values for ^{177}Lu -DOTATATE between MN and BI methods $y = (\tilde{\alpha}_{\text{MN}} - \tilde{\alpha}_{\text{BI}})/\tilde{\alpha}_{\text{BI}}$ plotted against the relative difference of the squared residuals SSE $x = (\text{SSE}_{\text{MN}} - \text{SSE}_{\text{BI}})/\text{SSE}_{\text{BI}}$.

TABLE 2: The mean fraction of time-integrated activity per unit activity $\tilde{\alpha}$ situated after the last experimental datum ($\tilde{\alpha}_{\text{tail}}/\tilde{\alpha}$) is reported for the methods TRph, TRexp, BI, MN, MNfix, VIS, FT.

$\tilde{\alpha}_{\text{tail}}/\tilde{\alpha}$	TRph	TRexp	BI	MN	MNfix	FT	VIS
^{177}Lu TOC	0.73	0.29	0.40	0.38	0.45	0.43	0.38
^{177}Lu TATE	0.73	0.34	0.42	0.43	0.35	0.38	0.41
^{90}Y TOC	0.56	0.28	0.26	0.24	0.39	0.33	0.25
^{90}Y TATE	0.57	0.32	0.27	0.28	0.28	0.28	0.26

Figure 3 points out whether it is possible to univocally identify a “best” $\tilde{\alpha}$ through the analysis of the residuals. MN and BI methods are compared, with the relative difference of the $\tilde{\alpha}$ values ($\Delta\tilde{\alpha} = [\tilde{\alpha}_{\text{MN}} - \tilde{\alpha}_{\text{BI}}]/\tilde{\alpha}_{\text{BI}}$) plotted against the relative difference of SSE ($\Delta S = [\text{SSE}_{\text{MN}} - \text{SSE}_{\text{BI}}]/\text{SSE}_{\text{BI}}$). Points are spread out, showing no correlation between $\Delta\tilde{\alpha}$ and ΔS . Thus, two curves with similar residuals could lead to very different $\tilde{\alpha}$ values, in other words the best $\tilde{\alpha}$ could not be identified.

3.4. Best $\tilde{\alpha}$. The $\tilde{\alpha}$ values of the best method indicated by the F-test ($\tilde{\alpha}_{\text{FT}}$) and those identified by visual analysis ($\tilde{\alpha}_{\text{VIS}}$) were considered as reference.

The F-test preferred monoexponential methods in most cases (MNfix: 50%, MN: 38%), while BI in only 12% of cases. According to the visual analysis, the MN was chosen in 50% of cases, and BI was selected in the 50% left (see Figure 4 for the ^{177}Lu cases in which the discrepancy among FT and VIS was larger than 10%). Although close to the MN in 21% of cases, the MNfix was avoided in general and definitely considered inappropriate in 79% cases (46 over 58).

For ^{177}Lu , in 24% cases (14 over 58), MN discrepancies of $\tilde{\alpha}$ with the best visual model were larger than 20% (reaching even 70%), while for ^{90}Y discrepancies higher than 20% were seldom found (3 out of 58 cases only), the largest discrepancy being 25%.

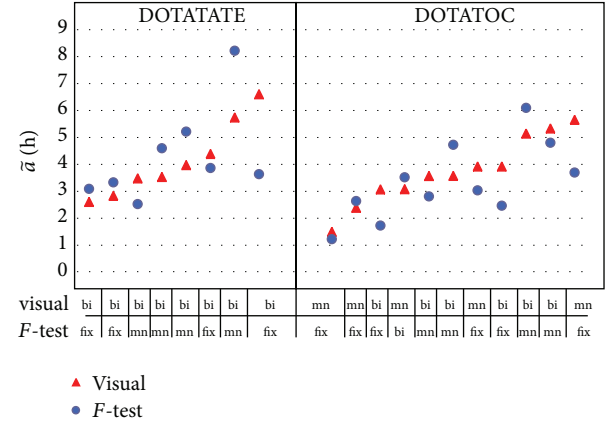


FIGURE 4: ^{177}Lu $\tilde{\alpha}_{\text{FT}}$ and $\tilde{\alpha}_{\text{VIS}}$ for the cases in which there was a discrepancy greater than 10% between the visual and the F-test (8 cases for TATE, 11 for TOC).

3.5. $\tilde{\alpha}$ Comparison. Table 3 reports the mean \pm SD values of the ratio—case by case—between the $\tilde{\alpha}$ values from methods TRexp, BI, MN, and MNfix and the $\tilde{\alpha}_{\text{FT}}$ and $\tilde{\alpha}_{\text{VIS}}$ values. Mean ratios are close to 1, in agreement with the reference method (F-test or visual), although SD values are not negligible especially for ^{177}Lu peptides, reaching 0.20–0.30 (^{177}Lu) and 0.10–0.15 (^{90}Y).

Table 3 reports also the results obtained excluding either the experimental point at 6 h or at 3 d.

Regarding the TRexp method, the 6 h point has negligible impact, while the lack of the 3 d point causes a remarkable underestimation versus both the F-test and the visual results: for example, for ^{177}Lu peptides, the mean ratio $\tilde{\alpha}_{\text{TRexp}}/\tilde{\alpha}_{\text{VIS}}$ of ~ 0.7 indicated a mean 30% underestimate ($\tilde{\alpha}_{\text{TRexp}}/\tilde{\alpha}_{\text{VIS}} = 0.72 \pm 0.16$).

At first glance, MN and MNfix may seem to perform similarly on average, the $\tilde{\alpha}$ ratios with the FT and VIS methods being quite close (SD ~ 0.20 for Lu, ~ 0.10 for Y). Actually, we found that in 9 cases MNfix gave a result closer to $\tilde{\alpha}$ VIS than the one obtained by MN. However, this might just be due to chance, as the quality of the MN fit, having one parameter more, must be better than the MNfix one (this emerges looking at R^2 and SSE values in Table 1). This unintended occurrence biased the MNfix results, whose SD would have been worse than MN otherwise.

Excluding TRexp, concerning ^{177}Lu , it should be noted that standard deviations are around 0.20 in all situations, regardless of the analytical function considered and of the number of data points –5 versus 4 (see Table 3). This suggests that the gathered data are either inadequate or not properly temporally placed. Conversely, concerning ^{90}Y the method used and the 6 h datum have a very negligible influence on $\tilde{\alpha}$; in addition, if the 3d datum is lacking, SDs are higher (around 0.15).

The influence of the 6 h and 3 d points on the fits is shown in Figure 5 by means of the datasets of two patients. For these specific examples, biexponential fits are the best according to the visual method, while F-test would have preferred

TABLE 3: Ratio of $\tilde{\alpha}$ computed with BI, MN, MNfix, TRexp methods with best $\tilde{\alpha}$ determined by means of F -test and visual choice. “6 h-point excluded” and “3 d-point excluded” mean that fitting was conducted skipping the 6 h and the 3 d point, respectively. The shared λ (MNfix) was only computed in the 5-point case.

Mean ± 1SD	$\bar{\alpha}$ ratios					
	¹⁷⁷ Lu peptides			⁹⁰ Y peptides		
	5 points	6 h point excluded	3 d point excluded	5 points	6 h point excluded	3 d point excluded
<i>F-test</i>						
BI/FT	1.10 ± 0.29	1.09 ± 0.29	1.08 ± 0.21	1.04 ± 0.10	1.03 ± 0.09	1.04 ± 0.09
MN/FT	1.05 ± 0.16	1.04 ± 0.17	1.09 ± 0.31	1.02 ± 0.06	1.03 ± 0.07	1.03 ± 0.13
MNfix/FT	1.00 ± 0.18	Na	Na	0.99 ± 0.10	Na	Na
TRexp/FT	0.90 ± 0.30	0.91 ± 0.31	0.78 ± 0.18	1.07 ± 0.22	1.09 ± 0.22	0.97 ± 0.16
<i>Visual</i>						
BI/VIS	1.02 ± 0.07	1.02 ± 0.19	1.03 ± 0.18	1.01 ± 0.05	1.00 ± 0.06	1.01 ± 0.09
MN/VIS	1.02 ± 0.22	1.00 ± 0.23	1.05 ± 0.36	1.00 ± 0.08	1.00 ± 0.09	1.01 ± 0.16
MNfix/VIS	0.97 ± 0.20	Na	Na	0.97 ± 0.11	Na	Na
TRexp/VIS	0.88 ± 0.24	0.89 ± 0.24	0.72 ± 0.16	1.06 ± 0.20	1.07 ± 0.21	0.90 ± 0.14

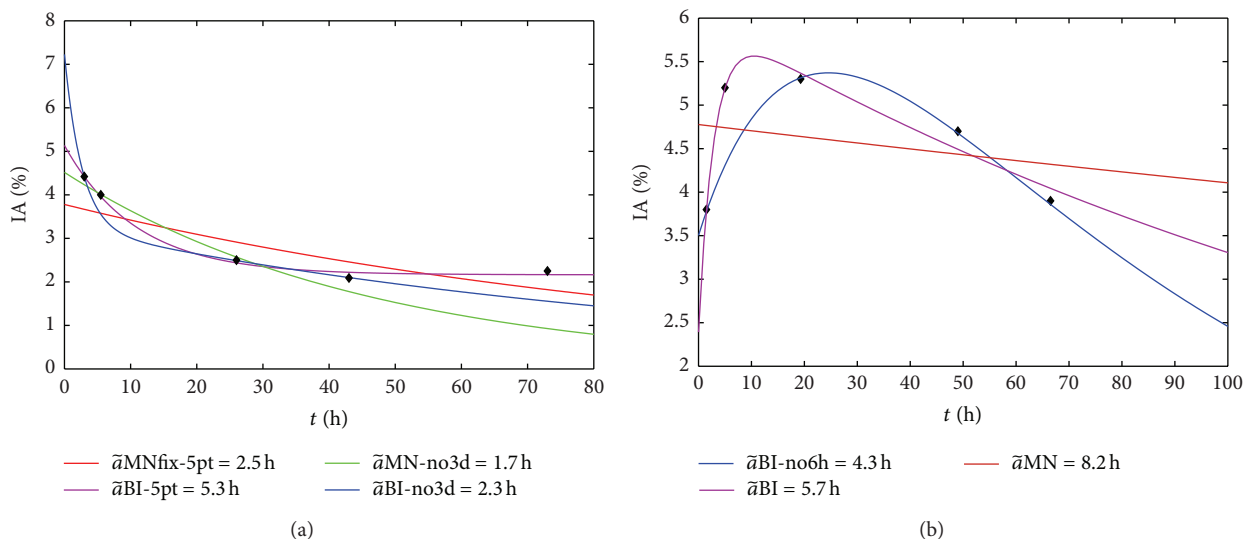


FIGURE 5: (a) pt no. 35 ^{177}Lu DOTATATE: MNfix and BI obtained with all experimental points (red and violet lines, resp.) and MN and BI skipping the 3 d point (green and blue lines, resp.); (b) pt no. 45 ^{177}Lu DOTATOC: MN and BI obtained with all experimental points (red and violet lines, resp.) and BI skipping the 6 h point (blue line).

the MNfix method for (a), the MN for (b). For the same patient, \tilde{a}_{BI} varies according to the following ratios: $\tilde{a}_{(\text{no } 6\text{h})}/\tilde{a}_{(\text{5points})} = 0.75$; $\tilde{a}_{(\text{no } 3\text{d})}/\tilde{a}_{(\text{5points})} = 0.44$.

3.6. Impact of Different Kinetic on BED. Relative differences on \tilde{a} due to different methods extend to D and BED. Figure 6 reports D and BED to the kidneys calculated with methods BI, MN, MNfix, VIS, for ^{177}Lu and ^{90}Y , respectively. F -test results are neglected because they are similar to VIS results on average (see Figure 2).

Regarding the absorbed dose, intermethod variations are the same as those found for \bar{a} (see \bar{a} comparison). Concerning the BED, it is remarkable that for ^{177}Lu the relative effectiveness factor (RE) for each patient is almost the same irrespective of the method (BI, MN, or MNfix) by means of computation. For ^{177}Lu the relative variation of RE for both MN and

MNfix compared to BI (mean \pm SD) is $1 \pm 1\%$ with a maximum of 5%, for ^{90}Y is $4 \pm 4\%$ with a maximum of 22%.

For ^{177}Lu , the mean RE is barely 1.1 with a narrow inter-patient variability range (~ 0.05), while for ^{90}Y it is about 1.5 with a greater variability (~ 0.30).

3.7. Influence of the Peptide and of Risk Factors. Irrespective of the radionuclide and of the method used for computation, the time-integrated activity in kidneys, as well as D , was significantly higher for DOTATATE (t -test: $P = 0.008$). This is in agreement with Esser and coll [4] whose finding showed for the same patient undergoing ^{177}Lu therapy, $\bar{\alpha}$ (DOTATATE) = $1.4 \cdot \bar{\alpha}$ (DOTATOC). It should be noted that regarding tumor $\bar{\alpha}$, they found $\bar{\alpha}$ (DOTATATE) = $2.1 \cdot \bar{\alpha}$ (DOTATOC). However, we were not concerned with tumor dosimetry in this study.

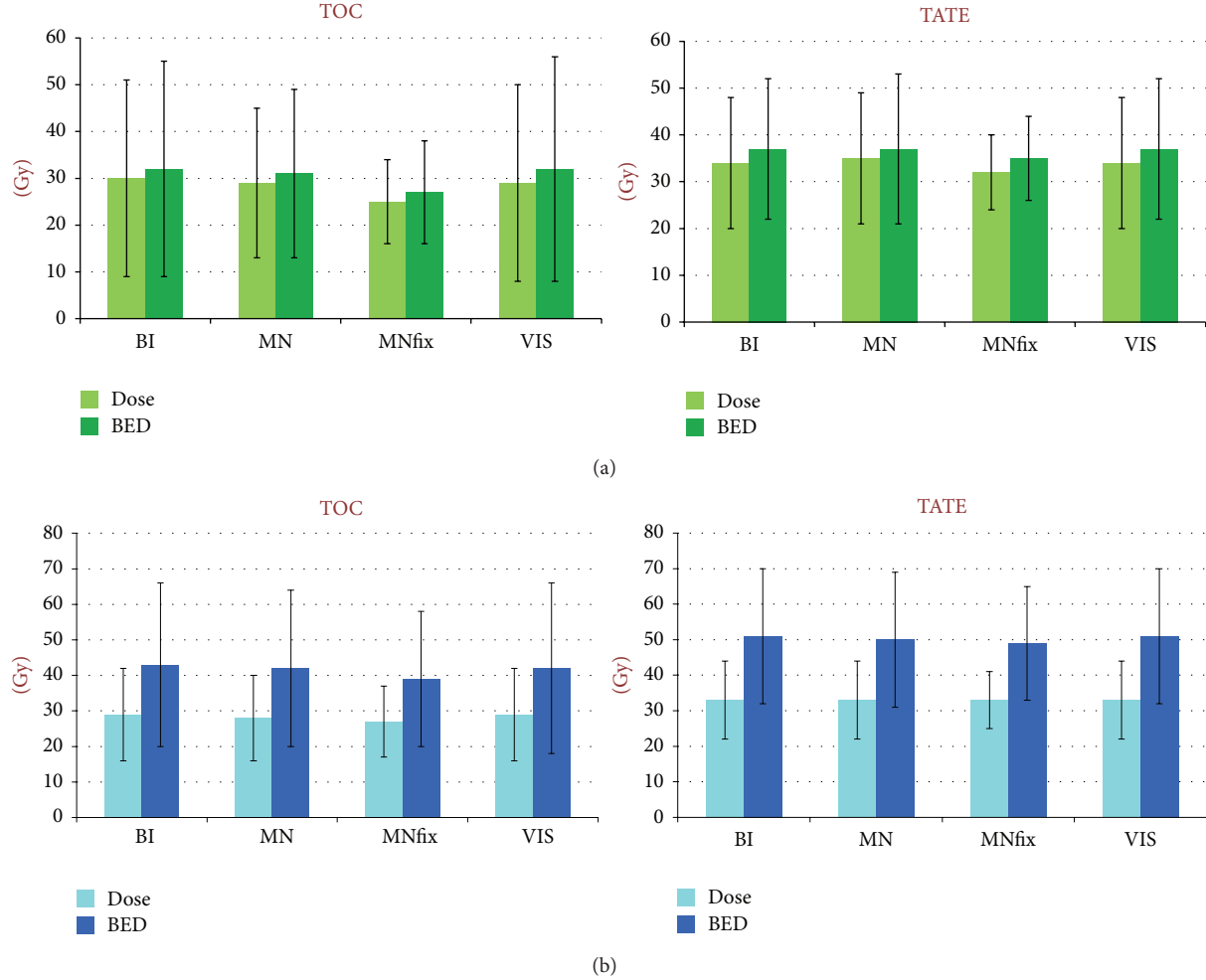


FIGURE 6: D and BED in case of ^{177}Lu therapy (upper panels) and ^{90}Y therapy (lower panels). The histograms report mean and 1 SD. ^{177}Lu and ^{90}Y -therapy administer a similar total dose for the specific schemes considered (29.8 GBq in 4 cycles versus 7.4 GBq in 2 cycles, resp.). Conversely, BED is noticeably greater for ^{90}Y because of the lower fractionation. Mean \pm SD values are similar, but relevant differences among patients can be found (see also Figure 4).

According to the visual choice, for ^{177}Lu , the mean \pm SD value of $\bar{\alpha}$ was 3.9 ± 1.4 h for DOTATATE and 3.2 ± 1.2 h for DOTATOC. The corresponding absorbed dose values were 1.0 ± 0.2 Gy/GBq and 0.7 ± 0.2 Gy/GBq.

For ^{90}Y , $\bar{\alpha}$ was 2.7 ± 0.9 h for DOTATATE and 2.1 ± 0.7 h for DOTATOC and absorbed doses 3.7 ± 1.5 Gy/GBq and 2.9 ± 1.3 Gy/GBq, respectively.

The t -test analysis highlighted a rather statistically significant difference between the mean $\bar{\alpha}$ values for patients with (RF) and without risk factors (NRF) (one-tailed t -test: $P < 0.10$). The RF cohort on average received a D 1.20–1.25 higher than the NRF one (Figure 7). An increased number of patients could confirm this explorative finding with a higher level of significance (e.g., $P = 0.05$).

4. Discussion

Tailoring peptide receptor radionuclide therapy (PRRT) according to dosimetry has been shown to be of great value in

clinical practice and should replace the criteria of administering a fixed of radioactivity amount or an activity correct for the patient body weight or surface [20].

Besides the red marrow, it is the kidneys that are the critical organs in this therapy, especially with ^{90}Y -peptides [1, 3, 21]. Much effort is being put into improving dosimetric accuracy in the quantification of activity: correcting S factors for patient-specific kidney mass [22], using SPECT instead of whole-body images [5], taking into account scatter and attenuation correction [23], including collimator response correction [7], computing a 3D activity distribution [6] to consider the equivalent uniform dose (EUD) instead of the mean absorbed dose.

Conversely, the impact of kinetics and image timing on the absorbed dose estimate specific for the kidneys has been neglected to a certain extent.

It has been stated [5] that a margin of error of 20% or less would be of great value when evaluating normal tissue complication probability (NTCP) [24].

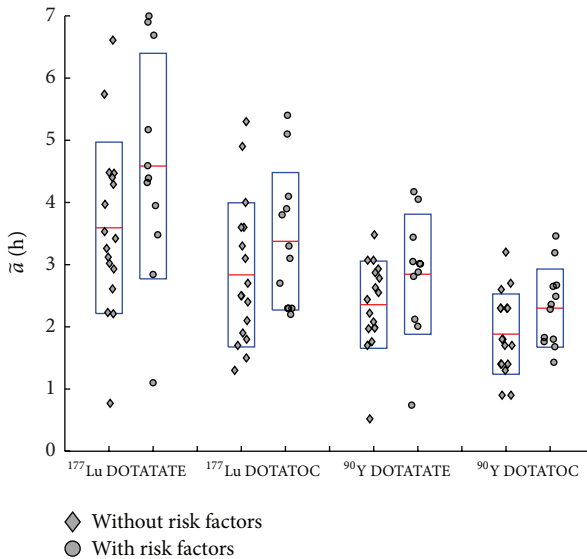


FIGURE 7: Time-integrated activity per unit activity \bar{a} for patients with risk factors (RF) (diamonds) and without (NRF) (dots). For each population, the mean value is indicated by the horizontal line, and the box extends to mean \pm SD. For DOTATATE, 11 patients were RF and 17 NRF, and the P -values of t -test were 0.05 and 0.06, for ^{177}Lu and ^{90}Y , respectively. For DOTATOC, 12 patients were RF and 17 NRF (one outlier was excluded), and P -values were 0.09 and 0.06, for ^{177}Lu and ^{90}Y , respectively.

In this work we have shown that data-collection/image-acquisition timing and the method for data interpolation cannot be overlooked, since calculation of absorbed dose could lead to errors even greater than 20% and greater than those originating from activity quantification. This is not acceptable, especially because such errors can be easily avoided by an adequate kinetic analysis.

Concerning the two issues of data-acquisition timings and interpolation, several dosimetric approaches exist in clinical practice, as shown in Table 4.

According to the EANM guidelines on internal dosimetry [26] three measurements for each kinetic phase are needed. Because the kinetics of DOTATOC and DOTATATE peptides in the kidneys are often associated with more than one phase—generally two—this would be demanding for patients as well as clinicians, since the acquisition of at least six images is difficult and time consuming. Consequently, finding a compromise that optimally balances accuracy and feasibility is of the utmost importance. The current situation for most clinical studies, in which no more than five points are available, is reflected in Table 4.

The choice of many investigators [5, 7, 9] has been to focus only on the slower phase which starts after 24 h, because this takes more than 70% of total time-integrated activity. Sandstrom pointed out that doing so there could be an overestimation, when extrapolating the first 24 h part. According to our results, a slight underestimation could be possible as well.

In our cohort we stopped data collection 3 days after therapy for logistic reasons, as it is cumbersome for most patients to stay one whole week in the proximity of the hospital.

TABLE 4: Characteristics of different dosimetric approaches concerning acquisition timing and interpolation method.

Investigator	Therapeutic nuclide	Acquisition timings	Interpolation method
Esser et al. [4], Sandström et al. [5], Larsson et al. [9]	^{177}Lu	1, 4, 7 d	MN
Hindorf et al. [25]	^{90}Y	Not fixed, up to 19–48 h, 2–4 acquisitions	Not reported for kidneys
Baechler et al. [17]	^{90}Y , ^{177}Lu , ^{111}In	0.5, 4 h, 1, 2 d	MN of last three points
Cremonesi et al. [3]	^{90}Y , ^{177}Lu	1, 4 h, 1, 2, 3 d	MN or BI
Garkavij et al. [7]	^{177}Lu	1 h, 1, 4, 7 d	TRexp

Our data showed that the method used to compute \bar{a} is crucial if data collection is stopped when the remaining administered activity is higher than 30% of the activity present in the kidneys at time zero; in contrast, we found that a careful choice of the method (excluding trapezoidal methods) results in negligible importance (differences smaller than 10%) when data reach two radionuclide effective half-lives. Moreover, in this situation the 6 h point could be spared. This finding therefore illustrates that the use of radionuclides with half-life shorter than $t_{1/2\text{eff}}$ ($^{177}\text{Lu}/^{90}\text{Y}$), like the β^+ -emitter ^{86}Y [3], is not advisable for PRRT dosimetry. For example, taking a median biological decay constant of $\lambda = 0.01 \text{ h}^{-1}$ (Table 1), $t_{1/2\text{eff}} (^{90}\text{Y}) \sim 35 \text{ h}$, $t_{1/2\text{eff}} (^{177}\text{Lu}) \sim 50 \text{ h}$, it would turn out that data are needed up to $\sim 70 \text{ h}$ for ^{90}Y peptides and $\sim 100 \text{ h}$ for ^{177}Lu peptides. If this is not possible, it must be pointed out that the obtained \bar{a} values could differ up to 70% depending on the method used for their calculation and the acquisition timings. In particular, a unique interpolating function cannot be used without taking into consideration the specific individual kinetics, because the weight of the tail becomes of major relevance. Thus, the question of choosing the best method among the several available (exponential functions, trapezoidal methods) arises. Moreover, establishing a principle for the selection of the most appropriate model allows an increased reproducibility of the results, as the user dependence is reduced [2].

Several criteria exist to choose the preferable model, but the small number of data points (five) is a major drawback in our study. The modified Akaike information criterion (AIC) proved to be an efficient approach [2] in blood serum dosimetry for radioimmunotherapy with anti-CD66 antibody, but in our case, it cannot be applied because of the small sample size (N) as compared to the number of parameters (K), four in a biexponential function, as the condition for its use ($N > K + 2$) does not apply. In our scenario, the AIC could be only used to evaluate the model most supported by the data for the whole data set, not for each single patient [27].

The F -test is feasible in principle, bearing in mind that the statistical power is low though (i.e., the probability density function F is broad). Moreover, these tests (F -test, AIC) are based on the residuals between the fitting function and

the measured data which stop at 3 days p.i., when 30%–40% of the activity reaching the kidneys at time zero is still not decayed (and in this way considered just by extrapolation): the great impact of the tail led to the paradox that on several occasions MNfix performed better than MN, although the former has one degree of freedom less (see $\tilde{\alpha}$ comparison). For this reason it is important to use all the available information—*theoretical and empirical*—in the model selection, besides the statistical criteria [2], which is why we put side by side the best models as determined by the *F*-test and visually, the latter is being used, as it was, as “reference.”

It is important to remember that the determination coefficient (R^2), although commonly used, is not actually a very useful indicator when using nonlinear regression functions [16], because it compares the sum of residuals with the distance of the data from their mean ($R^2 = 1 - SSE/TSS$; see *comparison of methods and statistical analysis*). When data are distanced from their mean value, as most often occurs in exponential curves, R^2 could be a misleadingly high parameter.

Despite all the limitations described previously for the various candidate criteria with so few data points (five, as generally available in practice), useful information could be gained analyzing our data.

- (i) *TRph*: the TRph cannot be applied with physical only decay starting from the 3 d point (or even before), because the physiological clearance in 52 on 58 cases was found after that; moreover, some investigators [5, 9] found biological clearance even up to 7 days (i.e., at 7 d, the measured activity was from 20% to 30% that of the one at 1 h and from 25% to 40% that of the one at 1 d). Pursuing this way, the overestimation of $\tilde{\alpha}$ is evident and is marked (Figure 2). Our interest in this method was drawn after its implementation in commercial software for dosimetry [28].
- (ii) *TRexp*: concerning TRexp, it comes to light that fitting a monoexponential function by means of only two points is not a reliable choice: $\tilde{\alpha}$ is very dependent on which ones are being used. For example we found that using the 1-2 d points instead of the 2-3 d for extrapolation, $\tilde{\alpha}$ decreased on average of 18% for either ^{177}Lu and ^{90}Y . Therefore, this method is not recommended when experimental data span is less than two effective radionuclide half-lives.
- (iii) *MNfix*: trying to use a single λ for all patients did not give satisfactory results for ^{177}Lu , as differences with the best visual model were $\pm 20\%$ (and could even be worse, because it was shown that in 9 cases the $\tilde{\alpha}_{\text{MNfix}}$ value was close to $\tilde{\alpha}_{\text{VIS}}$ just by chance). Conversely, for ^{90}Y it was not to be rejected (the mean ratio between the best $\tilde{\alpha}_{\text{VIS}}$ and $\tilde{\alpha}_{\text{MNfix}}$ is 0.97 ± 0.11 , with a maximum discrepancy of 35%). This is explained because of the lower effective half-life of ^{90}Y as compared to ^{177}Lu . It must be remembered that in the MNfix method the decay constant λ was fixed, but the initial activity was patient specific.

(iv) *MN and BI*: for ^{177}Lu a monoexponential function is a safe choice only having taken data after 24 h and reaching two effective radionuclide half-lives; conversely, when data are available from the injection up to 2-3 days a biexponential function is highly recommended (above all if accumulation or fast clearance is observed during the first day), as in this case the ratio of $\tilde{\alpha}$ for the monoexponential over the best visual model is 1.02 ± 0.22 , while with the biexponential model is 1.02 ± 0.07 ; that is, BI has a lower SD meaning a better agreement.

(v) *VIS*: when radio-peptide therapy cannot rely on the benefit of a dosimetry-based planning, Figure 7 might be of some help, providing the mean \pm SD of the best $\tilde{\alpha}$ values calculated from the visual method, for DOTA-TOC and DOTATATE peptides and ^{177}Lu and ^{90}Y radionuclides. Regarding 7.4 GBq ^{177}Lu DOTATATE administration, our findings are consistent with those from Sandstrom and coll, who reported an absorbed dose to the kidneys of 5 ± 2 Gy in a 24-patient cohort (cfr [5], *small VOI method*, mean value between left and right kidney D), to be compared with 6 ± 2 Gy of our 25-patient cohort, having excluded 3 outlier patients with doses of about 14 Gy/cycle.

(vi) *Risk factors*: it was recently shown [29] that impairment in renal function assessed by glomerular filtration rate led to higher mean kidney absorbed doses. We found that risk factors (hypertension, diabetes, lesions close to renal parenchyma, etc.), which are an evidence of renal impairment, led to a statistically significant increase in absorbed dose to the kidneys. In our cohort, patients with risk factors (RF) on average received a dose 1.20–1.25 times higher than patients without. This finding should be considered together with the clinical evidence [12] that the maximum tolerable BED is lower for patients with RF than without RF (28 Gy vs 40 Gy).

(vii) *BED*: finally, to take into account the effect related to the dose rate and to the response of the irradiated tissue, planning treatments are conducted constraining the BED as well [12, 17]. We found that for ^{177}Lu using formula (3) even with a fixed $G(\infty)$ value (i.e., obtained from formula (4) with λ_{fix}) does not give a dissimilar result if the more complicated $G(\infty)$ of formula (3) is being used. To give an example, the mean ratio of the RE values using the $G(\infty)$ for MNfix and BI functions is 1.01 ± 0.01 . In other words, what is important in the estimation of the BED for ^{177}Lu is the dose calculation accuracy only (besides the reliability of the α/β coefficient, obviously). For ^{90}Y , the same RE ratios were slightly greater, leading to a mean value of 1.04 ± 0.04 .

5. Conclusions

Accurate dosimetry is mandatory to fully exploit the potential of PRRT. Nonetheless, not only it does make high demands

on the level of staff commitment and facilities, but also on the patients themselves who in most cases can be discharged two days after therapy.

We found that if data are not available up to two effective half-lives (~4 days for ^{177}Lu , ~3 days for ^{90}Y), the estimation of kidney absorbed dose is consistently influenced by the interpolation method: concerning MNfix, MN, and BI, in 30% of cases for ^{177}Lu and 20% of cases for ^{90}Y differences between methods were higher than 10%, reaching 60% and even higher when considering also TRph and TRexp.

A monoexponential clearance with an averaged λ could be used in exceptional cases in ^{90}Y therapy, whereas for ^{177}Lu is totally inadequate. Concerning BED, RE is almost insensitive to the analytical time-activity curve being used, differences between analytical methods being within 10%.

The use of DOTATATE instead of DOTATOC caused a D increase of 1.25–1.30 (t -test, $P < 0.05$), while the effect on tumor was not evaluated. The risk-factor group had a D increase of 1.20–1.25 compared to the group without risk factors (t -test, $P < 0.10$).

Conflicts of Interests

The authors have no potential conflict of interests.

Acknowledgment

The authors are grateful to Mrs. Lorraine Yin for her kind English editing revision.

References

- [1] D. J. Kwekkeboom, B. L. Kam, M. Van Essen et al., "Somatostatin receptor-based imaging and therapy of gastroenteropancreatic neuroendocrine tumors," *Endocrine-Related Cancer*, vol. 17, no. 1, pp. R53–R73, 2010.
- [2] G. Glattling, P. Kletting, S. N. Reske, K. Hohl, and C. Ring, "Choosing the optimal fit function: comparison of the Akaike information criterion and the F-test," *Medical Physics*, vol. 34, no. 11, pp. 4285–4292, 2007.
- [3] M. Cremonesi, F. Botta, A. Di Dia et al., "Dosimetry for treatment with radiolabelled somatostatin analogues. A review," *Quarterly Journal of Nuclear Medicine and Molecular Imaging*, vol. 54, no. 1, pp. 37–51, 2010.
- [4] J. P. Esser, E. P. Krenning, J. J. M. Teunissen et al., "Comparison of [^{177}Lu -DOTA $^0\text{Tyr}^3$] octreotide and [^{177}Lu -DOTA $^0\text{Tyr}^3$] octreotide: which peptide is preferable for PRRT?" *European Journal of Nuclear Medicine and Molecular Imaging*, vol. 33, no. 11, pp. 1346–1351, 2006.
- [5] M. Sandström, U. Garske, D. Granberg, A. Sundin, and H. Lundqvist, "Individualized dosimetry in patients undergoing therapy with ^{177}Lu -DOTA-D-Phe $^1\text{Tyr}^3$ -octreotide," *European Journal of Nuclear Medicine and Molecular Imaging*, vol. 37, no. 2, pp. 212–225, 2010.
- [6] S. Baechler, R. F. Hobbs, A. Boubaker et al., "Three-dimensional radiobiological dosimetry of kidneys for treatment planning in peptide receptor radionuclide therapy," *Medical Physics*, vol. 39, pp. 6118–6128, 2012.
- [7] M. Garkavij, M. Nickel, K. Sjögren-Gleisner et al., " ^{177}Lu -[DOTA $^0\text{Tyr}^3$] octreotide therapy in patients with disseminated neuroendocrine tumors: analysis of dosimetry with impact on future therapeutic strategy," *Cancer*, vol. 116, no. 4, pp. 1084–1092, 2010.
- [8] M. Konijnenberg, "From imaging to dosimetry and biological effects," *Quarterly Journal of Nuclear Medicine and Molecular Imaging*, vol. 55, no. 1, pp. 44–56, 2011.
- [9] M. Larsson, P. Bernhardt, J. B. Svensson, B. W. Wängberg, H. Ahlman, and E. Forsslund-Aronsson, "Estimation of absorbed dose to the kidneys in patients after treatment with ^{177}Lu -octreotide: comparison between methods based on planar scintigraphy," *EJNMMI Research*, vol. 2, pp. 49–53, 2012.
- [10] E. Grassi, R. Sghedoni, M. Asti, F. Fioroni, D. Salvo, and G. Borasi, "Radiation protection in ^{90}Y -labelled DOTA-D-Phe $^1\text{Tyr}^3$ -octreotide preparations," *Nuclear Medicine Communications*, vol. 30, no. 2, pp. 176–182, 2009.
- [11] R. Sghedoni, E. Grassi, F. Fioroni et al., "Personnel exposure in labelling and administration of ^{177}Lu -DOTA-D-Phe $^1\text{Tyr}^3$ -octreotide," *Nuclear Medicine Communications*, vol. 32, no. 10, pp. 947–953, 2011.
- [12] L. Bodei, M. Cremonesi, M. Ferrari et al., "Long-term evaluation of renal toxicity after peptide receptor radionuclide therapy with ^{90}Y -DOTATOC and ^{177}Lu -DOTATATE: the role of associated risk factors," *European Journal of Nuclear Medicine and Molecular Imaging*, vol. 35, no. 10, pp. 1847–1856, 2008.
- [13] A. Filice, A. Fraternali, A. Frasoldati et al., "Radiolabeled somatostatin analogues therapy in advanced neuroendocrine tumors: a single centre experience," *Journal of Oncology*, vol. 2012, Article ID 320198, 10 pages, 2012.
- [14] S. Walrand, F. X. Hanin, S. Pauwels, and F. Jamar, "Tumour control probability derived from dose distribution in homogeneous and heterogeneous models: assuming similar pharmacokinetics, ^{125}Sn - ^{177}Lu is superior to ^{90}Y - ^{177}Lu in peptide receptor radiotherapy," *Physics in Medicine and Biology*, vol. 57, no. 13, pp. 4263–4275, 2012.
- [15] M. G. Stabin, R. B. Sparks, and E. Crowe, "OLINDA/EXM: the second-generation personal computer software for internal dose assessment in nuclear medicine," *Journal of Nuclear Medicine*, vol. 46, no. 6, pp. 1023–1027, 2005.
- [16] A.-N. Spiess and N. Neumeyer, "An evaluation of R^2 as an inadequate measure for nonlinear models in pharmacological and biochemical research: a monte carlo approach," *BMC Pharmacology*, vol. 10, article 6, 2010.
- [17] S. Baechler, R. F. Hobbs, A. R. Prideaux, R. L. Wahl, and G. Sgouros, "Extension of the biological effective dose to the MIRD schema and possible implications in radionuclide therapy dosimetry," *Medical Physics*, vol. 35, no. 3, pp. 1123–1134, 2008.
- [18] B. W. Wessels, M. W. Konijnenberg, R. G. Dale et al., "MIRD pamphlet no. 20: the effect of model assumptions on kidney dosimetry and response—implications for radionuclide therapy," *Journal of Nuclear Medicine*, vol. 49, no. 11, pp. 1884–1899, 2008.
- [19] R. F. Hobbs and G. Sgouros, "Calculation of the biological effective dose for piecewise defined dose-rate fits," *Medical Physics*, vol. 36, no. 3, pp. 904–907, 2009.
- [20] A. Imhof, P. Brunner, N. Marincek et al., "Response, survival, and long-term toxicity after therapy with the radiolabeled somatostatin analogue [^{90}Y -DOTA]-TOC in metastasized neuroendocrine cancers," *Journal of Clinical Oncology*, vol. 29, no. 17, pp. 2416–2423, 2011.
- [21] S. Walrand, R. Barone, S. Pauwels, and F. Jamar, "Experimental facts supporting a red marrow uptake due to radiometal

- transchelation in ^{90}Y -DOTATOC therapy and relationship to the decrease of platelet counts," *European Journal of Nuclear Medicine and Molecular Imaging*, vol. 38, no. 7, pp. 1270–1280, 2011.
- [22] M. W. Konijnenberg, "Is the renal dosimetry for [^{90}Y -DOTA 0 , Tyr 3]octreotide accurate enough to predict thresholds for individual patients?" *Cancer Biotherapy and Radiopharmaceuticals*, vol. 18, no. 4, pp. 619–625, 2003.
- [23] B. He, R. L. Wahl, G. Sgouros et al., "Comparison of organ residence time estimation methods for radioimmunotherapy dosimetry and treatment planning-patient studies," *Medical Physics*, vol. 36, no. 5, pp. 1595–1601, 2009.
- [24] A. Jackson, G. J. Kutcher, and E. D. Yorke, "Probability of radiation-induced complications for normal tissues with parallel architecture subject to non-uniform irradiation," *Medical Physics*, vol. 20, no. 3, pp. 613–625, 1993.
- [25] C. Hindorf, S. Chittenden, L. Causer, V. J. Lewington, H. R. Mäcke, and G. D. Flux, "Dosimetry for ^{90}Y -DOTATOC therapies in patients with neuroendocrine tumors," *Cancer Biotherapy and Radiopharmaceuticals*, vol. 22, no. 1, pp. 130–135, 2007.
- [26] M. Lassmann, C. Chiesa, G. Flux, and M. Bardis, "EANM Dosimetry Committee guidance document: good practice of clinical dosimetry reporting," *European Journal of Nuclear Medicine and Molecular Imaging*, vol. 38, no. 1, pp. 192–200, 2011.
- [27] P. Kletting, T. Kull, S. N. Reske, and G. Glatting, "Comparing time activity curves using the Akaike information criterion," *Physics in Medicine and Biology*, vol. 54, no. 21, pp. N501–N507, 2009.
- [28] E. Grassi, F. Fioroni, M. A. Sarti et al., "Validation of a voxel-based method for dosimetry in radionuclide therapy and comparison with a conventional tridimensional approach," in *Proceedings of the 25th Annual Meeting of the EANM*, pp. 27–31, October 2012.
- [29] J. Svensson, R. Hermann, M. Larsson et al., "Impairment in renal function predicts higher mean absorbed kidney doses in peptide receptor radionuclide therapy," in *Proceedings of the 25th Annual Meeting of the EANM*, pp. 27–31, October 2012.

Research Article

The Adjunctive Digital Breast Tomosynthesis in Diagnosis of Breast Cancer

Tsung-Lung Yang,^{1,2} Huei-Lung Liang,^{1,2} Chen-Pin Chou,^{1,2}
Jer-Shyung Huang,^{1,2} and Huay-Ben Pan^{1,2}

¹ Department of Radiology, Kaohsiung Veterans General Hospital, Kaohsiung 81362, Taiwan

² National Yang-Ming University, Taipei, Taiwan

Correspondence should be addressed to Huay-Ben Pan; panhb@vghks.gov.tw

Received 8 January 2013; Revised 19 April 2013; Accepted 9 May 2013

Academic Editor: Mei-Hsiu Liao

Copyright © 2013 Tsung-Lung Yang et al. This is an open access article distributed under the Creative Commons Attribution License, which permits unrestricted use, distribution, and reproduction in any medium, provided the original work is properly cited.

Purpose. To compare the diagnostic performance of digital breast tomosynthesis (DBT) and digital mammography (DM) for breast cancers. **Materials and Methods.** Fifty-seven female patients with pathologically proved breast cancer were enrolled. Three readers gave a subjective assessment superiority of the index lesions (mass, focal asymmetry, architectural distortion, or calcifications) and a forced BIRADS score, based on DM reading alone and with additional DBT information. The relevance between BIRADS category and index lesions of breast cancer was compared by chi-square test. **Result.** A total of 59 breast cancers were reviewed, including 17 (28.8%) mass lesions, 12 (20.3%) focal asymmetry/density, 6 (10.2%) architecture distortion, 23 (39.0%) calcifications, and 1 (1.7%) intracystic tumor. Combo DBT was perceived to be more informative in 58.8% mass lesions, 83.3% density, 94.4% architecture distortion, and only 11.6% calcifications. As to the forced BIRADS score, 84.4% BIRADS 0 on DM was upgraded to BIRADS 4 or 5 on DBT, whereas only 27.3% BIRADS 4A on DM was upgraded on DBT, as BIRADS 4A lesions were mostly calcifications. A significant *P* value (<0.001) between the BIRADS category and index lesions was noted. **Conclusion.** Adjunctive DBT gives exquisite information for mass lesion, focal asymmetry, and/or architecture distortion to improve the diagnostic performance in mammography.

1. Introduction

Breast cancer remains one of the leading causes of death in women over the age of 40 years [1, 2]. Mammography is an effective imaging tool for the detection of early-stage breast cancer, and it is the only screening modality proved to reduce mortality from breast cancer [3–5]. The sensitivity of screening mammography for breast cancer had been reported to be 80%–90% but may be as low as 48% in extremely dense breast [6] because of overlapping dense fibroglandular breast tissue, which substantially reduces the conspicuity of some breast lesions. Digital breast tomosynthesis (DBT) is expected to overcome the inherent limitations of mammography caused by overlapping of normal and pathological tissues during the standard two-dimensional (2D) projections [7–10]. In a DBT system, the X-ray tube moves along an arc during the examination, and a finite number of 2D projections

are acquired within a limited angle. The 3D volume of the compressed breast is reconstructed from the 2D projections, allowing enhancement of the information contained in each plane while blurring the off-focus information. Thus, DBT can provide better tissue visualization through the provision of 3D nonoverlapped tissue information. Several studies have shown that tomosynthesis may offer superior diagnostic accuracy, not only in the routine diagnostic practice [9, 11–14], but also in breast cancer screening [15], in the evaluation of breast lesions. Poplack et al. [16] concluded that subjectively, DBT has comparable or superior image quality versus full-field digital mammography (DM) and has the potential to reduce screening recall rates when used in conjunction with DM. Andersson et al. [12] concluded that cancer visibility on DBT in one view is superior to full-field DM in two views and that this would indicate the potential of DBT to increase sensitivity.

In this study, we compared the diagnostic performance of 59 pathologically proved breast malignancy in a multireader retrospective study to determine whether or not simultaneously viewing DM and DBT is perceived to be more informative in detection (including assessing the features of masses, asymmetries, architectural distortions, and microcalcifications) and diagnosis (BIRADS score) of breast cancers.

2. Materials and Methods

2.1. Patients. Inclusion criteria for this study were patients who had pathologically proved breast cancer and had undergone both DM and DBT during the period of January 2012 to November 2012. This retrospective review of research database was conducted with the approval of the institutional review board. The demographic data, including age, clinical symptom and sign, mammographic findings, and histopathologic staging, was recorded as a case report form in a secure research database. The mammographic findings included the density of breast, the type of malignant features (mass, architectural distortion, focal asymmetric density, and calcification), and breast imaging reporting and data system (BIRADS) score. If the findings were mixed, we recorded the most conspicuous findings. In cases where there was more than one lesion, a separate form was created for each lesion.

2.2. Image Acquisition. Selenia Dimensions (Hologic Inc., Bedford, MA) “combo-mode” imaging system with mediolateral oblique and craniocaudal projections was applied in this study with acquiring a traditional digital mammogram and a tomosynthesis scan during the same breast compression. It employs a tungsten (W) target and a selenium (Se) detector with a rhodium (Rh) filter, a silver (Ag) filter for 2D images, an aluminum (Al) filtration in tomosynthesis images. During acquisition, 15 low-dose projection images with exposure parameters of 29 kVp and 44 mAs are obtained over a 15° arc with a continuous exposure method. After acquisition, raw data of the projection images are used for reconstruction to yield images of 1 mm thickness in an orientation paralleling to the detector with totaling 30–80 tomosynthetic images per view depending on the breast thickness being compressed. The reconstructed pixel size is 110–120 μm . The total acquisition time for one breast tomosynthesis view is approximately 3 seconds. Radiation dose to single breast view is about 1.45 mGy.

The radiologists viewed individually or sequentially a dynamic cine mode at a mammography workstation (Hologic Inc., SecurView) that included two Barco 5-megapixel monitors (Kortrijk, Belgium), allowing the viewing of one, two, or four images per display for each monitor.

2.3. Image Assessment. The selection of cases was performed by one radiologist who did not participate in the subjective rating study and knew from the relevant reports the actual diagnosis of all cases, in particular, the index lesion of interest. The index lesion of interest location was recorded for each case by this radiologist on a data form so that readers knew which lesion to evaluate. Three board-certified radiologists

with varying breast imaging experience ranging from 5 to 15 years volunteered for the study. Readers were told to assume the screening DM examination was the woman’s baseline examination; hence, no prior DM examinations were provided for comparison. Readers were asked to provide a subjective assessment of how well the combination of DM and DBT examinations is compared with DM alone for the purpose of evaluating the index lesion. A scale of 0 to 2 was provided and used with 0 indicating that DM plus DBT was equivalent or comparable for diagnosis compared with DM, 1 indicating that DM plus DBT was somewhat better for diagnosis, 2 indicating that DM plus DBT was definitely better for diagnosis compared with DM alone. After the interpretation, readers were asked to provide a forced BI-RADS score (1–5) for each index lesion, based on DM reading alone and with additional DBT information.

2.4. Definitions. Based on ACR recommendation [17], type (1–4) of breast density indicates tissue density almost entirely fat, scattered fibroglandular density, heterogeneously dense, and extremely dense, respectively. Focal asymmetric breast density is defined as “asymmetry of tissue density with similar shape on two views but completely lacking borders and the conspicuity of a true mass.”

Architectural distortion is defined as the normal architecture of the breast that is distorted with no definite mass visible. This includes spiculations radiating from a point and focal retraction or distortion at the edge of the parenchyma. Architectural distortion can also be an associated finding. As to the calcifications, amorphous or coarse heterogeneous calcifications are of intermediate concern and fine pleomorphic or fine linear or fine linear branching calcifications are of higher probability of malignancy. Cluster, linear, or segmental distribution of microcalcifications is suspicious for malignancy. Cluster, linear, or segmental distribution of microcalcifications is suspicious for malignancy.

2.5. Data Analysis. We calculate the mean of 57 patient’s age. Then, we computed the frequency and proportion of the patient characteristics, the subjective ratings, and the BIRADS ratings of overall readers and cancer cases. For the purpose of this analysis, subjective ratings 1 and 2 were combined. Chi-square test was used to compare the relevance between BIRADS category and index lesions of breast cancer.

3. Results

Fifty-seven patients (mean age 53.5 years, range 26–89 years) with pathologically proved breast cancers who had undergone combo DBT for either screening or diagnostic purposes were enrolled in this retrospective study. Two patients had a second malignancy in the ipsilateral breast. Thus, a total of 59 breast cancers were reviewed in this study. Thirty patients (52.6%) were symptomatic with positive breast physical examination during mammography taken. The location of the breast cancers were 31 lesions on the right and 28 on the left. As to the breast composition (BI-RADS type), most (up to 79%) patients in our series had dense breast

TABLE 1: Demographic data of the 57 breast cancer patients.

Patient characteristics	N	Patients = 57
Age (mean)	53.7	
Symptom/sign: Y/N	30/27	52.6/47.4
Part: L/R	27/30	47.4/52.6
Type		
1	2	3.5
2	10	17.5
3	27	47.4
4	18	31.6
Characteristic		
Mass	17	28.8
Density	12	20.3
Distortion	6	10.2
Calcifications	23	39.0
None	1	1.7
BI-RADS		
0	20	35.1
4A	8	14.0
4B	9	15.8
4C	7	12.3
5	13	22.8
TNM stage		
Tis + T1mi	16	28.1
T1N0	17	29.8
T1N1 or above	24	42.1

(type 3 or 4) with type 1 in two (3.5%) patients, type 2 in 10 (17.5%), type 3 in 27 (47.3%), and type 4 in 18 (31.6%). Of the 59 index lesions, 17 (28.8%) lesions were presented as mass (Figure 1), 12 (20.3%) as focal asymmetry/density (Figure 2), 6 (10.2%) as architecture distortion (Figure 3), and 23 (39.0%) as calcifications (Figure 4). One intracystic tumor (1.7%), which was clinically palpable and diagnosed by US images, failed to show malignant feature on either DM or tomosynthesis images (Figure 5) and therefore was considered as truly false negative. BIRADS category of the fifty-seven patients was initially rated as 0 in 20 cases (35%), 4A in 8 (14%), 4B in 9 (15.8%), 4C in 7 (12%), and category 5 in 13 cases (22.8%), respectively, with final clinical staging of ductal carcinoma in situ (DCIS) in 16 cases (28.1%), stage 1 in 17 cases (29.8%), and T1N1 or above in 24 cases (42.1%). The demographic and clinical results of these 57 patients were listed in Table 1.

For the overall 59 target lesions interpreted by 3 readers, combo DBT was perceived to be more informative for diagnosis in 48% (85/177) of the subjective ratings (59 lesions \times 3 readers = 177 ratings). A superior rating of the index lesions was considered in 30 of 51 (58.8%) mass lesions, 30 of 36 (83.3%) density lesions, 17 of 18 (94.4%) architecture distortion lesions, while only 8 of 69 (11.6%) in calcification lesions. The 85 superior ratings of 1 or 2 occurred in 34 patients in which at least one radiologist had given a positive

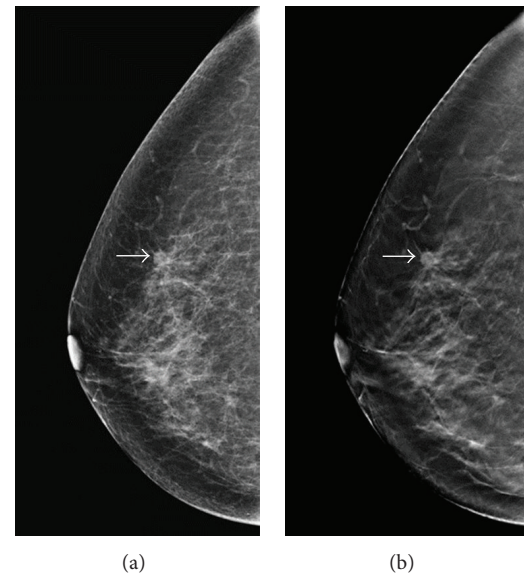


FIGURE 1: A 66-year-old woman for mammographic screening. (a) Digital mammogram showed a small oval-shaped, well-defined nodule (arrow) over upper-outer quadrant (UOQ) of right breast with BIRADS 0 rated by all the 3 readers. (b) Tomosynthesis revealed a nodule with lobular contour and obviously spiculated margin (arrow). The BIRADS score was rated as 4C by 1 reader and category 5 by 2 readers. The lesion was later proved pathologically to be a breast cancer (T1bN0M0).

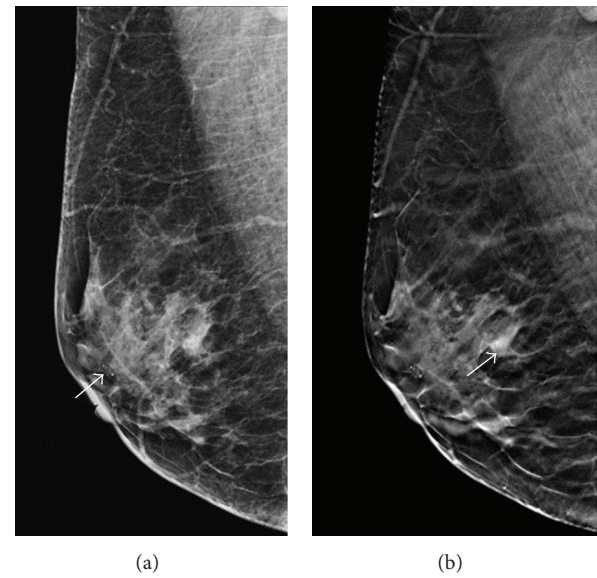


FIGURE 2: A 57-year-old woman for mammographic screening. (a) Digital mammogram showed a cluster of amorphous microcalcification (arrow) at the subareolar region of right breast, which was proved to be benign in nature by needle biopsy. The initial BIRADS score was rated as 0 by one reader and 4A by two readers. (b) Tomosynthesis revealed a focal asymmetric density around 7 mm in diameter (arrow), which was rated as BIRADS 4B by two readers and 5 by one reader. The lesion was later proved pathologically to be invasive cancer (T1cN0M0).

TABLE 2: The results of rating in each type of lesions and overall lesions.

Rating	Calcification		Density		Distortion		Mass		None		Overall	
	n	%	n	%	n	%	n	%	n	%	n	%
0	61	88.4	6	16.6	1	5.5	21	41.2	3	100	92	51.98
1	4	5.8	15	41.7	5	27.8	24	47	0	0	48	27.12
2	4	5.8	15	41.7	12	66.7	6	11.8	0	0	37	20.90
	69		36		18		51		3		177	

0: equal; 1: somewhat better; 2: definitely better.

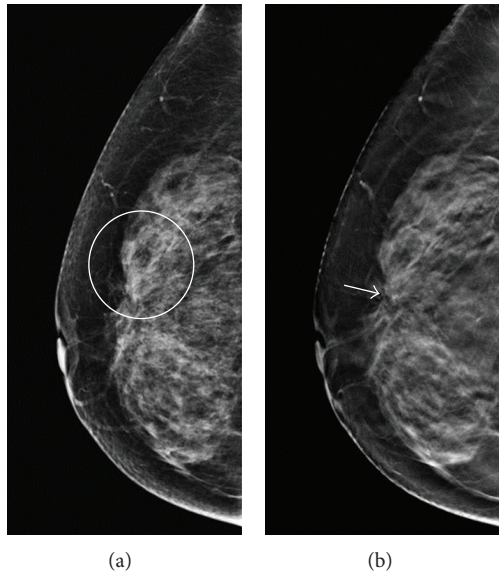


FIGURE 3: A 59-year-old woman for mammographic screening. (a) Digital mammogram showed focal increased density over UOQ of right breast (circle) with BIRADS rating 0 by all the 3 readers. (b) Tomosynthesis revealed obvious architecture distortion (arrow) with radiating spiculations tethered from retracted tissue. The BIRADS score was rated as 4B by 2 readers and 4C by one reader. Patient received partial mastectomy with pathologically proved intraductal cancer, intermediate type (TisN0M0).

rating. Of whom, 73.5% were dense breasts (type 3 or 4) with type 1 breast in 2 (5.9%) patients, type 2 breast in 7 (20.6%) patients, type 3 breast in 16 (47%) patients, and type 4 breast in 9 (26.5%) patients. The ratings of overall and each relevant index lesion were listed in Table 2.

As to the retrospective review of BI-RADS score in the 57 cancer patients (171 ratings), BI-RADS 0 and 4A were rated 64 (37.4%) and 33 (19.3%) on DM versus 10 (5.8%) and 29 (16.9%) on combo tomosynthesis, respectively. Of the 64 BIRADS 0 rated on DM, 10 (15.6%) ratings were still categorized as BIRADS 0 on combo tomosynthesis, while upgraded to 4A in 4 (6.3%), 4B in 22 (34.4%), 4C in 17 (26.6%), and category 5 in 11 (17.2%), whereas, in the 33 BIRADS 4A ratings on DM, 24 (72.7%) were still categorized the same, while being upgraded to 4B in 5 (15.2%) and 4C in 4 (12.1%), respectively,

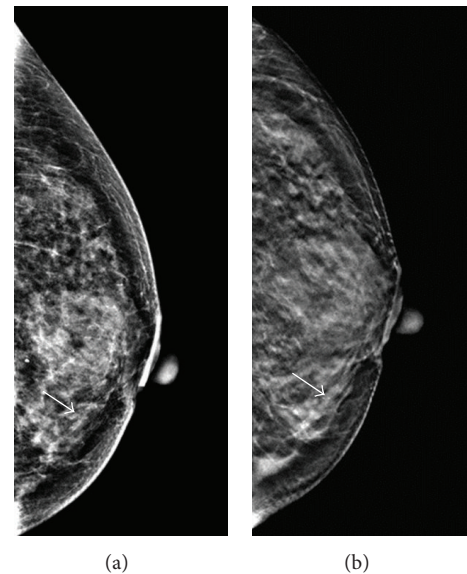


FIGURE 4: A 55-year-old female had partial mastectomy 5 years ago due to intraductal carcinoma in situ in right breast with yearly mammographic follow up. (a) Digital mammogram showed microcalcifications (arrow) with segmental distribution over the lower-inner quarter of the left breast. The BIRADS score was rated as 0 by two readers and 4A by one reader. (b) Tomosynthesis revealed the microcalcifications being inside the dilated tubular structure, which was toward the nipple. The BIRADS score was upgraded to 4B by one reader and 4C by two readers. The lesion was proved pathologically to be an invasive cancer (T1cN0M0).

with additional reviewing of the 3D tomosynthesis images. Of the BIRADS 4A patient group, calcification was the dominant lesion in 31 (93.9%) of the 33 ratings. The overall forced BI-RADS scores on digital mammograms and tomosynthesis were listed in Table 3. Although there seemed to be of little improvement of the DBT diagnosis on calcification lesions, markedly improved diagnostic performance of density, distortion, and mass lesions was noted in this study. The forced BIRADS score of 0, 4, and 5 versus each type of lesion was listed in Table 4. Comparing the BIRADS category (category 0 versus 4A versus 4B + 4C + 5) and index lesions by the use of chi-square test, a significant *P* value (<0.001) was noted (Table 5).

4. Discussion

The malignant features of breast cancers can be classified as mass, focal asymmetry, architecture distortion, and microcalcification. Better delineations of the lesion border and margin result in a more definitive interpretation. Previous studies concluded that the shape and margin of the mass in tomosynthesis were well characterized than DM [9, 13]. Thus, small undulating contour or subtle speculated margins of masses can be identified on a thin slide without normal breast tissue masking. Our study confirmed that 58.8% of mass index lesions had superior rating on tomosynthesis versus DM alone.

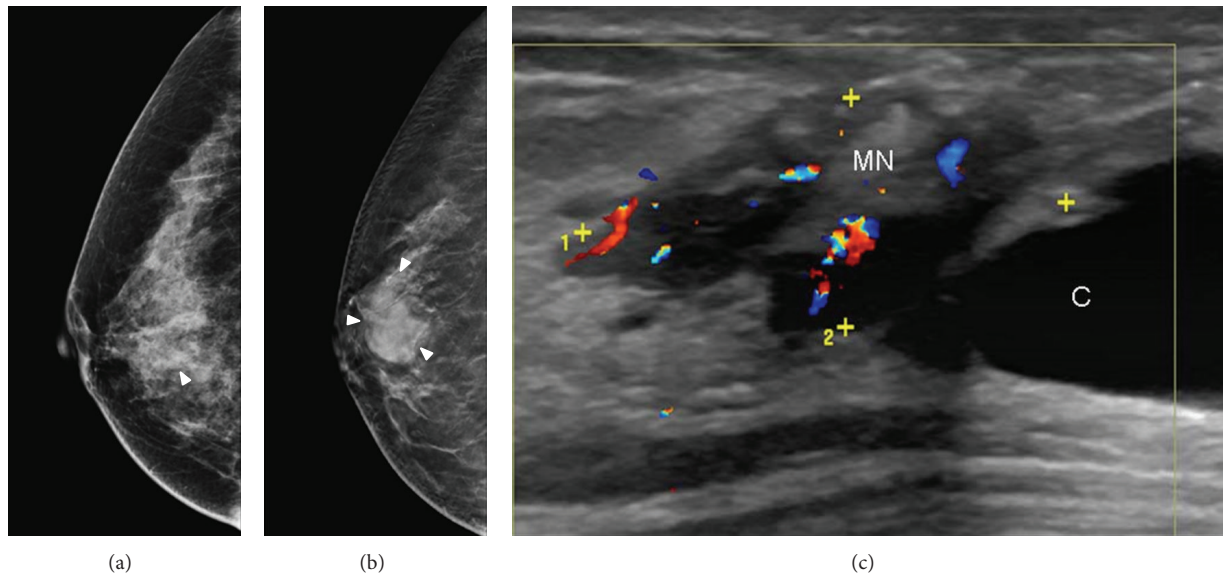


FIGURE 5: A 61-year-old woman with palpable mass in the right breast. (a) Digital mammograms showed focal increased density (arrowhead) without architectural distortion in the right breast. (b) Tomosynthesis clearly delineated the smooth border of a mass lesion (arrowhead) without showing malignant feature. This case was considered as true negative in both digital mammography and tomosynthesis. (c) Color ultrasound showed a cystic-like lesion (C) with hypervascular mural nodule (MN). The lesion was proved to be ductal carcinoma in situ, TisN0M0.

TABLE 3: The overall forced BI-RADS score on digital mammograms and tomosynthesis.

3D	2D								All (rating)
	2	3	0	4A	4B	4C	5		
2	2	0	0	0	0	0	0	2	
3	0	0	0	0	0	0	0	0	
0	0	0	10	0	0	0	0	10	
4A	0	1	4	24	0	0	0	29	
4B	0	1	22	5	12	0	0	40	
4C	1	0	17	4	13	7	0	42	
5	0	0	11	0	8	13	16	48	
All	3	2	64	33	33	20	16	171	

TABLE 4: The forced BI-RADS score (0, 4, 5) of each type of lesions on digital mammograms and tomosynthesis.

3D	2D															Total
	Cal			Density			Distortion			Mass						
	0	4	5	0	4	5	0	4	5	0	4	5	0	4	5	
BI-RADS																
0	4	0	0	4	0	0	0	0	0	0	0	0	0	0	0	8
4	5	54	0	21	3	0	10	0	0	7	8	0	108			
5	2	0	4	2	2	1	2	2	0	5	16	12	48			
Total	11	54	4	27	5	1	12	2	0	12	24	12	164			

Focal asymmetric breast density is found in approximately 3% of mammograms [18]. A review of the literature

TABLE 5: Comparison of BI-RADS score and lesions type.

Lesion	BI-RADS (3D)			Total
	0	4A	4B, 4C, 5	
Calcification	4	26	39	69
Density	4	3	28	35
Distortion	0	0	15	15
Mass	0	0	48	48
Total	8	29	130	167

P value < 0.001 (chi-square test).

showed that malignancy can be found in 0%–14% of asymmetric breast tissue biopsies, and any associated features of possible malignancy, or a clinically palpable mass mandates tissue diagnosis [19]. However, the lesion presented as focal asymmetric breast density on 2D mammograms may lack its conspicuous borders, making the diagnosis of malignancy difficult in a sole “asymmetry” finding. Although, the focal density on DBT is presented as an ill-defined mass but it still definitely has a border and volume size. Thereafter, it can be easily distinguished from an island of normal breast tissue. In other words, a lesion with 5 mm in size would be detected in at least five 1 mm contiguous slices even if it presented as a focal asymmetry. In our study, 83.3% density reading were rated as superior to that of DM only with 85.2% (23/27) BI-RADS 0 being upgraded to BI-RADS 4 or 5.

On mammograms, the breast is seen as a directionally oriented-textured image due to the presence of several piecewise linear structures such as ligaments, ducts, and blood vessels. The presence of tumor, inflammation, trauma, or surgery may change the orientation of normal architecture,

whereas the presence of overlapping dense fibroglandular breast tissue may substantially reduce the conspicuity of the changes. It was reported that architectural distortion accounted for 12% to 45% of overlooked or misinterpreted breast cancer cases in screening mammographies [20, 21], and it constituted the most commonly missed abnormality in false-negative cases. As the barrier of false negative for distortion lesions is chiefly related to overlapped tissue, DBT was proved to be an expectant method to solve this problem [14]. In our study, 94.4% distortion reading were rated as superior to that of DM only with all the BIRADS 0 being upgraded to BIRADS 4 or 5.

Our study also showed markedly improved diagnostic accuracy for noncalcified lesions on tomosynthesis mammograms with 78.2% initially scored as BIRADS 0 on DM being upgraded to equal or higher than RIRADS 4B, which may allow for the replacement of conventional supplemental mammographic views. Our series showed only mild-modest improvement of the diagnostic accuracy in the patient group initially scored as BIRADS 4A with 72.7% of patients remaining with the same score. It was because most of the lesions (93.9%) in this patient group were microcalcifications. The clinical benefits of tomosynthesis on calcified lesions may be still debated with the concern of not depicting calcifications as well as traditional mammography [16]. However, increasing the slice thickness would increase the ability to perceive a 3D configuration of calcifications, and the extents of accompanying microcalcifications may be better depicted on BDT than on 2D mammograms [22]. Thereafter, Spangler et al. [22] concluded that DM appeared to be slightly more sensitive than DBT for the detection of calcification (84% versus 75%). However, diagnostic performance as measured by area under the curve using BIRADS was not significantly different. Other studies had also supported the diagnostic performance of digital breast tomosynthesis in conjunction with [23] or independently [24, 25] of full-field DM.

A major limitation of this study was that it involved a nonblinded retrospective review of only pathologically proved breast cancer images. The true diagnostic accuracy of combo DBT in general population is unclear. But with more familiarity with the imaging features of breast malignancy on DBT, it may help us interpret the tomosynthesis more precisely. In addition, the term of focal asymmetry is defined in 2D side by side interpretation, but for ease to compare with previous tomosynthesis studies, we still use the term of focal asymmetry instead of focal density.

In conclusion, adjunctive DBT gives exquisite information for mass lesion, focal asymmetry, and/or architecture distortion to improve the diagnosis in mammography with comparable performance to the pattern of microcalcifications on 2D mammogram, yet the additional associating findings such as intraductal calcification may give some clues to confirm malignancy.

Conflict of Interests

The authors have no potential conflict of interests to disclose.

References

- [1] C. Mettlin, "Global breast cancer mortality statistics," *Ca-A Cancer Journal for Clinicians*, vol. 49, no. 3, pp. 138–144, 1999.
- [2] R. A. Smith, "Breast cancer screening among women younger than age 50: a current assessment of the issues," *Ca-A Cancer Journal for Clinicians*, vol. 50, no. 5, pp. 312–336, 2000.
- [3] L. Nystrom, L. E. Rutqvist, S. Wall et al., "Breast cancer screening with mammography: overview of Swedish randomised trials," *The Lancet*, vol. 341, no. 8851, pp. 973–978, 1993, Published correction appears in *The Lancet*, vol. 342, p.1372, 1993.
- [4] L. Tabar, C. J. Fagerberg, A. Gad et al., "Reduction in mortality from breast cancer after mass screening with mammography: randomised trial from the Breast Cancer Screening Working Group of the Swedish National Board of Health and Welfare," *The Lancet*, vol. 1, no. 8433, pp. 829–832, 1985.
- [5] J. M. Lewin, C. J. D'Orsi, and R. E. Hendrick, "Digital mammography," *Radiologic Clinics of North America*, vol. 42, no. 5, pp. 871–884, 2004.
- [6] T. M. Kolb, J. Lichy, and J. H. Newhouse, "Comparison of the performance of screening mammography, physical examination, and breast US and evaluation of factors that influence them: an analysis of 27,825 patient evaluations," *Radiology*, vol. 225, no. 1, pp. 165–175, 2002.
- [7] L. T. Niklason, B. T. Christian, L. E. Niklason et al., "Digital tomosynthesis in breast imaging," *Radiology*, vol. 205, no. 2, pp. 399–406, 1997.
- [8] J. T. Dobbins III and D. J. Godfrey, "Digital x-ray tomosynthesis: current state of the art and clinical potential," *Physics in Medicine and Biology*, vol. 48, no. 19, pp. R65–R106, 2003.
- [9] M. P. Jeong, E. A. Franken Jr., M. Garg, L. L. Fajardo, and L. T. Niklason, "Breast tomosynthesis: Present considerations and future applications," *Radiographics*, vol. 27, supplement 1, pp. S231–S240, 2007.
- [10] E. A. Rafferty, "Digital Mammography: novel Applications," *Radiologic Clinics of North America*, vol. 45, no. 5, pp. 831–843, 2007.
- [11] G. Gennaro, A. Toledano, C. Di Maggio et al., "Digital breast tomosynthesis versus digital mammography: a clinical performance study," *European Radiology*, vol. 20, no. 7, pp. 1545–1553, 2010.
- [12] I. Andersson, D. M. Ikeda, S. Zackrisson et al., "Breast tomosynthesis and digital mammography: a comparison of breast cancer visibility and BIRADS classification in a population of cancers with subtle mammographic findings," *European Radiology*, vol. 18, no. 12, pp. 2817–2825, 2008.
- [13] M. L. Zuley, A. I. Bandos, M. A. Ganott et al., "Digital breast tomosynthesis versus supplemental diagnostic mammographic views for evaluation of noncalcified breast lesions," *Radiology*, vol. 266, pp. 89–95, 2013.
- [14] P. Skaane, R. Gullien, H. Bjørndal et al., "Digital breast tomosynthesis (DBT): initial experience in a clinical setting," *Radiologica*, vol. 53, pp. 524–529, 2012.
- [15] A. Tejerina Bernal, A. Tejerina Bernal, and F. Rabadr Doreste, "Breast imaging: how we manage diagnostic technology at a multidisciplinary breast center," *Journal of Oncology*, vol. 2012, Article ID 213421, 9 pages, 2012.
- [16] S. P. Poplack, T. D. Tosteson, C. A. Kogel, and H. M. Nagy, "Digital breast tomosynthesis: Initial experience in 98 women with abnormal digital screening mammography," *American Journal of Roentgenology*, vol. 189, no. 3, pp. 616–623, 2007.

- [17] American College of Radiology (ACR), *Illustrated Breast Imaging Reporting and Data System (BI-RADS)*, American College of Radiology, Reston, Va, USA, 4th edition, 2003.
- [18] C. W. Piccoli, S. A. Feig, and J. P. Palazzo, "Developing asymmetric breast tissue," *Radiology*, vol. 211, no. 1, pp. 111–117, 1999.
- [19] F. Sperber, U. Metser, A. Gat, A. Shalmon, and N. Yaal-Hahoshen, "Focal asymmetric breast density: mammographic, sonographic and pathological correlation in 97 lesions—a call to restrain biopsies," *Israel Medical Association Journal*, vol. 9, no. 10, pp. 720–723, 2007.
- [20] B. C. Yankaskas, M. J. Schell, R. E. Bird, and D. A. Desrochers, "Reassessment of breast cancers missed during routine screening mammography: a community-based study," *American Journal of Roentgenology*, vol. 177, no. 3, pp. 535–541, 2001.
- [21] H. C. Burrell, A. J. Evans, A. Robin, M. Wilson, and S. E. Pinder, "False-negative breast screening assessment. What lessons can we learn?" *Clinical Radiology*, vol. 56, no. 5, pp. 385–388, 2001.
- [22] M. L. Spangler, M. L. Zuley, J. H. Sumkin et al., "Detection and classification of calcifications on digital breast tomosynthesis and 2D digital mammography: a comparison," *American Journal of Roentgenology*, vol. 196, no. 2, pp. 320–324, 2011.
- [23] D. Gur, G. S. Abrams, D. M. Chough et al., "Digital breast tomosynthesis: observer performance study," *American Journal of Roentgenology*, vol. 193, no. 2, pp. 586–591, 2009.
- [24] D. Kontos, P. R. Bakic, A.-K. Carton, A. B. Troxel, E. F. Conant, and A. D. A. Maidment, "Parenchymal texture analysis in digital breast tomosynthesis for breast cancer risk estimation: a preliminary study," *Academic Radiology*, vol. 16, no. 3, pp. 283–298, 2009.
- [25] H. J. Teertstra, C. E. Loo, M. A. A. J. Van Den Bosch et al., "Breast tomosynthesis in clinical practice: initial results," *European Radiology*, vol. 20, no. 1, pp. 16–24, 2010.

Review Article

Managing Lymphoma with Non-FDG Radiotracers: Current Clinical and Preclinical Applications

Fan-Lin Kong,¹ Richard J. Ford,² and David J. Yang¹

¹ Department of Experimental Diagnostic Imaging, Box 59, The University of TX MD Anderson Cancer Center, 1515 Holcombe Boulevard, Houston, TX 77030, USA

² Department of Hematopathology, The University of Texas MD Anderson Cancer Center, 1515 Holcombe Boulevard, Houston, TX 77030, USA

Correspondence should be addressed to Fan-Lin Kong; kongfanlin2007@gmail.com

Received 1 April 2013; Accepted 27 May 2013

Academic Editor: Mei-Hsiu Liao

Copyright © 2013 Fan-Lin Kong et al. This is an open access article distributed under the Creative Commons Attribution License, which permits unrestricted use, distribution, and reproduction in any medium, provided the original work is properly cited.

Nuclear medicine imaging modalities such as positron emission tomography (PET) and single-photon emission computed tomography (SPECT) have played a prominent role in lymphoma management. PET with [¹⁸F]Fluoro-2-deoxy-D-glucose (FDG) is the most commonly used tool for lymphoma imaging. However, FDG-PET has several limitations that give the false positive or false negative diagnosis of lymphoma. Therefore, development of new radiotracers with higher sensitivity, specificity, and different uptake mechanism is in great demand in the management of lymphoma. This paper reviews non-FDG radiopharmaceuticals that have been applied for PET and SPECT imaging in patients with different types of lymphoma, with attention to diagnosis, staging, therapy response assessment, and surveillance for disease relapse. In addition, we introduce three radiolabeled anti-CD20 antibodies for radioimmunotherapy, which is another important arm for lymphoma treatment and management. Finally, the relatively promising radiotracers that are currently under preclinical development are also discussed in this paper.

1. Introduction

According to the 2011 report from the National Cancer Institute's Surveillance, Epidemiology and End Results Program, an estimated total of 662,789 individuals in the US are living with, or in remission from lymphoma in 2011 [1]. About 75,190 people in the US are expected to be diagnosed with lymphoma in 2011, which include 8,830 cases of Hodgkin's lymphoma (HL) and 66,360 cases of non-Hodgkin's lymphoma (NHL). In fact, NHL is the seventh most common cancer in the US [1].

Lymphoma treatment and prognosis, especially for NHL, are heavily dependent on the disease type and staging. For instance, patients with stage I-II aggressive NHL respond to a short course of chemo/radiotherapy better than a full course of chemotherapy alone [2]. In early stage HL, 20%–30% of patients will relapse after mantle irradiation, which largely reflects inaccurate staging [3]. Therefore, it is extremely important to reach an accurate diagnosis, which can facilitate more precise staging and prognostic estimations, as well

as evaluation of response to therapy. The major imaging modalities utilized in lymphoma are divided into two general types: the anatomic imaging modalities, such as computed tomography (CT) and magnetic resonance imaging (MRI), and the functional imaging modalities using ionizing radiation, such as positron emission tomography (PET) and single photon emission computed tomography (SPECT). CT and MRI can only provide limited information of lymphoma patients who have normal-sized lymph nodes, and they cannot differentiate tumor from lymphadenopathy, infection, hemorrhage, acute radiation pneumonitis, or radiation fibrosis [4, 5]. On the other hand, PET, SPECT, and their integration with CT can detect the biological alterations (increased glycolysis, DNA synthesis, amino acid transports, etc.) in tumor lesions in contrast to normal tissues and thus better distinguish viable tumor cells from necrotic cells or fibrosis. The principles of PET and SPECT imaging are both based on the detection of radiolabeled ligands; however, the radionuclides for these two modalities are quite different.

PET detects the annihilation radiation emitted from a certain positron-emitting radionuclide, while SPECT detects the radionuclides that emit gamma-ray photons (Figure 1).

[¹⁸F]Fluoro-2-deoxy-D-glucose (FDG), an ¹⁸F-labeled glucose analogue, is the most commonly used radiotracer for PET imaging in lymphoma patients. In the most recent review of the literature search from 1999 to 2011 by Ansell and Armitage, FDG-PET is recommended for initial staging and re-staging at completion of therapy in patients with HL, diffuse large B-cell lymphoma (DLBCL), and follicular lymphoma (FL) [5]. However, its usage can be limited in cases of indolent diseases with low metabolic activity. In addition, FDG is not tumor specific and can also accumulate in inflammatory lesions such as tuberculosis, abscesses, and sarcoidosis [6–8]. FDG is not recommended for relapse monitoring and may not be reliable for initial staging and re-staging in patients with peripheral T-cell lymphoma and mantle cell lymphoma [9]. Furthermore, FDG-PET may not be definitive for interim response assessment in patients with HL and DLBCL, and detection of potential transformation sites. Therefore, development of new radiotracers with higher sensitivity, specificity, and different uptake mechanism is in great demand in the management of lymphoma.

This paper first reviews the clinically used non-FDG radiopharmaceuticals for PET and SPECT imaging, respectively (Table 1), and discusses their advantages and limitations in staging, treatment monitoring, and relapse surveillance in lymphoma patients. The discussion also covers the current available radiopharmaceuticals for radioimmunotherapy (Table 2), which is another important option for lymphoma treatment and management. Lastly, a number of novel radiotracers that are currently under preclinical investigations have been focused on.

2. Non-FDG Radiopharmaceuticals Used in Clinic

2.1. Non-FDG Radiopharmaceuticals for PET

2.1.1. ¹⁸F-Fluorothymidine (FLT). ¹⁸F-fluorothymidine (FLT), a derivative of the cytostatic drug zidovudine, was developed as a proliferation imaging tracer in 1998 [10]. FLT is entrapped into cells during their S-phase, and its uptake correlates with the thymidine kinase-1 (TK-1) activity, which is a key enzyme for DNA synthesis and cellular growth [11]. FLT uptake in tumor cells is directly correlated with the proliferation marker Ki67 [12]. Buck et al. demonstrated that FLT could accurately discriminate between indolent and aggressive lymphoma in 34 patients with a cutoff SUV value of 3, and FLT uptake was significantly correlated with Ki67 immunohistochemical staining in biopsied tissues [6]. This important finding showed that FLT-PET might be superior to FDG-PET in lymphoma grading because the cutoff SUV for aggressive lymphoma using FDG is >13, and that for indolent lymphoma is <6, and about 45% of the patients remain in a grey zone [13]. More recently, Herrmann et al. conducted a pilot study using FLT-PET in Mantle cell lymphoma patients and showed a strong positive correlation between proliferation assessed

with Ki67 staining or MIPI-Ki67 (a combined clinical and biologic score) and FLT uptake [14].

In addition, FLT-PET is considered as a promising sensitive tool for predicting response to treatment and survival in lymphoma patients. Although FDG-PET can identify patients who have an excellent prognosis after standard treatment, it has failed to accurately identify patients who would benefit from alternative treatment strategies or who should be included into clinical trials because of a dismal outcome with R-CHOP-like therapy [15]. In 2011, Herrmann et al. reported the largest clinical trial of FLT-PET in lymphoma patients and found FLT uptake as a negative predictor of response to R-CHOP treatment in 66 DLBCL patients. In this study, they also showed that FLT uptake was significantly correlated with the International Prognostic Index, which is a frequently used clinical tool to aid in predicting the prognosis of patients with aggressive NHL [16].

In respect to treatment monitoring and evaluation, FLT appears to be more accurate and specific than FDG, particularly in the setting of interim PET analyses. This is possibly because FDG uptake often occurs in chemo/radiation therapy-mediated inflammatory lesions besides neoplastic tissues, both of which demand more glucose uptake than other normal tissues. Herrmann et al. evaluated FLT-PET for assessing early response of high-grade NHL to rituximab immunotherapy combined with CHOP chemotherapy or CHOP alone and found that successful R-CHOP/CHOP treatment was associated with a decrease in FLT uptake even 2 days after administration of R-CHOP, whereas no reduction of FLT uptake after rituximab treatment alone, indicating no early antiproliferative effect of immunotherapy using rituximab [17]. Moreover, a significant difference in tumorous FLT uptake between patients in partial response and complete response was observed in the 14 patients receiving a PET scan early after chemotherapy completion ($n = 8$, 2 days after R-CHOP; $n = 6$, 7 days after R-CHOP/CHOP) [17].

2.1.2. ¹¹C-Methionine (MET). ¹¹C-methionine (MET) is the most commonly used radiolabelled amino acid for lymphoma imaging. Methionine is essential for protein synthesis and conversion to the predominant biologic methyl group donor S-adenosylmethionine, and it involves polyamine synthesis and transsulfuration pathway [18]. MET accumulates strongly in most lymphomas, and it has low uptake in macrophages and nonneoplastic cells. MET uptake reflects increased amino acid uptake and protein synthesis and is positively related to cellular proliferation activity. Previously, Nuutinen et al. investigated whether MET uptake was associated with the histological grade of malignancy and survival in NHL and HL patients with newly diagnosed or recurrent lymphoma, and demonstrated that it was able to differentiate the high grade lymphomas from the low grade histotypes if using influx constant K_i instead of the traditional SUV calculation. In addition, they found that it was not feasible to use MET-PET for prediction of patient survival [19].

MET is preferable to FDG in some situations where FDG is inaccurate, for example, in hyperglycaemic patients [20]. Leskinen-Kallio et al. demonstrated that MET was superior to

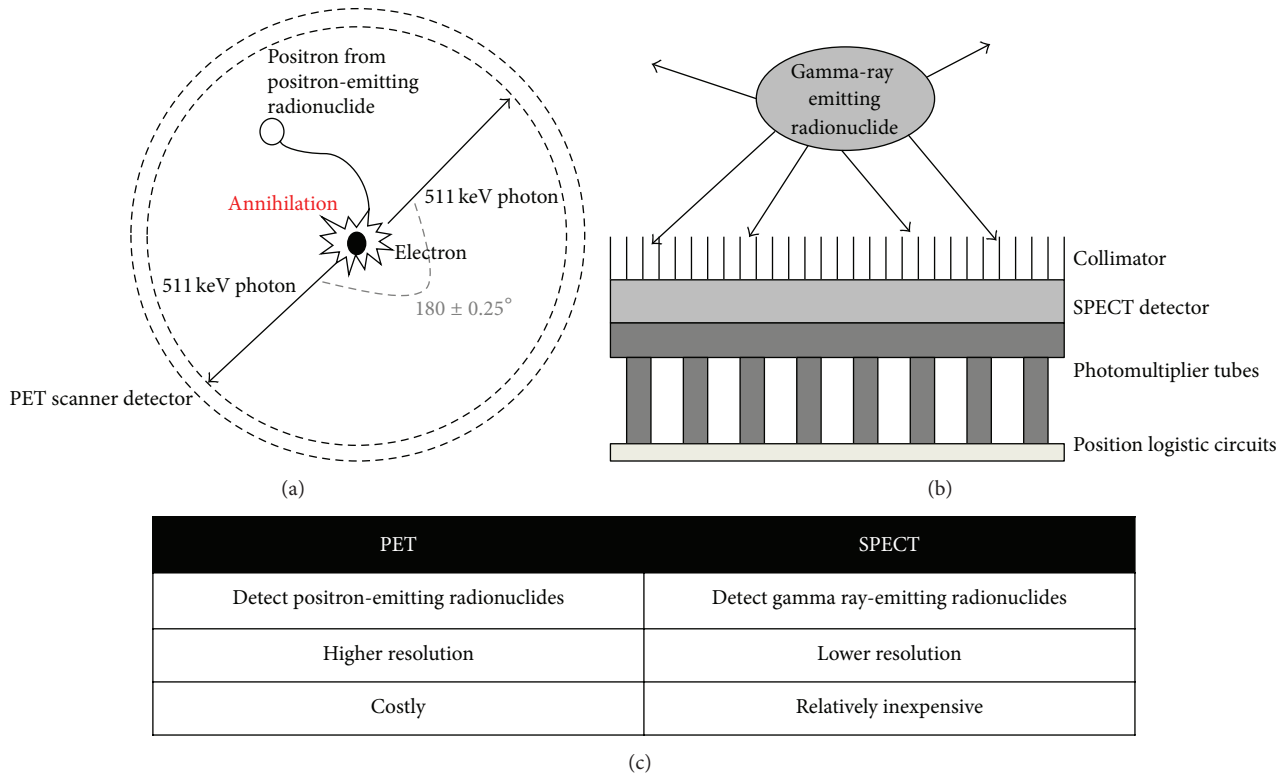


FIGURE 1: Comparison of positron emission tomography (PET) and single-photon emission computed tomography (SPECT). (a) Schematic representation of the principle behind PET, (b) schematic representation of the principle behind SPECT, and (c) comparison between PET and SPECT.

TABLE 1: The clinically used radiopharmaceuticals for positron emission tomography (PET) and single-photon emission computed tomography (SPECT) imaging.

Modality	Radiopharmaceutical	Radionuclide	Half-life	Source	Uptake mechanism
PET	[¹⁸ F]Fluorodeoxyglucose	¹⁸ F	109 min	Cyclotron	Glucose transporter
	3'-Deoxy-3'-[¹⁸ F]fluorothymidine	¹⁸ F	109 min	Cyclotron	DNA replication
	¹¹ C-methionine	¹¹ C	20.4 min	Cyclotron	Amino acid transporter
SPECT	⁶⁷ Ga-citrate	⁶⁷ Ga	78.3 hr	Cyclotron	Transferrin receptor
	Thallium-201	²⁰¹ Tl	73.0 hr	Cyclotron	Multiple factors (i.e., Na-K-ATPase, non-energy-dependent cotransporter, etc.)
	^{99m} Tc-sestamibi	^{99m} Tc	6.0 hr	Generator	P-glycoprotein
	^{99m} Tc-tetrofosmin	^{99m} Tc	6.0 hr	Generator	P-glycoprotein
	¹¹¹ In-labeled Octreotide	¹¹¹ In	67.4 hr	Cyclotron	Somatostatin receptor

TABLE 2: The current available radiopharmaceuticals for radioimmunotherapy of lymphoma.

	⁹⁰ Y-Zevalin	¹³¹ I-Bexxar	¹³¹ I-Rituximab
Radioisotope	⁹⁰ Y ($t_{1/2} = 2.67$ days)	¹³¹ I ($t_{1/2} = 8.01$ days)	¹³¹ I ($t_{1/2} = 8.01$ days)
Anti-CD20 antibody	Ibritumomab tiuxetan	Tositumomab	Rituximab
Antibody type	Monoclonal murine	Monoclonal murine	Monoclonal chimeric
Predose injection	Unlabeled rituximab	Unlabeled tositumomab	Unlabeled rituximab
Pretherapy imaging	Yes (for biodistribution)	Yes (for dosimetry)	Yes (for dosimetry)
Pretherapy dose	¹¹¹ In-Zevalin (5 mCi)	¹³¹ I-Bexxar (5 mCi)	¹³¹ I-Rituximab (5 mCi)
Treatment dose	0.4 mCi/kg (up to 32 mCi)	75 cGy (whole body)	75 cGy (whole body)

FDG in detecting intermediate- and low-grade lymphomas, and MET could accumulate strongly in all except one of the neoplastic lesions from 14 NHL patients [18].

The central nervous system (CNS) generally has high glucose consumption, which leads to high FDG uptake in the normal neuronal tissues and thus renders low contrast from tumors to normal tissues in the CNS. And yet, MET has demonstrated its effectiveness in detecting CNS lymphoma, which represents 6% of all intracranial neoplasms and 1% of all lymphomas [21–23]. In comparison to FDG, MET has lower uptake in normal brain, hence, has better contrast in visualizing tumor lesions. Ogawa et al. first performed MET-PET in 10 patients with histologically verified CNS lymphoma before and after radiation therapy [23]. They found that all tumors could clearly be defined by MET before treatment, and the uptake decreased markedly after radiation therapy. In addition, MET-PET could even demonstrate the residual tumor that was difficult to be detected on CT and MRI because of the influence of radiation therapy and surgical treatment. Kawase et al. showed that both MET and FDG could detect primary CNS lymphoma with 100% sensitivity in 13 immunocompetent patients [21]. However, Kawai et al. obtained a somehow contrary conclusion and pointed out that MET and FDG were both only useful in detecting the lesions with typical MRI findings, but not in the lesions with atypical MRI presentations such as disseminated, ring-like enhanced, or nonenhancing lesions [22].

2.2. Non-FDG Radiopharmaceuticals for SPECT

2.2.1. ^{67}Ga -Citrate. Among the single photon-emitting radiotracers, ^{67}Ga -citrate has been considered a cornerstone in the evaluation of lymphoma for decades. ^{67}Ga accumulates in viable lymphoma cells by binding to transferrin receptors, but typically, it is not taken up by fibrotic tissues. Although ^{67}Ga imaging has been widely used in investigating treatment response, survival prediction, and diagnosis of recurrence after treatment [24], it has several limitations: (1) low spatial resolution, (2) low sensitivity for detection of hepatic and/or splenic lymphoma involvement due to the physiological uptake in these organs, and (3) low accumulation in low-grade lymphoma [25].

Many research groups have compared the performance of FDG-PET with ^{67}Ga scintigraphy in lymphoma imaging. Their findings collectively suggested that FDG-PET is superior to ^{67}Ga scintigraphy in pretreatment staging in both HL and NHL patients and can detect extra sites, especially the small regions of disease activity [26–28]. In addition, FDG-PET appears to be more sensitive in the followup of patients with de novo HL [27]. Fusion imaging with ^{67}Ga -SPECT and CT is of significance in improving diagnosis by allowing precise localization of radiopharmaceutical uptake and detection of lesions not demonstrated by CT. In 2005, Palumbo et al. for the first time demonstrated that ^{67}Ga -citrate performance could be improved by using SPECT/CT fusion imaging, suggesting that this modality could represent an alternative to PET [29]. They found that hybrid imaging provided additional data in 54.2% patients, thus leading

oncologists to reconsider the therapeutic approach in 33.2% patients. Moreover, 9 more lesions below the diaphragm were detected by SPECT/CT as compared with SPECT alone. This is of particular interest because one limitation of ^{67}Ga scintigraphy is its restricted ability to identify subdiaphragmatic disease. However, the limitation of this study was that the authors only compared the results with SPECT alone but did not compare with FDG-PET. Further studies of comparison between FDG-PET or FDG-PET/CT and ^{67}Ga -SPECT/CT would be of significant clinic interest.

2.2.2. Thallium-201 (^{201}Tl). Thallium-201 (^{201}Tl) behaves biologically like potassium. Its tumor uptake is related to multiple factors such as blood flow, tumor type, tumor viability, vascular immaturity, increased cell membrane permeability, and activity of sodium-potassium adenosinetriphosphatase (Na-K-ATPase), non-energy-dependent cotransporter, and calcium ion channel [30]. Ando et al. demonstrated that ^{201}Tl mainly accumulated in viable tumor tissues, less so in connective tissues, and barely in necrotic tumor tissues and inflammatory sites [31].

^{201}Tl scintigraphy is valuable in evaluating chemo/radiotherapy treatment response because the activity of Na-K-ATPase in tumor cells decreases after treatment, and thus less ^{201}Tl uptake should be observed. Haas et al. evaluated the usage of ^{201}Tl in staging and monitoring treatment response after radiotherapy in FL patients [32]. They concluded that although ^{201}Tl had limited value in staging FL patients, it was accurate in monitoring the responses of radiation treatment. If an FL patient with a positive ^{201}Tl at diagnosis is treated by radiation, the treatment response can be reliably ascertained by ^{201}Tl scintigraphy alone.

In comparison to ^{67}Ga scintigraphy which is highly sensitive in high-grade lymphoma detection, ^{201}Tl is more frequently utilized in imaging low-grade lymphomas [33]. In addition, ^{201}Tl scintigraphy is more convenient than ^{67}Ga scintigraphy because it can be performed immediately after injection. The optimal time of ^{201}Tl scintigraphy is 3–4 hours after injection whereas that of ^{67}Ga scintigraphy is 2 days due to the longer half-life of ^{67}Ga [34]. For practical purposes, nevertheless, ^{67}Ga and ^{201}Tl scintigraphy should complement one another in the follow-up of indolent lymphoma. For instance, if a patient who used to be negative on ^{67}Ga scintigraphy and positive on ^{201}Tl converts to a positive status on ^{67}Ga , it is likely that the indolent tumor has transformed to an aggressive pattern.

Furthermore, ^{201}Tl brain SPECT has been successfully applied for differentiating CNS lymphoma from toxoplasmosis in patients with AIDS [35–37]. Lorberboym et al. demonstrated that the retention index of ^{201}Tl in patients with lymphomas was significantly higher than that in patients with adenocarcinoma or nonmalignant lesions [36]. Moreover, Skiest et al. found that diagnostic accuracy of focal CNS lesions in patients with AIDS could be significantly improved with combining ^{201}Tl brain SPECT with serum toxoplasma IgG [37].

2.2.3. ^{99m}Tc -Sestamibi and ^{99m}Tc -Tetrofosmin. ^{99m}Tc -sestamibi and ^{99m}Tc -tetrofosmin, which were originally developed as myocardial perfusion agents, have been frequently used as predictors of chemotherapeutic response in lymphoma patients [38]. These agents preferentially accumulate in the mitochondria of malignant cells due to the higher metabolic rate, and thus the higher transmembrane electrical potentials generated across the membrane bilayers in these cells when compared with normal cells (Figure 2). These two small lipophilic monovalent cations are both transport substrates for the intraextracellular efflux pump of the transmembrane P-glycoprotein (Pgp). Of note, Pgp is encoded by the multidrug-resistance gene (*MDRI*) that is overexpressed in some drug resistant lymphoma cells [39, 40]. The net cellular accumulation of ^{99m}Tc -sestamibi has been shown to be inversely proportional to the level of Pgp expression *in vitro* [41, 42]. Therefore, the uptake, washout rate, and retention of ^{99m}Tc -sestamibi and ^{99m}Tc -tetrofosmin can aid in identification of drug resistance and provide prognostic information [43]. In other words, the patients with negative or decreased radiotracer activity tend to have unfavorable response to chemotherapy compared to those with prominent radiotracer accumulation irrespective of lymphoma types. For instance, Song et al. demonstrated that the slow tumor clearance of ^{99m}Tc -sestamibi could predict a good response to chemotherapy, and difference in ^{99m}Tc -sestamibi clearance distinguishes responding and nonresponding tumors in the early course of chemotherapy in diffuse large B-cell and peripheral T-cell lymphoma patients [44]. Kao et al. found that patients with a good chemotherapy response had positive ^{99m}Tc -sestamibi results and negative Pgp and MRP (multidrug resistance associated protein) expression before treatment, while patients with a poor response had negative ^{99m}Tc -sestamibi results and positive Pgp and MRP expression [45]. Liang et al. concluded that ^{99m}Tc -tetrofosmin uptake, in inverse correlation with Pgp or MRP expression levels, could accurately predict chemotherapy response in 25 lymphoma patients [46].

In another study, Lazarowski et al. demonstrated that the patients with low grade lymphoma had the strongest correlation between ^{99m}Tc -sestamibi uptake and chemosensitivity, while patients with HL had an indefinable correlation [47]. In addition, the later scan (180 min after injection) could provide more accurate prediction of chemoresistance than early scan (30 min after injection) [47]. In general, factors related to ^{99m}Tc -sestamibi and ^{99m}Tc -tetrofosmin uptake in tumors are blood flow, tissue viability, vascular permeability, tumor necrosis, metabolic demand, tumor mitochondrial activity, and Pgp and/or MRP expression in tumor tissues [44].

When comparing these two radiotracers, ^{99m}Tc -tetrofosmin can be easily labeled with ^{99m}Tc at room temperature without heating; hence, it is more convenient than ^{99m}Tc -sestamibi in clinical practice [48]. Although ^{99m}Tc -tetrofosmin has lower uptake in lymphoma cell lines [49], it undergoes more rapid clearance from the plasma and background structures when compared to ^{99m}Tc -sestamibi. Current clinical investigations have demonstrated that both

radiotracers are competent for prediction of chemotherapy response; however, no study has ever compared these two radiotracers to each other in lymphoma patients. The optimal imaging time-point for both tracers is 3-4 hours after injection. It should be noted that these radiotracers are not ideal in investigating the infradiaphragmatic regions because both radiotracers are eliminated by the biliary-intestinal route [50].

2.2.4. Somatostatin Receptor Scintigraphy. Somatostatin receptor scintigraphy (SRS) using ^{111}In -labeled octreotide has been frequently applied in neuroendocrine tumor imaging. It has also been successfully used in detecting somatostatin receptor-expressing lymphomas such as mucosa associated lymphoid tissue- (MALT-) type lymphoma. Octreotide is a synthetic somatostatin analogue that is available as Octreoscan (Mallinckrodt Inc., MO), in which the gamma-emitting radioisotope ^{111}In has been chelated with octreotide via chelator DTPA. The overall sensitivity of SRS with Octreoscan for HL is 95%-100%, and for NHL is around 80% [51]. Nevertheless, the sensitivity is decreased in detection of abdominal lesions, and the specificity of this technique is relatively low due to the variable expression of specific somatostatin receptor subtypes in lymphomas. For instance, Valencak et al. did not recommend the use of SRS for routine staging of primary cutaneous T-cell and B-cell lymphoma with Octreoscan based on the unfavorable outcome of a study involving 22 patients. In this study, only 4 out of 15 patients with cutaneous T-cell lymphoma and 3 out of 7 patients with B-cell lymphoma could be detected by Octreoscan [52].

Although SRS with Octreoscan does not seem to have a significant impact on patients with lymphomas for diagnostic purposes, it appears to be an excellent tool for staging and noninvasive therapy-monitoring in extragastric MALT-type lymphomas. In a study of 30 patients with extragastric manifestations of MALT-type lymphoma, Raderer et al. found that Octreoscan is superior to conventional imaging techniques in terms of noninvasive evaluation of treatment efficacy [53]. In addition, it allows distinction between gastric versus extragastric origin of the MALT-type lymphoma in patients with lesions located outside the GI tract. While no positive scans were obtained in patients with gastric MALT-type lymphomas irrespective of size and stage, excellent visualization of lymphomas originating in extragastric sites could be achieved using Octreoscan [54]. Furthermore, it was suggested that Octreoscan may identify patients suitable for therapy with labeled or unlabeled somatostatin analogues; however, no clinical studies have yet supported this idea. In another study, Li et al. compared ^{67}Ga scintigraphy results with those obtained by ^{111}In -DOTA-D¹Phe¹-Tyr³-octreotide and ^{111}In -DOTA-lanreotide scintigraphy, which were two octreotide analogues, in 18 patients with proven MALT-type lymphoma [55]. Although there were no statistically significant differences in patient- and site-related sensitivities among three radiotracers, the sensitivity of ^{111}In -labeled compounds tended to be superior to that of ^{67}Ga scintigraphy

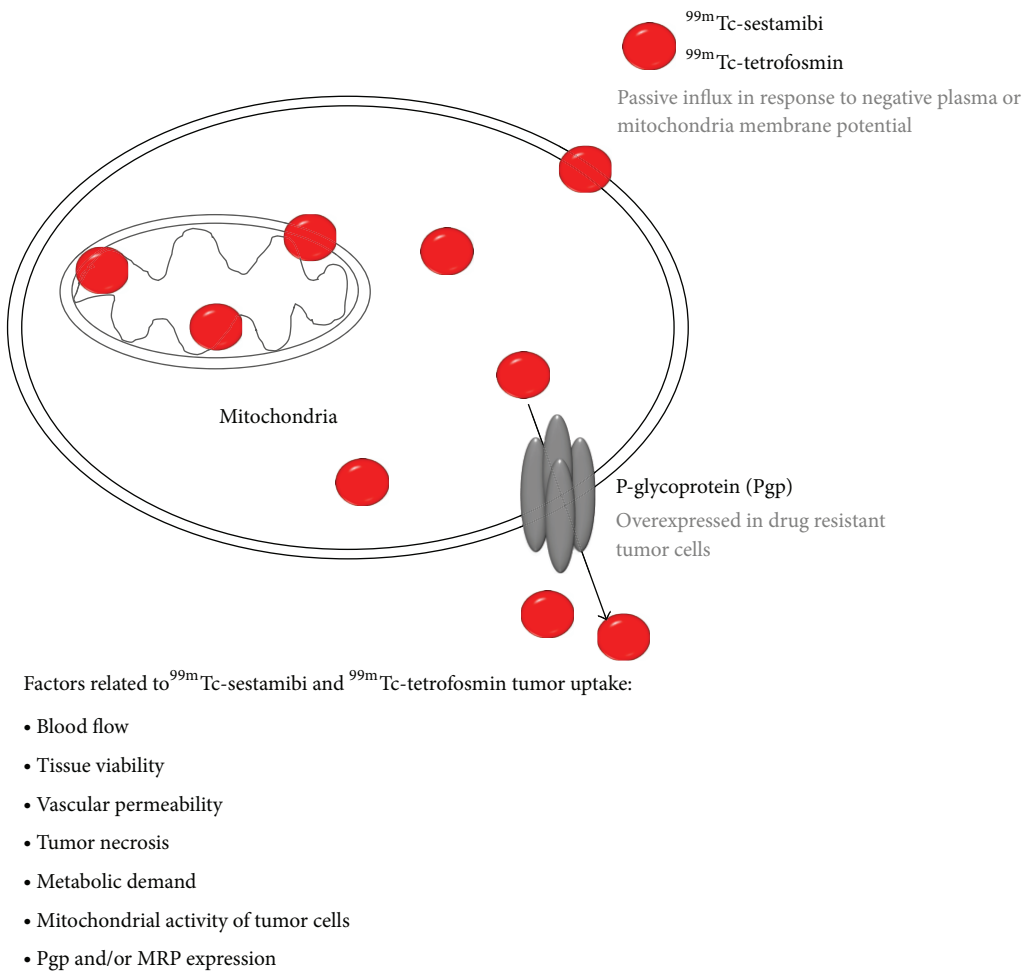


FIGURE 2: The uptake and efflux of ^{99m}Tc -sestamibi and ^{99m}Tc -tetrofosmin in tumor cells.

for infradiaphragmatic involvement but inferior for supradiaphragmatic lesions.

3. Radiopharmaceuticals for Radioimmunotherapy Management

Low-grade lymphomas are refractory to most treatments, and each subsequent treatment is less effective. Radioimmunotherapy with a tumor-specific antibody conjugated to a beta-emitting radioisotope will deliver radiation not only to tumor cells that bind to the antibody, but also, due to a cross-fire effect, to neighboring tumor cells that are inaccessible to the antibody or with insufficient target-antigen expression. At present, the most successful radioimmunotherapy agents for lymphomas are radiolabeled anti-CD20 monoclonal antibodies such as ^{90}Y -labeled Zevalin (Ibritumomab Tiuxetan) and ^{131}I -labeled Bexxar (Tositumomab) [56]. CD20 is a transmembrane protein that acts as a calcium channel and plays an important role in cell cycle progression and differentiation of normal and malignant B-cells. CD20 is present in the lymphoma cells in more than 90% patients with B-cell NHL, and it is not expressed on uncommitted hematopoietic

precursor stem cells. When anti-CD20 antibodies bind to the antigen, they induce apoptosis, antibody-dependent cellular cytotoxicity, and complement-dependent cytotoxicity in lymphoma cells [57]. Therefore, CD20 is a suitable target for imaging and treatment of NHL. Clinical practices have indicated that radioimmunotherapy using Zevalin and Bexxar is an effective and safe adjunctive treatment for patients with NHL refractory/relapsed to conventional treatment [56–61]. Next we introduce three radiolabeled anti-CD20 antibodies: Zevalin, Bexxar, and ^{131}I -rituximab. Zevalin and Bexxar have been approved by FDA while ^{131}I -rituximab is still under clinical trial.

3.1. Radiolabeled Zevalin. Zevalin (Ibritumomab Tiuxetan) is a murine IgG_{1a} kappa monoclonal antibody that binds specifically to the CD20 antigen on normal and malignant B-lymphocytes [62]. It is the first radioimmunoconjugate approved by US FDA in 2002 and Europe in 2004 for radioimmunodiagnosis (^{111}In -Zevalin) or radioimmunotherapy (^{90}Y -Zevalin) in patients with follicular NHL refractory to rituximab. By using the chelator Tiuxetan (MX-DTPA), ^{111}In (gamma emitter; $t_{1/2} = 67.2$ hrs) and ^{90}Y

(pure beta emitter; $t_{1/2} = 64$ hrs) can be stably linked to Ibritumomab for imaging and treatment, respectively. In fact, ^{111}In -Zevalin scan is required for ^{90}Y -Zevalin therapy by US FDA to measure organ-specific accumulation and determine whether pretreatment dosimetry is necessary. In the FDA approved protocol, 250 mg/m² unlabeled rituximab is given to the patient 48–72 hrs prior to performing the ^{111}In -Zevalin scan (5 mCi/1.6 mg) in order to minimize uptake of ^{111}In -Zevalin in normal tissues and blood mononuclear cells [63]. The patients with relapsed low-grade, follicular, or transformed B-cell NHL can be treated in an outpatient setting with a reported response rate of 74% with no significant adverse side effects. Interestingly, Iagaru et al. observed an inverse correlation between the extent of disease visible on ^{111}In -Zevalin scans and the response to ^{90}Y -Zevalin in 28 NHL patients, with a higher rate of complete response observed to ^{90}Y -Zevalin in patients with negative ^{111}In -Zevalin findings and a higher rate of disease progression noted despite therapy in patients with positive ^{111}In -Zevalin findings [64]. However, these findings need to be confirmed in a larger prospective trial. In addition to the aforementioned NHLs, Iwamoto et al. demonstrated the feasibility of $^{111}\text{In}/^{90}\text{Y}$ -Zevalin in treatment management in 6 patients with primary CNS lymphoma in a pilot study [65]. They showed that ^{111}In -Zevalin could penetrate into CNS lymphoma at higher levels than into normal brain; however, ^{90}Y -Zevalin administration with a 33% response rate did not represent an ideal treatment to patients.

As described previously, ^{111}In -Zevalin is required for radioimmunodiagnosis in the United States, but not most of the European countries. In the recent paper by Otte, he discussed and listed the reasons for not requiring ^{111}In -Zevalin before radioimmunotherapy as follows: (1) ^{90}Y -Zevalin dose is only based on patient's body weight and platelet count [66]; (2) the rate of truly altered biodistribution is very rare, with only 6 out of 953 patients (0.6%) according to the report by Conti et al [67]; (3) the correlation between ^{111}In -Zevalin and ^{90}Y -Zevalin distribution is only partly correct because partial disassociation of ^{90}Y and ^{111}In from the immunoconjugate may occur *in vivo*, and the free ^{90}Y deposits on bone surfaces while free ^{111}In preferentially goes to the germ cells of testes [68]; (4) the dosimetry study in clinical trials has shown no correlation between toxicity and the absorbed dose, and all absorbed dosages remained well below the thresholds of 4 Gy for the bone marrow and 20 Gy for other organs [69].

Perk et al. first radiolabeled Zevalin with a PET radioisotope zirconium-89 (^{89}Zr ; $t_{1/2} = 78.4$ hrs) in order to quantify ^{90}Y -Zevalin biodistribution and dosimetry more accurately for high-dose radioimmunotherapy [70]. Because Tiuxetan does not bind to the four-valent ^{89}Zr , the authors introduced N-succinyldesferal (N-sucDf) as a second chelator to Zevalin. Recently, Rizvi et al. reported a pilot study showing that pretherapy PET scan with ^{89}Zr -Zevalin could be used to accurately predict radiation dosimetry for treatment with ^{90}Y -Zevalin in 7 patients with relapsed B-cell NHL scheduled for autologous stem cell transplantation [71]. However, the highest absorbed dose of ^{89}Zr -Zevalin was found in liver, but

not in spleen as that of ^{111}In -Zevalin, suggesting a different biodistribution between two radiotracers [72].

3.2. ^{131}I - Tositumomab (Bexxar). Tositumomab is a murine IgG2a anti-CD20 monoclonal antibody, and its ^{131}I -labeled form has been approved in US in 2003 for the treatment of patients with CD20 positive follicular NHL, with and without transformation, whose disease is refractory to rituximab and has relapsed following chemotherapy [73]. Different from the weight-based dosing ^{90}Y -Zevalin, the gamma photons emitted by ^{131}I allow for applications in planar or SPECT imaging, while the comparatively long half-life (8.01 days) of ^{131}I confers patient-specific calculation of the radioactivity that needs be administered to achieve desired therapeutic effects [74]. In addition, ^{131}I has a tighter distribution of tumor-absorbing doses of radiation for a given tumor site and is predicted to be more efficacious in the treatment of lung nodules, particularly those with radii less than 2 cm, presumably due to the shorter path length of ^{131}I . This finding may be of particular relevance to small tumor foci near normal tissues, if it can be extrapolated beyond lungs [75].

Because ^{131}I -labeled antibody clearance varies significantly among patients, prescription of ^{131}I - Tositumomab (product name Bexxar) activity must be based on a calculated total-body dose derived from quantitative whole-body imaging. Briefly, patients first receive an infusion of unlabeled Tositumomab to optimize the biodistribution and tumor-targeting of Bexxar. After 1 hr, Bexxar (5 mCi) is administered, and patients then undergo dosimetric whole-body imaging on at least three occasions during the following week [76]. This approach is necessary to ensure that a therapeutic dose is delivered and to reduce the risk of treatment-related toxicity. Once the minimum required activity being calculated, patient receives a second infusion of unlabeled Tositumomab, followed by the therapeutic radiolabeled Bexxar, usually 1-2 weeks after the dosimetric study [77]. The maximum tolerated total body dose has been established at 75 cGy in patients with adequate bone marrow reserves and less than 25% bone marrow involvement by lymphoma, 65 cGy in patients with mild thrombocytopenia, and 45 cGy in patients who have received stem cell transplantation [77]. The optimal time to initially assess the response after Bexxar therapy remains unclear so far. And yet, Jacene et al. found that a response at 12 weeks after treatment correlated with long-term survival, and therefore they proposed this time point for initial treatment evaluation [74].

Iagaru et al. compared Bexxar with ^{90}Y -Zevalin in the management of 67 patients with low-grade refractory or relapsed NHL [78]. Both treatments provided an effective and safe adjunctive therapeutic regimen for the patients; however, ^{90}Y -Zevalin appeared to be more effective than Bexxar in terms of objective, complete, and partial responses, but with a higher frequency of adverse effects. Nevertheless, no statistical significance was obtained from this retrospective study due to small number of patients. Jacene et al. performed a similar study and concluded that both drugs were well tolerated, but Bexxar caused significantly less severe declines

in platelet counts and therefore may be a more appropriate choice for patients with limited bone marrow reserve [74].

3.3. ^{131}I -Rituximab. Rituximab is a chimeric IgG1 kappa anti-CD20 antibody that mediates complement- and antibody-dependent cytotoxicity *in vitro*. In fact, the introduction of rituximab has truly revolutionized the management of patients with B-cell NHL [79]. In addition to serving as a single agent as standard therapy for relapsed or refractory indolent NHL, rituximab has also been used in combination with CHOP chemotherapy (cyclophosphamide, doxorubicin, vincristine, and prednisone) in treatment of both indolent and aggressive NHLs.

Similar to Bexxar, rituximab can be radiolabeled with ^{131}I through a relatively simple mAb radioiodination procedure without the requirement of chelators. ^{131}I -rituximab, however, has a higher whole body radiation dose as well as mean biological and effective whole body half-life compared with Bexxar (85 hrs versus 56 hrs) [80–82]. In a physician-sponsored Phase II trial, Turner et al. found that ^{131}I -rituximab was effective with an objective response rate (ORR) of 71% in 35 patients with a median followup of 14 months. Completed remission (CR) was achieved in 54% of the patients with median duration of 20 months. These results were similar to those of Bexxar (ORR: 71%, CR: 34%, median progression free survival: 12 months for all responders and 20 months for CR patients) [76]. In another pilot study in 7 mantle cell lymphoma patients who had relapsed after high-dose chemotherapy with autologous stem cell transplantation, Behr et al. performed the treatment with myeloablative doses of 261–495 mCi of ^{131}I -rituximab and found that this high-dose therapy appeared to be associated with a high response rate. However, 5 of 7 patients developed hypothyroidism in this trial despite thyroid blocking, suggesting the moderate toxicity of myeloablative dose of ^{131}I -rituximab [59]. Leahy and Turner reported the largest-to-date single-center routine clinical study with 142 consecutive patients who received ^{131}I -rituximab radioimmunotherapy for low-grade, predominantly follicular, relapsed NHL in 10 years. Toxicity was limited to hematologic grade 4 neutropenia, the ORR was 67%, CR was 50%, and overall median survival was 32 months [61]. Taken together, the current data with nonmyeloablative and myeloablative treatment using ^{131}I -rituximab clearly suggest that ^{131}I -rituximab can achieve high ORR and CR rates in relapsed or refractory NHLs, and both the hematologic and nonhematologic toxicities are similar to Bexxar, as long as critical radiation doses of 75 cGy to the total body (for nonmyeloablative) or 2700 cGy to lung (for myeloablative) are not exceeded [83].

4. Non-FDG Radiotracers under Preclinical Development

4.1. $^{124}\text{I}/^{64}\text{Cu}$ -Labeled Anti-CD20 Minibody. The currently available immunoPET tracers are all based on *intact* antibodies, and as a result, days are required for the activity

levels to drop sufficiently to allow acceptable target-to-background ratios [84]. Therefore, redesigning antibodies without compromising their specificity by reducing their size is of high interest from many research groups recently. Olafsen et al. developed ^{124}I -labeled recombinant anti-CD20 rituximab fragment (scFv-C_H3 dimer; 80 kDa) and evaluated it with PET/CT in mice bearing human CD20-expressing lymphoma. They found that this agent termed as radiolabeled “minibody” had exceptional high-contrast PET images with fast blood clearance *in vivo*. The average uptake in CD20-positive tumors was $12.9 \pm 3.4\%$ ID/g, and the ratio of CD20-positive tumor to CD20-negative tumor uptake was 7.0 ± 3.1 at 21 hr, suggesting its high specificity to target CD20. The authors also radiolabeled this minibody with ^{64}Cu using chelator DOTA; however, its tumor uptake was not as good as that of ^{124}I -labeled compound because of the residual activity in CD20-negative tumors and the liver [84].

4.2. ^{18}F -Labeled Isatin Sulfonamide (^{18}F -ICMT-11). The capacity to evade apoptosis has been defined as one of the hallmarks of cancer. Therefore, monitoring tumor cell death induced by anticancer treatment can provide important predictive value in routine patient management or early clinical trials. During apoptosis, the activation of caspases, a family of cysteine proteases, induces the DNA degradation, which is the most noticeable and specific feature of apoptosis. And caspase-3, the central effector caspase, has been identified as an attractive biomarker of apoptosis. Isatin-based isatin 5-sulfonamide (ICMT-11) has been identified as a caspase inhibitor with subnanomolar affinity for caspase-3, high metabolic stability, and moderate lipophilicity [85]. Nguyen et al. radiolabeled ICMT-11 with ^{18}F , and investigated its ability to image the drug-induced tumor apoptotic process in 38C13 murine B-cell lymphoma models. They demonstrated that ^{18}F -ICMT-11 could bind to lymphoma *in vivo* by up to 2-fold at 24 hr posttreatment compared to vehicle treatment, and this increased signal activity was associated with increased apoptosis [86]. Although these preliminary results were very promising, more preclinical studies should be conducted to further warrant the usefulness of this radiotracer in imaging lymphoma.

4.3. Radiolabeled LLP2A Analogues. The integrins play a crucial role in lymphocyte homing and passing through the lymphocyte endothelial wall or to inflammation sites and may contribute to dissemination of NHL. One of its subtypes integrin $\alpha 4\beta 1$, expressed in human hematopoietic cells, regulates lymphocyte trafficking. It is also found widely expressed in leukemia, lymphoma, melanoma, and sarcomas [87]. N-[[4-[[[(2-ethylphenyl) amino]carbonyl] amino]phenyl]acetyl]-N(epsilon)-6-[(2E)-1-oxo-3-(3-pyridinyl-2-propenyl)]-1-lysyl-1-2-aminohexanedioyl-(1-amino-1-cyclohexane)carboxamide (LLP2A) is a high-affinity, high-specificity peptidomimetic ligand that binds the activated $\alpha 4\beta 1$ integrin [88]. Denardo et al. synthesized 7 different ^{111}In - or ^{64}Cu -labeled LLP2A derivatives and investigated their imaging potentials in Raji Burkitt lymphoma model ($\alpha 4\beta 1$ -positive) [88]. In this study, they concluded that the

DOTA-chelated derivative ^{111}In -LLP2A-DOTA exhibited the best tumor-to-nontumor ratios and showed the greatest potential for planar and SPECT imaging targeting the $\alpha 4\beta 1$ in human lymphoma, and its ^{64}Cu -labeled counterpart also demonstrated excellent tumor targeting competency in PET scans at both 4 hr and 24 hr, which warrants further investigations [88]. The same group recently reported two ^{99m}Tc -labeled LLP2A derivatives ^{99m}Tc -LLP2A-HYNIC and ^{99m}Tc -LLP2A-HYNIC-PEG and evaluated their safety and imaging potentials in NHL-bearing dog model. Both tracers showed moderate tumor uptake over background, and tumor uptake in canine B-cell lymphoma decreased after chemotherapy [89].

5. Summary

In this review, we have discussed the clinically used non-FDG radiopharmaceuticals for PET and SPECT imaging of lymphoma, as well as the radiotracers currently under preclinical development. In addition, we have introduced several common radiopharmaceuticals for radioimmunotherapy, which is another crucial component for lymphoma treatment and management. One issue we would like to point out here is that most of the clinically used SPECT radiopharmaceuticals have not been evaluated with the hybrid SPECT/CT system, which can provide higher sensitivity and specificity through a better definition of organs involved in radiotracer uptake and determination of their precise relationship with adjacent structures [90]. Therefore, we suggest that the clinical studies of SPECT-based radiotracers should be validated by SPECT/CT in future. Furthermore, as noted, most of the radiopharmaceuticals we introduce here are designed based on a specific cancer biomarker such as increased DNA synthesis, upregulated amino acid transporter or somatostatin receptor expression, specific CD20 expression in B-cells, and cellular apoptosis. We believe that the advances in molecular biology of lymphoma research can lead to an increased understanding of the cancer biomarkers that contribute to lymphoma progression and thus warrant the development of more personalized and specific lymphoma-targeted imaging agents and treatments.

Conflict of Interests

All authors have no commercial associations that might pose a conflict of interests in connection with the submitted paper.

Acknowledgment

This work was supported in part by sponsored research agreement made by Cell Point L.L.C (MDA LS01-212) and the John S. Dunn Foundation.

References

- [1] National Cancer Institute Surveillance, "E.a.E.R.S.P. SEER stat fact sheets: lymphoma," 2011, <http://seer.cancer.gov/statfacts/html/lymph.html>.
- [2] T. P. Miller, S. Dahlberg, J. R. Cassady et al., "Chemotherapy alone compared with chemotherapy plus radiotherapy for localized intermediate- and high-grade non-Hodgkin's lymphoma," *The New England Journal of Medicine*, vol. 339, no. 1, pp. 21–26, 1998.
- [3] S. J. Horning, R. T. Hoppe, J. Mason et al., "Stanford-Kaiser Permanente G1 study for clinical stage I to IIA Hodgkin's disease: subtotal lymphoid irradiation versus vinblastine, methotrexate, and bleomycin chemotherapy and regional irradiation," *Journal of Clinical Oncology*, vol. 15, no. 5, pp. 1736–1744, 1997.
- [4] M. A. Vermoolen, M. J. Kersten, R. Fijnheer, M. S. van Leeuwen, T. C. Kwee, and R. A. J. Nivelstein, "Magnetic resonance imaging of malignant lymphoma," *Expert Review of Hematology*, vol. 4, no. 2, pp. 161–171, 2011.
- [5] S. M. Ansell and J. O. Armitage, "Positron emission tomographic scans in lymphoma: convention and controversy," *Mayo Clinic Proceedings*, vol. 87, no. 6, pp. 571–580, 2012.
- [6] A. K. Buck, M. Bommer, S. Stilgenbauer et al., "Molecular imaging of proliferation in malignant lymphoma," *Cancer Research*, vol. 66, no. 22, pp. 11055–11061, 2006.
- [7] J. J. Cerci, E. Trindade, V. Buccheri et al., "Consistency of FDG-PET accuracy and cost-effectiveness in initial staging of patients with hodgkin lymphoma across jurisdictions," *Clinical Lymphoma, Myeloma and Leukemia*, vol. 11, no. 4, pp. 314–320, 2011.
- [8] L. Zanoni, J. J. Cerci, and S. Fanti, "Use of PET/CT to evaluate response to therapy in lymphoma," *Quarterly Journal of Nuclear Medicine and Molecular Imaging*, vol. 55, no. 6, pp. 633–647, 2011.
- [9] C. Burton, P. Ell, and D. Linch, "The role of PET imaging in lymphoma," *The British Journal of Haematology*, vol. 126, no. 6, pp. 772–784, 2004.
- [10] A. F. Shields, J. R. Grierson, B. M. Dohmen et al., "Imaging proliferation *in vivo* with [^{18}F]FLT and positron emission tomography," *Nature Medicine*, vol. 4, no. 11, pp. 1334–1336, 1998.
- [11] H. Barthel, M. Perumal, J. Latigo et al., "The uptake of 3'-deoxy-3'-[^{18}F]fluorothymidine into L5178Y tumours *in vivo* is dependent on thymidine kinase 1 protein levels," *The European Journal of Nuclear Medicine and Molecular Imaging*, vol. 32, no. 3, pp. 257–263, 2005.
- [12] J. Yue, L. Chen, A. R. Cabrera et al., "Measuring tumor cell proliferation with ^{18}F -ftl pet during radiotherapy of esophageal squamous cell carcinoma: a pilot clinical study," *Journal of Nuclear Medicine*, vol. 51, no. 4, pp. 528–534, 2010.
- [13] H. Schöder, A. Noy, M. Gönen et al., "Intensity of ^{18}F fluorodeoxyglucose uptake in positron emission tomography distinguishes between indolent and aggressive non-Hodgkin's lymphoma," *Journal of Clinical Oncology*, vol. 23, no. 21, pp. 4643–4651, 2005.
- [14] K. Herrmann, A. K. Buck, T. Schuster et al., "A pilot study to evaluate 3'-deoxy-3'- ^{18}F - fluorothymidine PET for initial and early response imaging in mantle cell lymphoma," *Journal of Nuclear Medicine*, vol. 52, no. 12, pp. 1898–1902, 2011.
- [15] C. H. Moskowitz, H. Schöder, J. Teruya-Feldstein et al., "Risk-adapted dose-dense immunochemotherapy determined by interim FDG-PET in advanced-stage diffuse large B-cell lymphoma," *Journal of Clinical Oncology*, vol. 28, no. 11, pp. 1896–1903, 2010.
- [16] K. Herrmann, A. K. Buck, T. Schuster et al., "Predictive value of initial ^{18}F -FLT uptake in patients with aggressive non-hodgkin lymphoma receiving R-CHOP treatment," *Journal of Nuclear Medicine*, vol. 52, no. 5, pp. 690–696, 2011.

- [17] K. Herrmann, H. A. Wieder, A. K. Buck et al., "Early response assessment using 3'-deoxy-3'-[¹⁸F]fluorothymidine positron emission tomography in high-grade non-Hodgkin's lymphoma," *Clinical Cancer Research*, vol. 13, no. 12, pp. 3552–3558, 2007.
- [18] S. Leskinen-Kallio, U. Ruotsalainen, K. Nagren, M. Teras, and H. Joensuu, "Uptake of carbon-11-methionine and fluorodeoxyglucose in non-Hodgkin's lymphoma: a PET study," *Journal of Nuclear Medicine*, vol. 32, no. 6, pp. 1211–1218, 1991.
- [19] J. Nuutinen, S. Leskinen, P. Lindholm et al., "Use of carbon-11 methionine positron emission tomography to assess malignancy grade and predict survival in patients with lymphomas," *The European Journal of Nuclear Medicine*, vol. 25, no. 7, pp. 729–735, 1998.
- [20] E. Sutinen, S. Jyrkkiö, M. Varpula et al., "Nodal staging of lymphoma with whole-body PET: comparison of [¹¹C]methionine and FDG," *Journal of Nuclear Medicine*, vol. 41, no. 12, pp. 1980–1988, 2000.
- [21] Y. Kawase, Y. Yamamoto, R. Kameyama, N. Kawai, N. Kudomi, and Y. Nishiyama, "Comparison of ¹¹C-methionine PET and ¹⁸F-FDG PET in patients with primary central nervous system lymphoma," *Molecular Imaging and Biology*, vol. 13, no. 6, pp. 1284–1289, 2011.
- [22] N. Kawai, S. Okubo, K. Miyake et al., "Use of PET in the diagnosis of primary CNS lymphoma in patients with atypical MR findings," *Annals of Nuclear Medicine*, vol. 24, no. 5, pp. 335–343, 2010.
- [23] T. Ogawa, I. Kanno, J. Hatazawa et al., "Methionine PET for follow-up of radiation therapy of primary lymphoma of the brain," *Radiographics*, vol. 14, no. 1, pp. 101–110, 1994.
- [24] D. Front and O. Israel, "Present state and future role of gallium-67 scintigraphy in lymphoma," *Journal of Nuclear Medicine*, vol. 37, no. 3, pp. 530–532, 1996.
- [25] L. Kostakoglu and S. J. Goldsmith, "Fluorine-18 fluorodeoxyglucose positron emission tomography in the staging and follow-up of lymphoma: is it time to shift gears?" *The European Journal of Nuclear Medicine*, vol. 27, no. 10, pp. 1564–1578, 2000.
- [26] P. Lin, J. Chu, A. Kneebone et al., "Direct comparison of ¹⁸F-fluorodeoxyglucose coincidence gamma camera tomography with gallium scanning for the staging of lymphoma," *Internal Medicine Journal*, vol. 35, no. 2, pp. 91–96, 2005.
- [27] J. W. Friedberg, A. Fischman, D. Neuberg et al., "FDG-PET is superior to gallium scintigraphy in staging and more sensitive in the follow-up of patients with de novo Hodgkin lymphoma: a blinded comparison," *Leukemia and Lymphoma*, vol. 45, no. 1, pp. 85–92, 2004.
- [28] S. S. Foo, P. L. Mitchell, S. U. Berlangieri, C. L. Smith, and A. M. Scott, "Positron emission tomography scanning in the assessment of patients with lymphoma," *Internal Medicine Journal*, vol. 34, no. 7, pp. 388–397, 2004.
- [29] B. Palumbo, S. Sivolella, I. Palumbo, A. M. Liberati, and R. Palumbo, "67Ga-SPECT/CT with a hybrid system in the clinical management of lymphoma," *The European Journal of Nuclear Medicine and Molecular Imaging*, vol. 32, no. 9, pp. 1011–1017, 2005.
- [30] J. Lin, W. T. Leung, S. K. W. Ho et al., "Quantitative evaluation of thallium-201 uptake in predicting chemotherapeutic response of osteosarcoma," *The European Journal of Nuclear Medicine*, vol. 22, no. 6, pp. 553–555, 1995.
- [31] A. Ando, I. Ando, and M. Katayama, "Biodistributions of 201Tl in tumor bearing animals and inflammatory lesion induced animals," *The European Journal of Nuclear Medicine*, vol. 12, no. 11, pp. 567–572, 1987.
- [32] R. L. M. Haas, R. A. Valdés-Olmos, C. A. Hoefnagel et al., "Thallium-201-chloride scintigraphy in staging and monitoring radiotherapy response in follicular lymphoma patients," *Radiotherapy and Oncology*, vol. 69, no. 3, pp. 323–328, 2003.
- [33] L. Kostakoglu and S. J. Goldsmith, "Lymphoma imaging: nuclear medicine," *Cancer Treatment and Research*, vol. 131, pp. 363–412, 2006.
- [34] A. S. Arbab, K. Koizumi, S. Hiraike, K. Toyama, T. Arai, and T. Araki, "Will thallium-201 replace gallium-67 in salivary gland scintigraphy?" *Journal of Nuclear Medicine*, vol. 37, no. 11, pp. 1819–1823, 1996.
- [35] M. Lorberboym, L. Estok, J. Machac et al., "Rapid differential diagnosis of cerebral toxoplasmosis and primary central nervous system lymphoma by thallium-201 SPECT," *Journal of Nuclear Medicine*, vol. 37, no. 7, pp. 1150–1154, 1996.
- [36] M. Lorberboym, F. Wallach, L. Estok et al., "Thallium-201 retention in focal intracranial lesions for differential diagnosis of primary lymphoma and nonmalignant lesions in AIDS patients," *Journal of Nuclear Medicine*, vol. 39, no. 8, pp. 1366–1369, 1998.
- [37] D. J. Skiest, W. Erdman, W. E. Chang, O. K. Oz, A. Ware, and J. Fleckenstein, "SPECT thallium-201 combined with Toxoplasma serology for the presumptive diagnosis of focal central nervous system mass lesions in patients with AIDS," *Journal of Infection*, vol. 40, no. 3, pp. 274–281, 2000.
- [38] O. Schillaci, A. Spanu, and G. Madeddu, "[^{99m}Tc]sestamibi and [^{99m}Tc]tetrofosmin in oncology: SPET and fusion imaging in lung cancer, malignant lymphomas and brain tumors," *Quarterly Journal of Nuclear Medicine and Molecular Imaging*, vol. 49, no. 2, pp. 133–144, 2005.
- [39] C. Rodriguez, T. Commes, J. Robert, and J.-F. Rossi, "Expression of P-glycoprotein and anionic glutathione S-transferase genes in non-Hodgkin's lymphoma," *Leukemia Research*, vol. 17, no. 2, pp. 149–156, 1993.
- [40] Q. Liu, K. Ohshima, and M. Kikuchi, "High expression of MDR-1 gene and P-glycoprotein in initial and re-biopsy specimens of relapsed B-cell lymphoma," *Histopathology*, vol. 38, no. 3, pp. 209–216, 2001.
- [41] D. Piwnica-Worms, M. L. Chiu, M. Budding, J. F. Kronauge, R. A. Kramer, and J. M. Croop, "Functional imaging of multidrug-resistant P-glycoprotein with an organotechnetium complex," *Cancer Research*, vol. 53, no. 5, pp. 977–984, 1993.
- [42] V. Rao, M. L. Chiu, J. F. Kronauge, and D. Piwnica-Worms, "Expression of recombinant human multidrug resistance P-glycoprotein in insect cells confers decreased accumulation of technetium-99m-sestamibi," *Journal of Nuclear Medicine*, vol. 35, no. 3, pp. 510–515, 1994.
- [43] L. Kostakoglu, N. Elahi, P. Kiratlı et al., "Clinical validation of the influence of P-glycoprotein on technetium-99m-sestamibi uptake in malignant tumors," *Journal of Nuclear Medicine*, vol. 38, no. 7, pp. 1003–1008, 1997.
- [44] H.-C. Song, J.-J. Lee, H.-S. Bom et al., "Double-phase Tc-99m MIBI scintigraphy as a therapeutic predictor in patients with non-Hodgkin's lymphoma," *Clinical Nuclear Medicine*, vol. 28, no. 6, pp. 457–462, 2003.
- [45] C. H. Kao, S. C. Tsai, J. J. Wang, Y. J. Ho, S. T. Ho, and S. P. Changlai, "Evaluation of chemotherapy response using technetium-99M-sestamibi scintigraphy in untreated adult malignant lymphomas and comparison with other prognosis

- factors: a preliminary report," *International Journal of Cancer*, vol. 95, no. 4, pp. 228–231, 2001.
- [46] J.-A. Liang, Y.-C. Shiau, S.-N. Yang et al., "Using technetium-99m-tetrofosmin scan to predict chemotherapy response of malignant lymphomas, compared with P-glycoprotein and multidrug resistance related protein expression," *Oncology Reports*, vol. 9, no. 2, pp. 307–312, 2002.
- [47] A. Lazarowski, J. Dupont, J. Fernández et al., "99mTechnetium-SESTAMIBI uptake in malignant lymphomas. Correlation with chemotherapy response," *Lymphatic Research and Biology*, vol. 4, no. 1, pp. 23–28, 2006.
- [48] J. D. Kelly, A. M. Forster, B. Higley et al., "Technetium-99m-tetrofosmin as a new radiopharmaceutical for myocardial perfusion imaging," *Journal of Nuclear Medicine*, vol. 34, no. 2, pp. 222–227, 1993.
- [49] H.-J. Ding, Y.-C. Shiau, S.-C. Tsai, J.-J. Wang, S.-T. Ho, and A. Kao, "Uptake of 99mTc tetrofosmin in lymphoma cell lines: a comparative study with 99mTc sestamibi," *Applied Radiation and Isotopes*, vol. 56, no. 6, pp. 853–856, 2002.
- [50] R. M. Aigner, G. F. Fueger, W. Zinke, and H. Sill, "99Tcm-tetrofosmin scintigraphy in Hodgkin's disease," *Nuclear Medicine Communications*, vol. 18, no. 3, pp. 252–257, 1997.
- [51] D. Ferone, C. Semino, M. Boschetti, G. L. Cascini, F. Minuto, and S. Lastoria, "Initial staging of lymphoma with octreotide and other receptor imaging agents," *Seminars in Nuclear Medicine*, vol. 35, no. 3, pp. 176–185, 2005.
- [52] J. Valencak, F. Trautinger, M. Raderer et al., "Somatostatin receptor scintigraphy in primary cutaneous T- and B-cell lymphomas," *Journal of the European Academy of Dermatology and Venereology*, vol. 24, no. 1, pp. 13–17, 2010.
- [53] M. Raderer, T. Traub, M. Formanek et al., "Somatostatin-receptor scintigraphy for staging and follow-up of patients with extraintestinal marginal zone B-cell lymphoma of the mucosa associated lymphoid tissue (MALT)-type," *The British Journal of Cancer*, vol. 85, no. 10, pp. 1462–1466, 2001.
- [54] M. Raderer, J. Valencak, F. Pfeffel et al., "Somatostatin receptor expression in primary gastric versus nongastric extranodal B-cell lymphoma of mucosa-associated lymphoid tissue type," *Journal of the National Cancer Institute*, vol. 91, no. 8, pp. 716–718, 1999.
- [55] S. Li, A. Kurtaran, M. Li et al., "¹¹¹In-DOTA-DPhel-Tyr3-octreotide, ¹¹¹In-DOTA-lanreotide and 67Ga citrate scintigraphy for visualisation of extranodal marginal zone B-cell lymphoma of the MALT type: a comparative study," *The European Journal of Nuclear Medicine and Molecular Imaging*, vol. 30, no. 8, pp. 1087–1095, 2003.
- [56] A. Iagaru, M. L. Goris, and S. S. Gambhir, "Perspectives of molecular imaging and radioimmunotherapy in lymphoma," *Radiologic Clinics of North America*, vol. 46, no. 2, pp. 243–252, 2008.
- [57] D. G. Maloney, "Anti-CD20 antibody therapy for B-cell lymphomas," *The New England Journal of Medicine*, vol. 366, no. 21, pp. 2008–2016, 2012.
- [58] T. Alcindor and T. E. Witzig, "Radioimmunotherapy with yttrium-90 ibritumomab tiuxetan for patients with relapsed CD20+ B-cell non-Hodgkin's lymphoma," *Current Treatment Options in Oncology*, vol. 3, no. 4, pp. 275–282, 2002.
- [59] T. M. Behr, F. Griesinger, J. Riggert, S. Gratz, M. Behe, C. C. Kaufmann et al., "High-dose myeloablative radioimmunotherapy of mantle cell non-Hodgkin lymphoma with the iodine-131-labeled chimeric anti-CD20 antibody C2B8 and autologous stem cell support. Results of a pilot study," *Cancer*, vol. 94, no. 4, Supplement, pp. 1363–1372, 2002.
- [60] L. I. Gordon, T. E. Witzig, G. A. Wiseman et al., "Yttrium 90 ibritumomab tiuxetan radioimmuno-therapy for relapsed or refractory low-grade non-hodgkin's lymphoma," *Seminars in Oncology*, vol. 29, no. 1, pp. 87–92, 2002.
- [61] M. F. Leahy and J. H. Turner, "Radioimmunotherapy of relapsed indolent non-Hodgkin lymphoma with 131I-rituximab in routine clinical practice: 10-year single-institution experience of 142 consecutive patients," *Blood*, vol. 117, no. 1, pp. 45–52, 2011.
- [62] F. Hagemeister, "Rituximab for the treatment of non-hodgkins lymphoma and chronic lymphocytic leukaemia," *Drugs*, vol. 70, no. 3, pp. 261–272, 2010.
- [63] M. E. Juweid, "Radioimmunotherapy of B-cell non-Hodgkin's lymphoma: from clinical trials to clinical practice," *Journal of Nuclear Medicine*, vol. 43, no. 11, pp. 1507–1529, 2002.
- [64] A. Iagaru, S. S. Gambhir, and M. L. Goris, "⁹⁰Y-ibritumomab therapy in refractory non-Hodgkin's lymphoma: observations from ¹¹¹In-ibritumomab pretreatment imaging," *Journal of Nuclear Medicine*, vol. 49, no. 11, pp. 1809–1812, 2008.
- [65] F. M. Iwamoto, J. Schwartz, N. Pandit-Taskar et al., "Study of radiolabeled indium-111 and yttrium-90 ibritumomab tiuxetan in primary central nervous system lymphoma," *Cancer*, vol. 110, no. 11, pp. 2528–2534, 2007.
- [66] A. Otte, "Diagnostic imaging prior to ⁹⁰Y-ibritumomab tiuxetan (Zevalin) treatment in follicular non-Hodgkin's lymphoma," *Hellenic Journal of Nuclear Medicine*, vol. 11, no. 1, pp. 12–15, 2008.
- [67] P. S. Conti, C. White, P. Pieslor, A. Molina, J. Aussie, and P. Foster, "The role of imaging with ¹¹¹In-ibritumomab tiuxetan in the ibritumomab tiuxetan (Zevalin) regimen: results from a Zevalin Imaging Registry," *Journal of Nuclear Medicine*, vol. 46, no. 11, pp. 1812–1818, 2005.
- [68] D. R. Fisher, S. Shen, and R. F. Meredith, "MIRD dose estimate report No. 20: radiation absorbed-dose estimates for ¹¹¹In-And⁹⁰Y-ibritumomab Tiuxetan," *Journal of Nuclear Medicine*, vol. 50, no. 4, pp. 644–652, 2009.
- [69] G. A. Wiseman, E. Kornmehl, B. Leigh et al., "Radiation dosimetry results and safety correlations from ⁹⁰Y-ibritumomab tiuxetan radioimmuno-therapy for relapsed or refractory non-Hodgkin's lymphoma: combined data from 4 clinical trials," *Journal of Nuclear Medicine*, vol. 44, no. 3, pp. 465–474, 2003.
- [70] L. R. Perk, O. J. Visser, M. S. Walsum et al., "Preparation and evaluation of 89Zr-Zevalin for monitoring of ⁹⁰Y-Zevalin biodistribution with positron emission tomography," *The European Journal of Nuclear Medicine and Molecular Imaging*, vol. 33, no. 11, pp. 1337–1345, 2006.
- [71] S. N. F. Rizvi, O. J. Visser, M. J. W. D. Vosjan et al., "Biodistribution, radiation dosimetry and scouting of ⁹⁰Y-ibritumomab tiuxetan therapy in patients with relapsed B-cell non-Hodgkin's lymphoma using ⁸⁹Zr-ibritumomab tiuxetan and PET," *The European Journal of Nuclear Medicine and Molecular Imaging*, vol. 39, no. 3, pp. 512–520, 2012.
- [72] G. A. Wiseman, B. Leigh, W. D. Erwin et al., "Radiation dosimetry results for Zevalin radioimmuno-therapy of rituximab-refractory non-Hodgkin lymphoma," *Cancer*, vol. 94, no. 4, supplement, pp. 1349–1357, 2002.
- [73] B. Andemariam and J. P. Leonard, "Radioimmunotherapy with tositumomab and iodine-131 tositumomab for non-Hodgkin's lymphoma," *Biologics*, vol. 1, no. 2, pp. 113–120, 2007.
- [74] H. A. Jacene, R. Filice, W. Kasecamp, and R. L. Wahl, "Comparison of ⁹⁰Y-ibritumomab tiuxetan and 131I-tositumomab in

- clinical practice," *Journal of Nuclear Medicine*, vol. 48, no. 11, pp. 1767–1776, 2007.
- [75] H. Song, Y. Du, G. Sgouros, A. Prideaux, E. Frey, and R. L. Wahl, "Therapeutic potential of ^{90}Y - and ^{131}I -labeled anti-CD20 monoclonal antibody in treating non-Hodgkin's lymphoma with pulmonary involvement: a Monte Carlo-based dosimetric analysis," *Journal of Nuclear Medicine*, vol. 48, no. 1, pp. 150–157, 2007.
- [76] M. S. Kaminski, J. Estes, K. R. Zasadny et al., "Radioimmunotherapy with iodine-131I tositumomab for relapsed or refractory B-cell non-Hodgkin lymphoma: updated results and long-term follow-up of the University of Michigan experience," *Blood*, vol. 96, no. 4, pp. 1259–1266, 2000.
- [77] V. Lewington, "Development of ^{131}I -tositumomab," *Seminars in Oncology*, vol. 32, supplement 1, pp. S50–S56, 2005.
- [78] A. Iagaru, E. S. Mittra, K. Ganjoo, S. J. Knox, and M. L. Goris, " ^{131}I -tositumomab (Bexxar) vs. ^{90}Y -ibritumomab (Zevalin) therapy of low-grade refractory/relapsed non-hodgkin lymphoma," *Molecular Imaging and Biology*, vol. 12, no. 2, pp. 198–203, 2010.
- [79] S. J. Horning, A. Younes, V. Jain et al., "Efficacy and safety of tositumomab and iodine-131 tositumomab (Bexxar) in B-cell lymphoma, progressive after rituximab," *Journal of Clinical Oncology*, vol. 23, no. 4, pp. 712–719, 2005.
- [80] J. H. Turner, A. A. Martindale, J. Boucek, P. G. Claringbold, and M. F. Leahy, " ^{131}I -anti CD20 radioimmunotherapy of relapsed or refractory non-Hodgkins lymphoma: a phase II clinical trial of a nonmyeloablative dose regimen of chimeric rituximab radiolabeled in a hospital," *Cancer Biotherapy and Radiopharmaceuticals*, vol. 18, no. 4, pp. 513–524, 2003.
- [81] K. Scheidhauer, I. Wolf, H.-J. Baumgartl et al., "Biodistribution and kinetics of ^{131}I -labelled anti-CD20 MAB IDEC-C2B8 (rituximab) in relapsed non-Hodgkin's lymphoma," *The European Journal of Nuclear Medicine*, vol. 29, no. 10, pp. 1276–1282, 2002.
- [82] M. S. Kaminski, K. R. Zasadny, I. R. Francis et al., "Radioimmunotherapy of B-cell lymphoma with [^{131}I]anti-B1 (anti-CD20) antibody," *The New England Journal of Medicine*, vol. 329, no. 7, pp. 459–465, 1993.
- [83] M. E. Juweid, "Radioimmunotherapy with ^{131}I -rituximab: what we know and what we don't know," *Cancer Biotherapy and Radiopharmaceuticals*, vol. 18, no. 4, pp. 489–495, 2003.
- [84] T. Olafsen, D. Betting, V. E. Kenanova et al., "Recombinant anti-CD20 antibody fragments for small-animal PET imaging of B-cell lymphomas," *Journal of Nuclear Medicine*, vol. 50, no. 9, pp. 1500–1508, 2009.
- [85] G. Smith, M. Glaser, M. Perumal et al., "Design, synthesis, and biological characterization of a caspase 3/7 selective isatin labeled with $2-[^{18}\text{F}]\text{fluoroethylazide}$," *Journal of Medicinal Chemistry*, vol. 51, no. 24, pp. 8057–8067, 2008.
- [86] Q.-D. Nguyen, G. Smith, M. Glaser, M. Perumal, E. Årstad, and E. O. Aboagye, "Positron emission tomography imaging of drug-induced tumor apoptosis with a caspase-3/7 specific $[^{18}\text{F}]$ -labeled isatin sulfonamide," *Proceedings of the National Academy of Sciences of the United States of America*, vol. 106, no. 38, pp. 16375–16380, 2009.
- [87] B. Holzmann, U. Gossler, and M. Bittner, " $\alpha 4$ integrins and tumor metastasis," *Current Topics in Microbiology and Immunology*, vol. 231, pp. 125–141, 1997.
- [88] S. J. Denardo, R. Liu, H. Albrecht et al., " ^{111}In -LLP2A-DOTA polyethylene glycol-targeting $\alpha 4\beta 1$ integrin: comparative pharmacokinetics for imaging and therapy of lymphoid malignancies," *Journal of Nuclear Medicine*, vol. 50, no. 4, pp. 625–634, 2009.
- [89] A. L. Zwingenberger, M. S. Kent, R. Liu et al., "*In-vivo* biodistribution and safety of ^{99m}Tc -LLP2A-hynic in canine non-hodgkin lymphoma," *Plos One*, vol. 7, no. 4, Article ID e34404, 2012.
- [90] L. S. Zuckier, "Hybrid imaging in planar scintigraphy: new implementations and historical precedents," *Seminars in Nuclear Medicine*, vol. 42, no. 1, pp. 62–72, 2012.

Review Article

Clinical Application of Magnetic Resonance Imaging in Management of Breast Cancer Patients Receiving Neoadjuvant Chemotherapy

Jeon-Hor Chen^{1,2} and Min-Ying Su¹

¹ Center for Functional Onco-Imaging, Department of Radiological Sciences, University of California, Irvine, CA 92697-5020, USA

² Department of Radiology, E-Da Hospital and I-Shou University, Kaohsiung 82445, Taiwan

Correspondence should be addressed to Min-Ying Su; msu@uci.edu

Received 5 January 2013; Accepted 17 May 2013

Academic Editor: David J. Yang

Copyright © 2013 J.-H. Chen and M.-Y. Su. This is an open access article distributed under the Creative Commons Attribution License, which permits unrestricted use, distribution, and reproduction in any medium, provided the original work is properly cited.

Neoadjuvant chemotherapy (NAC), also termed primary, induction, or preoperative chemotherapy, is traditionally used to downstage inoperable breast cancer. In recent years it has been increasingly used for patients who have operable cancers in order to facilitate breast-conserving surgery, achieve better cosmetic outcome, and improve prognosis by reaching pathologic complete response (pCR). Many studies have demonstrated that magnetic resonance imaging (MRI) can assess residual tumor size after NAC, and that provides critical information for planning of the optimal surgery. NAC also allows for timely adjustment of administered drugs based on response, so ineffective regimens could be terminated early to spare patients from unnecessary toxicity while allowing other effective regimens to work sooner. This review article summarizes the clinical application of MRI during NAC. The use of different MR imaging methods, including dynamic contrast-enhanced MRI, proton MR spectroscopy, and diffusion-weighted MRI, to monitor and evaluate the NAC response, as well as how changes of parameters measured at an early time after initiation of a drug regimen can predict final treatment outcome, are reviewed. MRI has been proven a valuable tool and will continue to provide important information facilitating individualized image-guided treatment and personalized management for breast cancer patients undergoing NAC.

1. Clinical Significance and Concerns of NAC

Neoadjuvant chemotherapy (NAC) has become an important alternative treatment modality for breast cancer. NAC can downstage cancers and render them operable and/or facilitate breast-conserving surgery (BCS) [1–4]. In patients with inoperable locally advanced breast cancer, NAC is the standard of care and has been shown to improve both disease-free survival and overall survival. Patients with operable cancer may also choose to receive NAC to facilitate BCS [4–6]. In a meta-analysis of 14 randomized trials consisting of 5,500 women comparing NAC first followed by surgery and surgery first followed by adjuvant chemotherapy for operable breast cancer, it was found that, although overall survival was equivalent in these two groups, the mastectomy rate was

lower in the NAC group without hampering local control. NAC was also associated with fewer adverse effects [5].

As more effective therapies have become available, the main target of NAC has gone beyond down staging to a more far-reaching purpose of achieving pathological complete response (pCR). Emerging evidence suggests that induction of a pCR, or minimal residual cancer burden near pCR, is predictive of favorable long-term survival [6–8]. Depending on the treatment protocol, different chemo-regimens are used in combination or in a sequential order. A complete course of NAC usually takes several months. Patients receiving NAC do not always respond well. If a patient is not responding well to a certain regimen, the oncologist may change the drugs timely, not only to avoid unnecessary drug-related toxicity and complications, but also to allow the new regimen

to work sooner. It is therefore critical to find a reliable method for assessing patient's response at an earlier time. With more effective therapy regimens, even large locally advanced tumors can be treated to achieve pCR or minimal residual disease, and as such another important role of imaging is to predict the residual disease after NAC so the results can be used for surgical planning. When MRI can confidently diagnose that the cancer has completely remised or shrunk to a minimum disease, a small lumpectomy is usually sufficient, and that will likely lead to a good cosmetic outcome after surgery. An example of how NAC can change the surgery from mastectomy to lumpectomy is given in Figure 1.

Research evidence has suggested that BCS after NAC results in acceptable low rates of locoregional or ipsilateral recurrence in appropriately selected patients, even in those with T3/T4 or multifocal/multicentric cancers [9–11]. Factors that predict early recurrence include residual pathologic tumor size >2 cm, multifocal tumor, and lymphovascular invasion [12]. Therefore, an accurate pre- and post-NAC disease staging is very important for selecting the optimal patients suitable for breast-conserving surgeries, without subjecting them to the high risk of recurrence [9–15]. Current methods for assessing treatment response include clinical examination (palpation), sonography, mammography, MRI, and molecular imaging. Because the reliability of traditional methods (physical examination, mammography, and ultrasound) is questionable [13–16], MRI is increasingly being used to evaluate response of breast cancer undergoing NAC. MRI-measured tumor size after NAC has been proven to be well correlated with pathologically determined tumor size after completing therapy, and early change of tumor size has been shown to be a good response indicator [16–19]. However, changes in lesion size on MRI are usually not detected until several weeks following chemotherapy [18]. If early surrogate response indicator could be established to predict final treatment outcome, it would help to allow timely adjustment of drug regimens and achieve the goal of pCR.

2. Breast MRI Methods for NAC Response Evaluation

Dynamic contrast-enhanced MRI (DCE-MRI) is the current standard for breast MR imaging. The enhancement kinetics can be evaluated using 3 distinct features, the wash-in phase, the maximum enhancement, and the wash-out phase. Several heuristic parameters can be analyzed from the curve, such as wash-in slope (maximum slope, or the slope within a time period), the maximum percent enhancement, time to maximum, and the wash-out slope (within a time period). A more sophisticated analysis method is to perform pharmacokinetic analysis based on two compartmental models, such as the widely used unified Tofts model [20, 21]. The two compartments are the vascular space and the interstitial space (or the extravascular-extracellular space), with the transfer constant K^{trans} to leak from the vascular to the interstitial space and the rate constant k_{ep} from the interstitial space back to the vascular space. In addition to diagnosis, another major application of DCE-MRI is for predicting response of breast

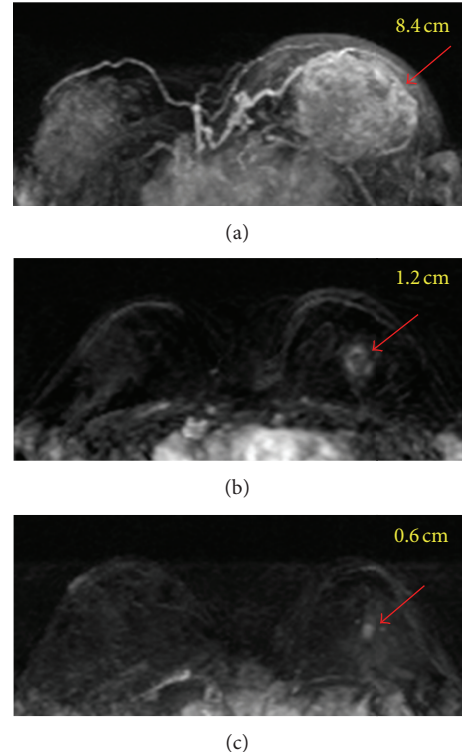


FIGURE 1: A 35-year-old patient with invasive ductal cancer in the left breast. From (a) to (c), the maximum intensity projection (MIP) images of pretreatment, F/U-1, and F/U-2 MRI are shown. Despite the large tumor, the boundary is clearly visible and this is a mass lesion. The diagnosed tumor size before treatment is 8.4 cm. This cancer is considered as inoperable and is recommended to receive NAC. After 2 cycles of treatment the tumor has shrunk to 1.2 cm, and the size is further decreased to 0.6 cm after completing NAC. Without NAC this patient will need mastectomy and will have a high risk of positive margin. NAC allows this patient to receive breast-conserving surgery, with a good cosmetic outcome.

cancer undergoing NAC. It is well known that the cancer therapy also causes vascular damage, and the enhancement kinetic pattern will change from the wash-out pattern to a less aggressive pattern of plateau or persistent enhancement [22]. In general, when there is tissue enhancement within the previous tumor bed after NAC, it is considered as residual disease regardless of the DCE kinetic pattern.

There are attempts to investigate whether information provided by MRI may serve as earlier response indicators than the size change. The parameters included percent enhancements measured at different times during the DCE imaging period, initial area under the curve, and pharmacokinetic parameters (such as K^{trans} and k_{ep}) measured by DCE-MRI; apparent diffusion coefficient (ADC) measured by diffusion-weighted imaging (DWI); and choline and water : fat ratio measured by proton MR spectroscopy (MRS). These imaging parameters are measured in pretreatment MRI and early follow-up MRI (after one or two cycles of NAC) to predict the final response. Final MRI following the completeness of NAC treatment is very important in evaluating

the residual tumor size hence an optimal surgical plan can be chosen. Besides focusing on evaluation of tumor itself, recently, there has been increasing interest in the evaluation of normal breast tissue, such as background parenchymal enhancement [23–30] and breast density [31]. In the following sections we will describe the measurement of these imaging parameters at different times during NAC and their clinical roles in improving management of patients.

3. Pretreatment MRI for Predicting NAC Response and Prognosis

Most NAC imaging studies focused on evaluating post-treatment responses. However, the features of tumors in pretreatment MRI are known to be associated with treatment responses. It was noted that large tumor size, a diffuse lesion without mass effect, and high intratumoral signal intensity on T2-weighted MR images were significantly associated with chemoresistance. Mass lesions showing the wash-out DCE kinetic pattern were significantly associated with chemosensitivity [32]. Similarly, in a study of triple negative tumors, it was noted that an irregularly shaped lesion ($P = 0.018$) and the presence of clear intra-tumoral necrosis ($P = 0.044$) were significantly associated with poor NAC response [33]. In a meta-analysis of nine studies, it was noted that several pretreatment MR parameters could differentiate between responders and nonresponders [34]. Predictive role of these parameters measured using different MR imaging methods will be described later in subsections.

Pretreatment DCE-MRI parameters had also been used to predict disease-free and overall survival for breast cancer patients receiving NAC [35]. Overall, a more aggressive disease with a larger tumor and higher angiogenic properties was associated with worse prognosis. It was noted that, in patients who exhibit high levels of vascular perfusion and permeability in pretreatment DCE-MRI, significantly lower disease-free survival (DFS) and overall survival (OS) are expected [35]. Univariate survival analysis has revealed that certain empirical DCE-MRI parameters (including maximum enhancement, enhancement at an early time, wash-in slope, and area under the initial curve) showed significant association with both DFS and OS [35]. In another study, a significant correlation between the total enhancing tumor volume and 5-year survival was found ($P < 0.05$) [36]. It was shown that a two-dimensional discriminator considering both the total enhancing tumor volume and the tumor volume showing wash-out DCE pattern further improved the prediction of survival, with $P < 0.001$ differentiating between survivors and nonsurvivors [36]. Similarly, in a study of 62 patients, pretreatment extravascular extracellular volume V_e ($P = 0.027$) and mean transit time (MTT) ($P = 0.002$) were associated with disease-free survival [37].

4. Early Response Predictors Using Different MR Imaging Methods

4.1. DCE-MRI. There is discrepancy in the published data regarding the usefulness of pharmacokinetic parameters in predicting NAC response [38–41]. Some found that they

could predict final response earlier than the size measurement did [40], but others did not [39, 41]. The explanation for these variations in reported data is multifactorial: patient number, tumor type, chemotherapeutic agent, the follow-up imaging time of MRI after commencing therapy, and the analysis methods, have all varied. Yu et al. [41] found that the changes of K^{trans} or k_{ep} after one cycle of AC by itself could not provide better information than the early tumor size change to predict response, but they could be combined with size change to better differentiate responders from nonresponders. Figure 2 shows 3 case examples. In this study by Yu et al., the DCE kinetics was measured by manually drawing a region of interest (ROI) based on the enhanced tumor, and only subtle changes in the DCE patterns were noted between pretreatment and after 1 cycle of AC follow-up MRI, but these changes could not differentiate between responders and non-responders after completing 4 cycles of AC. It was concluded that the followup performed soon after 1 cycle of AC (within 2 weeks after starting of treatment) was too early. Another study showed significant early reduction in both K^{trans} and k_{ep} in responders compared to non-responders [40]. Changes in V_e and K^{trans} were significantly different between non-, partial-, and complete responders ($P = 0.009$ and $P = 0.04$, resp.) [42]. Breast tumor is highly heterogeneous and the ROI-based analysis cannot provide detailed information about the responses in different parts of tumor. Therefore, for the purpose of evaluating therapeutic changes, the most useful analysis method is to perform pixel-by-pixel analysis of the DCE enhancement kinetics, and the obtained histograms for the analyzed parameters can be compared between studies performed before and after therapy to evaluate changes [22, 39].

Other than predicting the efficacy of cytotoxic chemotherapy, the more attractive role of DCE-MRI is to evaluate the response of antiangiogenic or antivascular therapy [43–48]. Evidence from phase I and II studies strongly suggests that K^{trans} can be used as a predictive biomarker to determine response to antiangiogenic drugs or vascular disruptive agents, with a change in K^{trans} of greater than 40% considered as the threshold required to represent definitive response [49]. The most widely used antiangiogenic agent, trastuzumab (Avastin), is a monoclonal antibody that neutralizes the vascular endothelial growth factor (VEGF) to inhibit angiogenesis, and it has been used for treating breast cancer in neoadjuvant setting. DCE-MRI provides a means for assessing the treatment-induced vascular changes to investigate the early therapeutic response to this targeted drug [50]. It may provide insightful information to evaluate the efficacy of drugs in clinical trial phases and to guide the design for future studies. However, since bevacizumab was often combined with chemotherapy for breast cancer treatment, the combined cytotoxic and antiangiogenic effects were observed, and as such the role of DCE-MRI for predicting the sole efficacy of bevacizumab could not be established.

4.2. Proton MR Spectroscopy. 1H -MRS can be used to detect the elevated choline concentration in breast cancer. High levels of choline-containing metabolites (referred to as total

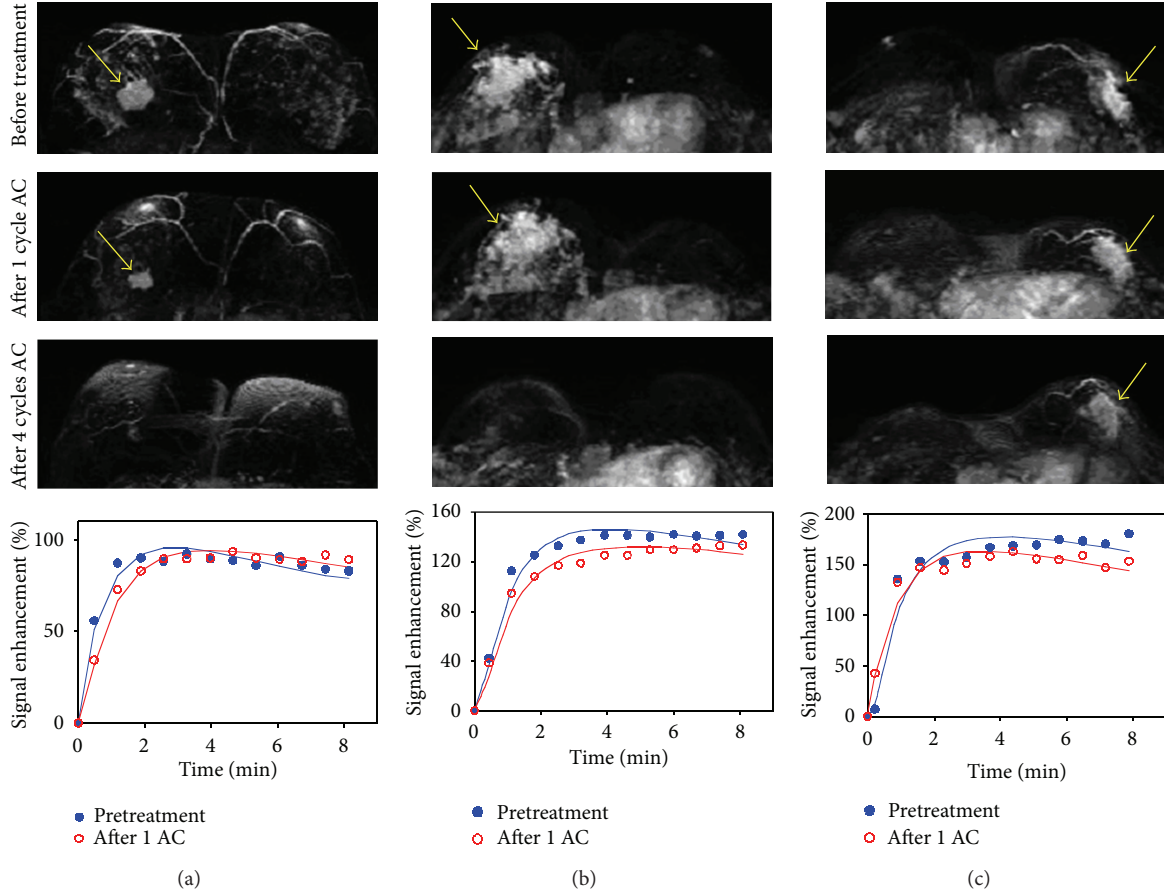


FIGURE 2: The DCE kinetics measured at baseline before treatment and after 1 cycle of chemotherapy from 3 case examples. From top to bottom, the maximum intensity projection (MIP) images of pretreatment, F/U-1 MRI after 1 cycle of treatment, and F/U-2 MRI after 4 cycles of treatment are shown. (a) A responder after 1 cycle of AC regimen, which shows a slower wash-in and a slower wash-out after chemotherapy. (b) A confirmed responder after 4 cycles which has not yet shown a good response after 1 cycle, but the change of DCE kinetic is similar to the responder in (a) thus indicating that it may be a responder. The follow-up MRI is performed 8 days after the administration of chemotherapy, which may be too early to show size change. (c) A nonresponder which does not show tumor shrinkage after 4 cycles of AC treatment, and the DCE shows a faster wash-in and a faster wash-out after 1 cycle of chemotherapy. However, despite the noticeable differences in the DCE patterns, the changes are subtle.

choline or tCho) are mainly due to the increase of phospholipid metabolism and cellular membranes proliferation. Many studies have investigated the role of ^1H -MRS for therapy response prediction but inconsistent results were reported [51–58]. Therefore, the value of MRS was not well established, partly due to its technical difficulty in quantification [51–53]. In early studies, Kvistad et al. [51] and Jagannathan et al. [52] demonstrated that ^1H -MRS at 1.5 T was useful to assess the response of locally advanced breast cancer to NAC. They, however, used qualitative observations not quantitative measurements of tCho concentration to monitor changes. Meisamy et al. [53] reported a quantitative ^1H -MRS study in 13 patients using a 4.0 T scanner and found that the change in tCho level within 24 hours was significantly different between the responder and the nonresponder groups; however, this result could not be further verified by other studies. Baek et al. reported significant difference in tCho level between clinical responders and non-responders evaluated based on the size changes at a later time [54]. In a follow-up study by

Baek et al. [55] using pathologic response as the outcome, it was found that the tCho changes were greater than the tumor size changes in the pCR group in both F/U-1 (after 3–4 weeks) and F/U-2 (after 6–8 weeks) studies but not in non-pCR group. The results suggested that, when the tCho reduction was higher than the tumor size reduction, the tumor was more likely to achieve pCR [55]. However, as the treatment continues, the change in tumor size halfway through therapy (6–8 weeks) was the most accurate predictor of pCR, with area under the ROC curve of 0.9, while that for the change in tCho was 0.73. Example of a pCR case is shown in Figure 3, and a non-pCR case is shown in Figure 4. Tozaki et al. showed that, after one cycle of chemotherapy, a reduction in the choline signal was more sensitive than DW-MRI in demonstrating pathological response [56, 57]. It was also shown that the changes in Cho after the second cycle of chemotherapy may be more sensitive than changes in the tumor size to predict the pathological response [56]. Another study found that a significant decrease in tCho SNR

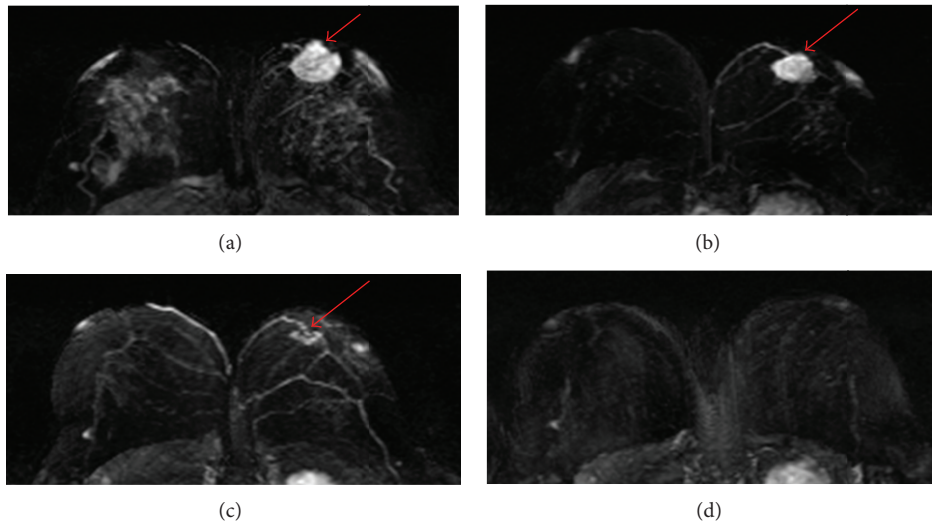


FIGURE 3: A 41-year-old patient with a mass lesion (invasive ductal cancer) in the left breast. From (a) to (d), the maximum intensity projection (MIP) images of pretreatment, F/U-1, F/U-2, and F/U-3 MRI are shown. The tumor size is 4.0 cm before treatment, which shrinks down to 2.7 cm in F/U-1 (32% reduction), 1.2 cm in F/U-2, and reaches a complete response in F/U-3 after completing NAC. This patient is confirmed as pCR in post-NAC pathological examination. The total choline concentration measured by MRS is $[t\text{Cho}] = 2.33 \pm 0.54 \text{ mmol/kg}$ before therapy, which decreases to $1.15 \pm 0.25 \text{ mmol/kg}$ in F/U-1, showing 51% reduction. Tumor size is too small in F/U-2 and F/U-3 for MRS measurements. For this pCR case, the tumor size reduction is 32% at F/U-1, and $[t\text{Cho}]$ reduction is greater at 51%.

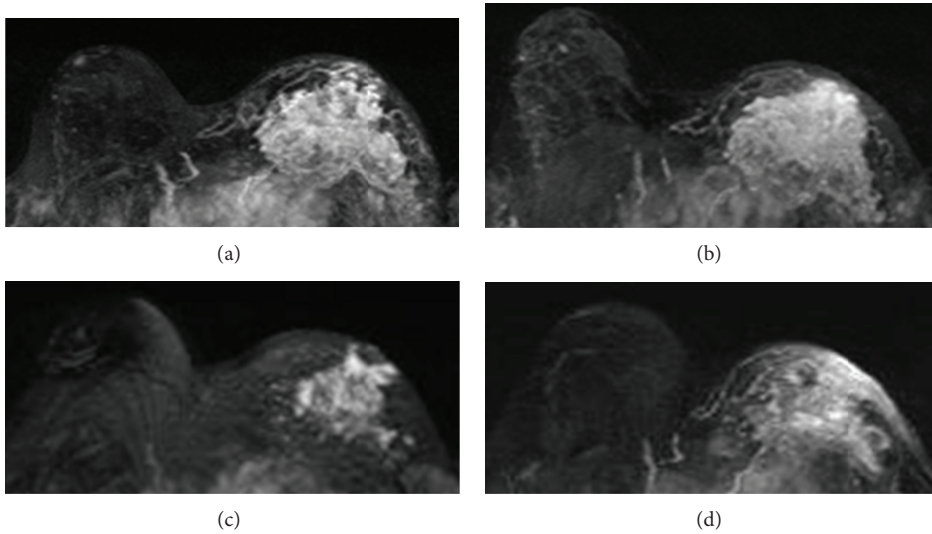


FIGURE 4: A 29-year-old patient with non-mass-like enhancement lesion in the left breast. From (a) to (d), the maximum intensity projection (MIP) images of pretreatment, F/U-1, F/U-2, and F/U-3 MRI are shown. The extent of tumor size is 8.2 cm before treatment, remains about the same at 8.0 cm in F/U-1, shrinks down to 4.5 cm in F/U-2, and progresses again to 6.2 cm in F/U-3. The choline measured by MRS shows $[t\text{Cho}] = 0.77 \pm 0.11 \text{ mmol/kg}$ before treatment, which decreases to 0.20 mmol/kg in F/U-1, and then increases to 1.01 mmol/kg in F/U-2, and further increases to 1.70 mmol/kg in F/U-3. The transient decrease of tCho in F/U-1 precedes the size reduction observed later in F/U-2. And then the increase of tCho in F/U-2 indicates treatment failure, and the tumor grows larger in F/U-3.

was detected after treatment, but responders could not be distinguished from non-responders [58]. It was concluded that, with the currently observed low choline detection rate, technological challenges related to choline detection have to be resolved before MRS can provide a reliable quantitative imaging biomarker for predicting NAC response [58].

Performing MRS quantification over a course of treatment is particularly challenging because it is known that

water content and T2 vary under normal physiological conditions [38]. In addition, as the lesion shrinks, it is more difficult to quantify tCho because there is less tumor tissue to be measured. This is an inherent problem with the relatively low sensitivity of 1H-MRS compared with MRI, which limits the utility of 1H-MRS. Further work is also necessary to account for the changes of water T2 relaxation rate, which also decreases in successful therapy. Other than tCho, several

studies also reported an association between the water:fat ratio measured by MR spectroscopy with NAC response [38, 59–61]. As tumor shrinks, the water content will decrease, and the ratio to the fat content may serve as a response indicator. Manton et al. found that, while pharmacokinetic parameters and ADC could not detect early treatment response, early changes in water:fat ratios and water T2 relaxation time did demonstrate substantial prognostic efficacy after two cycles of NAC [38]. However, many factors other than tumor response may also affect the water:fat ratios and water T2 measurements, and these two parameters were not considered as reliable response indicators either.

4.3. Diffusion-Weighted Imaging. DW-MRI is developed to probe the microscopic motion of water molecules, and the measured apparent diffusion coefficient (ADC) is sensitive to cell density, membrane integrity, and tissue microstructure [62]. Tumors, in general, have a high cell density with restricted water diffusion. The decrease of cellular density after NAC will lead to increased ADC, and that shows promise as an early surrogate biomarker for detecting early response before tumor shrinkage occurs. In a meta-analysis of 6 studies, DW-MRI sensitivity was 0.93 (95% CI 0.82–0.97) and specificity was 0.82 (95% CI 0.70–0.90) [63] in predicting pathological response. Induction of successful apoptosis will result in loss of cell membrane integrity, and the altered barrier will allow more free water diffusion, which can be used as a very early sign of treatment response. The later cell death and shrinkage will increase extracellular space, which translates to a rise in the ADC value of up to 35% [64–66].

The initial results using ADC as a predictor were encouraging, showing earlier change than size reduction [64–67]. It was noted that the change in ADC after the first cycle was statistically significant compared with the change in tumor volume or diameter [65]. The coupling of the diffusion imaging with the established morphological MRI provides superior evaluation of response to NAC compared with morphological MRI alone [68]. Changes in MRI-derived tumor diameter and ADC after only one cycle of NAC could provide a valuable tool for early evaluation of treatment effects [69, 70]. ADC measured after four cycles of NAC was shown to be a strong independent predictor of pCR [71]. After 3–6 cycles of NAC, the best cut-off for differentiating pCR from non-pCR was a 54.9% increase in the ADC, which could reach 100% sensitivity and 70.4% (19/27) specificity [72]. However, while ADC can be precisely measured for mass type lesions, it is difficult for lesions that present as non-mass-like enhancements, and it is challenging to use ADC to predict the NAC response for non-mass type lesions [70].

Breast cancer with a low pretreatment ADC tended to respond better to chemotherapy [73, 74]. There was a significant negative correlation between pre-chemotherapy ADC and the percentage change of tumor volume [74]. It was noted that high ADC values indicate necrotic tissue with low cellularity [75, 76]. Necrotic areas in tumors are usually poorly perfused, which may reduce the delivery of chemotherapeutic agents to the tumor. Furthermore, tumor tissues near necrotic regions are likely in hypoxic status and have slower metabolisms and thus less sensitive to cytotoxic

chemotherapy [73]. However, other studies did not find significant difference in pre-chemotherapy ADCs between pathologic complete response cases and those with residual diseases [66, 77]. The conflicting findings may be owing to different DWI acquisition methods (e.g., *b* value, fat suppression technique) and methodological differences in measurements of ADC and residual tumor size used in the different studies [74]. The optimal *b* values for diffusion-weighted MRI in the breast have not been established yet. While there was a standard recommended protocol for DCE-MRI of the breast, there has been no guideline for the DWI scanning protocol. The imaging parameters and analysis methods all have a bearing on the measurement of ADC values [66]. Further studies are needed to standardize the protocol, so that the measured ADC values can be compared across different studies.

5. Accuracy of MRI in Determining Residual Disease after Completing NAC

Many studies have investigated the role of breast MRI as a diagnostic tool for evaluating the extent of residual disease after NAC [78, 79]. Despite the superior accuracy when compared with other modalities, MRI can over- or underestimate residual tumor extent. This inaccurate assessment may be influenced by tumor response, chemotherapeutic agent, or NAC-induced reactive changes within the tumor [80]. The general agreement is that MRI is very accurate for mass type lesions that show clear tumor boundary and present concentric shrinkage after therapy (Figures 5 and 6). In contrast, MRI is not accurate for non-mass-like enhancement lesions that are more likely to break up into pieces and present residual disease as scattered cells or cell clusters (Figures 7 and 8). Invasive lobular cancers and cancers with extensive ductal carcinoma *in situ* components are more likely to present non-mass type lesions, and the accuracy of MRI may be compromised [81, 82].

Another observation is that the accuracy of MRI is affected by the molecular characteristics of cancer [81–90]. HER-2-positive cancer is more aggressive and there is targeted therapy trastuzumab (Herceptin) available; therefore, HER-2-positive cancer generally responds very well to trastuzumab-containing chemotherapy [81]. When the treatment is more effective, the rate of achieving pCR is higher, and it is less likely to present the scattered minimal residual disease confounding the accuracy of MRI diagnosis. Therefore, the diagnostic accuracy of post-NAC MRI is generally better in HER-2-positive than in HER-2-negative cancer. MRI is known to have a high false-negative rate in HER-2-negative patients [81]. For HER-2-negative patients receiving NAC with and without bevacizumab, the pathological response and the diagnostic performance of MRI are comparable. In both groups, MRI has a limitation in detecting residual disease broken down to small foci and scattered cells/clusters [82].

Hormonal receptor status (including estrogen receptor ER and progesterone receptor PR) also affects the response to chemotherapy and thus the diagnostic accuracy of post-NAC MRI. In general, hormonal-negative cancer is more

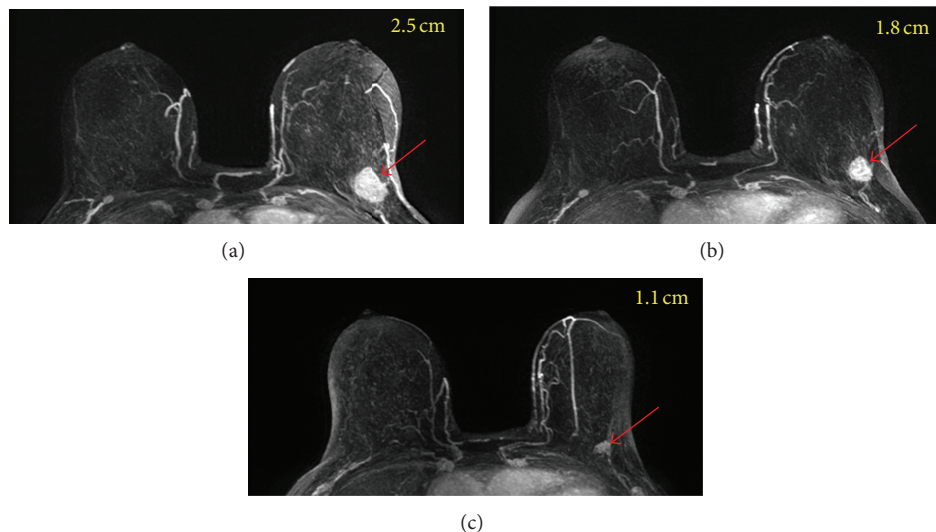


FIGURE 5: A 64-year-old patient with a well-circumscribed mass lesion (invasive ductal cancer) in the left breast. From (a) to (c), the maximum intensity projection (MIP) images of pretreatment, F/U-1, and F/U-2 MRI are shown. The tumor size is 2.5 cm before treatment and shows concentric shrinkage to 1.8 cm in F/U-1 and further down to 1.1 cm in F/U-2 after completing treatment. The residual tumor size determined in post-NAC pathological examination is 1.4 cm. For mass lesion that shows concentric shrinkage, MRI is accurate in diagnosing residual disease.

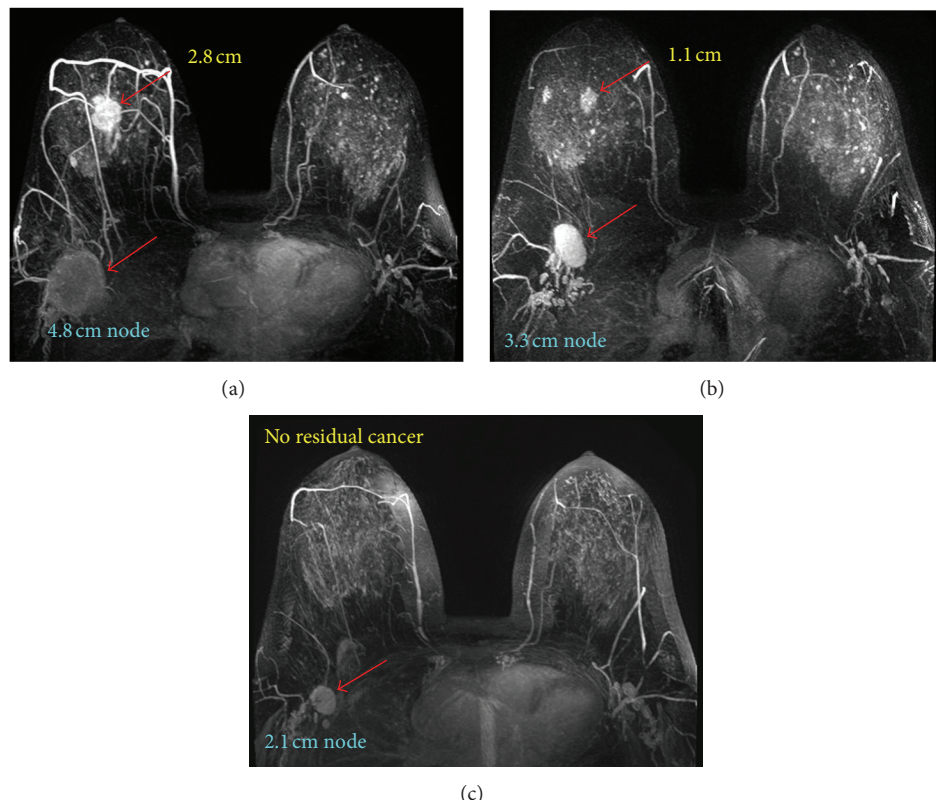


FIGURE 6: A 48-year-old patient with a mass lesion (invasive ductal cancer) in the right breast and an enlarged lymph node in the axilla. From (a) to (c), the maximum intensity projection (MIP) images of pretreatment, F/U-1, and F/U-2 MRI are shown. The size of the primary tumor in the breast is 2.8 cm before treatment, which shrinks down to 1.1 cm in F/U-1 and reaches a complete response in F/U-2 after completing NAC. The node is also responding well and shows size shrinkage from 4.8 cm before treatment to 3.3 cm in F/U-1 and to 2.1 cm in F/U-2. In addition to evaluating the response of primary tumor, MRI can also be used to evaluate the response in the nodes. This patient is confirmed to reach pCR in the post-NAC pathological examination, with one positive node.

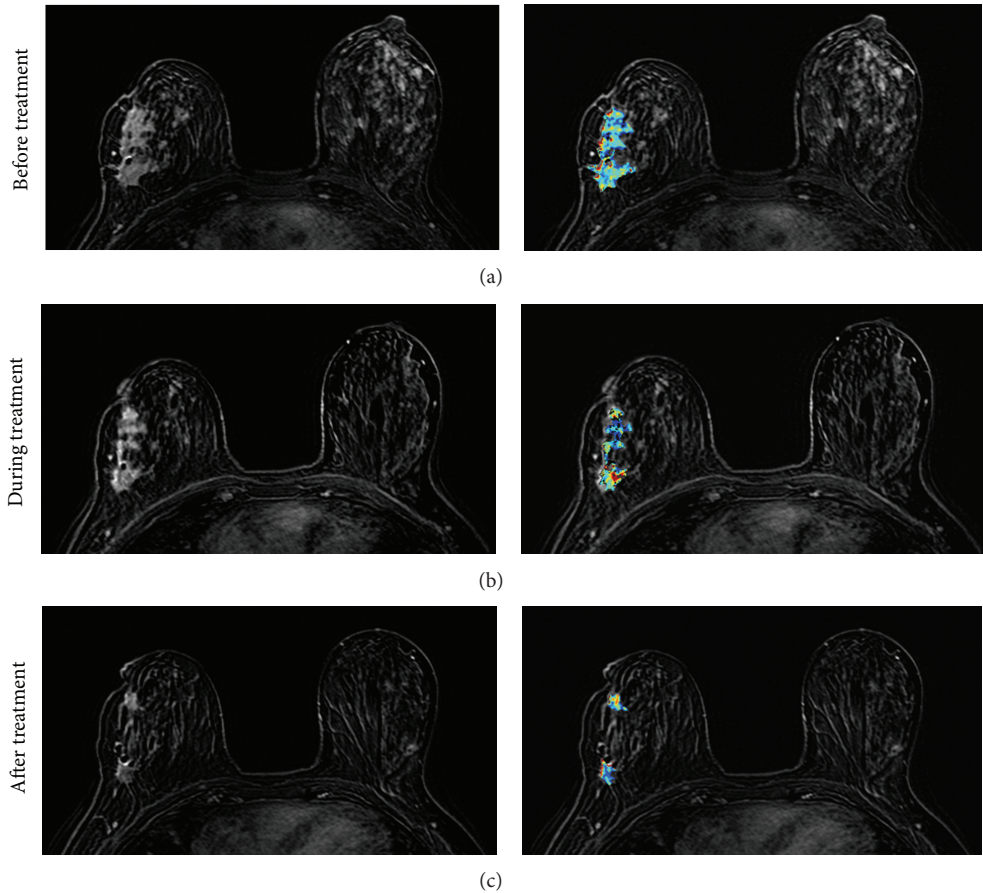


FIGURE 7: A 41-year-old patient with non-mass-like enhancement lesion (invasive ductal cancer with lobular features). From (a) to (c), the contrast-enhanced (subtraction) images selected from the same level in pretreatment, F/U-1, and F/U-2 MRI are shown. The tumor boundary cannot be clearly determined, and thus the extent of the tumor cannot be measured precisely. While the disease extent does not change much in F/U-1, it is noticeable that the area of the enhanced tissues is smaller in F/U-2 after completing NAC. The right panel shows the corresponding color-coded K^{trans} maps analyzed using pixel-by-pixel pharmacokinetic analysis within the enhanced tumor area, based on the unified Tofts model. It can be seen that the tumor breaks into two areas that show strong enhancements in F/U-2. The post-NAC pathological examination shows nearly continuous cancer clusters within a 6.5 cm region. It is typical for a non-mass lesion to show scattered diseases within the original tumor bed.

aggressive and responds better to chemotherapy, and as such the diagnostic accuracy of MRI in hormonal-negative cancer is better than in hormonal-positive cancer. It has been shown that MRI is more accurate in triple-negative or ER-negative/HER2-positive disease, but is less accurate in ER-positive/HER2-negative breast cancer [83–87]. For HER2-negative- and hormonal-receptor-positive cancers, they are more likely to show residual disease as small foci or scattered cells after NAC leading to underestimation of residual disease extent on MRI [84]. Another study, however, showed that, after multivariate analysis, molecular subtype and systemic regimen administered did not significantly influence the sensitivity, specificity, PPV, or NPV of MRI in predicting pathologic response [88]. The morphological appearance of tumor (mass versus non-mass) may have a more profound influence on the MRI accuracy than the molecular subtypes.

Since MRI done at 1.5 T showed a high false-negative diagnosis when the residual tumor was presenting as a scattered pattern with multiple small foci of invasive cancer cells

distributed in a large area [81, 82], it raises a question about whether a higher spatial resolution using 3 T may improve the accuracy. A recent study has found that breast MR done at 3.0 T still has the same limitation as 1.5 T in detection of small and scattered tumor cell clusters after NAC [84]. The higher field at 3 T comes with worse field homogeneity and longer T1 relaxation time [91, 92] which may cause lower signal and show less contrast enhancements leading to false-negative diagnosis [93–95]. Nevertheless, 3 T with a higher spatial resolution and signal-to-noise ratio may reveal more significant findings compared to 1.5 T and provide an improved assessment of the response to NAC [96]. Recently, dedicated 7 T breast MRI is proven technically feasible for monitoring NAC [97]. As more ultrahigh field MRI scanners become available, it will be interesting to see how this may be used to improve the accuracy, particularly for the non-mass lesions that present scattered minimal disease after NAC.

Preliminary results using DWI in assessing residual tumor extent after completing NAC have been reported [77],

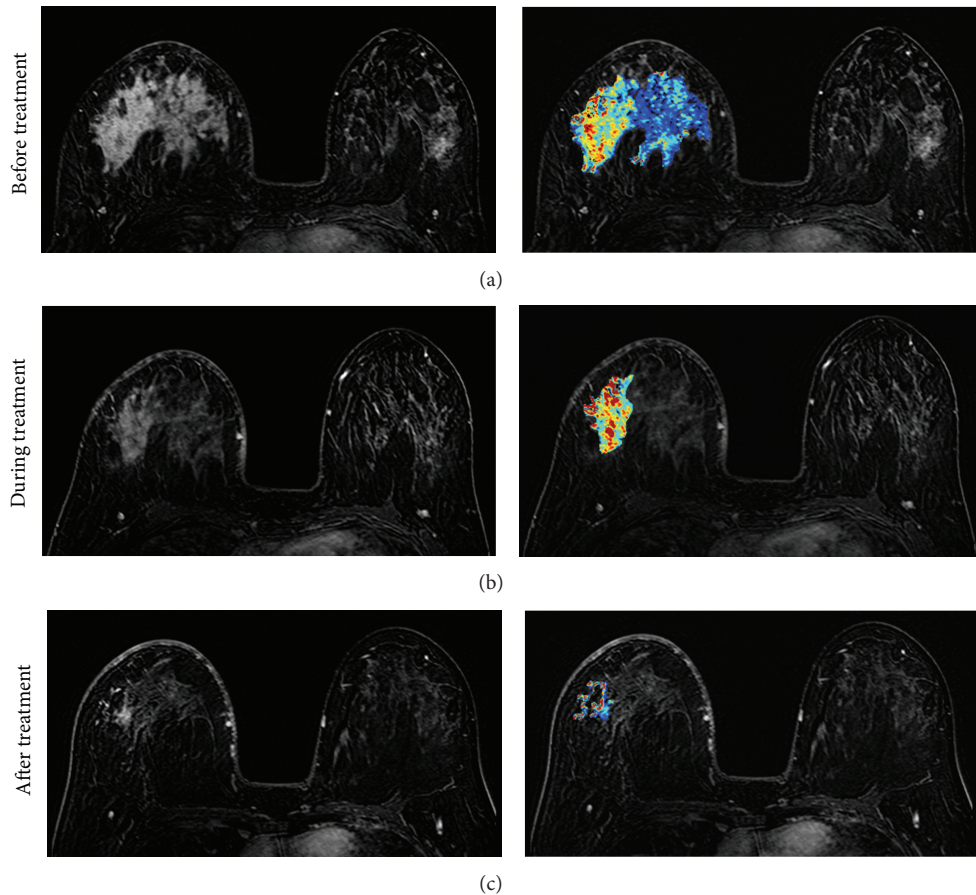


FIGURE 8: A 31-year-old patient with non-mass-like enhancement lesion (invasive ductal cancer with extensive carcinoma in situ components). From (a) to (c), the contrast-enhanced (subtraction) images selected from the same level in pretreatment, F/U-1, and F/U-2 MRI are shown. The tumor boundary cannot be clearly determined, and thus the extent of the tumor cannot be measured precisely. The area of the enhanced tumor tissues and the degree of enhancement are decreasing with treatment, indicating a good response to the chemotherapy. The right panel shows the corresponding color-coded K^{trans} maps analyzed using pixel-by-pixel pharmacokinetic analysis. The post-NAC pathological examination shows scattered cancer cells within a 10 cm region. It is typical for a non-mass lesion to show scattered diseases within the original tumor bed. Despite the decreased cancer cell density responding to NAC, this patient still needs mastectomy.

which found that the accuracy for depicting residual tumor was 96% for DWI, compared with an accuracy of 89% for contrast-enhanced MR imaging ($P = 0.06$). The use of DW imaging to visualize residual breast cancer without the need for contrast medium could be advantageous in women with impaired renal function [77]. However, since the spatial resolution of DWI is often worse than that of DCE-MRI, the advancement of scanner technology, including better gradient coil with a higher strength and less geometrical distortion, is important for DWI to reliably diagnose residual disease after completing NAC.

In patients who had more extensive pretreatment disease, despite an excellent response to NAC, the surgeons still tended to apply an aggressive approach and recommended mastectomy. Given that the confirmation of pCR or minimal residual disease would change surgeons' recommendations for less aggressive, conservation surgery, the maturity of MRI for NAC response prediction may provide reliable staging information to aid in the recommendation of the optimal surgical procedure [98].

6. Breast Stromal (Parenchymal) Enhancement Related to NAC

Background parenchymal enhancement refers to the enhancement of the normal breast glandular tissue. Age, menstrual or menopausal status, and hormonal use can affect breast glandular tissue enhancements [23–25, 30, 99, 100], and this normal tissue enhancement may impact the diagnostic performance of breast MRI [28, 99, 101–103]. The value of normal tissue enhancement in the diseased breast on MRI was noted to be associated with response to NAC [104]. Higher signal enhancement ratios in breast stroma after one cycle of chemotherapy are significantly associated with decreased local recurrence and longer disease-free survival [104]. A high stromal signal enhancement ratio may reflect greater microvessel density and thus better delivery of the chemotherapeutic agent to the tumor, which would result in a better clinical response and decreased likelihood of recurrence after surgery [104]. This research area is very new with little data, and more research is needed to investigate the

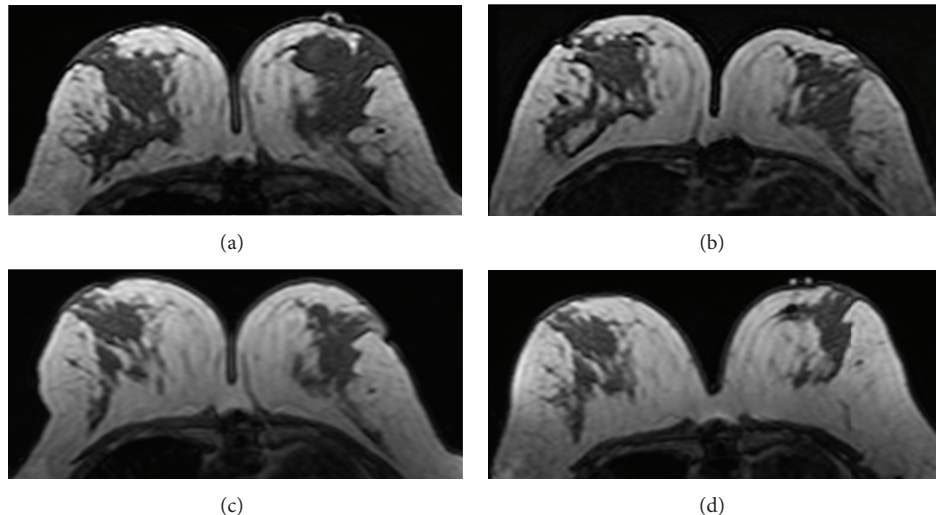


FIGURE 9: This is the same 41-year-old patient shown in Figure 3. The cancer is in the left breast, and the breast density is measured from the normal breast in the right side. From (a) to (d), the non-fat-sat T1-weighted images selected from the same level in pretreatment, F/U-1, F/U-2, and F/U-3 MRI are shown. It is noticed that the normal breast density decreases with chemotherapy. The measured percent density (fibroglandular tissue volume divided by the breast volume) is 13.4% before treatment, which decreases to 9.2% in F/U-1 after receiving 2 cycles of AC regimen and further down to 8.7% in F/U-2 and 8.2% in F/U-3.

significance of the background stromal tissue enhancement during the NAC treatment and prognosis.

7. Reduction of Breast Density following NAC

Breast density is a strong independent risk factor associated with the risk of developing breast cancer. It was found that an increase in BI-RADS density category within 3 years is associated with an increase in breast cancer risk and a decrease in density is associated with a decreased risk [105]. Change in mammographic breast density is an excellent predictor of response to tamoxifen in the preventive setting [106]. It was proven that women receiving tamoxifen and experiencing a 10% or greater reduction in breast density had 63% reduction in breast cancer risk (odds ratio = 0.37, 95% CI = 0.20 to 0.69, $P = 0.002$), whereas those who took tamoxifen but experienced less than a 10% reduction in breast density had no risk reduction (odds ratio = 1.13, 95% CI = 0.72 to 1.77, $P = 0.60$).

After NAC, normal breast tissue shows significant atrophy of the terminal ductal lobular units [107]. This includes reduction of the lobular acini, lobular sclerosis, and the attenuation of the lobular/ductal epithelium. By using MR imaging, it was found that patients receiving NAC showed decreased breast density in the normal breast, and the effects were significant after initial treatment with one to two cycles of the AC regimen (Figure 9) [31]. Our recent findings (unpublished data) also find that the taxane-based regimen causes density atrophy in the normal breast. Since the density reduction was age-dependent (more pronounced in younger patient), the NAC-related density reduction was more likely mediated through the suppression of ovarian function [108, 109]. Whether this density change in the normal breast is associated with patient's prognosis and the future risk

of developing contralateral breast cancer warrants further investigation.

8. Conclusion

In this review paper we summarized the clinical application of MRI in management of breast cancer patients undergoing NAC. As many patients may become good candidates for breast-conserving surgery, the most well-established role of MRI is to evaluate the extent of residual disease after NAC for surgical planning. During the NAC treatment, MRI can be performed at different times to evaluate the response to different drug regimens, and that provides opportunities for timely adjustment of treatment protocols to improve the chance of achieving pCR while avoiding unnecessary toxicity. DCE-MRI with a high spatial resolution and a good tissue contrast is essential to evaluate the change of tumor size, which is still the most reliable response indicator. Proton MR spectroscopy can detect early response based on the changes in choline or water:fat ratio, but the difficulty in quantification makes MRS not a reliable tool for predicting NAC response. Diffusion-weighted MRI has a great potential to provide early response indicator based on the altered cell membrane and cell death, but the relatively low spatial resolution and image distortion limit DWI to become a good tool for evaluating the extent of residual disease after NAC. The background parenchymal enhancement and the density of the normal breast tissue are two emerging parameters that are currently being investigated. These MR imaging parameters may also have a prognostic value to predict patient's disease-free and overall survival, which needs to be further established. Overall, MRI is a valuable imaging modality for evaluating the pretreatment disease, response during NAC, and the residual disease after completing NAC. With the

continuing technology advancement and more widespread use of MRI, it will benefit many more breast cancer patients in the future by providing them with individualized image-guided treatment and personalized management.

Acknowledgment

This work was supported in part by NIH/NCI Grants R01 CA127927 and R03 CA136071.

References

- [1] M. Kaufmann, G. N. Hortobagyi, A. Goldhirsch et al., "Recommendations from an international expert panel on the use of neoadjuvant (primary) systemic treatment of operable breast cancer: an update," *Journal of Clinical Oncology*, vol. 24, no. 12, pp. 1940–1949, 2006.
- [2] M. Kaufmann, G. Von Minckwitz, H. D. Bear et al., "Recommendations from an international expert panel on the use of neoadjuvant (primary) systemic treatment of operable breast cancer: new perspectives 2006," *Annals of Oncology*, vol. 18, no. 12, pp. 1927–1934, 2007.
- [3] J. R. Gralow, H. J. Burstein, W. Wood et al., "Preoperative therapy in invasive breast cancer: pathologic assessment and systemic therapy issues in operable disease," *Journal of Clinical Oncology*, vol. 26, no. 5, pp. 814–819, 2008.
- [4] S. Loibl, G. Von Minckwitz, G. Raab et al., "Surgical procedures after neoadjuvant chemotherapy in operable breast cancer: results of the GEPARDUO trial," *Annals of Surgical Oncology*, vol. 13, no. 11, pp. 1434–1442, 2006.
- [5] J. S. D. Mieog, J. A. Van Der Hage, and C. J. H. Van De Velde, "Neoadjuvant chemotherapy for operable breast cancer," *British Journal of Surgery*, vol. 94, no. 10, pp. 1189–1200, 2007.
- [6] P. Rastogi, S. J. Anderson, H. D. Bear et al., "Preoperative chemotherapy: updates of national surgical adjuvant breast and bowel project protocols B-18 and B-27," *Journal of Clinical Oncology*, vol. 26, no. 5, pp. 778–785, 2008.
- [7] J. S. Jeruss, E. A. Mittendorf, S. L. Tucker et al., "Combined use of clinical and pathologic staging variables to define outcomes for breast cancer patients treated with neoadjuvant therapy," *Journal of Clinical Oncology*, vol. 26, no. 2, pp. 246–252, 2008.
- [8] W. F. Symmans, F. Peintinger, C. Hatzis et al., "Measurement of residual breast cancer burden to predict survival after neoadjuvant chemotherapy," *Journal of Clinical Oncology*, vol. 25, no. 28, pp. 4414–4422, 2007.
- [9] A. M. Chen, F. Meric-Bernstam, K. K. Hunt et al., "Breast conservation after neoadjuvant chemotherapy: the M.D. Anderson cancer center experience," *Journal of Clinical Oncology*, vol. 22, no. 12, pp. 2303–2312, 2004.
- [10] F. Peintinger, W. F. Symmans, A. M. Gonzalez-Angulo et al., "The safety of breast-conserving surgery in patients who achieve a complete pathologic response after neoadjuvant chemotherapy," *Cancer*, vol. 107, no. 6, pp. 1248–1254, 2006.
- [11] J. L. Oh, M. J. Dryden, W. A. Woodward et al., "Locoregional control of clinically diagnosed multifocal or multicentric breast cancer after neoadjuvant chemotherapy and locoregional therapy," *Journal of Clinical Oncology*, vol. 24, no. 31, pp. 4971–4975, 2006.
- [12] A. M. Chen, F. Meric-Bernstam, K. K. Hunt et al., "Breast conservation after neoadjuvant chemotherapy: a prognostic index for clinical decision-making," *Cancer*, vol. 103, no. 4, pp. 689–695, 2005.
- [13] S. J. Vinnicombe, A. D. MacVicar, R. L. Guy et al., "Primary breast cancer: mammographic changes after neoadjuvant chemotherapy, with pathologic correlation," *Radiology*, vol. 198, no. 2, pp. 333–340, 1996.
- [14] H. Junkermann and D. Von Fournier, "Imaging procedures for assessment of the response of mammary carcinoma to preoperative chemotherapy," *Radiologe*, vol. 37, no. 9, pp. 726–732, 1997.
- [15] J. Herrada, R. B. Iyer, E. N. Atkinson, N. Sneige, A. U. Buzdar, and G. N. Hortobagyi, "Relative value of physical examination, mammography, and breast sonography in evaluating the size of the primary tumor and regional lymph node metastases in women receiving neoadjuvant chemotherapy for locally advanced breast carcinoma," *Clinical Cancer Research*, vol. 3, no. 9, pp. 1565–1569, 1997.
- [16] L. Esserman, E. Kaplan, S. Partridge et al., "MRI phenotype is associated with response to doxorubicin and cyclophosphamide neoadjuvant chemotherapy in stage III breast cancer," *Annals of Surgical Oncology*, vol. 8, no. 6, pp. 549–559, 2001.
- [17] C. Balu-Maestro, C. Chapellier, A. Bleuse, I. Chanalet, C. Chauvel, and R. Largillier, "Imaging in evaluation of response to neoadjuvant breast cancer treatment benefits of MRI," *Breast Cancer Research and Treatment*, vol. 72, no. 2, pp. 145–152, 2002.
- [18] A. Rieber, H.-B. Brambs, A. Gabelmann, V. Heilmann, R. Kreienberg, and T. Kühn, "Breast MRI for monitoring response of primary breast cancer to neo-adjuvant chemotherapy," *European Radiology*, vol. 12, no. 7, pp. 1711–1719, 2002.
- [19] P. L. Choyke, A. J. Dwyer, and M. V. Knopp, "Functional tumor imaging with dynamic contrast-enhanced magnetic resonance imaging," *Journal of Magnetic Resonance Imaging*, vol. 17, no. 5, pp. 509–520, 2003.
- [20] P. S. Tofts and A. G. Kermode, "Measurement of the blood-brain barrier permeability and leakage space using dynamic MR imaging. 1. Fundamental concepts," *Magnetic Resonance in Medicine*, vol. 17, no. 2, pp. 357–367, 1991.
- [21] P. S. Tofts, "Modeling tracer kinetics in dynamic Gd-DTPA MR imaging," *Journal of Magnetic Resonance Imaging*, vol. 7, no. 1, pp. 91–101, 1997.
- [22] M. W. Ah-See, A. Makris, N. J. Taylor et al., "Early changes in functional dynamic magnetic resonance imaging predict for pathologic response to neoadjuvant chemotherapy in primary breast cancer," *Clinical Cancer Research*, vol. 14, no. 20, pp. 6580–6589, 2008.
- [23] C. K. Kuhl, H. B. Bieling, J. Gieseke et al., "Healthy premenopausal breast parenchyma in dynamic contrast-enhanced MR imaging of the breast: normal contrast medium enhancement and cyclical-phase dependency," *Radiology*, vol. 203, no. 1, pp. 137–144, 1997.
- [24] M. Müller-Schimpffle, K. Ohmenhäuser, P. Stoll, K. Dietz, and C. D. Claussen, "Menstrual cycle and age: influence on parenchymal contrast medium enhancement in MR imaging of the breast," *Radiology*, vol. 203, no. 1, pp. 145–149, 1997.
- [25] P. A. Baltzer, M. Dietzel, T. Vag et al., "Clinical MR mammography: impact of hormonal status on background enhancement and diagnostic accuracy," *RoFo Fortschritte auf dem Gebiet der Rontgenstrahlen und der Bildgebenden Verfahren*, vol. 183, no. 5, pp. 441–447, 2011.
- [26] S. A. Jansen, V. C. Lin, M. L. Giger, H. Li, G. S. Karczmar, and G. M. Newstead, "Normal parenchymal enhancement patterns in women undergoing MR screening of the breast," *European Radiology*, vol. 21, no. 7, pp. 1374–1382, 2011.

- [27] C. Klifa, S. Suzuki, S. Aliu et al., "Quantification of background enhancement in breast magnetic resonance imaging," *Journal of Magnetic Resonance Imaging*, vol. 33, no. 5, pp. 1229–1234, 2011.
- [28] T. Uematsu, M. Kasami, and J. Watanabe, "Does the degree of background enhancement in breast MRI affect the detection and staging of breast cancer?" *European Radiology*, vol. 21, no. 11, pp. 2261–2267, 2011.
- [29] T. Uematsu, M. Kasami, and J. Watanabe, "Background enhancement of mammary glandular tissue on breast dynamic MRI: imaging features and effect on assessment of breast cancer extent," *Breast Cancer*, vol. 19, no. 3, pp. 259–265, 2012.
- [30] V. King, J. D. Brooks, J. L. Bernstein, A. S. Reiner, M. C. Pike, and E. A. Morris, "Background parenchymal enhancement at breast MR imaging and breast cancer risk," *Radiology*, vol. 260, no. 1, pp. 50–60, 2011.
- [31] J. Chen, K. Nie, S. Bahri et al., "Decrease in breast density in the contralateral normal breast of patients receiving neoadjuvant chemotherapy: MR imaging evaluation," *Radiology*, vol. 255, no. 1, pp. 44–52, 2010.
- [32] T. Uematsu, M. Kasami, and S. Yuen, "Neoadjuvant chemotherapy for breast cancer: correlation between the baseline MR imaging findings and responses to therapy," *European Radiology*, vol. 20, no. 10, pp. 2315–2322, 2010.
- [33] H. Kawashima, M. Inokuchi, H. Furukawa, and S. Kitamura, "Triple-negative breast cancer. Are the imaging findings different between responders and nonresponders to neoadjuvant chemotherapy?" *Academic Radiology*, vol. 18, no. 8, pp. 963–969, 2011.
- [34] R. Prevost, M. L. Smidt, V. C. Tjan-Heijnen et al., "Pre-treatment differences and early response monitoring of neoadjuvant chemotherapy in breast cancer patients using magnetic resonance imaging: a systematic review," *European Radiology*, vol. 22, no. 12, pp. 2607–2616, 2012.
- [35] M. D. Pickles, D. J. Manton, M. Lowry, and L. W. Turnbull, "Prognostic value of pre-treatment DCE-MRI parameters in predicting disease free and overall survival for breast cancer patients undergoing neoadjuvant chemotherapy," *European Journal of Radiology*, vol. 71, no. 3, pp. 498–505, 2009.
- [36] M. G. Heldahl, T. F. Bathen, J. Rydland et al., "Prognostic value of pretreatment dynamic contrast-enhanced MR imaging in breast cancer patients receiving neoadjuvant chemotherapy: overall survival predicted from combined time course and volume analysis," *Acta Radiologica*, vol. 51, no. 6, pp. 604–612, 2010.
- [37] S. P. Li, A. Makris, M. J. Beresford et al., "Use of dynamic contrast-enhanced MR imaging to predict survival in patients with primary breast cancer undergoing neoadjuvant chemotherapy," *Radiology*, vol. 260, no. 1, pp. 68–78, 2011.
- [38] D. J. Manton, A. Chaturvedi, A. Hubbard et al., "Neoadjuvant chemotherapy in breast cancer: early response prediction with quantitative MR imaging and spectroscopy," *British Journal of Cancer*, vol. 94, no. 3, pp. 427–435, 2006.
- [39] A. R. Padhani, C. Hayes, L. Assersohn et al., "Prediction of clinicopathologic response of breast cancer to primary chemotherapy at contrast-enhanced mr imaging: initial clinical results," *Radiology*, vol. 239, no. 2, pp. 361–374, 2006.
- [40] M. D. Pickles, M. Lowry, D. J. Manton, P. Gibbs, and L. W. Turnbull, "Role of dynamic contrast enhanced MRI in monitoring early response of locally advanced breast cancer to neoadjuvant chemotherapy," *Breast Cancer Research and Treatment*, vol. 91, no. 1, pp. 1–10, 2005.
- [41] H. J. Yu, J. Chen, R. S. Mehta, O. Nalcioglu, and M. Su, "MRI measurements of tumor size and pharmacokinetic parameters as early predictors of response in breast cancer patients undergoing neoadjuvant anthracycline chemotherapy," *Journal of Magnetic Resonance Imaging*, vol. 26, no. 3, pp. 615–623, 2007.
- [42] C. de Bazelaire, R. Calmon, I. Thomassin et al., "Accuracy of perfusion MRI with high spatial but low temporal resolution to assess invasive breast cancer response to neoadjuvant chemotherapy: a retrospective study," *BMC Cancer*, vol. 11, article no. 361, 2011.
- [43] S. Mehta, N. P. Hughes, F. M. Buffa et al., "Assessing early therapeutic response to bevacizumab in primary breast cancer using magnetic resonance imaging and gene expression profiles," *Journal of the National Cancer Institute*, vol. 2011, no. 43, pp. 71–74, 2011.
- [44] J. C. Miller, H. H. Pien, D. Sahani, A. G. Sorensen, and J. H. Thrall, "Imaging angiogenesis: application and potential for drug development," *Journal of the National Cancer Institute*, vol. 97, no. 3, pp. 172–187, 2005.
- [45] A. R. Padhani and M. O. Leach, "Antivascular cancer treatments: functional assessments by dynamic contrast-enhanced magnetic resonance imaging," *Abdominal Imaging*, vol. 30, no. 3, pp. 324–341, 2005.
- [46] S. Rehman and G. C. Jayson, "Molecular imaging of antiangiogenic agents," *Oncologist*, vol. 10, no. 2, pp. 92–103, 2005.
- [47] O. M. Hahn, C. Yang, M. Medved et al., "Dynamic contrast-enhanced magnetic resonance imaging pharmacodynamic biomarker study of sorafenib in metastatic renal carcinoma," *Journal of Clinical Oncology*, vol. 26, no. 28, pp. 4572–4578, 2008.
- [48] A. Moreno-Aspitia, R. F. Morton, D. W. Hillman et al., "Phase II trial of sorafenib in patients with metastatic breast cancer previously exposed to anthracyclines or taxanes: north central cancer treatment group and mayo clinic trial n0336," *Journal of Clinical Oncology*, vol. 27, no. 1, pp. 11–15, 2009.
- [49] J. P. B. O'Connor, A. Jackson, G. J. M. Parker, and G. C. Jayson, "DCE-MRI biomarkers in the clinical evaluation of antiangiogenic and vascular disrupting agents," *British Journal of Cancer*, vol. 96, no. 2, pp. 189–195, 2007.
- [50] A. Thukral, D. M. Thomasson, C. K. Chow et al., "Inflammatory breast cancer: dynamic contrast-enhanced MR in patients receiving bevacizumab - Initial experience," *Radiology*, vol. 244, no. 3, pp. 727–735, 2007.
- [51] K. A. Kvistad, I. J. Bakken, I. S. Gribbestad et al., "Characterization of neoplastic and normal human breast tissues with in vivo ¹H MR spectroscopy," *Journal of Magnetic Resonance Imaging*, vol. 10, pp. 159–164, 1999.
- [52] N. R. Jagannathan, M. Kumar, V. Seenu et al., "Evaluation of total choline from in-vivo volume localized proton MR spectroscopy and its response to neoadjuvant chemotherapy in locally advanced breast cancer," *British Journal of Cancer*, vol. 84, no. 8, pp. 1016–1022, 2001.
- [53] S. Meisamy, P. J. Bolan, E. H. Baker et al., "Neoadjuvant chemotherapy of locally advanced breast cancer: predicting response with in vivo ¹H MR spectroscopy - A pilot study at 4 T," *Radiology*, vol. 233, no. 2, pp. 424–431, 2004.
- [54] H. M. Baek, J. H. Chen, O. Nalcioglu, and M. Y. Su, "Proton MR spectroscopy for monitoring early treatment response of breast cancer to neo-adjuvant chemotherapy," *Annals of Oncology*, vol. 19, no. 5, pp. 1022–1024, 2008.
- [55] H. Baek, J. Chen, K. Nie et al., "Predicting pathologic response to neoadjuvant chemotherapy in breast cancer by using MR

- imaging and quantitative ^1H MR spectroscopy," *Radiology*, vol. 251, no. 3, pp. 653–662, 2009.
- [56] M. Tozaki, M. Sakamoto, Y. Oyama, K. Maruyama, and E. Fukuma, "Predicting pathological response to neoadjuvant chemotherapy in breast cancer with quantitative ^1H MR spectroscopy using the external standard method," *Journal of Magnetic Resonance Imaging*, vol. 31, no. 4, pp. 895–902, 2010.
- [57] M. Tozaki, Y. Oyama, and E. Fukuma, "Preliminary study of early response to neoadjuvant chemotherapy after the first cycle in breast cancer: comparison of ^1H magnetic resonance spectroscopy with diffusion magnetic resonance imaging," *Japanese Journal of Radiology*, vol. 28, no. 2, pp. 101–109, 2010.
- [58] T. F. Bathen, M. G. Heldahl, B. Sitter et al., "In vivo MRS of locally advanced breast cancer: characteristics related to negative or positive choline detection and early monitoring of treatment response," *Magma*, vol. 24, no. 6, pp. 347–357, 2011.
- [59] P. E. Sijens, H. K. Wijrdeman, M. A. Moerland, C. J. G. Bakker, J. W. A. H. Vermeulen, and P. R. Luyten, "Human breast cancer in vivo: $\text{H}-1$ and $\text{P}-31$ MR spectroscopy at 1.5 T," *Radiology*, vol. 169, no. 3, pp. 615–620, 1988.
- [60] M. Albert Thomas, N. Binesh, K. Yue, and N. Debruhl, "Volume-localized two-dimensional correlated magnetic resonance spectroscopy of human breast cancer," *Journal of Magnetic Resonance Imaging*, vol. 14, no. 2, pp. 181–186, 2001.
- [61] M. Kumar, N. R. Jagannathan, V. Seenu, S. N. Dwivedi, P. K. Julka, and G. K. Rath, "Monitoring the therapeutic response of locally advanced breast cancer patients: sequential in vivo proton MR spectroscopy study," *Journal of Magnetic Resonance Imaging*, vol. 24, no. 2, pp. 325–332, 2006.
- [62] E. A. M. O'Flynn and N. M. DeSouza, "Correction: functional magnetic resonance: biomarkers of response in breast cancer," *Breast Cancer Research*, vol. 13, no. 1, article 204, 2011.
- [63] L. Wu, J. Hu, H. Gu, J. Hua, J. Chen, and J. Xu, "Can diffusion-weighted MR imaging and contrast-enhanced MR imaging precisely evaluate and predict pathological response to neoadjuvant chemotherapy in patients with breast cancer?" *Breast Cancer Research and Treatment*, vol. 135, no. 1, pp. 17–28, 2012.
- [64] M. D. Pickles, P. Gibbs, M. Lowry, and L. W. Turnbull, "Diffusion changes precede size reduction in neoadjuvant treatment of breast cancer," *Magnetic Resonance Imaging*, vol. 24, no. 7, pp. 843–847, 2006.
- [65] U. Sharma, K. K. A. Danishad, V. Seenu, and N. R. Jagannathan, "Longitudinal study of the assessment by MRI and diffusion-weighted imaging of tumor response in patients with locally advanced breast cancer undergoing neoadjuvant chemotherapy," *NMR in Biomedicine*, vol. 22, no. 1, pp. 104–113, 2009.
- [66] L. Nilsen, A. Fangberget, O. Geier, D. R. Olsen, and T. Seierstad, "Diffusion-weighted magnetic resonance imaging for pretreatment prediction and monitoring of treatment response of patients with locally advanced breast cancer undergoing neoadjuvant chemotherapy," *Acta Oncologica*, vol. 49, no. 3, pp. 354–360, 2010.
- [67] K. C. Lee, B. A. Moffat, A. F. Schott et al., "Prospective early response imaging biomarker for neoadjuvant breast cancer chemotherapy," *Clinical Cancer Research*, vol. 13, no. 2, part 1, pp. 443–450, 2007.
- [68] P. Belli, M. Costantini, C. Ierardi et al., "Diffusion-weighted imaging in evaluating the response to neoadjuvant breast cancer treatment," *Breast Journal*, vol. 17, no. 6, pp. 610–619, 2011.
- [69] L. R. Jensen, B. Garzon, M. G. Heldahl, T. F. Bathen, S. Lundgren, and I. S. Gribbestad, "Diffusion-weighted and dynamic contrast-enhanced MRI in evaluation of early treatment effects during neoadjuvant chemotherapy in breast cancer patients," *Journal of Magnetic Resonance Imaging*, vol. 34, no. 5, pp. 1099–1109, 2011.
- [70] M. Kawamura, H. Satake, S. Ishigaki, A. Nishio, M. Sawaki, and S. Naganawa, "Early prediction of response to neoadjuvant chemotherapy for locally advanced breast cancer using MRI," *Nagoya Journal of Medical Science*, vol. 73, no. 3-4, pp. 147–156, 2011.
- [71] A. Fangberget, L. B. Nilsen, K. H. Hole et al., "Neoadjuvant chemotherapy in breast cancer-response evaluation and prediction of response to treatment using dynamic contrast-enhanced and diffusion-weighted MR imaging," *European Radiology*, vol. 21, no. 6, pp. 1188–1199, 2011.
- [72] S. H. Park, W. K. Moon, N. Cho et al., "Comparison of diffusion-weighted MR imaging and FDG PET/CT to predict pathological complete response to neoadjuvant chemotherapy in patients with breast cancer," *European Radiology*, vol. 22, no. 1, pp. 18–25, 2012.
- [73] S. H. Park, W. K. Moon, N. Cho et al., "Diffusion-weighted MR imaging: pretreatment prediction of response to neoadjuvant chemotherapy in patients with breast cancer," *Radiology*, vol. 257, no. 1, pp. 56–63, 2010.
- [74] C. Iacconi, M. Giannelli, C. Marini et al., "The role of mean diffusivity (MD) as a predictive index of the response to chemotherapy in locally advanced breast cancer: A Preliminary Study," *European Radiology*, vol. 20, no. 2, pp. 303–308, 2010.
- [75] P. D. Humphries, N. J. Sebire, M. J. Siegel, and Ø. E. Olsen, "Tumors in pediatric patients at diffusion-weighted MR imaging: apparent diffusion coefficient and tumor cellularity," *Radiology*, vol. 245, no. 3, pp. 848–854, 2007.
- [76] A. C. Guo, T. J. Cummings, R. C. Dash, and J. M. Provenzale, "Lymphomas and high-grade astrocytomas: comparison of water diffusibility and histologic characteristics," *Radiology*, vol. 224, no. 1, pp. 177–183, 2002.
- [77] R. Woodhams, S. Kakita, H. Hata et al., "Identification of residual breast carcinoma following neoadjuvant chemotherapy: diffusion-weighted imaging—comparison with contrast-enhanced MR imaging and pathologic findings," *Radiology*, vol. 254, no. 2, pp. 357–366, 2010.
- [78] H. G. Moon, W. Han, J. Q. Lee et al., "Age and HER2 expression status affect MRI accuracy in predicting residual tumor extent after neo-adjuvant systemic treatment," *Annals of Oncology*, vol. 20, no. 4, pp. 636–641, 2009.
- [79] S. C. Partridge, J. E. Gibbs, Y. Lu, L. J. Esserman, D. Sudilovsky, and N. M. Hylton, "Accuracy of MR imaging for revealing residual breast cancer in patients who have undergone neoadjuvant chemotherapy," *American Journal of Roentgenology*, vol. 179, no. 5, pp. 1193–1199, 2002.
- [80] S. Orel, "Who should have breast magnetic resonance imaging evaluation?" *Journal of Clinical Oncology*, vol. 26, no. 5, pp. 703–711, 2008.
- [81] J. H. Chen, B. Feig, G. Agrawal et al., "MRI evaluation of pathologically complete response and residual tumors in breast cancer after neoadjuvant chemotherapy," *Cancer*, vol. 112, no. 7, pp. 17–26, 2008.
- [82] S. Bahri, J. Chen, R. S. Mehta et al., "Residual breast cancer diagnosed by MRI in patients receiving neoadjuvant chemotherapy with and without bevacizumab," *Annals of Surgical Oncology*, vol. 16, no. 6, pp. 1619–1628, 2009.
- [83] C. E. Loo, M. E. Straver, S. Rodenhuis et al., "Magnetic resonance imaging response monitoring of breast cancer during

- neoadjuvant chemotherapy: relevance of breast cancer subtype," *Journal of Clinical Oncology*, vol. 29, no. 6, pp. 660–666, 2011.
- [84] J. Chen, S. Bahri, R. S. Mehta et al., "Breast cancer: evaluation of response to neoadjuvant chemotherapy with 3.0-T MR imaging," *Radiology*, vol. 261, no. 3, pp. 735–743, 2011.
- [85] K. P. McGuire, J. Toro-Burguete, H. Dang et al., "MRI staging after neoadjuvant chemotherapy for breast cancer: does tumor biology affect accuracy?" *Annals of Surgical Oncology*, vol. 18, no. 11, pp. 3149–3154, 2011.
- [86] H. Nakahara, Y. Yasuda, E. Machida et al., "MR and US imaging for breast cancer patients who underwent conservation surgery after neoadjuvant chemotherapy: comparison of triple negative breast cancer and other intrinsic subtypes," *Breast Cancer*, vol. 18, no. 3, pp. 152–160, 2011.
- [87] L. M. Marcos de Paz, A. Tejerina Bernal, M. L. Arranz Merino, and V. Calvo de Juan, "Breast MR imaging changes after neoadjuvant chemotherapy: correlation with molecular subtypes," *Radiología*, vol. 54, no. 5, pp. 442–448, 2012.
- [88] J. De Los Santos, W. Bernreuter, K. Keene et al., "Accuracy of breast magnetic resonance imaging in predicting pathologic response in patients treated with neoadjuvant chemotherapy," *Clinical Breast Cancer*, vol. 11, no. 5, pp. 312–319, 2011.
- [89] A. Kuzucan, J. Chen, S. Bahri et al., "Diagnostic performance of magnetic resonance imaging for assessing tumor response in patients with HER2-negative breast cancer receiving neoadjuvant chemotherapy is associated with molecular biomarker profile," *Clinical Breast Cancer*, vol. 12, no. 2, pp. 110–118, 2012.
- [90] J. H. Chen, R. S. Mehta, P. M. Carpenter, O. Nalcioglu, and M. Y. Su, "Magnetic resonance imaging in predicting pathological response of triple negative breast cancer following neoadjuvant chemotherapy," *Journal of Clinical Oncology*, vol. 25, no. 35, pp. 5667–5669, 2007.
- [91] D. G. Norris, "High Field Human Imaging," *Journal of Magnetic Resonance Imaging*, vol. 18, no. 5, pp. 519–529, 2003.
- [92] N. Morakkabati-Spitz, J. Gieseke, C. Kuhl et al., "MRI of the pelvis at 3 T: very high spatial resolution with sensitivity encoding and flip-angle sweep technique in clinically acceptable scan time," *European Radiology*, vol. 16, no. 3, pp. 634–641, 2006.
- [93] C. K. Kuhl, H. Kooijman, J. Gieseke, and H. H. Schild, "Effect of B1 inhomogeneity on breast MR imaging at 3.0 T," *Radiology*, vol. 244, no. 3, pp. 929–930, 2007.
- [94] R. M. Mann, C. K. Kuhl, K. Kinkel, and C. Boetes, "Breast MRI: guidelines from the European Society of Breast Imaging," *European Radiology*, vol. 18, no. 7, pp. 1307–1318, 2008.
- [95] C. A. Azlan, P. Di Giovanni, T. S. Ahearn, S. I. K. Semple, F. J. Gilbert, and T. W. Redpath, "B1 transmission-field inhomogeneity and enhancement ratio errors in dynamic contrast-enhanced MRI (DCE-MRI) of the breast at 3T," *Journal of Magnetic Resonance Imaging*, vol. 31, no. 1, pp. 234–239, 2010.
- [96] M. G. Heldahl, S. Lundgren, L. R. Jensen, I. S. Gribbestad, and T. F. Bathan, "Monitoring neoadjuvant chemotherapy in breast cancer patients: improved MR assessment at 3 T?" *Journal of Magnetic Resonance Imaging*, vol. 34, no. 3, pp. 547–556, 2011.
- [97] M. A. Korteweg, W. B. Veldhuis, F. Visser et al., "Feasibility of 7 Tesla breast magnetic resonance imaging determination of intrinsic sensitivity and high-resolution magnetic resonance imaging, diffusion-weighted imaging, and 1H-magnetic resonance spectroscopy of breast cancer patients receiving neoadjuvant therapy," *Investigative Radiology*, vol. 46, no. 6, pp. 370–376, 2011.
- [98] J. Chen, B. A. Feig, D. J. Hsiang et al., "Impact of MRI-evaluated neoadjuvant chemotherapy response on change of surgical recommendation in breast cancer," *Annals of Surgery*, vol. 249, no. 3, pp. 448–454, 2009.
- [99] E. A. Morris, "Diagnostic breast MR imaging: current status and future directions," *Radiologic Clinics of North America*, vol. 45, no. 5, pp. 863–880, 2007.
- [100] C. Kuhl, "The current status of breast MR imaging—part I: choice of technique, image interpretation, diagnostic accuracy, and transfer to clinical practice," *Radiology*, vol. 244, no. 2, pp. 356–378, 2007.
- [101] C. K. Kuhl, "Current status of breast MR imaging—part 2: clinical applications," *Radiology*, vol. 244, no. 3, pp. 672–691, 2007.
- [102] R. Cubuk, N. Tasali, B. Narin, F. Keskiner, L. Celik, and S. Guney, "Correlation between breast density in mammography and background enhancement in MR mammography," *Radiologia Medica*, vol. 115, no. 3, pp. 434–441, 2010.
- [103] E. S. Ko, B. H. Lee, H. Y. Choi, R. B. Kim, and W. Noh, "Background enhancement in breast MR: correlation with breast density in mammography and background echotexture in ultrasound," *European Journal of Radiology*, vol. 80, no. 3, pp. 719–723, 2011.
- [104] J. Hattangadi, C. Park, J. Rembert et al., "Breast stromal enhancement on MRI is associated with response to neoadjuvant chemotherapy," *American Journal of Roentgenology*, vol. 190, no. 6, pp. 1630–1636, 2008.
- [105] K. Kerlikowske, L. Ichikawa, D. L. Miglioretti et al., "Longitudinal measurement of clinical mammographic breast density to improve estimation of breast cancer risk," *Journal of the National Cancer Institute*, vol. 99, no. 5, pp. 386–395, 2007.
- [106] J. Cuzick, J. Warwick, E. Pinney et al., "Tamoxifen-induced reduction in mammographic density and breast cancer risk reduction: a nested case-control study," *Journal of the National Cancer Institute*, vol. 103, no. 9, pp. 744–752, 2011.
- [107] S. J. Schnitt and L. C. Collins, *Biopsy Interpretation of the Breast Treatment Effects*, Lippincott Williams and Wilkins, Philadelphia, Pa, USA, 2009.
- [108] S. E. Minton and P. N. Munster, "Chemotherapy-induced amenorrhea and fertility in women undergoing adjuvant treatment for breast cancer," *Cancer Control*, vol. 9, no. 6, pp. 466–472, 2002.
- [109] Y. Tham, K. Sexton, H. Weiss, R. Elledge, L. C. Friedman, and R. Kramer, "The rates of chemotherapy-induced amenorrhea in patients treated with adjuvant doxorubicin and cyclophosphamide followed by a taxane," *American Journal of Clinical Oncology*, vol. 30, no. 2, pp. 126–132, 2007.

Review Article

Advanced MR Imaging of Gliomas: An Update

**Hung-Wen Kao,^{1,2} Shih-Wei Chiang,^{2,3} Hsiao-Wen Chung,^{2,3}
Fong Y. Tsai,^{4,5} and Cheng-Yu Chen²**

¹ Department of Biomedical Imaging and Radiological Sciences, National Yang-Ming University, No. 155, Sec. 2, Linong Street, Taipei 112, Taiwan

² Department of Radiology, Tri-Service General Hospital, National Defense Medical Center, No. 325, Sec. 2, Cheng-Kung Road, Neihu, Taipei 114, Taiwan

³ Department of Electrical Engineering, National Taiwan University, No. 1, Sec. 4, Roosevelt Road, Taipei 106, Taiwan

⁴ Imaging Research Center, Taipei Medical University, No. 250, Wu-Hsing Street, Taipei 110, Taiwan

⁵ Department of Radiological Sciences, University of California at Irvine Medical Center, Irvine, 101 The City Drive South, Orange, CA 92868, USA

Correspondence should be addressed to Cheng-Yu Chen; sandy0928@seed.net.tw

Received 9 January 2013; Revised 12 April 2013; Accepted 13 May 2013

Academic Editor: Shaoli Song

Copyright © 2013 Hung-Wen Kao et al. This is an open access article distributed under the Creative Commons Attribution License, which permits unrestricted use, distribution, and reproduction in any medium, provided the original work is properly cited.

Recent advances in the treatment of cerebral gliomas have increased the demands on noninvasive neuroimaging for the diagnosis, therapeutic planning, tumor monitoring, and patient outcome prediction. In the meantime, improved magnetic resonance (MR) imaging techniques have shown much potentials in evaluating the key pathological features of the gliomas, including cellularity, invasiveness, mitotic activity, angiogenesis, and necrosis, hence, further shedding light on glioma grading before treatment. In this paper, an update of advanced MR imaging techniques is reviewed, and their potential roles as biomarkers of tumor grading are discussed.

1. Introduction

Cerebral gliomas are the most common and devastating primary brain tumors. Although these tumors are traditionally considered to be arising from normal glial cells, the origin of the tumors remains undetermined. More recently, neural stem cells or progenitors are proposed to be the source of glioma [1]. The World Health Organization (WHO) published a classification system of central nervous system tumors in 1979 and subsequently revised the system in 2000 and 2007. In 2007 system, the major neuroepithelial tumors include astrocytic, oligodendroglial, oligoastrocytic, ependymal, and choroid plexus tumors. The grading of gliomas mainly relies on histological features, including cellularity, nuclear atypia, mitotic activity, vascularity, and necrosis, observed on light microscopy with the aid of immunohistochemistry.

Among the gliomas, astrocytic tumors are the most common and usually divided into circumscribed and diffuse

tumors. The circumscribed tumors are generally in lower grade occurring in young patients while the diffuse tumors are the most common cerebral tumors in adults belonging to WHO grades, II, III, and IV [2]. As the names imply, circumscribed tumors, such as pilocytic astrocytoma (WHO grade I), are localized with distinct margin and diffuse tumors are notorious in their propensity to infiltrate surrounding parenchyma, irrespective of the grades. The WHO grade II astrocytomas consist of diffusely infiltrative and well-differentiated fibrillary, protoplasmic, or gemistocytic astrocytes with increased cellularity and nuclear atypia but without mitoses, endothelial proliferation, or necrosis. The WHO grade III astrocytomas, anaplastic astrocytomas, show higher cellularity and nuclear atypia than the WHO grade II tumors with mitoses but without endothelial proliferation or necrosis. The WHO grade IV astrocytomas, glioblastoma (formerly, glioblastoma multiforme), are the most common form of astrocytic tumors occurring in the subcortical white matter of the cerebral hemispheres. Glioblastomas are

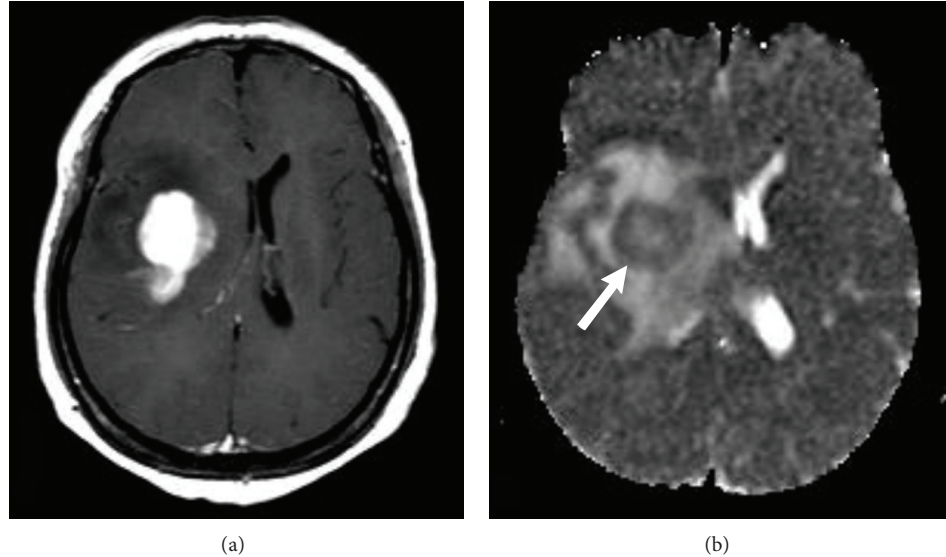


FIGURE 1: (a) Contrast-enhanced T1-weighted image shows a glioblastoma with strong enhancement after intravenous gadolinium injection. (b) The tumor shows decreased ADC values on ADC map (arrow in (b)).

densely cellular and pleomorphic tumors with highly mitotic activity, endothelial proliferation, and necrosis. While the majority of glioblastomas are primary (>90%), arising de novo with a short clinical history and without a precursor tumor, secondary glioblastoma (<10%) may transform from a lower grade astrocytoma over a period of years [3]. Nonetheless, the histopathological appearances of the primary and secondary glioblastomas are identical.

More recently, the advance of genetics and molecular knowledge of gliomas have shown exciting values not only in improving the correlation between the diagnosis and prognosis but also in guiding novel therapy of these devastating diseases [1, 4–6]. For example, mutations of the gene encoding isocitrate dehydrogenase 1 (IDH1) are very common in low-grade astrocytomas, anaplastic astrocytomas, oligodendroglomas, anaplastic oligodendroglomas, and secondary glioblastomas but very rare in de novo glioblastoma [7, 8]. The fact that similar genetic aberrations exist in a variety of gliomas suggests common progenitor cells of these tumors. In addition to mutations of IDH1, low-grade astrocytomas usually have TP53 mutation while oligodendroglomas typically show 1p/19q loss [8]. The concurrent deletion of chromosomes 1p and 19q, a result of an unbalanced translocation, is associated with increased chemosensitivity and a better prognosis [9, 10]. The most common genetic alteration in de novo glioblastomas is loss of heterozygosity (LOH) on chromosome 10 [11, 12]. LOH 1p is rare in both de novo and secondary glioblastomas but has been found to correlate with longer survival [13, 14].

Overall, the prognosis of high-grade gliomas remains poor despite advances in diagnosis and therapy. The median survival is 12 to 15 months in patients with glioblastomas and 2 to 3 years in patients with anaplastic gliomas [15, 16]. The treatment failure is thought to stem from complex biology and heterogeneity of the gliomas. Advances of the techniques in neuroimaging have improved the characterization of the

physiology and metabolism of the tumors noninvasively, leading to improved diagnosis and better detection of recurrence, as well as improving image-guided biopsy and therapy [17–21]. This paper provides an update of the functional MR imaging of gliomas, with focus on the imaging biomarkers of the pathological stigmas of gliomas, including cellularity, invasiveness, mitotic activity, angiogenesis, and necrosis.

2. MR Imaging of Cellularity and Invasiveness

2.1. Tumor Cellularity by Diffusion-Weighted Imaging. The cellularity of gliomas can be evaluated by either T2-weighted MR images or diffusion-weighted imaging (DWI) which measures free water molecular diffusion and has been widely used in the diagnosis of acute cerebral infarction and in differentiating tumor necrosis from abscess cavity [22, 23]. In tumor studies, DWI may serve as an early surrogate marker of therapeutic efficacy by implying persistent cellular density in the tumors where high cellularity may impede free water diffusion, resulting in a reduction of apparent diffusion coefficient (ADC) values. Generally, lower ADC values correspond to increased cellularity and high-grade gliomas (Figure 1). This correlation is, however, not linear. In a study by Higano et al. the minimum ADC varies significantly between WHO grade III ($(1.06 \pm 0.21) \times 10^{-3} \text{ mm}^2/\text{sec}$) and WHO grade IV gliomas ($(0.83 \pm 0.14) \times 10^{-3} \text{ mm}^2/\text{sec}$) at b value of 1000 sec/mm^2 [24]. Because the nests of tumor cells tend to be heterogeneous in distribution within the tumor, a measurement of ADC values by manual drawing of the region of interest from the imaging (ADC map) may cause significant sampling bias. A recent study using minimum histogram analysis of apparent diffusion coefficient (ADC) values, instead of mean value, has shown promising correlation with glioma grading [25, 26]. This study using high b value and cumulative ADC histogram analysis revealed a significantly higher

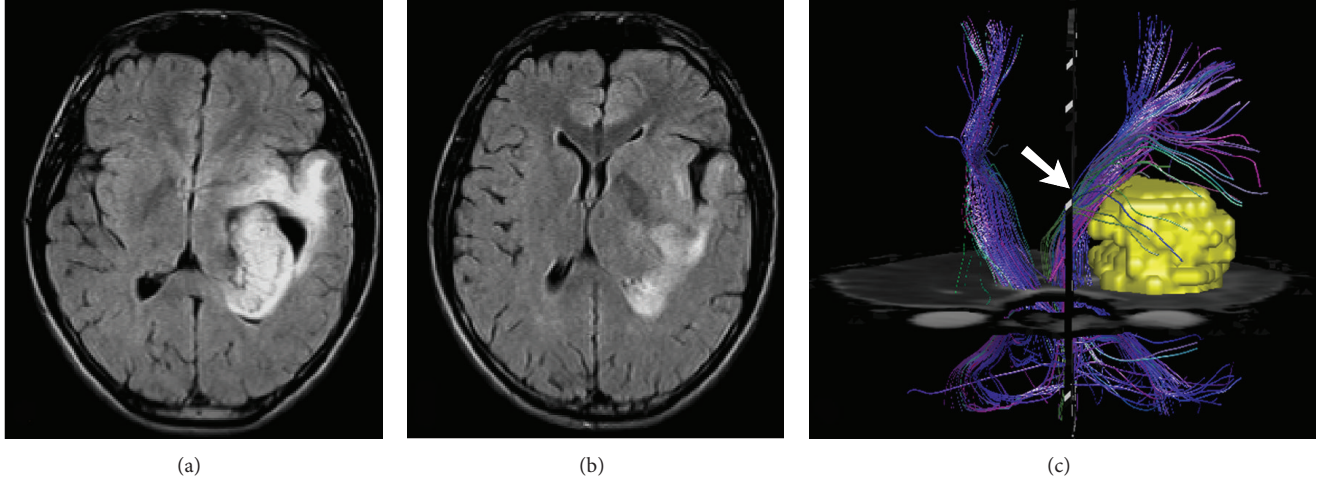


FIGURE 2: ((a), (b)) FLAIR images depict a diffuse and infiltrative oligodendrogloma, WHO grade III, which deviates the corticospinal tract (arrow in (c)) medially, as demonstrated on DTI tractography (c).

frequency of low ADC values in high-grade gliomas than those in low-grade ones [26]. The improved analysis methods indeed enhance the role of DWI as a biomarker of tumor cellularity for the diagnosis and monitoring treatment response.

2.2. Tumor Invasiveness by Diffusion Tensor Imaging. Peritumoral invasion is another index of tumor aggressiveness [24]. However, conventional MR imaging cannot accurately evaluate this invasive behavior due to overlapping of the edema and tumor cells. Recent studies have shown a potential role of diffusion tensor imaging (DTI) in this regard [24, 25]. The DTI measures direction and magnitude of water diffusion based on the data obtained from 6 or more gradient directions as opposed to 3 directions in DWI. The water movement within the white matter tracts is mainly restricted across the myelin sheaths, a principal contributor to directionally dependent water diffusion, that is, anisotropy. Mathematic indices such as fractional anisotropy (FA) derived from DTI data can imply microstructural integrity of brain tissue. Further application using fiber-tracking techniques can reveal the relationship between gliomas and adjacent white matter tracts (Figure 2), hence assisting surgical planning and monitoring tumor response to treatment [27–29]. However, measurements of FA for tumor grading may show conflicting results. Inoue et al. reported that the FA values of low-grade gliomas are significantly lower than those of high-grade by a threshold of 0.188 [30], while Goebell et al. showed low FA ratios in the tumor centers of both low-grade and high-grade gliomas [31]. In the peritumoral region, the T2-weighted hyperintense area surrounding the high-grade glioma, the FA value is typically reduced resulting from a combination of perifocal edema, tumor mass effect, and invasion of tumor cells [28, 32]. Low-grade gliomas tend to deviate, rather than destruct (Figure 3) or infiltrate (Figure 4), the adjacent white matter [28]. Therefore, FA value is less reduced in low-grade gliomas.

Gliomas may affect both the functional cortex and the corresponding white matter tracts. The combination of the DTI and functional MR imaging can delineate an entire

functional circuit (Figure 5), which can help surgical planning, reduce the surgery time, and minimize the need for intraoperative cortical stimulation [33]. However, the benefits remain to be proven in randomized trials.

2.3. Non-Gaussian Diffusion Kurtosis Imaging (DKI). The computational algorithms of DTI are based on the ideal Gaussian distribution of water movement. However, this is not realistic in vivo as the brain represents a complex environment where the movement of water is restricted. In addition, the ADC values obtained from routine diffusion imaging using b value at 1000 sec/mm^2 might only reflect extracellular water movement. Diffusion kurtosis imaging (DKI) is an extension of the DTI model capable of measuring the degree of non-Gaussian water diffusion [34]. The value of DKI has been shown in a study of Van Cauter et al. with kurtosis parameters contributing to better discrimination between high-grade and low-grade gliomas than with conventional diffusion parameters [35]. Further study is required to explore the role of DKI in evaluation of tumor invasiveness.

3. MR Imaging of Mitotic Activity

3.1. Gadolinium-Enhanced T1-Weighted Imaging. The mitotic activity or proliferation of gliomas significantly correlates with prognosis [36, 37]. Among various approaches available for assessing mitotic activity, MIB-1 antibody staining of the nuclear antigen Ki-67 is the most reliable and widely used method [38]. Ki-67 index has been shown to be a better prognostic indicator than histological grades [37, 39]. Several MR imaging techniques have been applied to correlate with tumoral mitotic activity. Among those techniques, conventional contrast-enhanced MR imaging was shown to be best correlated with Ki-67 index up to 8.1% in gliomas with contrast enhancement as opposed to 2.0% in those without enhancement [40]. However, the binary discrimination is insufficient in grading enhancing gliomas. As accelerated

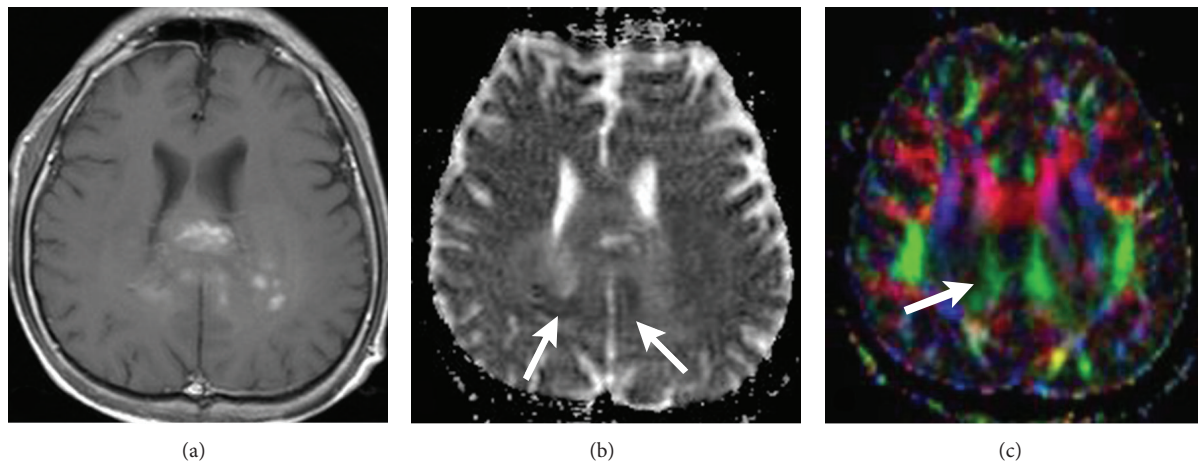


FIGURE 3: (a) Contrast-enhanced T1-weighted image demonstrates a butterfly glioblastoma involving the genu of corpus callosum with small areas of low ADC value on ADC map (arrows in (b)). On color-coded diffusion tensor imaging, the normal left-right-oriented red color (arrow in (c)) is lost due to destruction of the transverse tracts.

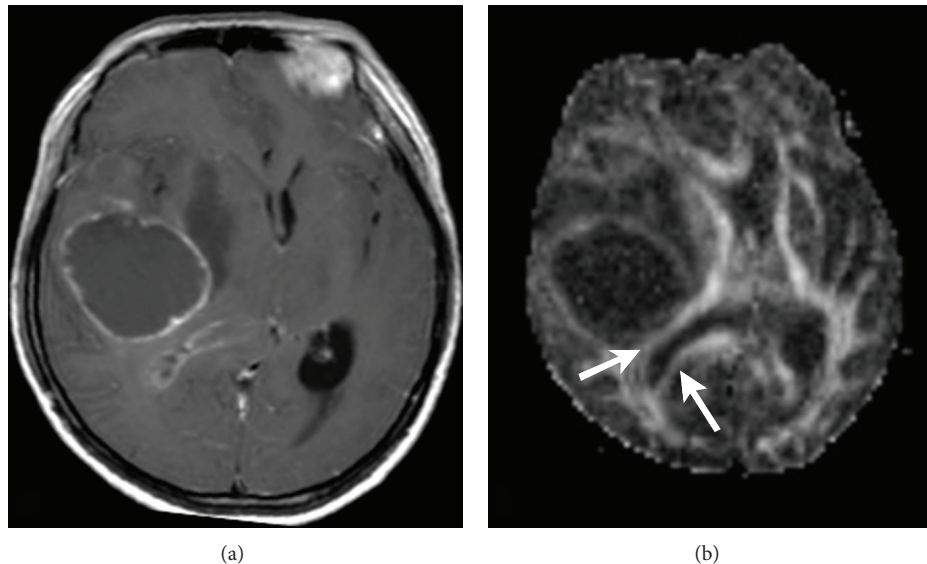


FIGURE 4: (a) Contrast-enhanced T1-weighted image shows a necrotic glioblastoma with rim-like enhancement. (b) On FA map, attenuated FA (arrows) of the adjacent tracts is shown, indicating tumor infiltration.

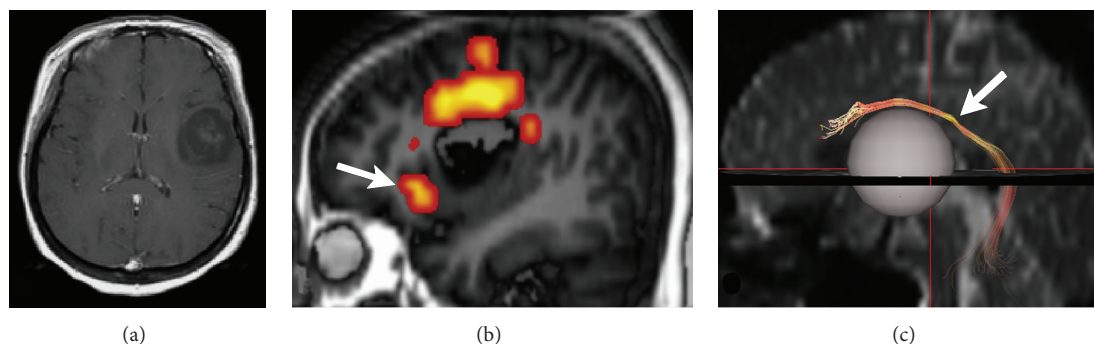


FIGURE 5: (a) Contrast-enhanced T1-weighted image shows an oligodendrogloma, WHO grade II, in the left frontal lobe. (b) Functional MR imaging and DTI tractography (c) demonstrate the activation of Broca's area (arrow in (b)) anterior to the tumor and the elevated arcuate fasciculus (arrow in (c)), respectively. The grey sphere in Figure 5(c) indicates the location of tumor.

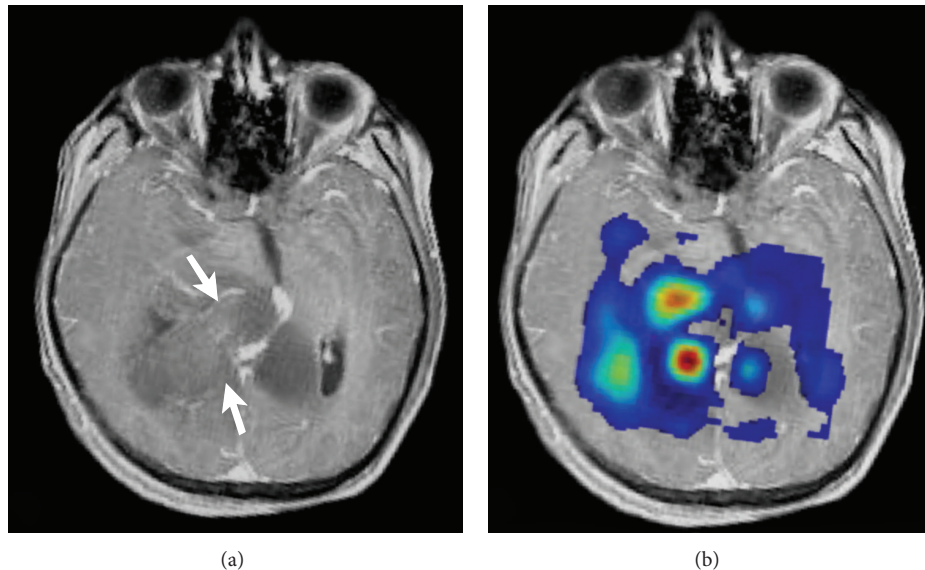


FIGURE 6: (a) Contrast-enhanced T1-weighted image depicts a glioblastoma involving the genu of corpus callosum. The arrows point two hot spots (targets) for stereotactic biopsy based on the regions of increased Cho/Cr ratios ((b) Cho/Cr map).

proliferative activity is coupled with high tumor cellularity and increased perfusion, DWI and perfusion MR imaging have been used to indirectly reflect mitotic activity of gliomas [24, 41, 42].

3.2. Tumor Activity and Image-Guided Biopsy by Proton MR

Spectroscopy. Proton MR spectroscopy (MRS) can noninvasively measure the brain metabolites in vivo. Some metabolites commonly used in clinical MRS study include but are not limited to N-acetyl aspartate (NAA, at 2.02 ppm), choline (Cho, at 3.2 ppm), creatine/phosphocreatine (Cr, 3.0 ppm), lactate (Lac, at 1.33 ppm), lipids (Lip, at 0.9–1.5 ppm range), and *myo*-inositol (mI, at 3.56 ppm). Although no tumor-specific metabolite has been labeled, the ratios of metabolites such as Cho/Cr ratio (Figure 6) have been used to assess cellular proliferation. Cho/Cr ratio has been shown to be parallel with the Ki-67 index in studies of single-voxel MRS [43–45]. In a study of multivoxel MRS, Tamiya et al. also showed a positive correlation between Cho/Cr ratio and Ki-67 index while NAA/Cho ratio has a negative relationship with the index [46].

Another important clinical application of MRS is image-guided biopsy. Although conventional contrast-enhanced MR imaging is useful in delineating gliomas, the tumor regions where the most active mitotic activity exists may not always enhance and vice versa. Irrespective of contrast enhancement, chemical shift imaging using multivoxel ratios of Cho/NAA (the choline map) can be a valuable tool in locating high proliferative potential regions for accurate biopsy targets [47]. Furthermore, the resonances of Lac and Lip were found to be independent predictors of intermediate (Ki-67 index, 4–8%) and high (Ki-67 index, >8%) proliferative activities, respectively [48], while a higher level of mI is related to a lower grade of astrocytomas (Figure 7) [49].

4. Imaging of Angiogenesis

4.1. Perfusion-Weighted MR Imaging. Malignant gliomas are characterized by high degree of angiogenesis, a marker of histological grading system and one of the major therapeutic targets in the development of novel treatments [50]. The principal proangiogenic factor is vascular endothelial growth factor (VEGF), which can result in increased neovascularity, microvascular permeability, and vasodilatation [51–56]. The neovasculatures in gliomas function abnormally with irregularity of the endothelial lining and disruption of the blood-brain barrier (BBB) [57, 58]. The abnormal caliber and number of tumor vessels resulting from abnormal angiogenesis can be histologically measured by microvascular density or area (MVA), which may represent an independent prognostic biomarker [59]. However, the MVA calculation is time consuming and clinically arduous. A fast and noninvasive alternative in assessing MVA is dynamic susceptibility-weighted contrast-enhanced (DSC) MR imaging, which measures changes in tissue T2* following injection of contrast agent [60]. With a model that assumes that the contrast agent is restricted to the intravascular compartment, DSC MR imaging can generate a series of perfusion parameters, including relative cerebral blood volume (rCBV), referring to volume of blood in a given region of brain tissue, relative cerebral blood flow, referring to volume of blood per unit time passing through a given region of brain tissue, and mean transit time, referring to the average time for blood to pass through a given region of brain tissue. Among the parameters, rCBV is generally considered associated with tumor energy metabolism and provides a reliable estimate of tumor MVA [21, 61].

Dynamic contrast-enhanced (DCE) MR imaging is another perfusion method, which relies on the relaxivity effects, rather than the susceptibility effects assessed in DSC

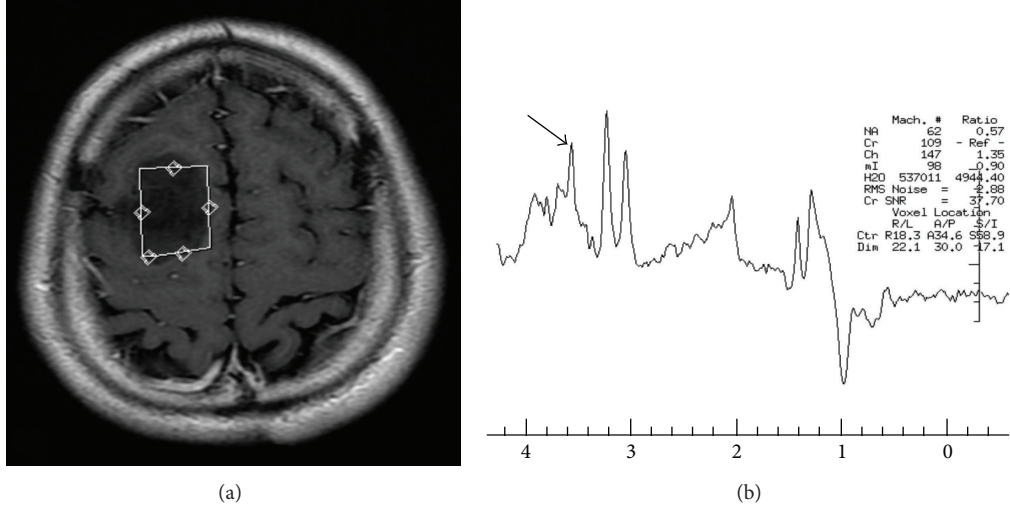


FIGURE 7: (a) Contrast-enhanced T1-weighted image shows a nonenhanced low-grade astrocytoma in the right superior frontal lobe with a high mI level on spectrum of proton MRS (arrow in (b)).

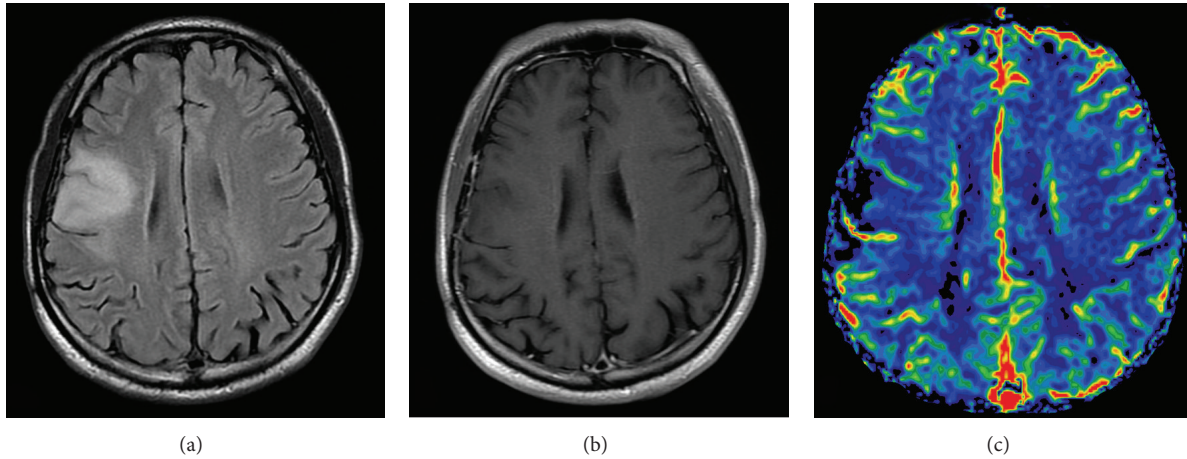


FIGURE 8: (a) FLAIR image shows a hyperintense low-grade glioma, WHO grade II, without significant contrast enhancement on T1-weighted image (b) or increase of the rCBV (c).

method, and measures T1 signal changes following injection of contrast agent. Because gadolinium exerts stronger relaxivity effects than the susceptibility ones, DCE method requires a smaller amount of contrast agent than DSC method does, allowing multiple repeated studies and better quantitation of the perfusion parameters [62, 63].

Tumor neovasculatures tend to have leaky BBB, so the small molecular-weight gadolinium-based contrast agent readily extravasates, causing underestimation of the tumor rCBV. Consequently, the correlation between the rCBV and histologic tumor grading may not be always consistent unless rCBV is corrected for contrast extravasation [64]. Nonetheless, low-grade gliomas usually show no increase in tumor rCBV (Figure 8) while high-grade gliomas may demonstrate high rCBV that in some cases extends outside the contrast-enhancing portion of the tumor (Figure 9). Contrast enhancement in tumor may suggest impaired blood-brain

barrier with leakage of contrast agents into the extravascular spaces. Tumor with relatively intact BBB may show no enhancement. Therefore, conventional contrast-enhanced T1-weighted images and rCBV map can complement each other in outlining tumor extent and differentiating tumor from perifocal edema (Figure 10).

As a standard of care, radiotherapy in combination of temozolomide chemotherapy for patients with newly diagnosed glioblastoma is related to enlarged enhancing areas on contrast-enhanced T1-weighted images without clinical worsening, a phenomenon known as pseudoprogression [65, 66]. Most often seen in patients with the concomitant radio-chemotherapy, pseudoprogression can also occur in patients treated with radiotherapy or chemotherapy alone. In contrast to tumor progression, pseudoprogression is associated with a favorable prognosis [66–68]. Although follow-up conventional MR imaging studies can validate the initial worsening

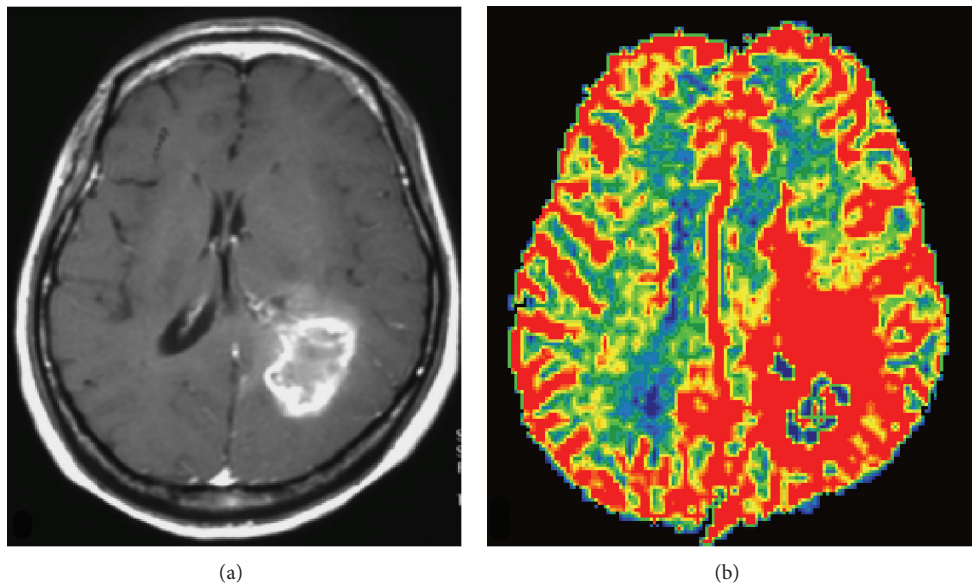


FIGURE 9: (a) Contrast-enhanced T1-weighted image demonstrates a ring-enhancing glioblastoma in the left parietal lobe with avid increase of rCBV (b) extending beyond the extent of the contrast enhancement.

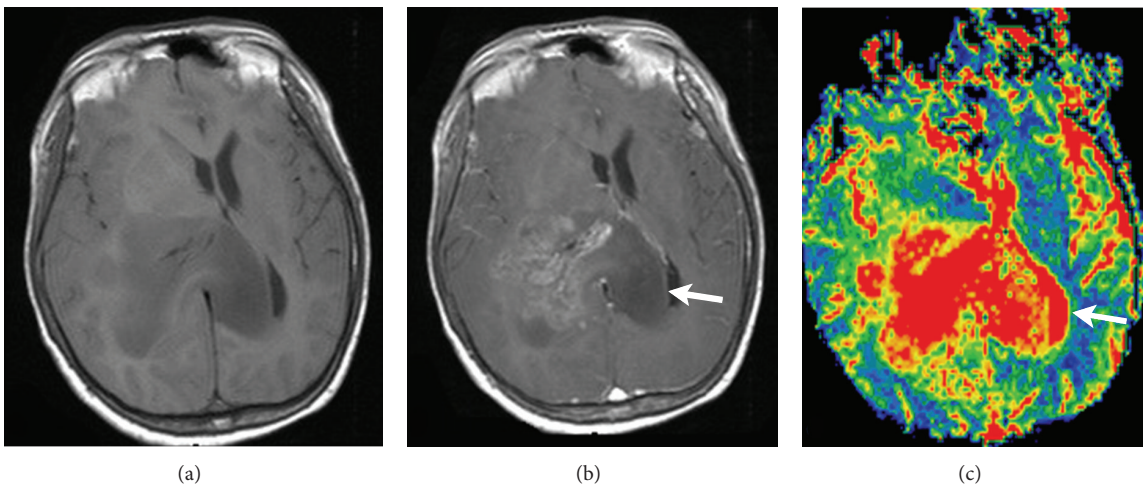


FIGURE 10: (a) Contrast-enhanced T1-weighted image shows a butterfly glioblastoma, involving the genu of corpus callosum. (b) The right aspect of the lesion appears to be heterogeneously contrast enhanced. (c) On rCBV map, the nonenhanced left aspect of the tumor (arrow) shows high rCBV (arrow in (c)). This helps differentiate tumor infiltration from perifocal edema.

imaging findings, DSC MR imaging has been shown to be helpful in evaluating treatment effects in the first place. In a study of Sugahara et al. an enhanced lesion with a normalized rCBV ratio (tumor rCBV/contralateral tissue rCBV) higher than 2.6 suggests tumor recurrence while a normalized rCBV ratio lower than 0.6 implies pseudoprogression [69].

4.2. Capillary Permeability Imaging. In addition to MVA, capillary permeability is another feature of angiogenesis in high-grade gliomas. MR imaging is capable of estimating the capillary permeability based on measuring the contrast leakage rate between the intravascular and extravascular spaces, known as the contrast transfer coefficient (K^{trans}) [70, 71]. Although controversies remain among different models,

the K^{trans} generally correlates with histological grading and length of survival in gliomas [72–74]. A typical low-grade glioma without increase of K^{trans} is shown in Figures 11 and 12 demonstrates high K^{trans} in a high-grade glioma. Although most researchers utilize MR imaging in assessing perfusion parameters of brain tumors, CT perfusion can be an alternative for patients contraindicated to MR imaging and provides parameters of tumor vascular physiology with various maps comparable to those generated by DSC MR perfusion imaging [75, 76]. Figure 13 shows comparable maps of rCBV and K^{trans} derived from CT and MR perfusion imaging.

4.3. Imaging of Tumor Response to Bevacizumab. Until recently, advances in molecular biology have shed light on

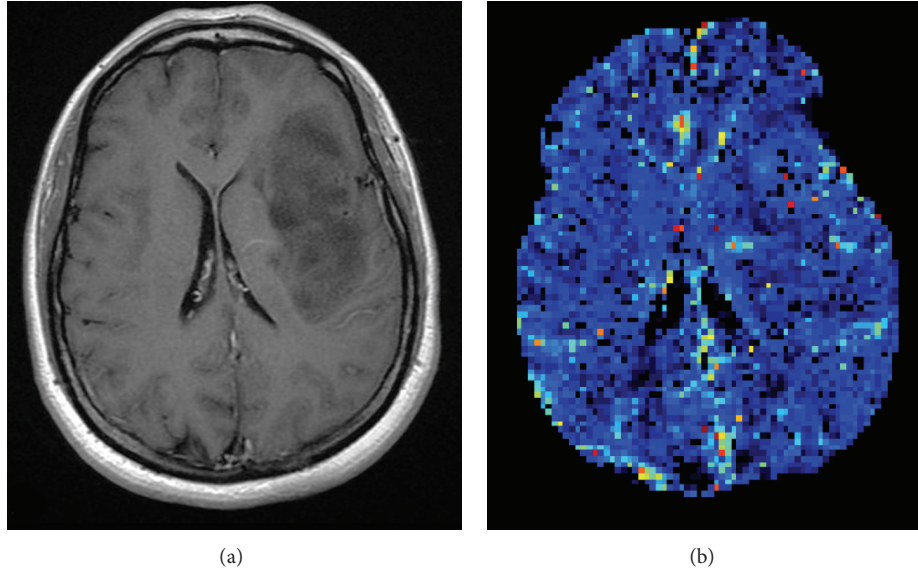


FIGURE 11: (a) Contrast-enhanced T1-weighted image depicts a nonenhanced astrocytoma, WHO grade II. (b) The K^{trans} map shows consistently no leakage of contrast medium in the tumor region, suggesting a low grade.

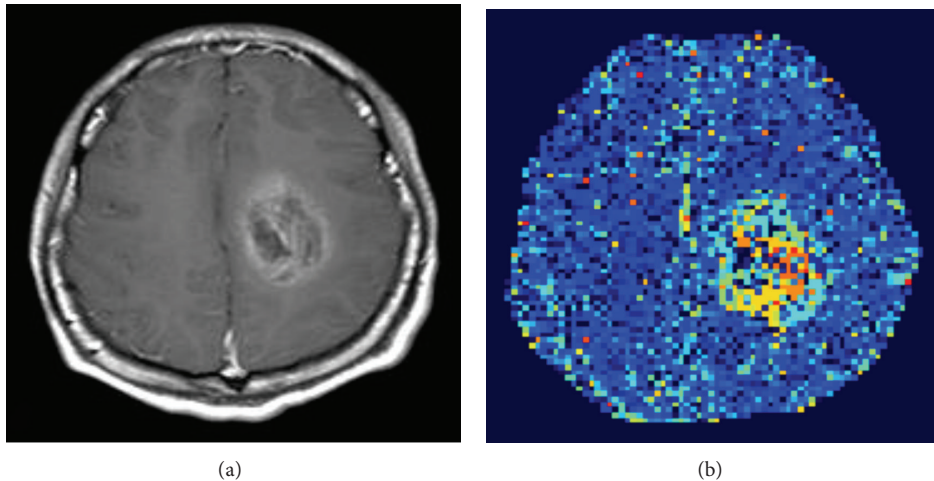


FIGURE 12: An anaplastic oligodendrogloma, WHO grade III, in the left frontal lobe shows contrast enhancement and leakage on T1-weighted image (a) and K^{trans} map (b), respectively.

the development of anti-VEGF monoclonal antibodies as a novel therapy for high-grade gliomas [77]. Bevacizumab is a FDA-approved monoclonal antibody that prevents the interaction of VEGF receptor tyrosine kinase and treats a variety of cancers, including glioblastomas [78–80]. However, in the maintenance of bevacizumab therapy, malignant gliomas inevitably recur and appear to be more aggressive with rebound edema [81]. The tumor response to bevacizumab treatment is unique in terms of imaging finding as the drug suppresses the enhancing component of tumor but not the non-enhancing and infiltrative tumor growth [82]. As a result, the traditional evaluation of treatment response, mostly defined by the McDonald criteria, based on contrast-enhanced CT or MR imaging, is not sufficient. New response

criteria were developed for clinical trials of brain tumors by incorporating T2 and FLAIR changes on MR imaging to evaluate the unique infiltrative progression pattern of malignant gliomas [83].

4.4. Imaging of Microvasculature by Susceptibility-Weighted Imaging. Taking the advantage of high sensitivity to tumor microvasculature and hemorrhagic products, susceptibility-weighted imaging (SWI) is recently introduced to the array of imaging tools for evaluating angiogenesis. SWI is a high-resolution, three-dimensional, gradient-echo T2* MR technique that is blood oxygen level dependent and shows high sensitivity to paramagnetic substances, such as blood products, iron, and calcifications [84, 85]. In the study of

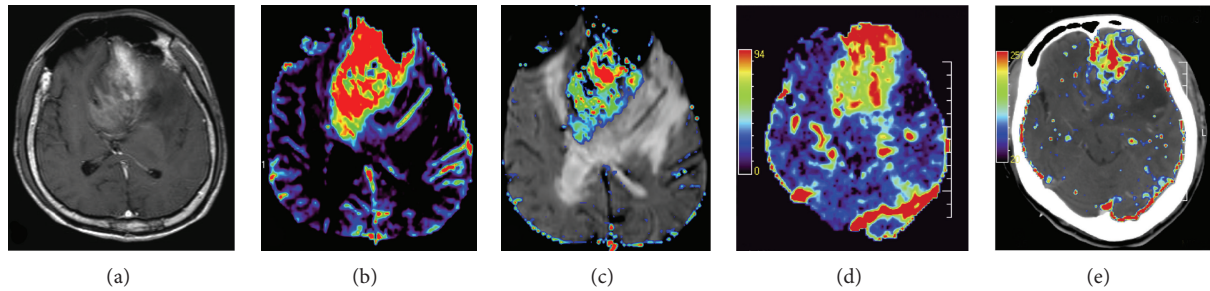


FIGURE 13: (a) Contrast-enhanced T1-weighted image shows an anaplastic oligodendrogloma, WHO grade III, involving the genu of corpus callosum and bilateral frontal lobes. rCBV (b) and K^{trans} (c) maps derived from MRI are comparable to those generated from CT perfusion imaging ((d) CT perfusion map; (e) CT K^{trans} map).

Park et al., glioblastomas showed increased intratumoral susceptibility signals that are significantly different from low-grade gliomas and lymphomas with a specificity of 100% [86]. In an ultrahigh-field-strength (7T) gradient-echo MR study, serpentine hypointensities within gliomas (tumoral pseudoblush) concur with microvascular size and density in histopathological examination and were considered as a promising imaging biomarker for increased tumoral microvascularity [87]. Furthermore, SWI is also useful in the assessment of the microvascular change in patients undertaking bevacizumab therapy [88].

4.5. Molecular MR Imaging. With recent advances of nanotechnology and biotechnology, scientists are capable of binding paramagnetic transition metal ion chelates, mainly gadolinium chelates, or superparamagnetic iron oxide (SPIO) nanoparticles with biologically active targeting moieties and provide a new MR imaging tool to evaluate tumor-specific vasculatures *in vivo* [89]. SPIO nanoparticles are biodegradable iron oxide crystals with polymer coatings and have properties that cause microscopic field inhomogeneity that dephase the neighboring proton magnetic moments and reduce the T_2^* relaxation time. In a study of Tomanek et al., an antibody-targeted MR contrast agent, consisting of SPIO and anti-insulin-like-growth-factor binding protein 7, was used to show abnormal vessels within a glioblastoma on T_2 -weighted images in a mouse model [90].

As the key regulatory systems in angiogenesis of gliomas, VEGF and VEGF receptors are targeted mainly in radioisotope-based imaging and recently assessed by a molecular MR imaging probe, anti-VEGF receptor-2 monoclonal antibody conjugated with a gadolinium-based contrast agent, in a rat C6 glioma model by He et al. [91]. The expression of VEGF receptor-2 on vascular endothelial cells in glioma tissue was successfully visualized *in vivo* with the degree of the expression concurring that of the tumor blood volume [91].

5. MR Imaging of Tumor Necrosis

5.1. Contrast-Enhanced T1-Weighted Imaging and Proton MRS. Necrosis is the hallmark of glioblastoma and is caused by tumor hypoxia as a result of increased cell proliferation and mitotic activity, as well as insufficient tissue perfusion. On

conventional contrast-enhanced T1-weighted images, tumor necrosis can be easily diagnosed with the fact that necrotic zones are typically less enhanced, giving the tumor an appearance of irregular rim enhancing mass (Figure 4(a)). However, imaging diagnosis of necrosis can be problematic in early stages or in micronecrosis in which the necrotic region may show to be enhanced or not enhanced at all. MRS is an imaging tool of choice to show characteristic metabolites accumulated in the necrotic regions, even when necrosis is not overtly seen on contrast-enhanced T1-weighted images. The anaerobic glycolysis and cell death with membrane breakdown in the hypoxic tumor can be revealed by the increased Lac and Lip peaks on MRS (Figure 14) [92–94]. The presence of Lip and/or Lac in high-grade gliomas has been found in a number of studies [95–98].

5.2. Radiation-Induced Necrosis and Tumor Recurrence. The differentiation between radiation necrosis and recurrent high-grade gliomas remains challenging despite advances of imaging modalities because both entities share similar imaging features, such as irregular rim-like contrast enhancement, mass effect, and vasogenic edema. Although guidelines based on experiences on conventional MR imaging were intended to resolve the dilemma [99, 100], advanced imaging techniques have been shown to provide more reliable and accessible differentiation between the two conditions. In an MRS study of Nakajima et al., the Lac/Cho ratios are significantly higher in radiation necrosis (2.35 ± 1.81 (mean \pm standard deviation)) than those in tumor recurrence (0.63 ± 0.25) [101]. DSC perfusion MR imaging was also shown to have higher relative peak height and rCBV in patients with recurrent glioma than in patients with radiation necrosis [102]. In a study of Larsen et al., a threshold of $2.0 \text{ mL}/100 \text{ g}$ for CBV was suggested to have 100% sensitivity and specificity for detecting gliomas in progression [103].

Another clinical dilemma is the differentiation between ring-enhancing brain abscess and tumor necrosis on T1-weighted images. DWI is routinely used to differentiate the two conditions by showing restricted water diffusion of the high viscosity and cellularity of pus cells in the abscess cavity. However, the restricted diffusion within ring-enhancing lesions is not pathognomonic for brain abscess,

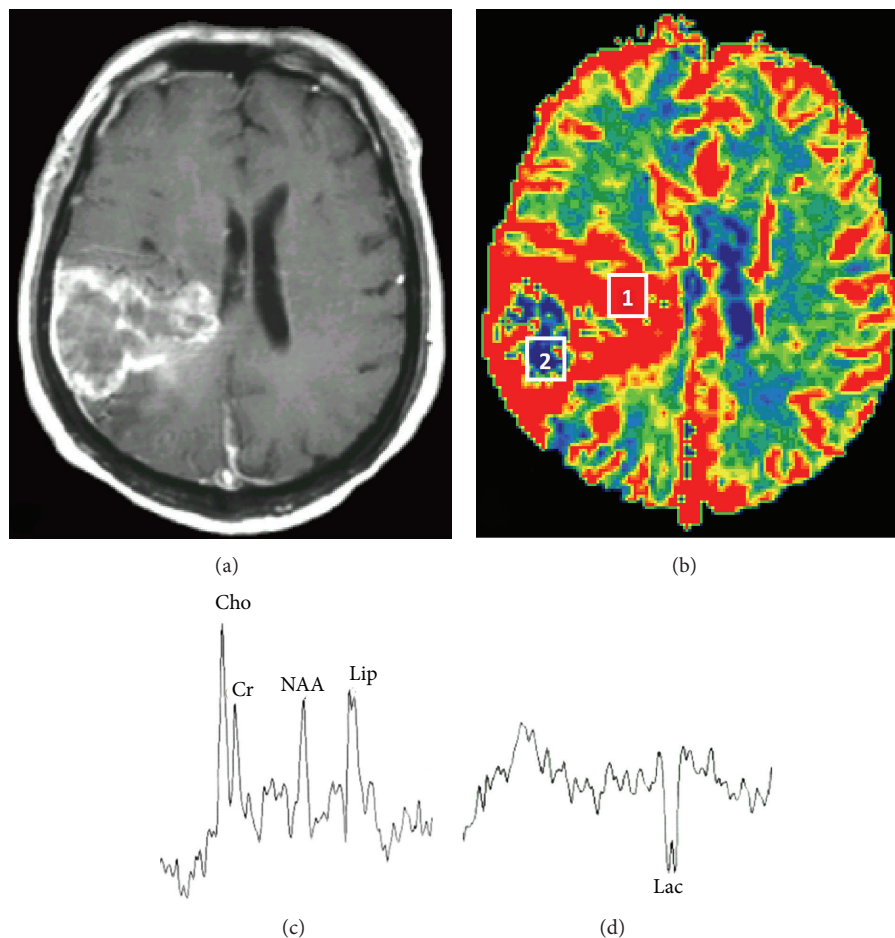


FIGURE 14: (a) Contrast-enhanced T1-weighted image demonstrates a necrotic glioblastoma in the right parietal lobe with increased rCBV (b) in the periphery of the tumor and peritumoral regions. (c) A single-voxel MRS, echo time 135 ms, obtained from region 1 of increased rCBV (b) shows a high Lip peak, suggesting micronecrosis. (d) MRS obtained from the region 2 of low rCBV (b) depicts an inverted Lac peak, representing hypoxia in the necrotic region.

and a small number of glioblastomas may show restricted diffusion in the necrotic regions, probably resulting from a various combination of intratumoral hemorrhage, cytotoxic edema, or superimposed pyogenic infection [104, 105]. The dilemma has recently been successfully resolved by the application of perfusion MR imaging, which reveals distinct pathophysiological alterations between brain abscess and glioblastoma. In a prospective study Chiang et al. showed decreased rCBV in the necrotic wall of the abscess where regional poor vascularity exists and increased rCBV in the periphery of the high-grade gliomas owing to the presence of active angiogenesis [106]. Furthermore, a characteristic dual rim sign, presumably resulting from the granulation tissue, on SWI, found only along the wall of brain abscess but not in glioblastomas, has been proposed by Toh et al. to effectively differentiate the two conditions [107].

6. Conclusion

Advanced MR imaging techniques can potentially help evaluate the underlying key histopathological features of

gliomas by showing the physiologic changes and metabolic activities, thus improving diagnosis and tumor grading. These functional tools help in better understanding of the tumor behavior and also provide a new window to guide and monitor the treatment of gliomas. Application of these imaging techniques could lead to sophisticated and personalized patient care.

Acknowledgment

This research was supported by the National Science Council, Taiwan (NSC95-2314-B-016-036-MY2).

References

- [1] D. N. Louis, "Molecular pathology of malignant gliomas," *Annual Review of Pathology*, vol. 1, pp. 97–117, 2006.
- [2] P. Y. Wen and S. Kesari, "Malignant gliomas in adults," *New England Journal of Medicine*, vol. 359, no. 5, pp. 492–507, 2008.
- [3] P. Kleihues and H. Ohgaki, "Primary and secondary glioblastomas: from concept to clinical diagnosis," *Neuro-Oncology*, vol. 1, no. 1, pp. 44–51, 1999.

- [4] W. A. Freije, F. E. Castro-Vargas, Z. Fang et al., "Gene expression profiling of gliomas strongly predicts survival," *Cancer Research*, vol. 64, no. 18, pp. 6503–6510, 2004.
- [5] G. Reifenberger and V. P. Collins, "Pathology and molecular genetics of astrocytic gliomas," *Journal of Molecular Medicine*, vol. 82, no. 10, pp. 656–670, 2004.
- [6] R. Yamanaka, T. Arao, N. Yajima et al., "Identification of expressed genes characterizing long-term survival in malignant glioma patients," *Oncogene*, vol. 25, no. 44, pp. 5994–6002, 2006.
- [7] M. E. Figueroa, O. Abdel-Wahab, C. Lu et al., "Leukemic IDH1 and IDH2 mutations result in a hypermethylation phenotype, disrupt TET2 function, and impair hematopoietic differentiation," *Cancer Cell*, vol. 18, no. 6, pp. 553–567, 2010.
- [8] N. Thon, S. Eigenbrod, S. Kreth et al., "IDH1 mutations in grade II astrocytomas are associated with unfavorable progression-free survival and prolonged postrecurrence survival," *Cancer*, vol. 118, no. 2, pp. 452–460, 2012.
- [9] C. Walker, D. G. Du Plessis, K. A. Joyce et al., "Molecular pathology and clinical characteristics of oligodendroglial neoplasms," *Annals of Neurology*, vol. 57, no. 6, pp. 855–865, 2005.
- [10] J. S. Smith, A. Perry, T. J. Borell et al., "Alterations of chromosome arms 1p and 19q as predictors of survival in oligodendroglomas, astrocytomas, and mixed oligoastrocytomas," *Journal of Clinical Oncology*, vol. 18, no. 3, pp. 636–645, 2000.
- [11] H. Ohgaki, P. Dessen, B. Jourde et al., "Genetic pathways to glioblastoma: a population-based study," *Cancer Research*, vol. 64, no. 19, pp. 6892–6899, 2004.
- [12] B. K. A. Rasheed, R. E. McLendon, H. S. Friedman et al., "Chromosome 10 deletion mapping in human gliomas: a common deletion region in 10q25," *Oncogene*, vol. 10, no. 11, pp. 2243–2246, 1995.
- [13] M. Nakamura, F. Yang, H. Fujisawa, Y. Yonekawa, P. Kleihues, and H. Ohgaki, "Loss of heterozygosity on chromosome 19 in secondary glioblastomas," *Journal of Neuropathology and Experimental Neurology*, vol. 59, no. 6, pp. 539–543, 2000.
- [14] T. Homma, T. Fukushima, S. Vaccarella et al., "Correlation among pathology, genotype, and patient outcomes in glioblastoma," *Journal of Neuropathology and Experimental Neurology*, vol. 65, no. 9, pp. 846–854, 2006.
- [15] W. J. Curran Jr., C. B. Scott, J. Horton et al., "Recursive partitioning analysis of prognostic factors in three radiation therapy oncology group malignant glioma trials," *Journal of the National Cancer Institute*, vol. 85, no. 9, pp. 704–710, 1993.
- [16] M. D. Prados, W. Seiferheld, H. M. Sandler et al., "Phase III randomized study of radiotherapy plus procarbazine, lomustine, and vincristine with or without BUdR for treatment of anaplastic astrocytoma: final report of RTOG 9404," *International Journal of Radiation Oncology Biology Physics*, vol. 58, no. 4, pp. 1147–1152, 2004.
- [17] Y. Cao, P. C. Sundgren, C. I. Tsien, T. T. Chenevert, and L. Junck, "Physiologic and metabolic magnetic resonance imaging in gliomas," *Journal of Clinical Oncology*, vol. 24, no. 8, pp. 1228–1235, 2006.
- [18] M. D. Jenkinson, D. G. D. Plessis, C. Walker, and T. S. Smith, "Advanced MRI in the management of adult gliomas," *British Journal of Neurosurgery*, vol. 21, no. 6, pp. 550–561, 2007.
- [19] S. J. Price, "The role of advanced MR imaging in understanding brain tumour pathology," *British Journal of Neurosurgery*, vol. 21, no. 6, pp. 562–575, 2007.
- [20] A. Gupta, R. J. Young, S. Karimi et al., "Isolated diffusion restriction precedes the development of enhancing tumor in a subset of patients with glioblastoma," *American Journal of Neuroradiology*, vol. 32, no. 7, pp. 1301–1306, 2011.
- [21] L. S. Hu, J. M. Eschbacher, A. C. Dueck et al., "Correlations between perfusion MR imaging cerebral blood volume, microvessel quantification, and clinical outcome using stereotactic analysis in recurrent high-grade glioma," *American Journal of Neuroradiology*, vol. 33, no. 1, pp. 69–76, 2012.
- [22] K. Noguchi, N. Watanabe, T. Nagayoshi et al., "Role of diffusion-weighted echo-planar MRI in distinguishing between brain abscess and tumour: a preliminary report," *Neuroradiology*, vol. 41, no. 3, pp. 171–174, 1999.
- [23] T. W. Stadnik, C. Chaskis, A. Michotte et al., "Diffusion-weighted MR imaging of intracerebral masses: comparison with conventional MR imaging and histologic findings," *American Journal of Neuroradiology*, vol. 22, no. 5, pp. 969–976, 2001.
- [24] S. Higano, X. Yun, T. Kumabe et al., "Malignant astrocytic tumors: clinical importance of apparent diffusion coefficient in prediction of grade and prognosis," *Radiology*, vol. 241, no. 3, pp. 839–846, 2006.
- [25] T. Sugahara, Y. Korogi, M. Kochi et al., "Usefulness of diffusion-weighted MRI with echo-planar technique in the evaluation of cellularity in gliomas," *Journal of Magnetic Resonance Imaging*, vol. 9, no. 1, pp. 53–60, 1999.
- [26] Y. Kang, S. H. Choi, Y. J. Kim et al., "Gliomas: histogram analysis of apparent diffusion coefficient maps with standard- or high-b-value diffusion-weighted MR imaging—correlation with tumor grade," *Radiology*, vol. 261, no. 3, pp. 882–890, 2011.
- [27] S. Mori, K. Frederiksen, P. C. M. Van Zijl et al., "Brain white matter anatomy of tumor patients evaluated with diffusion tensor imaging," *Annals of Neurology*, vol. 51, no. 3, pp. 377–380, 2002.
- [28] S. J. Price, N. G. Burnet, T. Donovan et al., "Diffusion tensor imaging of brain tumours at 3 T: a potential tool for assessing white matter tract invasion?" *Clinical Radiology*, vol. 58, no. 6, pp. 455–462, 2003.
- [29] S. Lu, D. Ahn, G. Johnson, and S. Cha, "Peritumoral diffusion tensor imaging of high-grade gliomas and metastatic brain tumors," *American Journal of Neuroradiology*, vol. 24, no. 5, pp. 937–941, 2003.
- [30] T. Inoue, K. Ogasawara, T. Beppu, A. Ogawa, and H. Kabasawa, "Diffusion tensor imaging for preoperative evaluation of tumor grade in gliomas," *Clinical Neurology and Neurosurgery*, vol. 107, no. 3, pp. 174–180, 2005.
- [31] E. Goebell, S. Paustenbach, O. Vaeterlein et al., "Low-grade and anaplastic gliomas: differences in architecture evaluated with diffusion-tensor MR imaging," *Radiology*, vol. 239, no. 1, pp. 217–222, 2006.
- [32] A. I. Holodny, M. D. Ollenschleger, W. C. Liu, M. Schulder, and A. J. Kalnin, "Identification of the corticospinal tracts achieved using blood-oxygen-level-dependent and diffusion functional MR imaging in patients with brain tumors," *American Journal of Neuroradiology*, vol. 22, no. 1, pp. 83–88, 2001.
- [33] M. Schulder, J. A. Maldjian, W. C. Liu et al., "Functional image-guided surgery of intracranial tumors located in or near the sensorimotor cortex," *Journal of Neurosurgery*, vol. 89, no. 3, pp. 412–418, 1998.
- [34] J. H. Jensen, J. A. Helpern, A. Ramani, H. Lu, and K. Kaczynski, "Diffusional kurtosis imaging: the quantification of non-Gaussian water diffusion by means of magnetic resonance imaging," *Magnetic Resonance in Medicine*, vol. 53, no. 6, pp. 1432–1440, 2005.

- [35] S. Van Cauter, J. Veraart, J. Sijbers et al., "Gliomas: diffusion kurtosis MR imaging in grading," *Radiology*, vol. 263, no. 2, pp. 492–501, 2012.
- [36] H. Wakimoto, M. Aoyagi, T. Nakayama et al., "Prognostic significance of Ki-67 labeling indices obtained using MIB-1 monoclonal antibody in patients with supratentorial astrocytomas," *Cancer*, vol. 77, no. 2, pp. 373–380, 1996.
- [37] T. Hoshino, D. Ahn, M. D. Prados, K. Lamborn, and C. B. Wilson, "Prognostic significance of the proliferative potential of intracranial gliomas measured by bromodeoxyuridine labeling," *International Journal of Cancer*, vol. 53, no. 4, pp. 550–555, 1993.
- [38] P. E. McKeever, D. A. Ross, M. S. Strawderman, J. A. Brunberg, H. S. Greenberg, and L. Junck, "A comparison of the predictive power for survival in gliomas provided by MIB-1, bromodeoxyuridine and proliferating cell nuclear antigen with histopathologic and clinical parameters," *Journal of Neuropathology and Experimental Neurology*, vol. 56, no. 7, pp. 798–805, 1997.
- [39] P. K. Sallinen, H. K. Haapasalo, T. Visakorpi et al., "Prognostication of astrocytoma patient survival by Ki-67 (MIB-1), PCNA, and S-phase fraction using archival paraffin-embedded samples," *Journal of Pathology*, vol. 174, no. 4, pp. 275–282, 1994.
- [40] O. Tynninen, H. J. Aronen, M. Ruhala et al., "MRI enhancement and microvascular density in gliomas. Correlation with tumor cell proliferation," *Investigative Radiology*, vol. 34, no. 6, pp. 427–434, 1999.
- [41] R. Kiss, O. Dewitte, C. Decaestecker et al., "The combined determination of proliferative activity and cell density in the prognosis of adult patients with supratentorial high-grade astrocytic tumors," *American Journal of Clinical Pathology*, vol. 107, no. 3, pp. 321–331, 1997.
- [42] N. Sadeghi, I. Salmon, C. Decaestecker et al., "Stereotactic comparison among cerebral blood volume, methionine uptake, and histopathology in brain glioma," *American Journal of Neuroradiology*, vol. 28, no. 3, pp. 455–461, 2007.
- [43] G. Barbarella, R. Ricci, G. Pirini et al., "In vivo single voxel 1H MRS of glial brain tumors: correlation with tissue histology and in vitro MRS," *International Journal of Oncology*, vol. 12, no. 2, pp. 461–468, 1998.
- [44] H. Shimizu, T. Kumabe, R. Shirane, and T. Yoshimoto, "Correlation between choline level measured by proton MR spectroscopy and Ki-67 labeling index in gliomas," *American Journal of Neuroradiology*, vol. 21, no. 4, pp. 659–665, 2000.
- [45] A. Matsumura, T. Isobe, I. Anno, S. Takano, and H. Kawamura, "Correlation between choline and MIB-1 index in human gliomas. A quantitative proton MR spectroscopy study," *Journal of Clinical Neuroscience*, vol. 12, no. 4, pp. 416–420, 2005.
- [46] T. Tamiya, K. Kinoshita, Y. Ono, K. Matsumoto, T. Furuta, and T. Ohmoto, "Proton magnetic resonance spectroscopy reflects cellular proliferative activity in astrocytomas," *Neuroradiology*, vol. 42, no. 5, pp. 333–338, 2000.
- [47] T. R. McKnight, K. R. Lamborn, T. D. Love et al., "Correlation of magnetic resonance spectroscopic and growth characteristics within Grades II and III gliomas," *Journal of Neurosurgery*, vol. 106, no. 4, pp. 660–666, 2007.
- [48] R. Guillemin, C. Menuel, H. Duffau et al., "Proton magnetic resonance spectroscopy predicts proliferative activity in diffuse low-grade gliomas," *Journal of Neuro-Oncology*, vol. 87, no. 2, pp. 181–187, 2008.
- [49] M. Castillo, J. K. Smith, and L. Kwock, "Correlation of myoinositol levels and grading of cerebral astrocytomas," *American Journal of Neuroradiology*, vol. 21, no. 9, pp. 1645–1649, 2000.
- [50] K. H. Plate, G. Breier, H. A. Weich, and W. Risau, "Vascular endothelial growth factor is a potential tumour angiogenesis factor in human gliomas in vivo," *Nature*, vol. 359, no. 6398, pp. 845–848, 1992.
- [51] O. Kargiotis, J. S. Rao, and A. P. Kyritsis, "Mechanisms of angiogenesis in gliomas," *Journal of Neuro-Oncology*, vol. 78, no. 3, pp. 281–293, 2006.
- [52] M. R. Machein and K. H. Plate, "VEGF in brain tumors," *Journal of Neuro-Oncology*, vol. 50, no. 1–2, pp. 109–120, 2000.
- [53] D. R. Senger, L. Van De Water, L. F. Brown et al., "Vascular permeability factor (VPF, VEGF) in tumor biology," *Cancer and Metastasis Reviews*, vol. 12, no. 3–4, pp. 303–324, 1993.
- [54] H. Ashrafpour, N. Huang, P. C. Neligan et al., "Vasodilator effect and mechanism of action of vascular endothelial growth factor in skin vasculature," *American Journal of Physiology*, vol. 286, no. 3, pp. H946–H954, 2004.
- [55] D. D. Ku, J. K. Zaleski, S. Liu, and T. A. Brock, "Vascular endothelial growth factor induces EDRF-dependent relaxation in coronary arteries," *American Journal of Physiology*, vol. 265, no. 2, part 2, pp. H586–H592, 1993.
- [56] D. R. Senger, S. J. Galli, A. M. Dvorak, C. A. Perruzzi, V. Susan Harvey, and H. F. Dvorak, "Tumor cells secrete a vascular permeability factor that promotes accumulation of ascites fluid," *Science*, vol. 219, no. 4587, pp. 983–985, 1983.
- [57] P. Vajkoczy and M. D. Menger, "Vascular microenvironment in gliomas," *Cancer Treatment and Research*, vol. 117, pp. 249–262, 2004.
- [58] N. A. Vick and D. D. Bigner, "Microvascular abnormalities in virally-induced canine brain tumors. Structural bases for altered blood-brain barrier function," *Journal of the Neurological Sciences*, vol. 17, no. 1, pp. 29–39, 1972.
- [59] P. Birner, M. Piribauer, I. Fischer et al., "Vascular patterns in glioblastoma influence clinical outcome and associate with variable expression of angiogenic proteins: evidence for distinct angiogenic subtypes," *Brain Pathology*, vol. 13, no. 2, pp. 133–143, 2003.
- [60] L. Østergaard, "Principles of cerebral perfusion imaging by bolus tracking," *Journal of Magnetic Resonance Imaging*, vol. 22, no. 6, pp. 710–717, 2005.
- [61] H. J. Aronen, F. S. Pardo, D. N. Kennedy et al., "High microvascular blood volume is associated with high glucose uptake and tumor angiogenesis in human gliomas," *Clinical Cancer Research*, vol. 6, no. 6, pp. 2189–2200, 2000.
- [62] B. L. Dean, C. Lee, J. E. Kirsch, V. M. Runge, R. M. Dempsey, and L. C. Pettigrew, "Cerebral hemodynamics and cerebral blood volume: MR assessment using gadolinium contrast agents and T1-weighted turbo-FLASH imaging," *American Journal of Neuroradiology*, vol. 13, no. 1, pp. 39–48, 1992.
- [63] T. Hackländer, J. R. Reichenbach, M. Hofer, and U. Mödder, "Measurement of cerebral blood volume via the relaxing effect of low-dose gadopentetate dimeglumine during bolus transit," *American Journal of Neuroradiology*, vol. 17, no. 5, pp. 821–830, 1996.
- [64] J. L. Boxerman, K. M. Schmainda, and R. M. Weisskoff, "Relative cerebral blood volume maps corrected for contrast agent extravasation significantly correlate with glioma tumor grade, whereas uncorrected maps do not," *American Journal of Neuroradiology*, vol. 27, no. 4, pp. 859–867, 2006.

- [65] R. Stupp, W. P. Mason, M. J. Van Den Bent et al., "Radiotherapy plus concomitant and adjuvant temozolomide for glioblastoma," *New England Journal of Medicine*, vol. 352, no. 10, pp. 987–996, 2005.
- [66] D. Brandsma, L. Stalpers, W. Taal, P. Sminia, and M. J. van den Bent, "Clinical features, mechanisms, and management of pseudoprogression in malignant gliomas," *The Lancet Oncology*, vol. 9, no. 5, pp. 453–461, 2008.
- [67] A. A. Brandes, E. Franceschi, A. Tosoni et al., "MGMT promoter methylation status can predict the incidence and outcome of pseudoprogression after concomitant radiochemotherapy in newly diagnosed glioblastoma patients," *Journal of Clinical Oncology*, vol. 26, no. 13, pp. 2192–2197, 2008.
- [68] R. Mangla, G. Singh, D. Ziegelitz et al., "Changes in relative cerebral blood volume 1 month after radiation-temozolomide therapy can help predict overall survival in patients with glioblastoma," *Radiology*, vol. 256, no. 2, pp. 575–584, 2010.
- [69] T. Sugahara, Y. Korogi, S. Tomiguchi et al., "Posttherapeutic intraaxial brain tumor: the value of perfusion-sensitive contrast-enhanced MR imaging for differentiating tumor recurrence from nonneoplastic contrast-enhancing tissue," *American Journal of Neuroradiology*, vol. 21, no. 5, pp. 901–909, 2000.
- [70] X. P. Zhu, K. L. Li, I. D. Kamaly-Asl et al., "Quantification of endothelial permeability, leakage space, and blood volume in brain tumors using combined T1 and T2^{*} contrast-enhanced dynamic MR imaging," *Journal of Magnetic Resonance Imaging*, vol. 11, no. 6, pp. 575–585, 2000.
- [71] K. L. Li, X. P. Zhu, D. R. Checkley et al., "Simultaneous mapping of blood volume and endothelial permeability surface area product in gliomas using iterative analysis of first-pass dynamic contrast enhanced MRI data," *British Journal of Radiology*, vol. 76, no. 901, pp. 39–50, 2003.
- [72] H. C. Roberts, T. P. L. Roberts, R. C. Brasch, and W. P. Dillon, "Quantitative measurement of microvascular permeability in human brain tumors achieved using dynamic contrast-enhanced MR imaging: correlation with histologic grade," *American Journal of Neuroradiology*, vol. 21, no. 5, pp. 891–899, 2000.
- [73] J. M. Provenzale, G. R. Wang, T. Brenner, J. R. Petrella, and A. G. Sorensen, "Comparison of permeability in high-grade and low-grade brain tumors using dynamic susceptibility contrast MR imaging," *American Journal of Roentgenology*, vol. 178, no. 3, pp. 711–716, 2002.
- [74] S. J. Mills, T. A. Patankar, H. A. Haroon, D. Balériaux, R. Swindell, and A. Jackson, "Do cerebral blood volume and contrast transfer coefficient predict prognosis in human glioma?" *American Journal of Neuroradiology*, vol. 27, no. 4, pp. 853–858, 2006.
- [75] B. Ding, H. W. Ling, K. M. Chen, H. Jiang, and Y. B. Zhu, "Comparison of cerebral blood volume and permeability in preoperative grading of intracranial glioma using CT perfusion imaging," *Neuroradiology*, vol. 48, no. 10, pp. 773–781, 2006.
- [76] S. K. Ellika, R. Jain, S. C. Patel et al., "Role of perfusion CT in glioma grading and comparison with conventional MR imaging features," *American Journal of Neuroradiology*, vol. 28, no. 10, pp. 1981–1987, 2007.
- [77] P. Carmeliet and R. K. Jain, "Angiogenesis in cancer and other diseases," *Nature*, vol. 407, no. 6801, pp. 249–257, 2000.
- [78] F. Kazazi-Hyseni, J. H. Beijnen, and J. H. M. Schellens, "Bevacizumab," *Oncologist*, vol. 15, no. 8, pp. 819–825, 2010.
- [79] N. Ferrara, K. J. Hillan, H. P. Gerber, and W. Novotny, "Discovery and development of bevacizumab, an anti-VEGF antibody for treating cancer," *Nature Reviews Drug Discovery*, vol. 3, no. 5, pp. 391–400, 2004.
- [80] L. G. Presta, H. Chen, S. J. O'Connor et al., "Humanization of an anti-vascular endothelial growth factor monoclonal antibody for the therapy of solid tumors and other disorders," *Cancer Research*, vol. 57, no. 20, pp. 4593–4599, 1997.
- [81] S. Ananthnarayan, J. Bahng, J. Roring et al., "Time course of imaging changes of GBM during extended bevacizumab treatment," *Journal of Neuro-Oncology*, vol. 88, no. 3, pp. 339–347, 2008.
- [82] A. D. Norden, G. S. Young, K. Setayesh et al., "Bevacizumab for recurrent malignant gliomas: efficacy, toxicity, and patterns of recurrence," *Neurology*, vol. 70, no. 10, pp. 779–787, 2008.
- [83] P. Y. Wen, D. R. Macdonald, D. A. Reardon et al., "Updated response assessment criteria for high-grade gliomas: response assessment in neuro-oncology working group," *Journal of Clinical Oncology*, vol. 28, no. 11, pp. 1963–1972, 2010.
- [84] E. M. Haacke, Y. Xu, Y. C. N. Cheng, and J. R. Reichenbach, "Susceptibility weighted imaging (SWI)," *Magnetic Resonance in Medicine*, vol. 52, no. 3, pp. 612–618, 2004.
- [85] A. Rauscher, J. Sedlacik, M. Barth, H. J. Mentzel, and J. R. Reichenbach, "Magnetic susceptibility-weighted MR phase imaging of the human brain," *American Journal of Neuroradiology*, vol. 26, no. 4, pp. 736–742, 2005.
- [86] S. M. Park, H. S. Kim, G. H. Jahng, C. W. Ryu, and S. Y. Kim, "Combination of high-resolution susceptibility-weighted imaging and the apparent diffusion coefficient: added value to brain tumour imaging and clinical feasibility of non-contrast MRI at 3 T," *British Journal of Radiology*, vol. 83, no. 990, pp. 466–475, 2010.
- [87] G. A. Christoforidis, M. Yang, A. Abduljalil et al., "Tumoral pseudoblush" identified within gliomas at high-spatial-resolution ultrahigh-field-strength gradient-echo MR imaging corresponds to microvascularity at stereotactic biopsy," *Radiology*, vol. 264, no. 1, pp. 210–217, 2012.
- [88] G. Grabner, I. Nobauer, K. Elandt et al., "Longitudinal brain imaging of five malignant glioma patients treated with bevacizumab using susceptibility-weighted magnetic resonance imaging at 7 T," *Magnetic Resonance Imaging*, vol. 30, no. 1, pp. 139–147, 2012.
- [89] M. E. De Backer, R. J. A. Nabuurs, M. A. Van Buchem, and L. Van Der Weerd, "MR-based molecular imaging of the brain: the next frontier," *American Journal of Neuroradiology*, vol. 31, no. 9, pp. 1577–1583, 2010.
- [90] B. Tomanek, U. Iqbal, B. Blasiak et al., "Evaluation of brain tumor vessels specific contrast agents for glioblastoma imaging," *Neuro-Oncology*, vol. 14, no. 1, pp. 53–63, 2012.
- [91] T. He, N. Smith, D. Saunders et al., "Molecular MRI assessment of vascular endothelial growth factor receptor-2 in rat C6 gliomas," *Journal of Cellular and Molecular Medicine*, vol. 15, no. 4, pp. 837–849, 2011.
- [92] K. Herholz, W. Heindel, P. R. Luyten et al., "In vivo imaging of glucose consumption and lactate concentration in human gliomas," *Annals of Neurology*, vol. 31, no. 3, pp. 319–327, 1992.
- [93] J. R. Alger, J. A. Frank, A. Bizzi et al., "Metabolism of human gliomas: assessment with H-1 MR spectroscopy and F-18 fluorodeoxyglucose PET," *Radiology*, vol. 177, no. 3, pp. 633–641, 1990.
- [94] C. Rémy, N. Fouilhé, I. Barba et al., "Evidence that mobile lipids detected in rat brain glioma by 1H nuclear magnetic resonance correspond to lipid droplets," *Cancer Research*, vol. 57, no. 3, pp. 407–414, 1997.

- [95] P. Zonari, P. Baraldi, and G. Crisi, "Multimodal MRI in the characterization of glial neoplasms: the combined role of single-voxel MR spectroscopy, diffusion imaging and echo-planar perfusion imaging," *Neuroradiology*, vol. 49, no. 10, pp. 795–803, 2007.
- [96] M. E. Meyerand, J. M. Pipas, A. Mamourian, T. D. Tosteson, and J. F. Dunn, "Classification of biopsy-confirmed brain tumors using single-voxel MR spectroscopy," *American Journal of Neuroradiology*, vol. 20, no. 1, pp. 117–123, 1999.
- [97] D. Yang, Y. Korogi, T. Sugahara et al., "Cerebral gliomas: prospective comparison of multivoxel 2D chemical-shift imaging proton MR spectroscopy, echoplanar perfusion and diffusion-weighted MRI," *Neuroradiology*, vol. 44, no. 8, pp. 656–666, 2002.
- [98] X. Li, D. B. Vigneron, S. Cha et al., "Relationship of MR-derived lactate, mobile lipids, and relative blood volume for gliomas in vivo," *American Journal of Neuroradiology*, vol. 26, no. 4, pp. 760–769, 2005.
- [99] A. J. Kumar, N. E. Leeds, G. N. Fuller et al., "Malignant gliomas: MR imaging spectrum of radiation therapy-and chemotherapy-induced necrosis of the brain after treatment," *Radiology*, vol. 217, no. 2, pp. 377–384, 2000.
- [100] M. E. Mullins, G. D. Barest, P. W. Schaefer, F. H. Hochberg, R. G. Gonzalez, and M. H. Lev, "Radiation necrosis versus glioma recurrence: conventional MR imaging clues to diagnosis," *American Journal of Neuroradiology*, vol. 26, no. 8, pp. 1967–1972, 2005.
- [101] T. Nakajima, T. Kumabe, M. Kanamori et al., "Differential diagnosis between radiation necrosis and glioma progression using sequential proton magnetic resonance spectroscopy and methionine positron emission tomography," *Neurologia Medico-Chirurgica*, vol. 49, no. 9, pp. 394–401, 2009.
- [102] R. F. Barajas Jr., J. S. Chang, M. R. Segal et al., "Differentiation of recurrent glioblastoma multiforme from radiation necrosis after external beam radiation therapy with dynamic susceptibility-weighted contrast-enhanced perfusion MR imaging," *Radiology*, vol. 253, no. 2, pp. 486–496, 2009.
- [103] V. A. Larsen, H. J. Simonsen, I. Law, H. B. Larsson, and A. E. Hansen, "Evaluation of dynamic contrast-enhanced T1-weighted perfusion MRI in the differentiation of tumor recurrence from radiation necrosis," *Neuroradiology*, vol. 55, no. 3, pp. 361–369, 2013.
- [104] B. Hakyemez, C. Erdogan, N. Yildirim, and M. Parlak, "Glioblastoma multiforme with atypical diffusion-weighted MR findings," *British Journal of Radiology*, vol. 78, no. 935, pp. 989–992, 2005.
- [105] A. Batra and R. P. Tripathi, "Atypical diffusion-weighted magnetic resonance findings in glioblastoma multiforme," *Australasian Radiology*, vol. 48, no. 3, pp. 388–391, 2004.
- [106] I. C. Chiang, T. J. Hsieh, M. L. Chiu, G. C. Liu, Y. T. Kuo, and W. C. Lin, "Distinction between pyogenic brain abscess and necrotic brain tumour using 3-tesla MR spectroscopy, diffusion and perfusion imaging," *British Journal of Radiology*, vol. 82, no. 982, pp. 813–820, 2009.
- [107] C. H. Toh, K. C. Wei, C. N. Chang et al., "Differentiation of pyogenic brain abscesses from necrotic glioblastomas with use of susceptibility-weighted imaging," *American Journal of Neuroradiology*, vol. 33, no. 8, pp. 1534–1538, 2012.

Review Article

The Potential Roles of ^{18}F -FDG-PET in Management of Acute Stroke Patients

Adomas Bunevicius, Hong Yuan, and Weili Lin

Biomedical Research Imaging Center, University of North Carolina at Chapel Hill, CB 7513, Chapel Hill, NC 27599, USA

Correspondence should be addressed to Weili Lin; weili.lin@med.unc.edu

Received 21 January 2013; Accepted 14 April 2013

Academic Editor: Fong Y. Tsai

Copyright © 2013 Adomas Bunevicius et al. This is an open access article distributed under the Creative Commons Attribution License, which permits unrestricted use, distribution, and reproduction in any medium, provided the original work is properly cited.

Extensive efforts have recently been devoted to developing noninvasive imaging tools capable of delineating brain tissue viability (penumbra) during acute ischemic stroke. These efforts could have profound clinical implications for identifying patients who may benefit from tPA beyond the currently approved therapeutic time window and/or patients undergoing neuroendovascular treatments. To date, the DWI/PWI MRI and perfusion CT have received the most attention for identifying ischemic penumbra. However, their routine use in clinical settings remains limited. Preclinical and clinical PET studies with [^{18}F]-fluoro-2-deoxy-D-glucose (^{18}F -FDG) have consistently revealed a decreased ^{18}F -FDG uptake in regions of presumed ischemic core. More importantly, an elevated ^{18}F -FDG uptake in the peri-ischemic regions has been reported, potentially reflecting viable tissues. To this end, this paper provides a comprehensive review of the literature on the utilization of ^{14}C -2-DG and ^{18}F -FDG-PET in experimental as well as human stroke studies. Possible cellular mechanisms and physiological underpinnings attributed to the reported temporal and spatial uptake patterns of ^{18}F -FDG are addressed. Given the wide availability of ^{18}F -FDG in routine clinical settings, ^{18}F -FDG PET may serve as an alternative, non-invasive tool to MRI and CT for the management of acute stroke patients.

1. Introduction

In the Western society, stroke is the fourth leading cause of death and a major cause of permanent disability [1, 2]. Ischemic stroke is the most common type of stroke, comprising approximately 87% of all strokes [1]. The main goal of current acute stroke management is to prevent at-risk tissue from infarction by restoring blood flow to ischemic penumbra areas. Intravenous (IV) thrombolysis with recombinant tissue plasminogen activator (tPA) has been well documented offering improved outcomes in ischemic stroke patients who received tPA within 4.5 hours after symptom onset [3–7]. However, this narrow therapeutic time window has substantially limited the amount of all stroke patients receiving tPA. As a result, extensive efforts have been devoted to identifying a subgroup of stroke patients who may benefit from tPA beyond the currently approved therapeutic window and/or to developing more effective therapeutic interventions. Specifically, noninvasive neuroimaging methods have been widely implicated offering insights into the presence or absence

of salvageable tissues (penumbra), which could be used, potentially, to extend the tPA therapeutic window beyond 4.5 hours. In contrast, the advent of intra-arterial thrombolysis and the introduction of endovascular clot retrieval devices (e.g., MERCI, Penumbra, and Solitaire) have shown great potential in improving the efficacy of vascular recanalization, which in turn may further extend the therapeutic window [8, 9]. While promising results in extending the tPA time window and utilizing new endovascular clot retrieval devices have been reported, both methods carry additional risks of mortality, morbidity, and serious complications, underscoring the critical role of careful patient selection [10].

In a clinical setting, the accurate determination of stroke onset (time since last seen normal), competent neurological examination, and noncontrast computed tomography (CT) scans to rule out intracerebral hemorrhage are vital for selecting ischemic stroke patients who may benefit from reperfusion therapies [3]. Despite significant advancements in neuroimaging, only non-contrast CT has a proven value for the management of acute stroke patients [3, 11]. Nevertheless,

the search for imaging tools capable of providing insights into tissue viability continues to gain interest, which in turn may improve patient selection for reperfusion treatments beyond the currently approved therapeutic window for tPA. The presence of neuroimaging-based evidence of salvageable brain tissue beyond the currently recommended rt-PA therapeutic window further emphasizes the need for identifying such tools [12–15]. Consequently, it was suggested that the currently employed “time-to-treat” approach may not be ideal and should be replaced by “tissue-to-treat” [16]. Clearly, one of the prerequisites for the utilization of the “tissue-to-treat” approach is the availability of accurate neuroimaging-based surrogate markers capable of discerning tissue viability. Such imaging-based biomarkers may distinguish stroke patients who could potentially benefit from tPA beyond 4.5 hour, and/or from neuroendovascular treatments. The optimal imaging modality should be rapid, accurate, and readily available in a busy clinical setting and accompanied by automatic data analysis techniques [16].

In recent years, diffusion-weighted imaging/perfusion-weighted imaging (DWI/PWI) magnetic resonance imaging (MRI) [12, 15] and perfusion CT [17] have received considerable attention and have been suggested as imaging signatures for identifying the presence or absence of salvageable tissues. Specifically, the notion of diffusion/perfusion mismatch (DPM) has gained substantial interest as an effective tool to reveal the presence of ischemic penumbra [11, 12, 15, 18]. The underlying concept of DPM is that the abnormal *diffusion* areas represent the ischemic core, which will progress to infarction independent of treatments. In contrast, regions with abnormal *perfusion* represent tissues at risk of infarction if blood flow is not restored in a timely manner. As a result, brain regions with abnormal perfusion that reside outside of the abnormal diffusion areas, known as DPM, may be indicative of viable tissues, but they are at an increased risk of irreversible injury in the absence of timely reperfusion [19, 20]. Conversely, the absence of DPM would suggest no salvageable tissues. Figure 1 shows acute diffusion/perfusion images as well as the final lesions from two representative patients. The upper row shows a patient with matched diffusion/perfusion deficits (imaged at 4.30 hours after onset and no tPA), suggesting the absence of salvageable tissues. Indeed, the acute diffusion/perfusion deficits spatially match with the final lesion. Acute DPM is observed in the patient shown in the bottom row (imaged at 1.19 hours with tPA), suggesting the presence of ischemic penumbra. Consistent with the DPM hypothesis, the mismatched region was not recruited into final infarction, demonstrating the potential clinical utility of DPM in an acute ischemic stroke. However, despite these promising results [12, 15], unacceptable reliability due to acute reversal of DWI lesions and the failure of all lesions to evolve to the final infarct have substantially limited clinical acceptance of DPM [16, 21, 22]. In addition, there is a lack of consensus on the choices of DWI and PWI thresholds delineating diffusion and perfusion abnormalities [23]. Therefore, a well-controlled clinical trial is needed to rigorously determine the clinical values of DPM prior to its routine clinical applications [24]. Although perfusion CT has been employed to identify patients for reperfusion therapies,

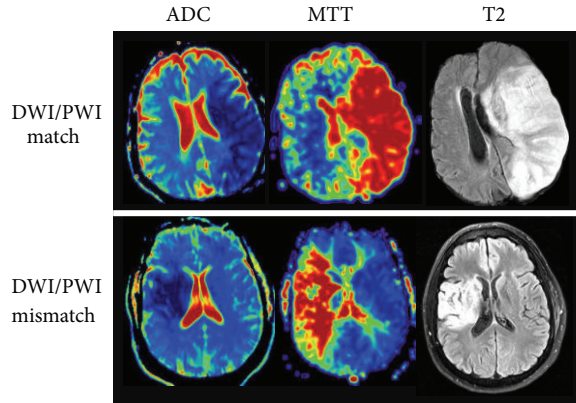


FIGURE 1: ADC and MTT maps demonstrating DWI/PWI match and mismatch in relation to the MRI T2 lesion.

it is limited by the need for an IV contrast injection, an additional radiation dose, and has less reliable threshold values when compared to DWI/PWI MRI [23, 25, 26].

In addition to MR and CT, PET has also been employed in an attempt to provide insights into brain tissue viability. This is perhaps not surprising, given its ability to provide *in vivo* measures of oxygen and glucose metabolism, the two main energy substrates of the brain. With ^{15}O -labeled tracers, quantitative measurements of cerebral hemodynamics (cerebral blood flow (CBF) and cerebral blood volume (CBV)) and oxygen metabolism (oxygen extraction fraction (OEF) and cerebral metabolic rate of oxygen utilization (CMRO_2)) can be obtained using PET. In particular, a number of seminal PET studies have demonstrated the existence of critical CBF thresholds and duration (Figure 2) below which functional and metabolic processes are disturbed and eventually cease [14, 18, 19, 27–30]. However, CBF alone cannot faithfully predict tissue fate; the duration to which neurons are under compromised perfusion is equally critical for final neuronal fate as shown in Figure 2 [27, 30, 31]. Furthermore, functional CBF threshold values have been shown to vary across neuron populations [30]. Regarding OEF, clinical and preclinical studies have demonstrated that areas with compromised CBF but increased OEF may be indicative of ischemic penumbra [32–35]. However, the final tissue fate of high OEF regions has been variable, suggesting that OEF is not a reliable marker of penumbral tissue [33, 35–37]. Finally, CMRO_2 has been suggested as a highly promising parameter in predicting tissue fate in both experimental [38, 39] and human [32, 36] stroke studies. Specifically, it has been shown that brain regions with reduced CBF but preserved CMRO_2 , are associated with neuronal survival, whereas brain regions with reduced CBF and CMRO_2 likely reflect irreversible tissue damage [29, 32, 36, 38–40]. Collectively, while PET with ^{15}O -labeled tracers provides essential physiological information that could predict tissue final fate during acute cerebral ischemia, the requirement of an in-house cyclotron to produce ultra-short half-life ^{15}O -labeled tracers (~2 min) significantly hampers its clinical utility.

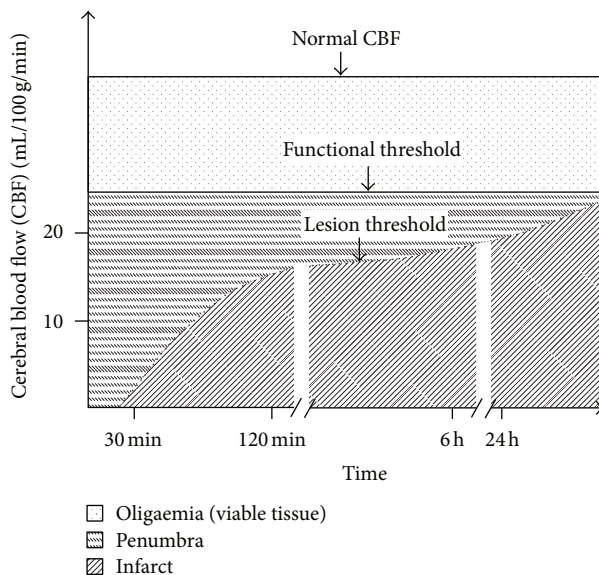


FIGURE 2: The association of cerebral blood flow thresholds and duration of ischemia with functional and structural tissue fates (adapted from [111, 112]).

Alternatively, fluorine-18 (or ^{18}F) has a half-life of 110 min, and [^{18}F]-fluoro-2-deoxy-D-glucose (^{18}F -FDG) has been utilized extensively to reveal *in vivo* glucose utilization in different clinical settings, most notably in oncology and cardiology. In myocardial infarction patients, PET with ^{18}F -FDG has been routinely applied to discern viable myocardium (hypoperfused or stunned myocardium with preserved glucose metabolism), before considering coronary artery bypass graft surgery [41–43]. Along those lines, it is highly plausible that ^{18}F -FDG may also offer valuable insights into cerebral glucose metabolism during cerebral ischemia, which consequently discerns tissue viability. In fact, there has been tremendous interest in evaluating the potential of ^{18}F -FDG in cerebral ischemia. The recent innovation of the hybrid PET/MR scanners [44] may further renew interest on the potential clinical utility of PET with ^{18}F -FDG in the management of acute stroke patients. To this end, this review paper will first provide an overview of glucose metabolism, followed by a comprehensive review of both animal and human studies utilizing ^{18}F -FDG in ischemic stroke. Special attention is given to discussing temporal and spatial ^{18}F -FDG uptake patterns during cerebral ischemia. Finally, the possible underlying biological mechanisms associated with the reported temporal and spatial ^{18}F -FDG uptake patterns will be discussed.

2. Cerebral Glucose Metabolism

Maintaining normal brain homeostasis is an energy-consuming process that depends on a continuous supply of oxygen and glucose, since the brain cannot store energy substrates. Despite its relatively low weight (about 2% of the body weight), the brain receives 15% of the total cardiac

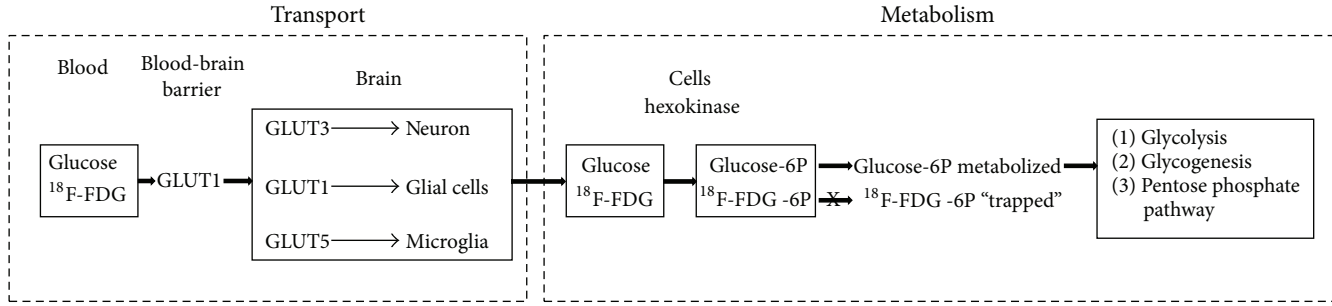
output, 20% of the total oxygen consumption, and 25% of the total glucose utilization. The majority of energy in the brain (87%) is consumed for signaling; only about 13% of its total energy consumption is deferred for maintaining resting membrane potential [14].

Normally, glucose is the primary metabolic substrate of brain cells. However, under certain conditions, brain cells can utilize other substrates, such as lactate, pyruvate, glutamate, and glutamine, which are endogenously synthesized and require glucose as their source of carbon. Under normal conditions, the glucose extraction fraction is approximately 10% [45, 46]. To enter brain cells, blood glucose is transported across the blood-brain barrier (BBB) and then across the plasma membranes of neurons and glial cells. This energy consuming process is mediated by glucose transporter (GLUT) proteins (Figure 3). Three major isoforms of GLUTs are considered important for glucose delivery to brain cells: GLUT1 is the primary glucose transporter in the blood-brain barrier, choroid plexus, ependyma, and glial cells and is not sensitive to insulin; GLUT3 is the predominant glucose transporter in neurons; GLUT5 is highly expressed in microglia [47]. Other types of GLUTs (2, 4, and 7) are expressed in lesser amounts and in more discrete brain regions [47]. When in cells, glucose is phosphorylated to glucose-6-phosphate (glucose-6P) by an enzyme, hexokinase. Once phosphorylated, glucose-6P is unable to exit the cell via the GLUTs and is trapped. Hence, phosphorylation of glucose is critical for the maintenance of the glucose concentration gradient across membranes ensuring a constant flow of glucose into cells via GLUTs [48]. Phosphorylation is also the rate-limiting step of glycolysis. Subsequently, glucose-6P can be processed into three metabolic pathways: (1) glycolysis; (2) glycogenesis; (3) pentose phosphate pathway. Glycolysis gives rise to two molecules of pyruvate, ATP and NADH. Pyruvate can then enter mitochondria and undergo the tricarboxylic acid (TCA) cycle and oxidative phosphorylation to produce 30 to 34 ATP molecules, CO_2 , and water. Oxygen is critical for the TCA cycle and oxidative phosphorylation. In healthy brains, OEF ranges from 30% to 40%, and CMRO₂ averages from 3.0 to 3.8 ml/100 g tissue/min [27, 45, 46]. Finally, minute quantities of glucose-6P can be processed via the pentose phosphate pathway producing NADPH (a reducing equivalent), and glucose-6P can also undergo glycogenesis in astrocytes.

3. Evaluation of Glucose Metabolism in Ischemic Stroke

This section will provide a comprehensive overview of representative studies where glucose metabolism was employed for the study of ischemic strokes. A summary of these representative studies using ^{18}F -FDG is provided in Table 1.

3.1. 2-Deoxy-D-Glucose (2-DG) Autoradiography in Ischemic Stroke. Early studies employed 2-DG as a surrogate marker of glucose metabolism. The 2-DG is a glucose analog with the 2-hydroxyl group replaced by hydrogen. Like glucose, the 2-DG is taken up by cells via GLUTs and phosphorylated by

FIGURE 3: Transport and metabolism of glucose and ^{18}F -FDG.

hexokinase. The 2-DG-6-phosphate cannot be further metabolized and is trapped in cells. The 2-DG is commonly marked with carbon-14 (^{14}C) and is used in animal models to assess 2-DG distribution by means of autoradiography. Using ^{14}C -2-DG, Ginsberg and colleagues demonstrated regions with decreased ^{14}C -2-DG uptake in the presumed ischemic core. More importantly, their results showed a concurrent increase of ^{14}C -2-DG uptake around the border of the ischemic core 60 minutes after a middle cerebral artery occlusion (MCAO) [49]. This unexpected finding could be of critical importance, particularly if the hyper ^{14}C -2-DG uptake regions represent probable ischemic penumbrae. Paschen et al. further investigated the relationship between blood flow, glucose metabolism, and energy status in a permanent gerbil MCAO model [50]. They found that normal CMR_{glc} was maintained at $\text{rCBF} > 40 \text{ ml}/100 \text{ g}/\text{min}$ but markedly increased at rCBF from 35 to $20 \text{ ml}/100 \text{ g}/\text{min}$, sharply reduced, and eventually ceased at $\text{rCBF} < 20 \text{ ml}/100 \text{ g}/\text{min}$ (Figure 4). Importantly, tissue ATP content was normal until rCBF fell below $20 \text{ ml}/100 \text{ g}/\text{min}$. Comparing the relation between CMR_{glc} versus CBF and ATP versus CBF, it is evident that the compensatory increase of CMR_{glc} at rCBF between 20 and $35 \text{ ml}/100 \text{ g}/\text{min}$ was sufficient to replenish cellular energy content, leading to unsalted ATP even with compromised CBF. This elevation of glucose metabolism in regions with compromised CBF can potentially have profound clinical implications and serve as an imaging signature of ischemic penumbra.

The utilization of ^{14}C -2-DG for probing *in vivo* glucose metabolism is limited by its inapplicability for human studies, as well as for longitudinal evaluations of glucose metabolism. Thus, noninvasive markers of glucose metabolism are important for the assessment of temporal and spatial changes of glucose metabolism in ischemic stroke.

3.2. ^{18}F -FDG PET in Ischemic Stroke. ^{18}F -FDG is a glucose analog in which the normal hydroxyl group in position 2' is replaced by a positron-emitting radioactive isotope ^{18}F [51]. Like glucose, the ^{18}F -FDG is transported by GLUTs and is phosphorylated by hexokinase into ^{18}F -FDG-6-phosphate (^{18}F -FDG-6P) (Figure 3). The majority of ^{18}F -FDG is trapped in brain cells ~ 1 hour after the injection, and thus PET scanning is usually initiated 40 minutes after the injection. The lack of the hydroxyl group prevents the ^{18}F -FDG-6P

from further metabolism and is thus trapped in cells. For this reason, the ^{18}F -FDG-6P serves as a good marker revealing the *in vivo* distribution of glucose uptake by cells. Under normal physiologic conditions, neurons residing in the cortical gray matter, basal ganglia, cerebellum, and brain stem have the greatest glucose demand, resulting in the most intense ^{18}F -FDG uptake [52, 53]. As mentioned previously, one of the major advantages of ^{18}F -FDG is its long half-life, ~ 110 min. Therefore, an onsite cyclotron is not needed. With its long half-life, ^{18}F -FDG has been widely used in experimental neurosciences and is the most commonly used radioisotope in clinical settings.

In the context of this review paper, we will focus our discussion on how ^{18}F -FDG has been employed in the study of cerebral ischemia, particularly in predicting tissue fate. Experimental stroke studies will first be discussed, followed by patient studies. We will also determine if a similar elevated glucose metabolism in peri-ischemic regions as reported by Ginsberg et al. and Paschen et al. using ^{14}C -2-DG was also reported using ^{18}F -FDG.

3.2.1. Animal Studies. ^{18}F -FDG has been widely used in experimental stroke research for more than two decades. However, early studies did not specifically investigate how ^{18}F -FDG uptake and metabolism can be used to discern ischemic penumbra [32] and thus they will not be discussed here.

Two recent studies evaluated ^{18}F -FDG metabolism 75 minutes [54] and 3 hours [55] after MCAO using an ischemic stroke model, respectively. Sobrado et al. carried out a longitudinal evaluation of ^{18}F -FDG metabolism and infarct size [55]. Both permanent (right MCA + bilateral ICA occlusion followed by reperfusion of contralateral CCA after 75 mins) and transient (right MCA + bilateral ICA occlusion followed by reperfusion of all 3 vessels at 75 mins) ischemia were studied. MRI was acquired at 3, 24, and 48 hours after MCAO [55]. They found that relative to the contralateral hemisphere, areas corresponding to ischemic core had decreased ^{18}F -FDG uptake in both transient and permanent MCAO models for all three time points. To further determine if ^{18}F -FDG could predict final tissue fates, abnormal ADC regions in the transient MCAO group were divided into two subcategories: progressed (recruited tissue) versus did not progress (recoverable tissue) to final infarction at 24 hours. Although

TABLE 1: Published studies in experimental and human stroke studies evaluating ¹⁸F-FDG uptake.

Study	Stroke model/number of patients	Procedures	Poststroke timing	Relevant findings
Animals				
Walberer et al., 2012 [54]	Embolic MCAO in rats	¹⁸ F-FDG PET	75 minutes	(i) At 60 minutes, rCBF correlated positively with Ki (FDG transport from blood to brain).
		MRI and histological examination (final infarct volume)	24 hours	(ii) Infarcted tissue at 24 hours could be predicted by Ki (net influx rate constant) at 75 min.
		¹⁵ O-H ₂ O PET (CBF)	Before, and at 5, 30, and 60 minutes	(iii) Parts of hypoperfused tissue that was infarcted at 24 hours had normal or elevated Ki at 1 hour.
Sobrado et al., 2011 [55]	Transient and permanent MCAO in rats	¹⁸ F-FDG PET	Before and at 3, 24, and 48 hours	(i) ¹⁸ F-FDG uptake in ischemic core regions was reduced for all time points after MCAO.
		MRI (T2WI, DWI and PWI)		(ii) At 3 hours after MCAO, areas that recovered with reperfusion at 24 hours had greater ¹⁸ F-FDG uptake when compared to brain areas that progressed to infarction at 24 hours.
		Nissl staining	3 hours	
Kuge et al., 2000 [57]	Thromboembolic MCAO in primates	¹⁸ F-FDG PET	24 hours	(i) Ischemic core: reduced CBF, CMR _{glc} , and negative TCC.
		¹² O-H ₂ O PET (CBF)	Before and 1, 2, 4, 6, and 24 hours	(ii) Ischemic penumbra: moderate decrease of CBF, increase of CMR _{glc} , and positive TCC staining.
		2,3,5-triphenyltetrazolium chloride (TTC) staining	24 hours	
Fukumoto et al., 2011 [58]	Thrombotic MCAO in rats	¹⁸ F-FDG PET	Before and days 1, 3, 7, and 14	(i) Peri-infarct areas: significantly increased PET uptake of ¹⁸ F-FDG at days 7 and 14 and of ¹¹ C-PK11195 at days 3, 7, and 14, plus Iba1 staining at day 7.
		¹¹ C-PK11195 PET (neuroinflammation)		(ii) Infarct core: reduced uptake of ¹⁸ F-FDG at days 1–14, increased ¹¹ C-(R)PK11195 bindings at days 7 and 14 and reduced ¹¹ C-FMZ binding at days 7 and 14.
		¹¹ C-FMZ PET (neuronal integrity)		
Heiss et al., 1992 [40]	16 hemispheric stroke patients	¹¹ C-PK11195; ¹¹ C-FMZ and ¹⁸ F-FDG autoradiography	7 days	
		Iba1 (microglia activation) and NeuN (neuronal damage) immunohistochemistry		
Humans				
Nasu et al., 2002 [60]	24 ischemic stroke patients	¹⁸ F-FDG, H ₂ ¹⁵ O, ¹⁵ O ₂ , and C ¹⁵ O PET	6–48 hours	(i) Core: severely reduced OEF, CMRO ₂ , CBF, and CMR _{glc} .
			13–25 days	(ii) Penumbra: reduced CMRO ₂ , CMR _{glc} , and CBF. (iii) Some penumbral areas had increased CMRO ₂ , OEF, CMR _{glc} and GEF and did not progress to final infarct. (iv) When compared to the first scan: Core—increased CBF; penumbra: reduced CMRO ₂ , CMR _{glc} , and OEF.
Heiss et al., 1992 [40]	16 hemispheric stroke patients	¹⁸ F-FDG PET, MRI, and CT	1–7 days Later time points	(i) In the acute phase ¹⁸ F-FDG hyperaccumulation foci around hypoaccumulation areas were evident in 7 out of 20 patients. (ii) Final tissue fate of hyper-accumulation areas was variable.

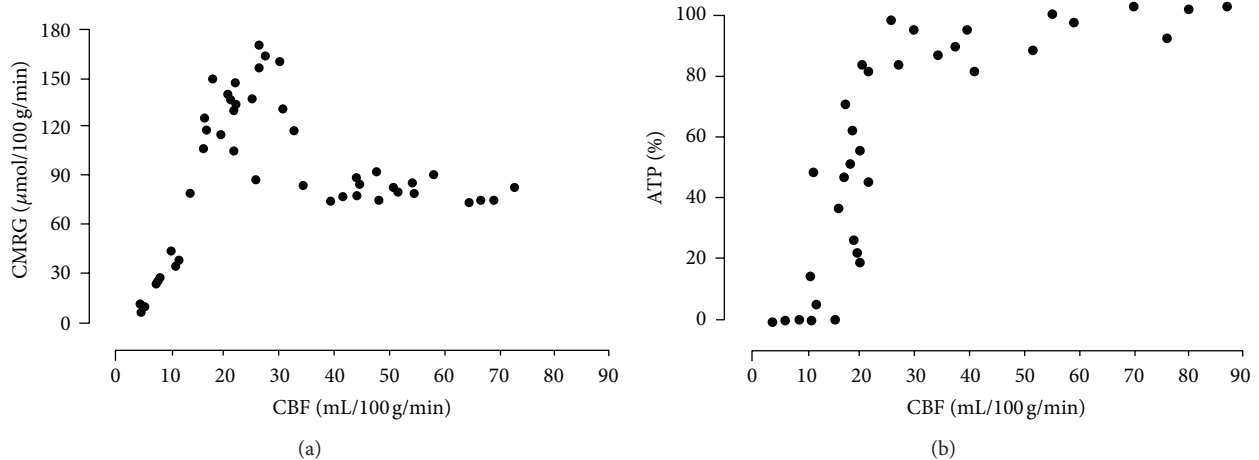


FIGURE 4: The association of cerebral blood flow (CBF) with cerebral metabolic rate of glucose (CMR_{glc}) and ATP content in a gerbil stroke model (adapted from [50], with permission).

a reduced ^{18}F -FDG uptake was observed in both categories, ^{18}F -FDG uptake was significantly greater in recoverable tissue when compared to the recruited tissue, suggesting that ^{18}F -FDG may provide a means of predicting final tissue fate. In addition to measuring ^{18}F -FDG uptake, Walberer et al. further evaluated how quantitative measures of the rate constants of ^{18}F -FDG uptake correlated with CBF and tissue fates in a rat embolic MCAO model [54]. Specifically, ^{18}F -FDG K1 (^{18}F -FDG transports from blood to the brain) and Ki (^{18}F -FDG net influx rate constraint) kinetic constants were measured 75 min after stroke, and their ability in predicting final tissue outcome (MR T2 images) at 24 hours was evaluated. Two major findings were reported in this study. First, a strong correlation ($r = 0.89$) between K1 and rCBF 60 minutes after MCAO was observed, suggesting that K1 of ^{18}F -FDG can be a reliable estimate of rCBF during the hyperacute phase of a stroke. Second, elevated Ki (preserved glucose consumption) and reduced K1 (reduced rCBF) were observed 75 min after stroke, suggesting the presence of viable tissues through a compensatory increase of glucose uptake and phosphorylation in the hypo-perfused tissue.

In contrast to utilizing ^{18}F -FDG during hyperacute stroke, Kuge et al. investigated ^{18}F -FDG uptake in a primate thromboembolic stroke model (autologous blood injection into the left ICA) 24 hours after MCAO [56]. They found that regions with a decrease of CBF and significant reduction of CMR_{glc} at 24 hours after MCAO were consistent with negative 2,3,5-triphenyltetrazolium chloride (TTC) staining indicating infarction [57]. More importantly, several areas surrounding the ischemic core had moderately decreased CBF (40%–80% of contralateral values) and increased CMR_{glc} at 24 hours, which corresponded to TTC positive staining.

More recently, Fukumoto et al. carried out a serial PET study (before and 1, 3, 7, and 14 days after stroke) using multiple radiotracers, including ^{18}F -FDG for glucose metabolism, ^{11}C -(R)PK11195 (peripheral benzodiazepine receptors) for neuroinflammation, and ^{11}C -FMZ (central benzodiazepine receptor) for neuronal integrity in a photochemically induced

thrombosis (PIT) MCAO rat model [58]. In the core, there was a significant reduction of ^{18}F -FDG uptake in all study time points that was accompanied by an increased ^{11}C -(R)PK11195 binding (suggesting neuroinflammation) at days 7 and 14 and reduced ^{11}C -FMZ binding (suggesting neuronal loss) at days 7 and 14. On the other hand, ^{18}F -FDG uptake in the peri-ischemic areas was comparable to the normal brain regions at days 1 and 3 and was significantly increased on days 7 and 14. The latter increase of ^{18}F -FDG coincided with increased ^{11}C -(R)PK11195 uptake at days 3 through 14. These findings suggest that the delayed increased FDG uptake in the peri-ischemic regions was largely attributed to inflammation. Furthermore, at poststroke day 7, there was a significant overlap between increased ^{18}F -FDG and ^{11}C -(R)PK11195 uptake on autoradiography, as well as increased Iba1 immunohistochemistry staining. Together, these findings imply microglial activation at post-MCAO day 7. Similar results were also reported by Rojas et al. [59] although neuroinflammation was more pronounced in the ischemic core when compared to penumbra at day 4 after stroke. The difference in animal models may account for the discrepancies between these two studies. Specifically, in the transient MCAO model, collateral circulation is significantly reduced by transient occlusion of both CCAs, possibly preventing activation of neuroinflammatory cascade in penumbral areas. Furthermore, reperfusion injury in the PIT model can damage microglial cells, leading to silenced neuroinflammation [58].

3.2.2. Clinical Studies. Despite promising findings from experimental stroke studies suggesting the potential clinical utility of ^{18}F -FDG in discerning viable brain tissues, the applications of ^{18}F -FDG in acute stroke patients are surprisingly scant; the majority of ^{18}F -FDG studies in human ischemic stroke have been conducted in subacute or chronic phases of stroke. Nevertheless, some interesting findings and indirect evidence of elevated ^{18}F -FDG uptake in the peri-ischemic

areas similar to observations in animal studies have been reported [40, 60]. Several representative studies are reviewed below.

In 16 hemispheric ischemic stroke patients, Heiss and colleagues carried out multitracer PET, including ^{18}F -FDG, H_2^{15}O , $^{15}\text{O}_2$, and C^{15}O_2 , at 6–48 hours (tp1, mean = 23 hours) and again 13–25 days (tp2, mean = 15.6 days) after stroke [40]. Probable core was defined as brain areas with the greatest reduction of CMRO_2 and CBF, whereas border zones of peri-infarct tissues were defined as 2 rims of 7.65 mm (or 3 pixels) surrounding the infarct core. Each rim was divided into 4 sectors, rendering 8 peri-infarct regions per patient. Not surprisingly, a significant reduction of OEF, CMRO_2 , CBF, and CMR_{glc} in the infarct core relative to the contralateral mirror region was observed at tp1, followed by hyperemia at tp2. For the border zone areas, although a significant reduction of CMRO_2 , CMR_{glc} , and CBF at tp1 was observed which continued to decrease at tp2, the authors noted that the observed changes were highly heterogeneous. Qualitative examination of the peri-infarct regions revealed different outcomes with metabolic derangements. Specifically, peri-infarct regions with a stable or increased CMRO_2 , OEF, CMR_{glc} , and glucose extraction fraction (GEF) at 24 hours after stroke were not infarcted, while low CMRO_2 , OEF, CMR_{glc} , and OEF were consistent with CT evidence of infarction 4 days after stroke. More recently, Nasu et al. conducted ^{18}F -FDG PET, MRI, and CT in 24 ischemic stroke patients 1 to 7 days after stroke onset [60]. Colocalized reduction of ^{18}F -FDG uptake and an abnormal MR was noted in 20 patients. Of which, hyper uptake of ^{18}F -FDG around the areas of decreased ^{18}F -FDG was noted in 7 patients. Unfortunately, final tissue fates of the hyperuptake ^{18}F -FDG regions were not evaluated in this study. Finally, chronic ^{18}F -FDG studies (days and months after ischemic stroke) in stroke patients were also reported by several groups, and a reduction of ^{18}F -FDG in the infarct areas is consistently reported [32, 45, 60, 61].

In summary, experimental studies of small animal [54, 55, 58] and primate [56] ischemic stroke models have revealed a consistent pattern of reduced ^{18}F -FDG uptake in the presumed ischemic core regions. However, the temporal and spatial patterns of ^{18}F -FDG uptake in the peri-ischemic regions are more variable in the literature. An acute elevated ^{14}C -2-DG uptake in the peri-infarct area was reported by Ginsberg et al. [49]. Paschen et al. [50] further demonstrated that this increased uptake region corresponded to the ischemic penumbra. Interestingly, ^{18}F -FDG studies conducted by Sobrado et al. [55] and Walberer et al. [54], both conducted during acute ischemia, failed to observe elevated ^{18}F -FDG uptake in the peri-infarct area. Instead, an elevated uptake was observed at later times, >1 day after MCAO, which is more consistent with neuroinflammation. Attempting to discern the potential discrepancies in the temporal and spatial uptake patterns of glucose at the peri-ischemic region, we recently conducted ^{18}F -FDG PET study using a transient intraluminal MCAO ischemic stroke rat model. ^{18}F -FDG uptake patterns 30, 60, 90, 120, and 150 mins after MCAO were revealed. Final tissue fate was determined using 24 hours T2-weighted MR images. In concert to findings reported

in the literature, we observed reduced ^{18}F -FDG uptake in the ischemic core regions immediately after MCAO that remained low across all time points (Figure 5). Elevated ^{18}F -FDG uptake in the peri-ischemic region was evident from 30 to 120 minutes, but largely diminished at 150 minutes after MCAO. More importantly, the majority of ^{18}F -FDG hyper-uptake regions were not recruited in the final infarction at 24 hours, suggesting that the compensatory increase of ^{18}F -FDG uptake may be associated with neuronal survival and is consistent with that reported by Paschen et al. [50]. Although additional studies are needed to further confirm our findings, our study suggests that acute elevated ^{18}F -FDG uptake may offer a pathophysiologically relevant marker of tissue viability.

Similar to the experimental stroke studies, a severe reduction of ^{18}F -FDG uptake at the presumed core area has also been consistently reported in human stroke studies [40, 45, 60, 61]. However, results on quantitative and qualitative temporal and spatial patterns of ^{18}F -FDG uptake in stroke patients, particularly during the acute phase, are lacking. With ongoing technological advancements of PET imaging that allow more precise evaluation of spatial ^{18}F -FDG uptake patterns, further studies specifically assessing ^{18}F -FDG metabolisms in acute ischemic stroke patients are warranted.

4. Possible Mechanisms Underlying Increased ^{18}F -FDG Uptake in the Probable Penumbral Tissue

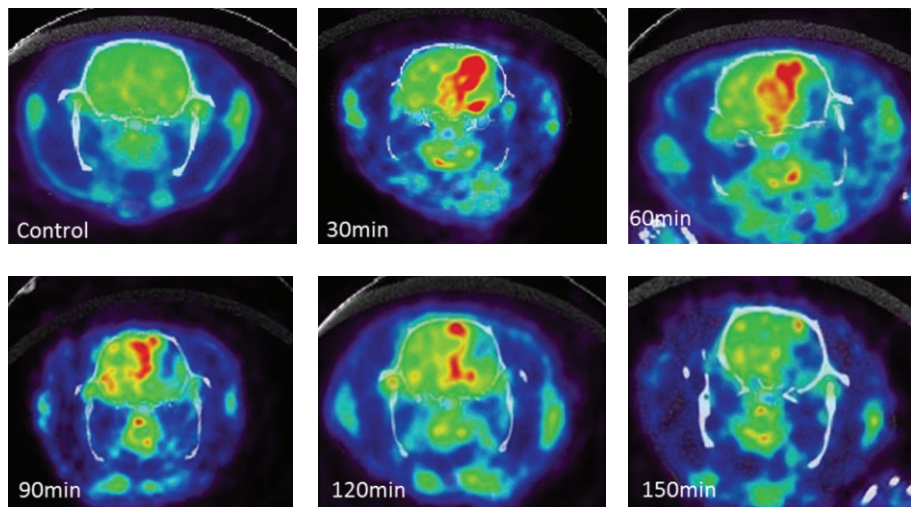
In light of the potential clinical utility of the observed acute ^{18}F -FDG hyper uptake in revealing the presence of ischemic penumbra, this section will discuss potential cellular and physiological mechanisms that may contribute to such ^{18}F -FDG hyper-uptake at the peri-ischemic regions (Table 2).

4.1. Cellular Mechanisms

4.1.1. Activation of GLUTs. As discussed previously, GLUTs play a critical role in transporting glucose from blood to the brain. Therefore, an upregulation of GLUTs expression may lead to an increased ^{18}F -FDG uptake in PET images. A number of studies have reported that GLUTs can be up-regulated in response to cerebral ischemia in a manner similar to the observed temporal and spatial patterns of ^{18}F -FDG uptake in ischemic stroke studies [54, 55]. Specifically, experimental studies of neuronal gene therapy have demonstrated that induction of brain GLUT1 overexpression during ischemic insult was associated with a significant increase of glucose transport using 2-DG autoradiography [62], as well as improved neuronal survival [63, 64]. Lee and Bondy reported that MCAO in rats induced a global and immediate (within an hour) increase of GLUT1 glial and neuronal mRNA expressions even in brain regions that normally do not express GLUT1 [65]. GLUT1 mRNA expression subsequently lateralized to the ischemic hemisphere and was mainly evident in the cortical regions surrounding the ischemic core at 24 hours. McCall et al. demonstrated an increased number

TABLE 2: Possible mechanisms of increased ^{18}F -FDG utilization in penumbral areas.

	<i>Cellular mechanisms</i>	<i>Time course</i>
Increased FDG transport		
GLUT1 upregulation	Increased ^{18}F -FDG transport across the blood-brain barrier	Acute
GLUT3 upregulation	Increased ^{18}F -FDG uptake by neurons	Acute
GLUT5 upregulation	Increased ^{18}F -FDG uptake by microglia cells	Subacute to chronic
Increased FDG phosphorylation		
Hexokinase upregulation	Increased ^{18}F -FDG-6P “trapping” in cells	Acute
Neuroinflammation		
Microglia activation	Increased ^{18}F -FDG uptake by activated cells	Acute
Leukocyte migration	Increased ^{18}F -FDG uptake by activated cells	Sub-acute
Macrophage migration	Increased ^{18}F -FDG uptake by activated cells	Sub-acute
<i>Physiologic associations</i>		
Peri-infarct spreading depression-like depolarization (PID)	Increased metabolic demand	Acute to sub-acute
Neuronal regeneration	Increased metabolic demand	Acute to sub-acute

FIGURE 5: ^{18}F -FDG uptake prior to MCAO (control) and at different times after MCAO in a transient intraluminal MCAO rat model.

of parenchymal and microvascular GLUT1s 24 hours and 4 days after MCAO [66]. Vannucci et al. studied changes of GLUT1 and GLUT3 mRNAs expressions after 2.5 hours of severe hypoxic-ischemic insult in 7-day-old rat brains [67]. They found elevated BBB GLUT1 mRNA expressions in both hemispheres 1 hour after ischemic insults. In addition, similar to observations by Lee and Bondy [65], this elevated GLUT1 mRNA expression only persisted in the ipsilateral hemisphere during 24 hours of recovery. In the same study, the authors further reported that the temporal expression of neuronal GLUT3 mRNA appeared tissue fate dependent. The GLUT3 mRNAs expression continued to decrease in the core throughout the entire study, while the penumbral areas exhibited an increase of GLUT3 mRNA expression at 1 hour but started to decrease 3 hours after ischemic insults. Finally, maximally increased GLUT5 expression at the peri-infarct areas has been reported in a rat MCAO model 5 days after stroke that remained elevated until 15 days after the insult [68], suggesting that GLUT5 activation is consistent with neuroinflammation in response to neuronal necrosis [47].

In summary, temporospatial changes of GLUTs 1 and 3 mRNA expressions in ischemic conditions may partially account for acutely increased ^{18}F -FDG PET uptake in the peri-ischemic regions [40, 54–56, 58, 60]. This up-regulation of GLUTs can serve as an important compensatory mechanism to facilitate glucose transport via the BBB and into cells in order to replenish energy stores and promote neuronal survival. In contrast, increased GLUT5 expression may be more associated with inflammation during the sub-acute phase.

4.1.2. Activation of Hexokinase. Phosphorylation by hexokinase is one of the principal steps in ^{18}F -FDG metabolism and is also a rate-limiting step of glucose metabolism. Up-regulation of phosphorylation in response to reduced oxygen availability has been suggested. Specifically, Paschen et al. demonstrated that a greater proportion of ^{14}C -2-DG was phosphorylated in ischemic regions when compared to healthy brain regions (90% versus 80%) in an MCAO

gerbil model [50]. As discussed previously, Walberer et al. demonstrated that part of the peri-infarct tissues had reduced K₁ and increased K_i ¹⁸F-FDG rate constants 1 hour after MCAO, suggesting a compensatory increase of the glucose phosphorylation rate that requires both hexokinase and ATP [54]. Studies of brain tumor cell cultures and in myocardial infarction animal models reported upregulated hexokinase mRNA expression in response to hypoxia [69–71]. Similarly, a study of cerebrocortical cell cultures found that 3 days of exposure to 1% oxygen increased activities of glycolytic and its related enzymes (hexokinase, lactate dehydrogenase, and pyruvate kinase), as well as decreased activities of the TCA cycle related enzymes (citrate synthase and glutamate dehydrogenase), suggesting that neurons are capable of adapting to prolonged hypoxia by upregulating glycolysis and downregulating oxidative energy metabolism [72]. Finally, upregulation of hexokinase was observed in a global cerebral ischemic model using 7-day postnatal rats [73]. Collectively, these findings suggest that changes of hexokinase activity and expression in response to hypoxia may contribute to the increased “trapping” of ¹⁸F-FDG-6P in the peri-ischemic regions.

4.1.3. Neuroinflammation. Neuroinflammation is a temporally and spatially dynamic process that includes resident brain cells (most importantly microglia) and blood-borne leukocytes and monocytes (for comprehensive review on neuroinflammation, see [74, 75]). It is generally believed that microglial activation is the first step of the neuroinflammatory process, followed by an influx of neutrophils 1 day after stroke, and infiltration of macrophages 2 days after stroke [74]. Since immune cells participating in acute (neutrophils) and chronic (macrophages) inflammatory responses have high metabolic demands, it may not be surprising that neuroinflammation results in an increased uptake of ¹⁸F-FDG [76–79].

Temporal and spatial progression of neuroinflammation was extensively studied in experimental stroke models. It was shown that mRNA expression of glial fibrillary acidic protein, a marker of reactive astrocytes, started to increase at 6 hours and continued to increase until day 3 after MCAO [80]. Using a permanent MCAO rat model, Mabuchi et al. found that activated microglia was evident in the peripheral area surrounding the infarction at 6 hours and continued to increase in number up to 48 hours after stroke, which coincided with a peak of macrophage accumulation along the boundary of infarction [81]. Furthermore, significant elevation of neuroinflammation 7 days after MCAO was demonstrated by an increased ¹¹C-(R)PK11195 uptake in activated microglia cells as well as by increased number and activation of microglial cells and macrophages using immunohistochemical examination in ischemic penumbra [58, 82] and core [59].

In contrast to experimental stroke studies, temporal progression and spatial distribution of neuroinflammation in humans are most likely different [74]. Postmortem autopsy studies demonstrated the appearance of neutrophils at day 1 and peaked at days 2–3, as well as invasion of macrophages

at day 5 (peak at 3 weeks) after stroke [83, 84]. However, post mortem studies are limited by their inability to provide temporal changes of neuroinflammation. In contrast, non-invasive imaging approaches have been employed to provide insights into the temporal behaviors of neuroinflammation [85–88]. Akopov et al. used SPECT to image 88 acute hemispheric stroke patients with technetium-99 m hexamethylpropyleneamine oxime-labeled leukocytes. An increased leukocyte accumulation was evident at 6 hours, progressively increased until 24 hours, and remained high up to 9 days after stroke [86]. Furthermore, ¹¹C-PK11195 PET has been employed to study microglial activation [87, 88]. Price et al. performed ¹¹C-PK11195 PET in 4 patients with left MCA territory strokes [88]. Significant binding potential of ¹¹C-PK11195 was evident in the core and penumbral regions at 2 days and remained evident up to 30 days after stroke. The ¹¹C-PK11195, however, lacks specificity to different subtypes of neuroinflammatory cells since it binds to mitochondrial peripheral benzodiazepine receptors that are expressed in astrocytes, macrophages, activated microglia, granulocytes, and lymphocytes [89, 90].

Activation of resident brain cells and transmigration of blood-borne immune cells can also be important determinants of the observed increased ¹⁸F-FDG uptake in the peri-infarct areas. However, to the best of our knowledge, there have been no studies systematically investigating temporal and spatial progression of *in vivo* neuroinflammation and its association with glucose metabolism in humans.

4.2. Physiological Associations. It is important to note that direct empirical evidence linking increased ¹⁸F-FDG uptake and to be discussed physiological mechanisms is currently lacking. Therefore, the proposed associations should be considered speculative rather than determinative. Nonetheless, we believe that it is important to discuss them because these mechanisms are physiologically relevant and are associated with cell activation that could lead to increased energy demand and thus ¹⁸F-FDG hyper-uptake.

4.2.1. Peri-Infarct Spreading Depression-Like Depolarization. Peri-infarct spreading depression-like depolarizations (PIDs) are characterized as cortical DC shifts (about 20 mV) that spread along the cerebral cortex at a regular interval with a speed of 3–5 mm/min [91, 92]. Increased neuronal energy demands in PIDs could potentially be associated with ¹⁸F-FDG hyper-uptake. Results from experimental stroke models revealed that PIDs are triggered by the anoxic release of potassium and excitatory amino acids, tend to occur in clusters, and are associated with a significantly increased metabolic rate and energy demands that are not coupled with increase of blood flow. As a result, PIDs could lead to transient episodes of ischemia and the growth of an infarct core into the penumbral zone [91–93]. Therefore, it is plausible that PIDs induced neuronal activation, and thus the increased metabolic demand in the penumbral areas can be associated with the observed increased ¹⁸F-FDG uptake. For example, repeated cortical spreading depression (induced by cortical application of 3.3 M KCl solution) in cats was associated

with increased cortical ^{18}F -FDG uptake and rCBF in PET 60–120 minutes after the experimental procedure [57]. With regards to the temporal relation between PIDs and the onset of ischemia, studies in animal MCAO models indicated that PIDs occur immediately after stroke and progress until the terminal injury [94, 95].

Dohmen et al. were the first to demonstrate PIDs in ischemic stroke patients [96]. Specifically, electrodes were placed at the peri-infarct region of 16 patients undergoing decompressive craniectomy between 9 and 105 hours (mean = 39.8 ± 27.3 hours) after malignant MCA strokes. Spontaneous PIDs were recorded in all but two patients, who were later found to have electrode strips placed over the infarcted tissue. Interestingly, the frequency of PIDs (25 PIDs in 198 hours or 1 PID per 8 hours of monitoring) was the greatest in the patient with the shortest time interval between stroke onset and monitoring (13 hours). Not surprisingly, an increasing ECoG recovery time was observed over time, indicating progressive hemodynamic and metabolic deterioration. These findings suggest that PIDs seem to occur more frequently during acute strokes and decrease with time. PIDs were also recorded in humans with traumatic brain injury and intracerebral hemorrhage, albeit with a lower frequency than those in ischemic stroke patients [97], suggesting that these electrophysiological abnormalities are common in response to impeding functional and structural damage.

4.2.2. Neuronal Regeneration. Neuronal regeneration starts early after ischemic insults and could also contribute to the observed increase of ^{18}F -FDG utilization in the peri-infarct areas. For example, increased expression of mRNA encoding neuropilin-(Npn-) 1, Npn-2, and semaphorin 3A (Sema3A), proteins involved in axonal growth, was reported within hours after MCAO in rats [98]. Furthermore, mRNA expression of brain-derived neurotrophic factor, a member of the neurotrophin family promoting survival and growth of various nerve cell populations [99] and modulating glutamine excitotoxicity in penumbral areas [100], and its full-length receptor have been shown to increase in ischemic penumbrae and reduce in ischemic cores 12 hours after MCAO [101]. However, the temporal and spatial relationship between neuronal regeneration and glucose metabolism in ischemic stroke has not been fully explored to date.

5. Increased ^{18}F -FDG Uptake versus Increased Glucose Metabolism

While the previous discussion offers some of the potential underlying biological mechanisms attributed to the observed hyper uptake of ^{18}F -FDG in the peri-ischemic areas, one remaining major question is whether or not the increased ^{18}F -FDG uptake truly reflects an increased glucose metabolism. To this end, it is important to discuss the lumped constant (LC), that is, the ratio of the metabolic rate of ^{18}F -FDG and the metabolic rate of glucose. LC accounts for the differences in transportation, phosphorylation, and volume of distribution between ^{18}F -FDG and glucose [102]. Therefore, an LC of 1 indicates that there are no changes between the metabolic

rates of ^{18}F -FDG and glucose; that is, the metabolic rate of ^{18}F -FDG is equal to the metabolic rate of glucose. However, there are significant differences between phosphorylation of ^{18}F -FDG and glucose. As a result, CMR_{glc} is usually estimated using a LC of 0.42. More recent studies in a cat MCAO model [103], and an *in vitro* cell model [104] separately demonstrated that ischemic or hypo-perfused tissues can result in a 20% to 78% increase of LC when compared to the normal brain tissue. These findings have profound implications on the utilization of ^{18}F -FDG for assessing glucose metabolism. Specifically, in the event when concurrently increased ^{18}F -FDG uptake and LC occurs, the increased ^{18}F -FDG uptake might not reflect increased glucose metabolism. To make the matter worse, the extent to which LC is altered in response to ischemia can be time and species dependent [105]. Therefore, one must be cautious in the interpretation of ^{18}F -FDG uptake as a marker of glucose metabolism.

6. Limitations of ^{18}F -FDG PET

Despite its potential clinical values, limitations on using ^{18}F -FDG PET for acute stroke patients should be acknowledged. Widely accepted standardized protocols for the acquisition and analysis of ^{18}F -FDG PET remain lacking, limiting the quantitative evaluation of ^{18}F -FDG PET across centers [106, 107]. Technical factors including optimal timing between ^{18}F -FDG injection and PET imaging, the partial-volume effects [108], and uniform determination of ROIs should be considered [106]. Furthermore, the relatively long time interval between injection and PET imaging could make it impractical for the management of acute stroke patients. Radiolabeled tracers are sources of radiation, and the combination of PET with CT further increases radiation doses. Finally, ensuring 24/7 availability of ^{18}F -FDG can impose challenges in some clinical centers.

Certain clinical situations that are common in the acute ischemic stroke settings can also dampen the clinical utility of ^{18}F -FDG-PET. Transient hyperglycemia is common in acute ischemic stroke patients [109], which can impact the ^{18}F -FDG PET results [107, 110]. Acute correction of hyperglycemia with insulin does not substantially improve ^{18}F -FDG PET image quality because of different dynamics of normalization of plasma versus intracellular glucose concentrations [107]. Sedative medications that alter global metabolism of glucose should be considered. Finally, the inability of acute stroke patients holding still during PET images can also lead to compromised PET image quality.

7. Conclusions

Although ^{18}F -FDG PET is widely available in clinical settings, its potential clinical utility for the management of acute stroke patients has not been extensively studied. Specifically, both experimental and clinical stroke studies have consistently demonstrated a reduction of ^{18}F -FDG uptake in the presumed core regions, whereas the ^{18}F -FDG uptake patterns in the peri-infarct regions are less consistent in the literature.

This paper comprehensively reviews the temporal and spatial variations of glucose metabolism in response to cerebral ischemia with special attention on the peri-infarct regions. In particular, an elevated ^{18}F -FDG (^{14}C -2-DG) uptake in the presumed ischemic penumbra regions has been observed, which appears capable of predicting final tissue fate. The potential cellular mechanisms accounting for the increased glucose utilization and ^{18}F -FDG uptake in the peri-infarct areas (activation of GLUTs, hexokinase, and neuroinflammation) were discussed. In addition, the possible physiological associations (PIPs and neuroregeneration) were proposed. Although the clinical utility of ^{18}F -FDG PET in managing acute stroke patients remains to be seen, rigorous and systematic evaluations of ^{18}F -FDG uptake patterns in acute ischemic stroke patients are warranted.

References

- [1] A. S. Go, D. Mozaffarian, V. L. Roger et al., "Heart disease and stroke statistics—2013 update: a report from the American Heart Association," *Circulation*, vol. 127, no. 1, pp. e6–e245, 2013.
- [2] G. A. Donnan, M. Fisher, M. Macleod, and S. M. Davis, "Stroke," *The Lancet*, vol. 371, no. 9624, pp. 1612–1623, 2008.
- [3] H. P. Adams, G. del Zoppo, M. J. Alberts et al., "Guidelines for the early management of adults with ischemic stroke: a guideline from the American Heart Association/American Stroke Association Stroke Council, Clinical Cardiology Council, Cardiovascular Radiology and Intervention Council, and the Atherosclerotic Peripheral Vascular Disease and Quality of Care Outcomes in Research Interdisciplinary Working Groups: The American Academy of Neurology affirms the value of this guideline as an educational tool for neurologists," *Circulation*, vol. 115, no. 20, pp. e478–534, 2007.
- [4] "Tissue plasminogen activator for acute ischemic stroke. The National Institute of Neurological Disorders and Stroke rt-PA Stroke Study Group," *New England Journal of Medicine*, vol. 333, no. 24, pp. 1581–1587, 1995.
- [5] T. G. Kwiatkowski, R. B. Libman, M. Frankel et al., "Effects of tissue plasminogen activator for acute ischemic stroke at one year. National Institute of Neurological Disorders and Stroke Recombinant Tissue Plasminogen Activator Stroke Study Group," *New England Journal of Medicine*, vol. 340, no. 23, pp. 1781–1787, 1999.
- [6] W. Hacke, M. Kaste, E. Bluhmki et al., "Thrombolysis with alteplase 3 to 4.5 hours after acute ischemic stroke," *New England Journal of Medicine*, vol. 359, no. 13, pp. 1317–1329, 2008.
- [7] K. R. Lees, E. Bluhmki, R. von Kummer et al., "Time to treatment with intravenous alteplase and outcome in stroke: an updated pooled analysis of ECASS, ATLANTIS, NINDS, and EPITHET trials," *The Lancet*, vol. 375, no. 9727, pp. 1695–1703, 2010.
- [8] K. A. Blackham, P. M. Meyers, T. A. Abruzzo et al., "Endovascular therapy of acute ischemic stroke: report of the Standards of Practice Committee of the Society of NeuroInterventional Surgery," *Journal of NeuroInterventional Surgery*, vol. 4, no. 2, pp. 87–93, 2012.
- [9] W. S. Smith, G. Sung, J. Saver et al., "Mechanical thrombectomy for acute ischemic stroke: final results of the multi MERCI trial," *Stroke*, vol. 39, no. 4, pp. 1205–1212, 2008.
- [10] Z. Darkhabani, T. Nguyen, M. A. Lazzaro et al., "Complications of endovascular therapy for acute ischemic stroke and proposed management approach," *Neurology*, vol. 79, no. 13, supplement 1, pp. S192–S198, 2012.
- [11] J. G. Merino and S. Warach, "Imaging of acute stroke," *Nature Reviews Neurology*, vol. 6, no. 10, pp. 560–571, 2010.
- [12] G. W. Albers, V. N. Thijs, L. Wechsler et al., "Magnetic resonance imaging profiles predict clinical response to early reperfusion: the diffusion and perfusion imaging evaluation for understanding stroke evolution (DEFUSE) study," *Annals of Neurology*, vol. 60, no. 5, pp. 508–517, 2006.
- [13] M. Paciaroni, V. Caso, and G. Agnelli, "The concept of ischemic penumbra in acute stroke and therapeutic opportunities," *European Neurology*, vol. 61, no. 6, pp. 321–330, 2009.
- [14] W. D. Heiss, "The ischemic penumbra: correlates in imaging and implications for treatment of ischemic stroke. The Johann Jacob Wepfer award 2011," *Cerebrovascular Diseases*, vol. 32, no. 4, pp. 307–320, 2011.
- [15] S. M. Davis, G. A. Donnan, M. W. Parsons et al., "Effects of alteplase beyond 3 h after stroke in the Echoplanar Imaging Thrombolytic Evaluation Trial (EPITHET): a placebo-controlled randomised trial," *The Lancet Neurology*, vol. 7, no. 4, pp. 299–309, 2008.
- [16] W. L. Lin and W. J. Powers, "Special issue: clinical imaging of hyperacute stroke," *Translational Stroke Research*, vol. 3, no. 2, pp. 173–177, 2012.
- [17] A. A. Konstas, M. Wintermark, and M. H. Lev, "CT perfusion imaging in acute stroke," *Neuroimaging Clinics of North America*, vol. 21, no. 2, pp. 215–238, 2011.
- [18] M. Fisher and B. Bastan, "Identifying and utilizing the ischemic penumbra," *Neurology*, vol. 79, no. 13, supplement 1, pp. S79–S85, 2012.
- [19] J. Sobesky, "Refining the mismatch concept in acute stroke: lessons learned from PET and MRI," *Journal of Cerebral Blood Flow & Metabolism*, vol. 32, no. 7, pp. 1416–1425, 2012.
- [20] M. Ebinger, D. A. De Silva, S. Christensen et al., "Imaging the penumbra—strategies to detect tissue at risk after ischemic stroke," *Journal of Clinical Neuroscience*, vol. 16, no. 2, pp. 178–187, 2009.
- [21] G. Schlaug, A. Benfield, A. E. Baird et al., "The ischemic penumbra: operationally defined by diffusion and perfusion MRI," *Neurology*, vol. 53, no. 7, pp. 1528–1537, 1999.
- [22] S. T. Engelter, S. G. Wetzel, L. H. Bonati, F. Fluri, and P. A. Lyer, "The clinical significance of diffusion-weighted MR imaging in stroke and TIA patients," *Swiss Medical Weekly*, vol. 138, no. 49–50, pp. 729–740, 2008.
- [23] K. A. Dani, R. G. Thomas, F. M. Chappell et al., "Computed tomography and magnetic resonance perfusion imaging in ischemic stroke: definitions and thresholds," *Annals of Neurology*, vol. 70, no. 3, pp. 384–401, 2011.
- [24] W. J. Powers, "Perfusion-diffusion mismatch: does it identify who will benefit from reperfusion therapy?" *Translational Stroke Research*, vol. 3, no. 2, pp. 182–187, 2012.
- [25] A. M. Allmendinger, E. R. Tang, Y. W. Lui et al., "Imaging of stroke: part 1, Perfusion CT—overview of imaging technique, interpretation pearls, and common pitfalls," *American Journal of Roentgenology*, vol. 198, no. 1, pp. 52–62, 2012.
- [26] A. Bivard, C. Levi, N. Spratt et al., "Perfusion CT in acute stroke: a comprehensive analysis of infarct and penumbra," *Radiology*, 2012.
- [27] W. J. Powers and A. R. Zazulia, "PET in cerebrovascular disease," *PET Clinics*, vol. 5, no. 1, Article ID 83106, 2010.

- [28] J. Astrup, B. K. Siejo, and L. Symon, "Thresholds in cerebral ischemia—the ischemic penumbra," *Stroke*, vol. 12, no. 6, pp. 723–725, 1981.
- [29] J. C. Baron, M. G. Bousser, and A. Rey, "Reversal of focal "misery-perfusion syndrome" by extra-intracranial arterial bypass in hemodynamic cerebral ischemia. A case study with ^{15}O positron emission tomography," *Stroke*, vol. 12, no. 4, pp. 454–459, 1981.
- [30] W. D. Heiss and G. Rosner, "Functional recovery of cortical neurons as related to degree and duration of ischemia," *Annals of Neurology*, vol. 14, no. 3, pp. 294–301, 1983.
- [31] F. W. Marcoux, R. B. Morawetz, and R. M. Crowell, "Differential regional vulnerability in transient focal cerebral ischemia," *Stroke*, vol. 13, no. 3, pp. 339–346, 1982.
- [32] W. D. Heiss, R. Graf, K. Wienhard et al., "Dynamic penumbra demonstrated by sequential multitracer PET after middle cerebral artery occlusion in cats," *Journal of Cerebral Blood Flow and Metabolism*, vol. 14, no. 6, pp. 892–902, 1994.
- [33] C. Giffard, A. R. Young, N. Kerrouche, J. M. Derlon, and J. C. Baron, "Outcome of acutely ischemic brain tissue in prolonged middle cerebral artery occlusion: a serial positron emission tomography investigation in the baboon," *Journal of Cerebral Blood Flow and Metabolism*, vol. 24, no. 5, pp. 495–508, 2004.
- [34] S. Pappata, M. Fiorelli, T. Rommel et al., "PET study of changes in local brain hemodynamics and oxygen metabolism after unilateral middle cerebral artery occlusion in baboons," *Journal of Cerebral Blood Flow and Metabolism*, vol. 13, no. 3, pp. 416–424, 1993.
- [35] O. Touzani, A. R. Young, J. M. Derlon et al., "Sequential studies of severely hypometabolic tissue volumes after permanent middle cerebral artery occlusion: a positron emission tomographic investigation in anesthetized baboons," *Stroke*, vol. 26, no. 11, pp. 2112–2119, 1995.
- [36] E. Shimosegawa, J. Hatazawa, M. Ibaraki, H. Toyoshima, and A. Suzuki, "Metabolic penumbra of acute brain infarction: a correlation with infarct growth," *Annals of Neurology*, vol. 57, no. 4, pp. 495–504, 2005.
- [37] M. Furlan, G. Marchai, F. Viader, J. M. Derlon, and J. C. Baron, "Spontaneous neurological recovery after stroke and the fate of the ischemic penumbra," *Annals of Neurology*, vol. 40, no. 2, pp. 216–226, 1996.
- [38] P. Frykholm, J. L. R. Andersson, J. Valtysson et al., "A metabolic threshold of irreversible ischemia demonstrated by PET in a middle cerebral artery occlusion—reperfusion primate model," *Acta Neurologica Scandinavica*, vol. 102, no. 1, pp. 18–26, 2000.
- [39] M. Sakoh, L. Østergaard, L. Røhl et al., "Relationship between residual cerebral blood flow and oxygen metabolism as predictive of ischemic tissue viability: sequential multitracer positron emission tomography scanning of middle cerebral artery occlusion during the critical first 6 hours after stroke in pigs," *Journal of Neurosurgery*, vol. 93, no. 4, pp. 647–657, 2000.
- [40] W. D. Heiss, M. Huber, G. R. Fink et al., "Progressive derangement of periinfarct viable tissue in ischemic stroke," *Journal of Cerebral Blood Flow and Metabolism*, vol. 12, no. 2, pp. 193–203, 1992.
- [41] J. Tillisch, R. Brunken, and R. Marshall, "Reversibility of cardiac wall-motion abnormalities predicted by positron tomography," *New England Journal of Medicine*, vol. 314, no. 14, pp. 884–888, 1986.
- [42] N. Tamaki, M. Kawamoto, E. Tadamura et al., "Prediction of reversible ischemia after revascularization: perfusion and metabolic studies with positron emission tomography," *Circulation*, vol. 91, no. 6, pp. 1697–1705, 1995.
- [43] "Positron emission tomography for the assessment of myocardial viability: an evidence-based analysis," *Ontario Health Technology Assessment Series*, vol. 10, no. 16, pp. 1–80, 2010.
- [44] V. Garibotto, S. Heinzer, S. Vulliemoz et al., "Clinical applications of hybrid PET/MRI in neuroimaging," *Clinical Nuclear Medicine*, vol. 38, no. 1, pp. e13–e18, 2013.
- [45] J. C. Baron, D. Rougemont, and F. Soussaline, "Local interrelationships of cerebral oxygen consumption and glucose utilization in normal subjects and in ischemic stroke patients: a positron tomography study," *Journal of Cerebral Blood Flow and Metabolism*, vol. 4, no. 2, pp. 140–149, 1984.
- [46] P. Lebrun Grandie, J. C. Baron, and F. Soussaline, "Coupling between regional blood flow and oxygen utilization in the normal human brain. A study with positron tomography and oxygen ^{15}O ," *Archives of Neurology*, vol. 40, no. 4, pp. 230–236, 1983.
- [47] S. J. Vannucci, F. Maher, and I. A. Simpson, "Glucose transporter proteins in brain: delivery of glucose to neurons and glia," *Glia*, vol. 21, no. 1, pp. 2–21, 1997.
- [48] J. E. Wilson, "Isozymes of mammalian hexokinase: structure, subcellular localization and metabolic function," *Journal of Experimental Biology*, vol. 206, no. 12, pp. 2049–2057, 2003.
- [49] M. D. Ginsberg, M. Reivich, A. Giandomenico, and J. H. Greenberg, "Local glucose utilization in acute focal cerebral ischemia: local dysmetabolism and diaschisis," *Neurology*, vol. 27, no. 11, pp. 1042–1048, 1977.
- [50] W. Paschen, G. Mies, and K. A. Hossmann, "Threshold relationship between cerebral blood flow, glucose utilization, and energy metabolites during development of stroke in gerbils," *Experimental Neurology*, vol. 117, no. 3, pp. 325–333, 1992.
- [51] J. S. Fowler and T. Ido, "Initial and subsequent approach for the synthesis of ^{18}FDG ," *Seminars in Nuclear Medicine*, vol. 32, no. 1, pp. 6–12, 2002.
- [52] G. K. V. Schultheiss, *Molecular Anatomic Imaging : PET-CT and SPECT-CT Integrated Modality*, Lippincott Williams & Wilkins, Philadelphia, Pa, USA, 2nd edition, 2007.
- [53] G. J. R. Cook, M. N. Maisey, and I. Fogelman, "Normal variants, artefacts and interpretative pitfalls in PET imaging with ^{18}F -fluoro-2-deoxyglucose and carbon-11 methionine," *European Journal of Nuclear Medicine*, vol. 26, no. 10, pp. 1363–1378, 1999.
- [54] M. Walberer, H. Backes, M. A. Rueger et al., "Potential of early $[(18)\text{F}]$ -2-fluoro-2-deoxy-D-glucose positron emission tomography for identifying hypoperfusion and predicting fate of tissue in a rat embolic stroke model," *Stroke*, vol. 43, no. 1, pp. 193–198, 2012.
- [55] M. Sobrado, M. Delgado, E. Fernández-Valle et al., "Longitudinal studies of ischemic penumbra by using ^{18}F -FDG PET and MRI techniques in permanent and transient focal cerebral ischemia in rats," *NeuroImage*, vol. 57, no. 1, pp. 45–54, 2011.
- [56] Y. Kuge, C. Yokota, M. Tagaya et al., "Serial changes in cerebral blood flow and flow-metabolism uncoupling in primates with acute thromboembolic stroke," *Journal of Cerebral Blood Flow and Metabolism*, vol. 21, no. 3, pp. 202–210, 2001.
- [57] Y. Kuge, Y. Hasegawa, C. Yokota et al., "Effects of single and repetitive spreading depression on cerebral blood flow and glucose metabolism in cats: a PET study," *Journal of the Neurological Sciences*, vol. 176, no. 2, pp. 114–123, 2000.
- [58] D. Fukumoto, T. Hosoya, S. Nishiyama et al., "Multiparametric assessment of acute and subacute ischemic neuronal damage:

- a small animal positron emission tomography study with rat photochemically induced thrombosis model," *Synapse*, vol. 65, no. 3, pp. 207–214, 2011.
- [59] S. Rojas, A. Martín, M. J. Arranz et al., "Imaging brain inflammation with [¹¹C]PK11195 by PET and induction of the peripheral-type benzodiazepine receptor after transient focal ischemia in rats," *Journal of Cerebral Blood Flow and Metabolism*, vol. 27, no. 12, pp. 1975–1986, 2007.
- [60] S. Nasu, T. Hata, T. Nakajima, and Y. Suzuki, "Evaluation of ¹⁸F-FDG PET in acute ischemic stroke: assessment of hyper accumulation around the lesion," *Kaku Igaku*, vol. 39, no. 2, pp. 103–110, 2002.
- [61] D. E. Kuhl, M. E. Phelps, and A. P. Kowell, "Effects of stroke on local cerebral metabolism and perfusion: mapping by emission computed tomography of ¹⁸FDG and ¹³NH₃," *Annals of Neurology*, vol. 8, no. 1, pp. 47–60, 1980.
- [62] D. Y. Ho, E. S. Mocarski, and R. M. Sapsolsky, "Altering central nervous system physiology with a defective herpes simplex virus vector expressing the glucose transporter gene," *Proceedings of the National Academy of Sciences of the United States of America*, vol. 90, no. 8, pp. 3655–3659, 1993.
- [63] M. A. Yenari, T. C. Dumas, R. M. Sapsolsky, and G. K. Steinberg, "Gene therapy for treatment of cerebral ischemia using defective herpes simplex viral vectors," *Annals of the New York Academy of Sciences*, vol. 939, pp. 340–357, 2001.
- [64] M. S. Lawrence, G. H. Sun, D. M. Kunis et al., "Overexpression of the glucose transporter gene with a herpes simplex viral vector protects striatal neurons against stroke," *Journal of Cerebral Blood Flow and Metabolism*, vol. 16, no. 2, pp. 181–185, 1996.
- [65] W. H. Lee and C. A. Bondy, "Ischemic injury induces brain glucose transporter gene expression," *Endocrinology*, vol. 133, no. 6, pp. 2540–2544, 1993.
- [66] A. L. McCall, A. M. Van Bueren, V. Nipper, M. Moholt-Siebert, H. Downes, and N. Lessov, "Forebrain ischemia increases GLUT1 protein in brain microvessels and parenchyma," *Journal of Cerebral Blood Flow and Metabolism*, vol. 16, no. 1, pp. 69–76, 1996.
- [67] S. J. Vannucci, L. B. Seaman, and R. C. Vannucci, "Effects of hypoxia-ischemia on GLUT1 and GLUT3 glucose transporters in immature rat brain," *Journal of Cerebral Blood Flow and Metabolism*, vol. 16, no. 1, pp. 77–81, 1996.
- [68] K. Li, S. J. Vannucci, F. Maher et al., "GLUT5 microglial response in adult and immature rat brain following stroke," *Society For Neuroscience Abstracts*, vol. 22, no. 1–3, p. 1423, 1996.
- [69] A. E. Greijer, P. van der Groep, D. Kemming et al., "Upregulation of gene expression by hypoxia is mediated predominantly by hypoxia-inducible factor I (HIF-I)," *Journal of Pathology*, vol. 206, no. 3, pp. 291–304, 2005.
- [70] R. Southworth, "Hexokinase-mitochondrial interaction in cardiac tissue: implications for cardiac glucose uptake, the ¹⁸FDG lumped constant and cardiac protection," *Journal of Bioenergetics and Biomembranes*, vol. 41, no. 2, pp. 187–193, 2009.
- [71] T. L. Clanton and P. F. Klawitter, "Physiological and genomic consequences of intermittent hypoxia: invited review: adaptive responses of skeletal muscle to intermittent hypoxia: the known and the unknown," *Journal of Applied Physiology*, vol. 90, no. 6, pp. 2476–2487, 2001.
- [72] G. H. Malthankar-Phatak, A. B. Patel, Y. Xia et al., "Effects of continuous hypoxia on energy metabolism in cultured cerebrocortical neurons," *Brain Research*, vol. 1229, no. 1, pp. 147–154, 2008.
- [73] R. C. Vannucci, R. M. Brucklacher, and S. J. Vannucci, "Glycolysis and perinatal hypoxic-ischemic brain damage," *Developmental Neuroscience*, vol. 27, no. 2–4, pp. 185–190, 2005.
- [74] J. R. Weinstein, I. P. Koerner, and T. Moller, "Microglia in ischemic brain injury," *Future Neurology*, vol. 5, no. 2, pp. 227–246, 2010.
- [75] K. L. Lambertsen, K. Biber, and B. Finsen, "Inflammatory cytokines in experimental and human stroke," *Journal of Cerebral Blood Flow & Metabolism*, vol. 32, no. 9, pp. 1677–1698, 2012.
- [76] S. Yamada, K. Kubota, R. Kubota, T. Ido, and N. Tamashashi, "High accumulation of fluorine-18-fluorodeoxyglucose in turpentine-induced inflammatory tissue," *Journal of Nuclear Medicine*, vol. 36, no. 7, pp. 1301–1306, 1995.
- [77] Y. Sugawara, T. D. Gutowski, S. J. Fisher, R. S. Brown, and R. L. Wahl, "Uptake of positron emission tomography tracers in experimental bacterial infections: a comparative biodistribution study of radiolabeled FDG, thymidine, L-methionine, ⁶⁷Ga-citrate, and ¹²⁵I-HSA," *European Journal of Nuclear Medicine*, vol. 26, no. 4, pp. 333–341, 1999.
- [78] A. H. Kaim, B. Weber, M. O. Kurrer, J. Gottschalk, G. K. Von Schulthess, and A. Buck, "Autoradiographic quantification of ¹⁸F-FDG uptake in experimental soft-tissue abscesses in rats," *Radiology*, vol. 223, no. 2, pp. 446–451, 2002.
- [79] K. Kubota, K. Ito, M. Morooka et al., "FDG PET for rheumatoid arthritis: basic considerations and whole-body PET/CT," *Annals of the New York Academy of Sciences*, vol. 1228, no. 1, pp. 29–38, 2011.
- [80] K. Yamashita, P. Vogel, K. Fritze, T. Back, K. A. Hossmann, and C. Wiessner, "Monitoring the temporal and spatial activation pattern of astrocytes in focal cerebral ischemia using in situ hybridization of GFAP mRNA: comparison with sgp-2 and hsp70 mRNA and the effect of glutamate receptor antagonists," *Brain Research*, vol. 735, no. 2, pp. 285–297, 1996.
- [81] T. Mabuchi, K. Kitagawa, T. Ohtsuki et al., "Contribution of microglia/macrophages to expansion of infarction and response of oligodendrocytes after focal cerebral ischemia in rats," *Stroke*, vol. 31, no. 7, pp. 1735–1743, 2000.
- [82] M. Schroeter, M. A. Dennin, M. Walberer et al., "Neuroinflammation extends brain tissue at risk to vital peri-infarct tissue: a double tracer [¹¹C]PK11195- and [¹⁸F]FDG-PET study," *Journal of Cerebral Blood Flow and Metabolism*, vol. 29, no. 6, pp. 1216–1225, 2009.
- [83] R. Chuaqui and J. Tapia, "Histologic assessment of the age of recent brain infarcts in man," *Journal of Neuropathology and Experimental Neurology*, vol. 52, no. 5, pp. 481–489, 1993.
- [84] P. J. Lindsberg, O. Carpén, A. Paetau, M. L. Karjalainen-Lindsberg, and M. Kaste, "Endothelial ICAM-1 expression associated with inflammatory cell response in human ischemic stroke," *Circulation*, vol. 94, no. 5, pp. 939–945, 1996.
- [85] C. Pozzilli, G. L. Lenzi, and C. Argentino, "Imaging of leukocytic infiltration in human cerebral infarcts," *Stroke*, vol. 16, no. 2, pp. 251–255, 1985.
- [86] S. E. Akopov, N. A. Simonian, and G. S. Grigorian, "Dynamics of polymorphonuclear leukocyte accumulation in acute cerebral infarction and their correlation with brain tissue damage," *Stroke*, vol. 27, no. 10, pp. 1739–1743, 1996.
- [87] A. Gerhard, J. Schwarz, R. Myers, R. Wise, and R. B. Banati, "Evolution of microglial activation in patients after ischemic stroke: a [¹¹C](R)-PK11195 PET study," *NeuroImage*, vol. 24, no. 2, pp. 591–595, 2005.

- [88] C. J. S. Price, D. Wang, D. K. Menon et al., "Intrinsic activated microglia map to the peri-infarct zone in the subacute phase of ischemic stroke," *Stroke*, vol. 37, no. 7, pp. 1749–1753, 2006.
- [89] P. J. Syapin and P. Skolnick, "Characterization of benzodiazepine binding sites in cultured cells of neural origin," *Journal of Neurochemistry*, vol. 32, no. 3, pp. 1047–1051, 1979.
- [90] X. Canat, P. Carayon, M. Bouaboula et al., "Distribution profile and properties of peripheral-type benzodiazepine receptors on human hemopoietic cells," *Life Sciences*, vol. 52, no. 1, pp. 107–118, 1993.
- [91] K. A. Hossmann, "Periinfarct depolarizations," *Cerebrovascular and Brain Metabolism Reviews*, vol. 8, no. 3, pp. 195–208, 1996.
- [92] M. Lauritzen, J. P. Dreier, M. Fabricius, J. A. Hartings, R. Graf, and A. J. Strong, "Clinical relevance of cortical spreading depression in neurological disorders: migraine, malignant stroke, subarachnoid and intracranial hemorrhage, and traumatic brain injury," *Journal of Cerebral Blood Flow and Metabolism*, vol. 31, no. 1, pp. 17–35, 2011.
- [93] G. G. Somjen, "Mechanisms of spreading depression and hypoxic spreading depression-like depolarization," *Physiological Reviews*, vol. 81, no. 3, pp. 1065–1096, 2001.
- [94] G. Mies, T. Iijima, and K. A. Hossmann, "Correlation between peri-infarct DC shifts and ischaemic neuronal damage in rat," *NeuroReport*, vol. 4, no. 6, pp. 709–711, 1993.
- [95] K. Ohta, R. Graf, G. Rosner, and W. D. Heiss, "Calcium ion transients in peri-infarct depolarizations may deteriorate ion homeostasis and expand infarction in focal cerebral ischemia in cats," *Stroke*, vol. 32, no. 2, pp. 535–543, 2001.
- [96] C. Dohmen, O. W. Sakowitz, M. Fabricius et al., "Spreading depolarizations occur in human ischemic stroke with high incidence," *Annals of Neurology*, vol. 63, no. 6, pp. 720–728, 2008.
- [97] M. Fabricius, S. Fuhr, R. Bhatia et al., "Cortical spreading depression and peri-infarct depolarization in acutely injured human cerebral cortex," *Brain*, vol. 129, no. 3, pp. 778–790, 2006.
- [98] H. Fujita, B. Zhang, K. Sato, J. Tanaka, and M. Sakanaka, "Expressions of neuropilin-1, neuropilin-2 and semaphorin 3A mRNA in the rat brain after middle cerebral artery occlusion," *Brain Research*, vol. 914, no. 1-2, pp. 1–14, 2001.
- [99] Y. A. Barde, "Neurotrophins: a family of proteins supporting the survival of neurons," *Progress in Clinical and Biological Research*, vol. 390, pp. 45–56, 1994.
- [100] C. Sommer, R. Kollmar, S. Schwab, M. Kiessling, and W. R. Schäbitz, "Exogenous brain-derived neurotrophic factor prevents postischemic downregulation of [³H]muscimol binding to GABA_A receptors in the cortical penumbra," *Molecular Brain Research*, vol. 111, no. 1-2, pp. 24–30, 2003.
- [101] I. Ferrer, J. Krupinski, E. Goutan, E. Martí, S. Ambrosio, and E. Arenas, "Brain-derived neurotrophic factor reduces cortical cell death by ischemia after middle cerebral artery occlusion in the rat," *Acta Neuropathologica*, vol. 101, no. 3, pp. 229–238, 2001.
- [102] M. E. Phelps, "Positron computed tomography studies of cerebral glucose metabolism in man: theory and application in nuclear medicine," *Seminars in Nuclear Medicine*, vol. 11, no. 1, pp. 32–49, 1981.
- [103] H. Nakai, Y. L. Yamamoto, M. Diksic, K. J. Worsley, and E. Takara, "Triple-tracer autoradiography demonstrates effects of hyperglycemia on cerebral blood flow, pH, and glucose utilization in cerebral ischemia of rats," *Stroke*, vol. 19, no. 6, pp. 764–772, 1988.
- [104] T. Noll, H. Mühlensiepen, R. Engels et al., "A cell-culture reactor for the on-line evaluation of radiopharmaceuticals: evaluation of the lumped constant of FDG in human glioma cells," *Journal of Nuclear Medicine*, vol. 41, no. 3, pp. 556–564, 2000.
- [105] H. Nakai, H. Matsuda, and E. Takara, "Simultaneous in vivo measurement of lumped constant and rate constants in experimental cerebral ischemia using F-18 FDG," *Stroke*, vol. 18, no. 1, pp. 158–167, 1987.
- [106] L. K. Shankar, J. M. Hoffman, S. Bacharach et al., "Consensus recommendations for the use of ¹⁸F-FDG PET as an indicator of therapeutic response in patients in National Cancer Institute Trials," *Journal of Nuclear Medicine*, vol. 47, no. 6, pp. 1059–1066, 2006.
- [107] A. Varrone, S. Asenbaum, T. Vander Borght et al., "EANM procedure guidelines for PET brain imaging using [¹⁸F]FDG, version 2," *European Journal of Nuclear Medicine and Molecular Imaging*, vol. 36, no. 12, pp. 2103–2110, 2009.
- [108] T. O. Videen, J. E. Dunford-Shore, M. N. Diringer, and W. J. Powers, "Correction for partial volume effects in regional blood flow measurements adjacent to hematomas in humans with intracerebral hemorrhage: implementation and validation," *Journal of Computer Assisted Tomography*, vol. 23, no. 2, pp. 248–256, 1999.
- [109] E. Melamed, "Reactive hyperglycaemia in patients with acute stroke," *Journal of the Neurological Sciences*, vol. 29, no. 2–4, pp. 267–275, 1976.
- [110] J. A. Thie, G. T. Smith, and K. F. Hubner, "2-deoxy-2-[F-18]fluoro-D-glucose-positron emission tomography sensitivity to serum glucose: a survey and diagnostic applications," *Molecular Imaging and Biology*, vol. 7, no. 5, pp. 361–368, 2005.
- [111] G. Florence, J. M. Guerit, and B. Gueguen, "Electroencephalography (EEG) and somatosensory evoked potentials (SEP) to prevent cerebral ischaemia in the operating room," *Neurophysiologie Clinique*, vol. 34, no. 1, pp. 17–32, 2004.
- [112] W. F. Haupt and S. Horsch, "Evoked potential monitoring in carotid surgery: a review of 994 cases," *Neurology*, vol. 42, no. 4, pp. 835–838, 1992.

Review Article

Toward the Era of a One-Stop Imaging Service Using an Angiography Suite for Neurovascular Disorders

Sheng-Che Hung,^{1,2} Chung-Jung Lin,^{1,2} Wan-Yuo Guo,^{1,2} Feng-Chi Chang,^{1,2} Chao-Bao Luo,^{1,2} Michael Mu-Huo Teng,^{1,2} and Cheng-Yen Chang^{1,2}

¹ Department of Radiology, Taipei Veterans General Hospital, 201, Section 2, Shih-Pai Road, Taipei 112, Taiwan

² National Yang-Ming University, Taipei 112, Taiwan

Correspondence should be addressed to Wan-Yuo Guo; wyluo@vghtpe.gov.tw

Received 28 January 2013; Revised 21 April 2013; Accepted 23 April 2013

Academic Editor: Fan-Lin Kong

Copyright © 2013 Sheng-Che Hung et al. This is an open access article distributed under the Creative Commons Attribution License, which permits unrestricted use, distribution, and reproduction in any medium, provided the original work is properly cited.

Transportation of patients requiring multiple diagnostic and imaging-guided therapeutic modalities is unavoidable in current radiological practice. This clinical scenario causes time delays and increased risk in the management of stroke and other neurovascular emergencies. Since the emergence of flat-detector technology in imaging practice in recent decades, studies have proven that flat-detector X-ray angiography in conjunction with contrast medium injection and specialized reconstruction algorithms can provide not only high-quality and high-resolution CT-like images but also functional information. This improvement in imaging technology allows quantitative assessment of intracranial hemodynamics and, subsequently in the same imaging session, provides treatment guidance for patients with neurovascular disorders by using only a flat-detector angiographic suite—a so-called one-stop quantitative imaging service (OSIS). In this paper, we review the recent developments in the field of flat-detector imaging and share our experience of applying this technology in neurovascular disorders such as acute ischemic stroke, cerebral aneurysm, and stenoocclusive carotid diseases.

1. An Actual Clinical Scenario of Stroke Management

A 67-year-old man presented at the hospital emergency unit with symptoms of acute right hemiplegia of less than 6 hours' duration. After a rapid assessment, the patient was taken to the computed tomography (CT) room, where noncontrast CT scan excluded intracranial hemorrhage. Immediate CT angiography depicted an occlusion at the proximal portion of the left middle cerebral artery, and a subsequent perfusion study identified a large penumbra, which manifested as prolonged time to peak (TTP) and preserved cerebral blood flow (CBF).

Because of the proximal cerebral artery occlusion and the risk of cell death in a large area of brain parenchyma, the patient was sent to the angiographic suite for revascularization with intra-arterial approach. After an interventional procedure lasting more than an hour, the occluded left middle

cerebral artery was opened by mechanical thrombectomy and a few smaller occluded branches were left untreated. The patient was then sent back to the stroke intensive care unit. He was followed up on the next day by CT angiography and perfusion imaging using multidetector CT (MDCT). The studies showed normal hemodynamic parameters in most of the penumbra and no hemorrhage in the brain parenchyma. He was discharged a few days later under a favorable clinical status with only minor neurological deficits.

2. Introduction

Recently, angiographic suites equipped with flat detectors have become a standard imaging practice. Flat-detector imaging is also known as flat-detector computed tomography (FDCT) or angiographic CT. Remarkable advances in imaging technology over the recent years have resulted in

notable improvement of imaging acquisition and postprocessing techniques in FDCT. In addition to digital subtraction angiography (DSA), which is obtained by subtraction of images before from after contrast medium injection and removing superimposed bone and soft tissue densities [1], FDCT can provide CT-like brain parenchyma images (DynaCT) and three-dimensional morphological and hemodynamic datasets of vasculatures, by combining one or more C-arm rotations. Consequently, a one-stop peritherapeutic imaging service has become feasible.

In this paper, we review the recent progress of FDCT technology in angiographic suite and share our clinical experience in coupling these imaging techniques with the clinical workflow of neurovascular disorders.

3. Technical Principles of Flat-Detector CT

A state-of-the-art flat panel detector consisted of two independent layers. The first is a fluorescence scintillator screen of cesium iodide, which absorbs and converts the X-rays into light photons, and the second is a layer of photodiodes, made up of hydrogenated amorphous silicon to convert light photons into a digital signal [2, 3]. The original development of flat-panel detectors was aimed at improving standard radiography by providing a higher dynamic range and a fast and repeated direct digital readout. With the improvement of three-dimensional reconstruction techniques [4–7] and reduction of artifacts, the concept of applying flat detectors for X-ray computed tomography had been investigated for several years. The FDCT can be installed in a gantry similar to that of a conventional MDCT [8], or on a C-arm system. The C-arm based system is named because of its configuration and used primarily for fluoroscopic imaging during surgical and angiographic procedures. It can be immobile, mounted on the floor or ceiling of the angiographic room, or mobile that can operate in any medical scenario, for example, operation theater or intensive care unit. In this paper, the term FDCT refers to an angiographic suite equipped with a C-arm system and a flat detector. The system can generate CT images by a series of projection data over an angular range of 180 degrees plus fan angle. If equipped with a large size detector to cover a wide field of view, for example, 40 by 40 cm², the FDCT can obtain a large scanning volume in a single rotation. Thus, the term of cone beam FDCT is interchangeably used in the literature [9].

The earlier works of C-arm CT where originally performed by using an conventional image intensifier system in 1990s [10–12]. However, because of inherent limitations, namely, low dynamic range, image distortion, and low-contrast detectability, the application was limited to 3D rotational angiography that allowed visualizing high-contrast vessels typically by employing intra-arterial contrast medium injections [12, 13]. Compared with image intensifiers, flat detectors offer superior image quality, including improved detective quantum efficiency (DQE), modulation transfer function (MTF), dynamic range, and dose efficiency [14]. Furthermore, a C-arm system equipped with flat detectors

is capable of providing projection radiography, fluoroscopy, DSA, and CT-like images in one imaging suite. Thus, the C-arm FDCT gains wide popularity in current imaging practice because of the versatile applications in the angiographic suite [15, 16].

4. Angiographic Suite Equipped with FDCT

An angiographic suite equipped with FDCT enables early recognition of intracranial complications during endovascular therapeutic procedures, such as coiling an intracranial aneurysm, stenting a stenotic artery, or other interventional procedures [17, 18]. With its high spatial imaging resolution and capacity for correcting metallic artifacts, DynaCT can detect most brain parenchymal hemorrhages in emergency situations [18, 19]. The combination of DSA with DynaCT has proven superior to two-dimensional or even three-dimensional DSA alone for the management of neuroendovascular complications [20].

In conjunction with intra-arterial or intravenous contrast medium injection, FDCT angiography provides images with higher spatial resolution than MDCT angiography does. Moreover, FDCT is able to directly demonstrate the relationship between endovascular devices or vascular malformations and the surrounding parenchymal structures for guiding a treatment or planning a therapeutic strategy. The direct demonstration has not been possible since the invention of conventional DSA early in the last century [21, 22].

5. Functional Imaging

For functional analysis of hemodynamics, the contrast medium injection protocol and imaging reconstruction algorithm of FDCT are modified and optimized. By subtracting a mask rotation run from a contrast medium-filled rotation run, in which contrast medium in tissues reaches a static state after bolus contrast medium injection, FDCT enables measurement of parenchymal cerebral blood volume (FDCT-PBV) [23, 24]. In a preliminary study by Struffert et al., the CBV values obtained with FDCT-PBV were strongly correlated to those obtained with MDCT. The mean difference of CBV values between FDCT and MDCT was small (0.04 ± 0.55 mL/100 mL) [25]. On-site CBV measurement enables peritherapeutic monitoring of hemodynamics and allows a timely management when endovascular treatments are encountered.

Advancements in protocols of contrast medium injection, imaging acquisition, rotational speed, and reconstruction algorithms have improved remarkably the temporal resolution of C-arm FDCT for hemodynamic measurement. A recent study by Ganguly et al. demonstrated the feasibility of measuring CBF, CBV, and mean transit time (MTT) directly with C-arm FDCT. The hemodynamic maps generated from C-arm FDCT correlated well with CT perfusion maps from MDCT [26].

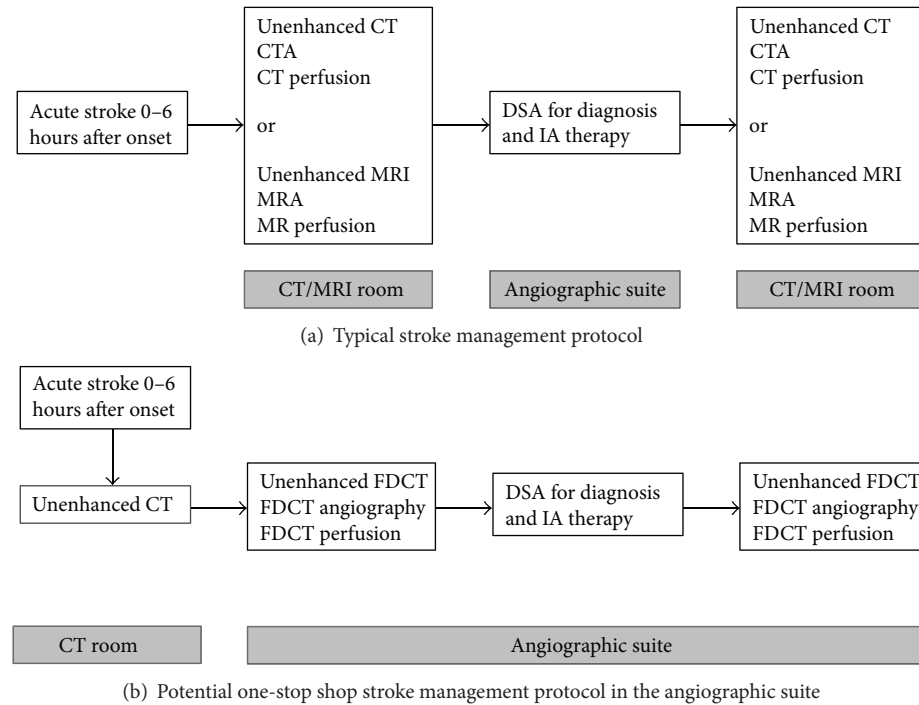


FIGURE 1: Shift of clinical paradigm in stroke management by employing flat-detector angiographic suite.

6. Clinical Experience

6.1. Acute Ischemic Stroke. According to the World Health Organization (WHO), stroke is the second leading cause of death worldwide (10.8%). Furthermore, human neural tissues are rapidly and irreversibly lost at an estimated rate of 1.9 million neurons each minute as stroke progresses [27]. These facts emphasize the importance of emergent management of stroke both from medical and public health aspects although patient's clinical status at presentation and appropriate treatments being given (medical, endovascular, and surgical approaches) determine the final clinical outcome.

Clinically, the time interval between ictus and hospital arrival determines the treatment option in stroke management. Advancements in imaging technology and imaging expertise, however, play a role in modifying the treatment paradigm. Magnetic resonance imaging and CT provide morphological and functional data regarding brain tissues that correlate well with stroke in the temporal and spatial domains. This information forms the foundation for treatment options. The evolving clinical scenario toward earlier diagnosis, prompter revascularization of occluded vessels, more timely tissue salvage, and better neurological function preservation becomes clinically appealing. Consequently, FDCT, as a one-stop imaging technique, provides pretherapeutic anatomic and physiological information for diagnosis and minimizes the time interval between diagnosis and revascularization procedure when a subsequent interventional neurovascular procedure is dynamically needed.

By combining C-arm rotational acquisition with intra-arterial contrast medium injection from the aortic arch, we can obtain (1) noncontrast DynaCT, (2) a three-dimensional volume of intracranial vasculature, and (3) an FDCT-PBV map. Noncontrast DynaCT helps detect intracranial hemorrhage at any peritherapeutic time point. DynaCT reliably detected intracerebral hematomas with an overall sensitivity up to 93.3% in a study of 44 patients [19], but lower when hematomas were small, located in the posterior fossa or adjacent to the skull base. DynaCT is also less sensitive to detect perimesencephalic subarachnoid hemorrhages (SAH) or minimal intraventricular hemorrhage. Peritherapeutic FDCT-PBV maps help identify the infarct core immediately before mechanical thrombectomy, guide the treatment decision, and predict final infarct size immediately following revascularization [28, 29] (Figure 1).

A partly hypothetical clinical scenario of stroke management of the same patient as reported in the first paragraph is as follows.

A 67-year-old man arrives at the hospital emergency unit with symptoms of acute right hemiplegia of less than 6 hours' duration. After clinical evaluation and exclusion of intracranial hemorrhage by initial noncontrast MDCT, the patient is directly transferred to an FDCT angiographic suite for vascular and perfusion imaging, where preparation for the revascularization procedure starts simultaneously. FDCT angiography shows total occlusion of the left middle cerebral artery and FDCT-PBV demonstrates an area of hypoperfusion in the left frontoparietal lobes. An intra-arterial revascularization procedure by mechanical thrombectomy

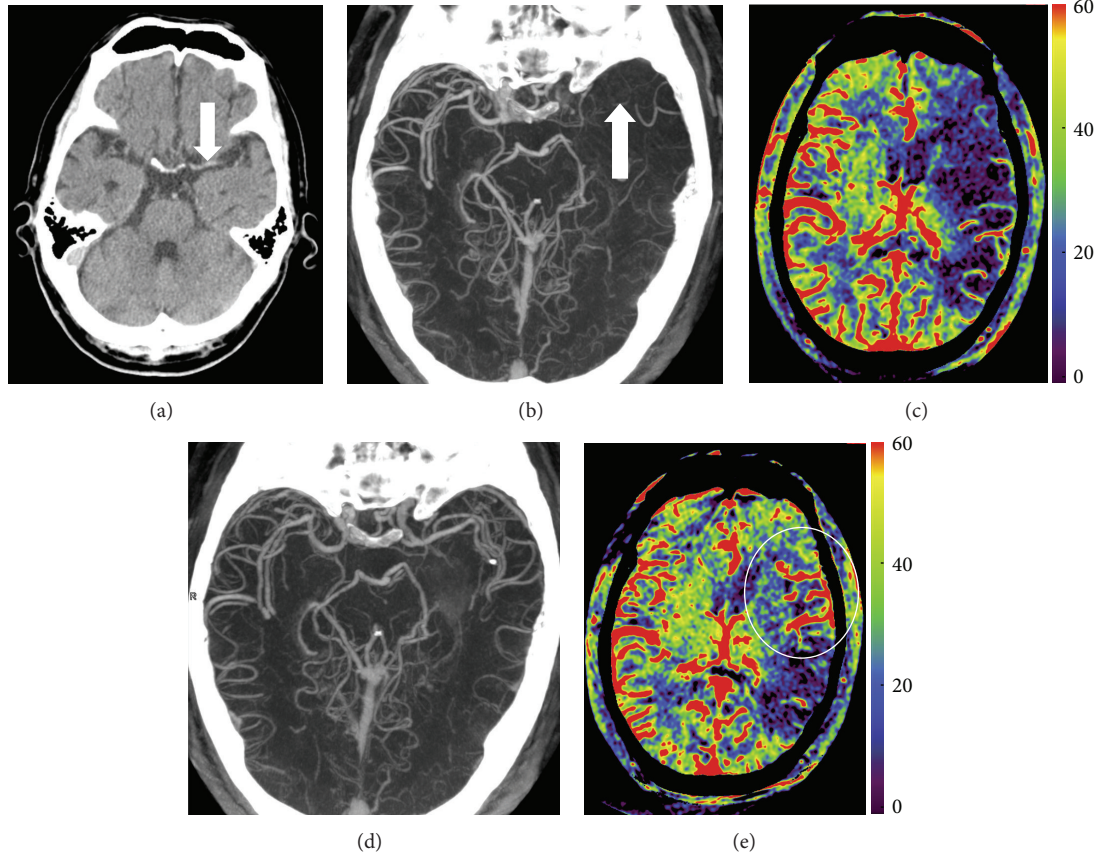


FIGURE 2: A 67-year-old man with left middle cerebral artery (MCA) occlusion. (a) Noncontrast computed tomography (CT) demonstrated a hyperdense MCA sign (arrow) and excluded intracranial hemorrhage. (b) Flat-detector CT (FDCT) angiography demonstrated the total occlusion of left MCA (arrow). (c) A parenchymal cerebral blood volume (FDCT-PBV) map depicted a large area of hypoperfusion in the corresponding left MCA territory, which was similar to the results of multidetector CT perfusion imaging (not shown). (d) After intra-arterial mechanical thrombectomy, recanalization of the left MCA was demonstrated by FDCT angiography. (e) An FDCT-PBV map depicted the recovery of CBV values (circle) in part of the hypoperfused parenchyma after revascularization.

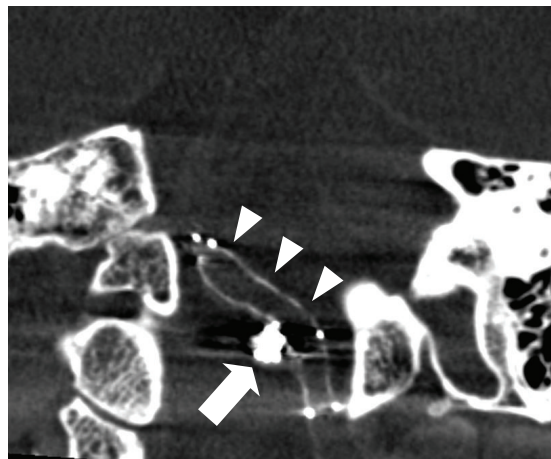


FIGURE 3: Intraprocedural DynaCT showed the relationship between stent struts (arrowheads) and coil mass (arrow) of a 50-year-old woman who received stent-assisted embolization for a left posterior inferior cerebellar artery aneurysm.

starts immediately. The occluded middle cerebral artery is opened in less than an hour. A few smaller occluded branches are left untreated. Immediately after revascularization, noncontrast DynaCT excludes intracranial hemorrhage. After the endovascular treatment, the patient is sent back to the stroke intensive care unit. Clinically, the posttherapeutic course is smooth. No imaging followup is requested. The patient is discharged a few days later with only minor neurological deficits and favorable clinical status (Figure 2).

6.2. Cerebral Aneurysm. Since the International Subarachnoid Aneurysm Trial (ISAT) and the Analysis of Treatment by Endovascular Approach of Nonruptured Aneurysms (ATENA), endovascular treatment has been established as a first-line treatment in the management of ruptured and nonruptured aneurysms [30, 31].

In our practice, DynaCT can be used to evaluate the degree of hydrocephalus and visualize the position of a shunt [32], monitor the extent of SAH immediately before and after

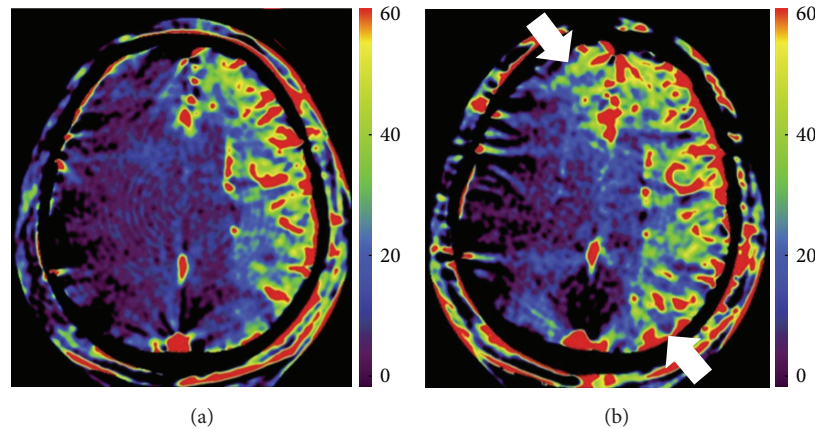


FIGURE 4: A 77-year-old man who underwent carotid artery stenting for left internal carotid artery high-grade stenosis. Prestenting (a) and poststenting (b) parenchymal cerebral blood volume (FDCT-PBV) maps in conjunction with selective intra-arterial contrast medium injection demonstrated increased CBV values and arterial territorial shifting (arrows).

endovascular procedures, and exclude intracranial complications before transferring the patient back to the ward from an angiographic suite [33]. For patients with broad-based cerebral aneurysms requiring stent-assisted coil embolization or flow diverter stents, precise confirmation of their positioning and relationship is important for endovascular treatment. However, stent struts are not radiopaque, and only the proximal and distal radiopaque stent markers are visible in fluoroscopy. Fluoroscopic localization and detection of stent morphology are difficult after deployment. Intraprocedural DynaCT enhances visualization of stent positioning with high spatial and contrast resolution and clearly illustrates the relationship between stent struts and coil mass (Figure 3). In a cohort study of eleven patients undergoing stent-assisted aneurysm embolization, the stent visibility was excellent in small aneurysms. However, the visibility was deteriorated in aneurysms larger than 10 mm in diameter due to beam hardening artifacts [34]. Besides, DynaCT enables early recognition of procedure-related complications, such as incomplete stent deployment, stent migration, stent fracture, and coil dislocation [35–37].

One of the future applications of the one-stop angiographic suite is management of cerebral vasospasm. Cerebral vasospasm with delayed cerebral ischemia is the leading cause of morbidity and mortality in patients with aneurysmal SAH and survived from the initial hemorrhage. DSA is used as the reference standard, but not all angiographic vasospasms are clinically symptomatic. A combination of CT angiography and CT perfusion is reported to yield high diagnostic accuracy and can potentially improve the diagnosis of cerebral vasospasm after SAH [38]. Our preliminary experience shows that FDCT-PBV maps may help to identify severely ischemic brain parenchyma. By reformatting the source images of FDCT-PBV, we can detect mild or moderate stenosis in proximal cerebral arteries with sensitivities of 84.7% and 90% by two independent raters, respectively, in a series of consecutive ten exams. This may optimize the treatment protocol of chemical angioplasty, which involves intra-arterial infusion of nimodipine, a dihydropyridine calcium channel blocker.

6.3. Stenoocclusive Carotid Disease. In symptomatic intracranial atherosclerotic disease, intracranial angioplasty and stenting are increasingly used as a therapeutic option [39–42]. Similar to the situation in stent-assisted coil embolization of intracranial aneurysms, DynaCT and FDCT angiography are capable of visualizing the strut of a stent *per se* and the surroundings during the procedure [37, 43]. Moreover, the peritherapeutic FDCT-PBV maps demonstrate hemodynamic improvements in CBV values and arterial territory shifting (Figure 4). We found that peritherapeutic CBV changes were inconsistent and variable, which concurred with previous studies [44, 45].

With the high incidence of in-stent restenosis (8%–30%) [46–48], regular imaging followup is mandatory for patients who have undergone intracranial stenting for their stenoocclusive arteries. DSA, although invasive, is the standard follow-up imaging. FDCT angiography with intravenous contrast medium injection is less invasive than transarterial DSA and provides superior spatial resolution compared with MDCT angiography in both parenchymal and vascular imaging [49].

7. Conclusion

In conclusion, FDCT angiographic suite provides one-stop imaging for neurovascular disorders with the following advantages.

7.1. On-Site Assessment of Peritherapeutic Intracranial Conditions. Intracranial conditions, for example, ventricular size and hemorrhage, may occur or change after emergent treatments or deteriorate between/during the procedures of endovascular treatment. Moreover, the hemodynamic status and infarct core may dynamically evolve along the time course of stroke. The freedom of reassessing brain morphology and hemodynamics at any time during the endovascular procedure of stroke treatment provides a precise and updated intracranial roadmap for timely tailoring of treatment plan.

7.2. Prompt Initiation of Intra-Arterial Revascularization Treatment. Selected patients, for example, those with suspected acute ischemic stroke (<6 hours) or suspected post-SAH vasospasm, could be brought directly to an FDCT angiographic suite where DynaCT, FDCT angiography, and FDCT-PBV could be obtained with one stop. The imaging service algorithm could optimize the overall workflow of stroke management by avoiding patient relocation among imaging scanners and data transferal. The new paradigm might minimize the risk and time delay of interventional procedures.

Acknowledgments

This research is cosponsored by Taipei Veterans General Hospital and Siemens Healthcare (Grant no. T1100200) and in part supported by NSC Grant 101-2314-B-075-047-MY2 and Taipei Veterans General Hospital Grant V102C-115.

References

- [1] D. P. Harrington, L. M. Boxt, and P. D. Murray, "Digital subtraction angiography: overview of technical principles," *American Journal of Roentgenology*, vol. 139, no. 4, pp. 781–786, 1982.
- [2] M. Kamran, S. Nagaraja, and J. V. Byrne, "C-arm flat detector computed tomography: the technique and its applications in interventional neuro-radiology," *Neuroradiology*, vol. 52, no. 4, pp. 319–327, 2010.
- [3] U. Neitzel, "Status and prospects of digital detector technology for CR and DR," *Radiation Protection Dosimetry*, vol. 114, no. 1–3, pp. 32–38, 2005.
- [4] R. Fahrig and D. W. Holdsworth, "Three-dimensional computed tomographic reconstruction using a C-arm mounted XRII: image-based correction of gantry motion nonidealities," *Medical Physics*, vol. 27, no. 1, pp. 30–38, 2000.
- [5] M. J. Daly, J. H. Siewerdsen, Y. B. Cho, D. A. Jaffray, and J. C. Irish, "Geometric calibration of a mobile C-arm for intraoperative cone-beam CT," *Medical Physics*, vol. 35, no. 5, pp. 2124–2136, 2008.
- [6] Y. Cho, D. J. Moseley, J. H. Siewerdsen, and D. A. Jaffray, "Accurate technique for complete geometric calibration of cone-beam computed tomography systems," *Medical Physics*, vol. 32, no. 4, pp. 968–983, 2005.
- [7] F. Noo, R. Clackdoyle, C. Mennessier, T. A. White, and T. J. Roney, "Analytic method based on identification of ellipse parameters for scanner calibration in cone-beam tomography," *Physics in Medicine and Biology*, vol. 45, no. 11, pp. 3489–3508, 2000.
- [8] R. Gupta, A. C. Cheung, S. H. Bartling et al., "Flat-panel volume CT: fundamental principles, technology, and applications," *Radiographics*, vol. 28, no. 7, pp. 2009–2022, 2008.
- [9] J. H. Siewerdsen, "Cone-beam CT with a flat-panel detector: from image science to image-guided surgery," *Nuclear Instruments and Methods in Physics Research A*, vol. 648, no. 1, pp. S241–S250, 2011.
- [10] R. Fahrig, A. J. Fox, S. Lownie, and D. W. Holdsworth, "Use of a C-arm system to generate true three-dimensional computed rotational angiograms: preliminary in vitro and in vivo results," *American Journal of Neuroradiology*, vol. 18, no. 8, pp. 1507–1514, 1997.
- [11] U. Linsenmaier, C. Rock, E. Euler et al., "Three-dimensional CT with a modified C-arm image intensifier: feasibility," *Radiology*, vol. 224, no. 1, pp. 286–292, 2002.
- [12] M. Grass, R. Koppe, E. Klotz et al., "Three-dimensional reconstruction of high contrast objects using C-arm image intensifier projection data," *Computerized Medical Imaging and Graphics*, vol. 23, no. 6, pp. 311–321, 1999.
- [13] W. A. Kalender and Y. Kyriakou, "Flat-detector computed tomography (FD-CT)," *European Radiology*, vol. 17, no. 11, pp. 2767–2779, 2007.
- [14] A. R. Cowen, A. G. Davies, and M. U. Sivananthan, "The design and imaging characteristics of dynamic, solid-state, flat-panel x-ray image detectors for digital fluoroscopy and fluorography," *Clinical Radiology*, vol. 63, no. 10, pp. 1073–1085, 2008.
- [15] D. A. Jaffray and J. H. Siewerdsen, "Cone-beam computed tomography with a flat-panel imager: initial performance characterization," *Medical Physics*, vol. 27, no. 6, pp. 1311–1323, 2000.
- [16] Y. Kyriakou, T. Struffert, A. Dörfler, and W. A. Kalender, "Basics principles of flat detector computed tomography (FD-CT)," *Radiologe*, vol. 49, no. 9, pp. 811–819, 2009.
- [17] H. J. Cloft and D. F. Kallmes, "Cerebral aneurysm perforations complicating therapy with Guglielmi detachable coils: a meta-analysis," *American Journal of Neuroradiology*, vol. 23, no. 10, pp. 1706–1709, 2002.
- [18] A. Dörfler, T. Struffert, T. Engelhorn, and C. Richter, "Rotational flat-panel computed tomography in diagnostic and interventional neuroradiology," *RoFo*, vol. 180, no. 10, pp. 891–898, 2008.
- [19] T. Struffert, G. Richter, T. Engelhorn et al., "Visualisation of intracerebral haemorrhage with flat-detector CT compared to multislice CT: results in 44 cases," *European Radiology*, vol. 19, no. 3, pp. 619–625, 2009.
- [20] N. S. Heran, J. K. Song, K. Namba, W. Smith, Y. Niimi, and A. Berenstein, "The utility of DynaCT in neuroendovascular procedures," *American Journal of Neuroradiology*, vol. 27, no. 2, pp. 330–332, 2006.
- [21] T. Struffert, S. Kloska, T. Engelhorn et al., "Optimized intravenous Flat Detector CT for non-invasive visualization of intracranial stents: first results," *European Radiology*, vol. 21, no. 2, pp. 411–418, 2011.
- [22] M. R. Levitt, D. L. Cooke, B. V. Ghodke, L. J. Kim, D. K. Hallam, and L. N. Sekhar, "'Stent view' flat-detector CT and stent-assisted treatment strategies for complex intracranial aneurysms," *World Neurosurgery*, vol. 75, no. 2, pp. 275–278, 2011.
- [23] M. Zellerhoff, Y. Deuerling-Zheng, C. M. Strother et al., "Measurement of cerebral blood volume using angiographic C-arm systems," in *Medical Imaging 2009: Biomedical Applications in Molecular, Structural, and Functional Imaging*, vol. 7262 of *Proceedings of SPIE*, pp. 72620H-1–72620H-8, 2009.
- [24] T. Struffert, Y. Deuerling-Zheng, S. Kloska et al., "Cerebral blood volume imaging by flat detector computed tomography in comparison to conventional multislice perfusion CT," *European Radiology*, vol. 21, no. 4, pp. 882–889, 2011.
- [25] T. Struffert, Y. Deuerling-Zheng, S. Kloska et al., "Flat detector CT in the evaluation of brain parenchyma, intracranial vasculature, and cerebral blood volume: a pilot study in patients with acute symptoms of cerebral ischemia," *American Journal of Neuroradiology*, vol. 31, no. 8, pp. 1462–1469, 2010.
- [26] A. Ganguly, A. Fieselmann, M. Marks et al., "Cerebral CT perfusion using an interventional C-arm imaging system: cerebral blood flow measurements," *American Journal of Neuroradiology*, vol. 32, no. 8, pp. 1525–1531, 2011.

- [27] J. L. Saver, "Time is brain—quantified," *Stroke*, vol. 37, no. 1, pp. 263–266, 2006.
- [28] P. Mordasini, M. El-Koussy, C. Brekenfeld et al., "Applicability of tableside flat panel detector CT parenchymal cerebral blood volume measurement in neurovascular interventions: preliminary clinical experience," *American Journal of Neuroradiology*, vol. 33, no. 1, pp. 154–158, 2012.
- [29] C. J. Lin, M. Yu, S. C. Hung et al., "In-room assessment of cerebral blood volume for guidance during intra-arterial thrombolytic therapy," *Interventional Neuroradiology*, vol. 18, no. 4, pp. 463–468, 2012.
- [30] A. Molyneux, R. Kerr, I. Stratton et al., "International Subarachnoid Aneurysm Trial (ISAT) of neurosurgical clipping versus endovascular coiling in 2143 patients with ruptured intracranial aneurysms: a randomized trial," *Journal of Stroke and Cerebrovascular Diseases*, vol. 11, no. 6, pp. 304–314, 2002.
- [31] L. Pierot, L. Spelle, and F. Vitry, "ATENA: the first prospective, multicentric evaluation of the endovascular treatment of unruptured intracranial aneurysms," *Journal of Neuroradiology*, vol. 35, no. 2, pp. 67–70, 2008.
- [32] P. von Gottberg, M. Psychogios, G. Schuetze et al., "Feasibility of flat panel detector computed tomography for position assessment of external ventricular drainage," *Neurologia i Neurochirurgia Polska*, vol. 47, no. 1, pp. 32–42, 2013.
- [33] M. Doelken, T. Struffert, G. Richter et al., "Flat-panel detector volumetric CT for visualization of subarachnoid hemorrhage and ventricles: preliminary results compared to conventional CT," *Neuroradiology*, vol. 50, no. 6, pp. 517–523, 2008.
- [34] G. Richter, T. Engelhorn, T. Struffert et al., "Flat panel detector angiographic CT for stent-assisted coil embolization of broad-based cerebral aneurysms," *American Journal of Neuroradiology*, vol. 28, no. 10, pp. 1902–1908, 2007.
- [35] J. H. Buhk, K. Kallenberg, A. Mohr, P. Dechent, and M. Knauth, "Evaluation of angiographic computed tomography in the follow-up after endovascular treatment of cerebral aneurysms—a comparative study with DSA and TOF-MRA," *European Radiology*, vol. 19, no. 2, pp. 430–436, 2009.
- [36] F. Clarencon, M. Piotin, S. Pistocchi, D. Babic, and R. Blanc, "Evaluation of stent visibility by flat panel detector CT in patients treated for intracranial aneurysms," *Neuroradiology*, vol. 54, no. 10, pp. 1121–1125, 2012.
- [37] P. Mordasini, F. Al-Senani, J. Gralla, D. D. Do, C. Brekenfeld, and G. Schroth, "The use of flat panel angioCT (DynaCT) for navigation through a deformed and fractured carotid stent," *Neuroradiology*, vol. 52, no. 7, pp. 629–632, 2010.
- [38] E. D. Greenberg, R. Gold, M. Reichman et al., "Diagnostic accuracy of CT angiography and CT perfusion for cerebral vasospasm: a meta-analysis," *American Journal of Neuroradiology*, vol. 31, no. 10, pp. 1853–1860, 2010.
- [39] L. Zhang, Q. Huang, Y. Zhang et al., "A single-center study of Wingspan stents for symptomatic atherosclerotic stenosis of the middle cerebral artery," *Journal of Clinical Neuroscience*, vol. 20, no. 3, pp. 362–366, 2013.
- [40] Y. S. Shin, B. M. Kim, S. H. Suh et al., "Wingspan stenting for intracranial atherosclerotic stenosis: clinical outcomes and risk factors for in-stent restenosis," *Neurosurgery*, vol. 72, no. 4, pp. 596–604, 2013.
- [41] Y. Zhou, Q. W. Yang, and H. Y. Xiong, "Angioplasty with stenting for intracranial atherosclerosis: a systematic review," *Journal of International Medical Research*, vol. 40, no. 1, pp. 18–27, 2012.
- [42] D. J. Fiorella, A. S. Turk, E. I. Levy et al., "US wingspan registry: 12-month follow-up results," *Stroke*, vol. 42, no. 7, pp. 1976–1981, 2011.
- [43] M. N. Psychogios, P. Schramm, J. H. Buhk et al., "Angiographic CT after intravenous contrast agent application: a noninvasive follow-up tool after intracranial angioplasty and stenting," *American Journal of Neuroradiology*, vol. 31, no. 10, pp. 1886–1891, 2010.
- [44] A. Waaijer, M. S. Van Leeuwen, M. J. P. Van Osch et al., "Changes in cerebral perfusion after revascularization of symptomatic carotid artery stenosis: CT measurement," *Radiology*, vol. 245, no. 2, pp. 541–548, 2007.
- [45] Y. Duan, G. Li, Y. Yang et al., "Changes in cerebral hemodynamics after carotid stenting of symptomatic carotid artery," *European Journal of Radiology*, vol. 81, no. 4, pp. 744–748, 2012.
- [46] H. L. Lutsep, "Stenting of Symptomatic Atherosclerotic Lesions in the Vertebral or Intracranial Arteries (SSYLVIA): study results," *Stroke*, vol. 35, no. 6, pp. 1388–1392, 2004.
- [47] J. C. Wojak, D. C. Dunlap, K. R. Hargrave, L. A. DeAlvare, H. S. Culbertson, and J. J. Connors, "Intracranial angioplasty and stenting: long-term results from a single center," *American Journal of Neuroradiology*, vol. 27, no. 9, pp. 1882–1892, 2006.
- [48] A. Bose, M. Hartmann, H. Henkes et al., "A novel, self-expanding, nitinol stent in medically refractory intracranial atherosclerotic stenoses: the Wingspan study," *Stroke*, vol. 38, no. 5, pp. 1531–1537, 2007.
- [49] J. H. Buhk, P. Lingor, and M. Knauth, "Angiographic CT with intravenous administration of contrast medium is a noninvasive option for follow-up after intracranial stenting," *Neuroradiology*, vol. 50, no. 4, pp. 349–354, 2008.

Research Article

Pharmacodynamic Analysis of Magnetic Resonance Imaging-Monitored Focused Ultrasound-Induced Blood-Brain Barrier Opening for Drug Delivery to Brain Tumors

Po-Chun Chu,¹ Wen-Yen Chai,^{1,2} Han-Yi Hsieh,¹ Jiun-Jie Wang,³ Shiaw-Pyng Wey,³ Chiung-Yin Huang,⁴ Kuo-Chen Wei,⁴ and Hao-Li Liu¹

¹ Department of Electrical Engineering, Chang-Gung University, 259 Wen-Hwa 1st Road, Kwei-Shan, Tao-Yuan 333, Taiwan

² Department of Diagnostic Radiology, Chang-Gung University and Memorial Hospital, 5 Fu-shin Street, Kwei-Shan, Tao-Yuan 333, Taiwan

³ Department of Medical Imaging and Radiological Sciences, Chang-Gung University, 259 Wen-Hwa 1st Road, Kwei-Shan, Tao-Yuan 333, Taiwan

⁴ Department of Neurosurgery, Chang-Gung Memorial Hospital, 5 Fu-shin Street, Kwei-Shan, Tao-Yuan 333, Taiwan

Correspondence should be addressed to Hao-Li Liu; haoliliu@mail.cgu.edu.tw

Received 21 January 2013; Accepted 25 February 2013

Academic Editor: Fan-Lin Kong

Copyright © 2013 Po-Chun Chu et al. This is an open access article distributed under the Creative Commons Attribution License, which permits unrestricted use, distribution, and reproduction in any medium, provided the original work is properly cited.

Microbubble-enhanced focused ultrasound (FUS) can enhance the delivery of therapeutic agents into the brain for brain tumor treatment. The purpose of this study was to investigate the influence of brain tumor conditions on the distribution and dynamics of small molecule leakage into targeted regions of the brain after FUS-BBB opening. A total of 34 animals were used, and the process was monitored by 7T-MRI. Evans blue (EB) dye as well as Gd-DTPA served as small molecule substitutes for evaluation of drug behavior. EB was quantified spectrophotometrically. Spin-spin (R_1) relaxometry and area under curve (AUC) were measured by MRI to quantify Gd-DTPA. We found that FUS-BBB opening provided a more significant increase in permeability with small tumors. In contrast, accumulation was much higher in large tumors, independent of FUS. The AUC values of Gd-DTPA were well correlated with EB delivery, suggesting that Gd-DTPA was a good indicator of total small-molecule accumulation in the target region. The peripheral regions of large tumors exhibited similar dynamics of small-molecule leakage after FUS-BBB opening as small tumors, suggesting that FUS-BBB opening may have the most significant permeability-enhancing effect on tumor peripheral. This study provides useful information toward designing an optimized FUS-BBB opening strategy to deliver small-molecule therapeutic agents into brain tumors.

1. Introduction

Focused ultrasound beams (FUS) in the presence of circulating microbubbles can temporarily open the blood-brain barrier (BBB opening) of capillaries in the central nervous system (CNS) parenchyma [1–3]. Bursts of acoustic ultrasound induce microbubble cavitation in the vasculature, and the resultant shear stress temporarily disrupts tight junctions to enhance blood-brain permeability. This BBB-opening process can be carried out at moderate acoustic pressures to minimize adverse effects on vasculature and prevent damage to neurons [3–7], while facilitating localized

delivery of chemotherapeutic agents from the vasculature to the pathological brain parenchyma and CNS [8–11]. Since more than 95% of the therapeutic agent normally cannot penetrate CNS tight junctions [12], this novel approach provides a unique opportunity for local delivery of therapeutic agents across the BBB and into the targeted site, thus opening a new frontier of CNS drug delivery.

Brain tumors could potentially be treated by FUS-BBB opening to enhance chemotherapeutic agent delivery. In the United States, at least 18,000 patients are diagnosed with glioblastoma multiforme (GBM) each year, comprising more than half of the malignant primary brain tumors [13],

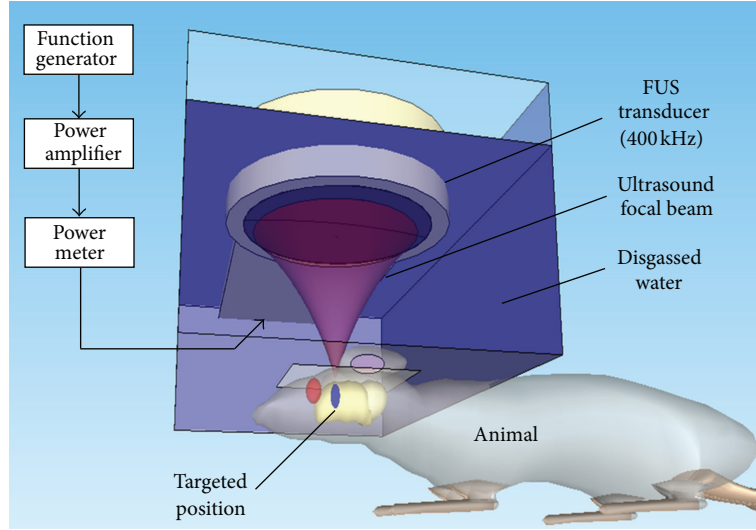


FIGURE 1: Schematic showing the experimental setup of the focused ultrasound exposure system.

and chemotherapy is an important treatment modality [14]. Recent preclinical studies showed that FUS-BBB opening can effectively enhance local deposition and concentration of chemotherapeutics including BCNU [11], liposomal doxorubicin [9, 15], and chemodrugs carried by novel nanocarriers [16].

Currently, FUS-mediated CNS drug delivery is monitored by magnetic resonance imaging (MRI) by intravenous (IV) injection of gadolinium diethylenetriamine penta-acetic acid (Gd-DTPA) contrast agent together with chemotherapeutic drug. The MRI signal intensity increase caused by the leakage of Gd-DTPA thus serves as an indicator to estimate drug concentration [4, 8, 9, 17]. Most studies have focused on analyzing the effects of FUS exposure parameters such as acoustic pressure amplitude, ultrasound frequency, pulse length, pulse repetition frequency, exposure duration, and microbubble dose on BBB opening [5, 18–23]. However, pharmacodynamic analysis including the dynamics and distribution of the specific molecular agent in the brain is critical for evaluating specific drug delivery. MRI could also be used for pharmacological endpoint evaluation using concurrently administered MR contrast agents as surrogate indicators of therapeutic drug concentrations. Although the kinetics of contrast agent permeability of a defective blood-brain barrier have been measured using MR compartment modeling [24–26], these studies were performed in normal animal brains, and so far the detailed pharmacodynamic behavior of contrast agents after FUS-BBB opening remains uncertain in brain tumors.

The purpose of this study was to conduct an MRI pharmacodynamic analysis of FUS-BBB opening in brain tumors in an animal model. Injected Gd-DTPA contrast agent was used to characterize pharmacodynamic changes as a function of time after BBB opening, in both normal and brain-glioma animals. We also attempted to establish the correlation between deposition of Gd-DTPA by *in vivo* semiquantification and the quantitation of another surrogate,

Evans blue dye, by spectrophotometry after sacrifice. Finally, we evaluated the pharmacodynamic changes affected by FUS-BBB opening in various grades of gliomas.

2. Methods

2.1. FUS Setup. A focused ultrasound transducer was used to generate ultrasound focal energy (IMASONIC, France; diameter = 60 mm, radius of curvature = 80 mm, frequency = 400 kHz, and electric-to-acoustic efficiency = 70%) (Figure 1). An arbitrary function generator (33120A, Agilent, Palo Alto, CA and DS345, Stanford Research Systems, Sunnyvale, CA) was used to generate the driving signal, which was then fed into a radiofrequency power amplifier (150A100B, Amplifier Research, Souderton, PA). The focal zone distribution of the intensity of the ultrasound field was measured in an acrylic water tank filled with deionized, degassed water. The measured diameter of the half-maximum pressure amplitude was 2 mm, and the length of the produced focal zone was 15 mm. Animals underwent isoflurane anesthesia before ultrasound treatment. The animal was laid prone and placed directly under an acrylic water tank (with a window of $4 \times 4 \text{ cm}^2$ at its bottom sealed with a thin film to allow entry of the ultrasound energy), using ultrasound gel to fill the interspaces between the animal head and the thin-film window. SonoVue SF6-coated ultrasound microbubbles (2–5 μm mean diameter, 2.4 $\mu\text{L}/\text{kg}$; Bracco Diagnostics Inc.) were IV administered by burst injection with 0.1 mL of saline solution containing 0.01 mL heparin. After injecting the microbubbles, burst-tone mode ultrasound at a pressure of 0.4 MPa (peak negative value; measured in the free-field) was delivered to the brain with the center of the focal zone positioned at a penetration depth of 4–5 mm under the scalp (burst length = 10 ms, pulse repetition frequency = 1 Hz, and total sonication duration = 90 s).

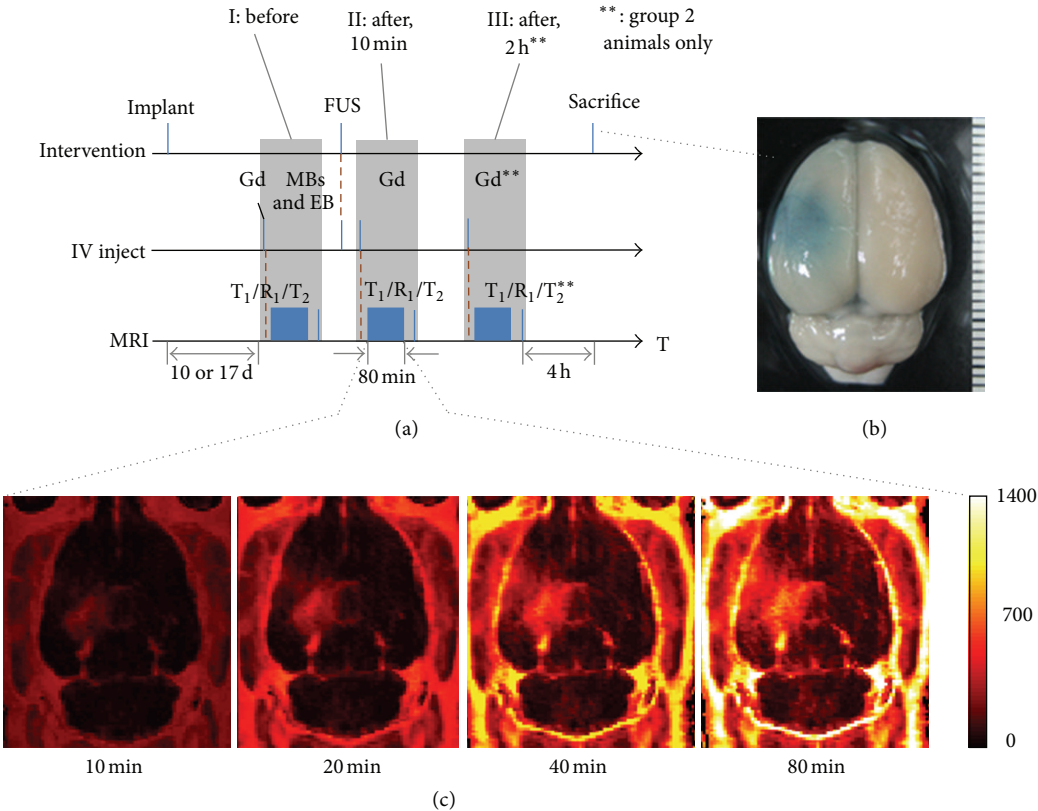


FIGURE 2: (a) Experimental protocol for 1st- and 2nd-group animal experiments. MRI images were acquired in time slots I/II for group 1 animals and in time slots I/II/III for group 2 animals; double asterisks (**) indicate group-2 experiments only. (b) FUS-exposed brain of a normal animal with Evans blue extravasations to identify the location of BBB opening. (c) R₁ accumulating map showing Gd-DTPA accumulation in the BBB-opening location of a normal animal over time.

2.2. Animal Experiment Design. All animal experiments were approved by the Institutional Animal Care and Use Committee of Chang Gung University and adhered to the experimental animal care guidelines. A total of 34 animals (male Sprague-Dawley rats (250–300 g)) were used, including normal ($n = 18$) and tumor animals ($n = 16$). Experiments were divided into two groups. In group 1, the aim was to confirm the correlation between Gd-DTPA leakage (concentration measured by relaxometry) and Evans blue (EB) dye (concentration measured spectrophotometrically) after FUS-BBB treatment. Subgroups included (1) normal rats ($n = 18$) and (2) tumor rats ($n = 4$), and the first subgroup underwent FUS-BBB opening. Subgroups were confirmed by dynamic contrast-enhanced (DCE) MRI with Gd-DTPA (molecular weight = 938 Da). In addition, EB dye (molecular weight = 960 Da) was IV injected into the animals, and the amount of EB deposited in the brain was quantified spectrophotometrically (procedure described below). In the first subgroup of group 1, contrast-enhanced T₁-weighted imaging was first performed to estimate Gd-DTPA concentration after BBB opening, followed by T₂-weighted imaging to provide a reference of tumor morphology. The second subgroup underwent the same scanning process without FUS induced.

In experimental group 2, our aim was to monitor the increase in Gd-DTPA accumulation in tumor-bearing animals after conducting FUS-BBB opening. Animals were divided into two subgroups: (1) animals receiving FUS exposure 10 days after tumor implantation (tumor volume typically $<0.05 \text{ cm}^3$) with FUS-BBB opening ($n = 6$) and (2) animals receiving FUS exposure 17 days after tumor implantation (tumor volume typically $>0.05 \text{ cm}^3$) with FUS-BBB opening ($n = 6$). Tumor volume was measured by T₂-weighted MRI. In group 2, animals were subjected to three 80-minute-long MR relaxometry-based imaging sessions (before FUS exposure, and 10-min and 120-min after FUS exposure). Detailed experimental procedures are shown in Figure 2.

2.3. Rat Brain Glioma Model. C6 glioma cells were harvested by trypsinization and cultured at a concentration of 1×10^5 cells/mL for implantation. For intracranial injection into the striatum of rat brains, cells were washed once with phosphate buffered saline (PBS). Male Sprague-Dawley rats (250–300 g) were anesthetized by intraperitoneal administration of ketamine (100 mg/kg) and immobilized on a stereotactic frame. A sagittal incision was made through the

skin overlying the calvarium, and a small dental drill was used to make a hole in the exposed cranium, 0.5 mm anterior and 3 mm lateral to the bregma on the left side of skull. C6 cell suspension (5 mL) was injected at a depth of 4.5 mm from the brain surface. The injection was performed over a 10-minute period, and the needle was withdrawn over another 2 minutes. Ten days after implantation, tumor sizes were measured by MRI.

2.4. Spectrophotometric Quantitation of Evans Blue Dye. EB dye (3% in saline) was IV injected (2 mg/kg), and the animals were sacrificed two hours later. All animals were first deeply anesthetized with 10% chloral hydrate and infused with heparinized saline through the cardiac ventricle until colorless infusion fluid was obtained from the atrium. After the rats had been sacrificed by decapitation, the hemispheres of the brain were separated along the transverse suture. Then both hemispheres were weighed and placed in formamide (1 mL/100 mg) at 60°C for 24 h. The sample was centrifuged for 20 mins at 14,000 rpm. The concentration of dye extracted from each brain was determined spectrophotometrically at 620 nm and was compared with a standard graph created by recording optical densities from serial dilutions of EB in 0.9% sodium chloride solution. The EB tissue content was quantified using a linear regression standard curve derived from seven concentrations of the dye.

2.5. MRI. For *in vitro* measurements, Gd-DTPA (Omniscan, 0.3 mL/kg, Magnevist) was diluted with physiological saline to 0.12, 0.24, 0.49, 0.97, 1.96, and 3.9 μ M. Circular wells (inner diameter = 5 mm) were filled with 200 λ of contrast agent sample or physiological saline as control and were placed in the MR scanner (Clinscan, Bruker, Germany; 7 Tesla). Spin-lattice relaxivity maps were calculated from two T_1 -weighted images with different flip angles (gradient recalled echo sequence, TR/TE = 2.3 ms/0.76 ms, slice thickness = 0.8 mm, matrix = 132 \times 192, and flip angle = 5°/20°). The correlation between R_1 (= 1/ T_1) mapping and Gd-DTPA concentration was determined [27].

In the animal experimental group, FUS-induced BBB opening was monitored by MRI with a 7-Tesla magnetic resonance scanner (Bruker ClinScan, Germany) and a 4-channel surface coil. The mouse was placed in an acrylic holder, positioned in the center of the magnet, and anesthetized with isoflurane gas (1-2%) at 50–70 breaths/min during the entire MRI procedure.

In the first experimental group, the distribution and dynamics of Gd-DTPA leakage were investigated immediately after conducting FUS-BBB opening. After FUS-BBB opening, animals were immediately relocated into the MR scanning room, and contrast-enhanced T_1 -weighted images with different flip angles were acquired to calculate spin-lattice relaxivity maps by transferring two images with different flip angles (gradient recalled echo sequence, TR/TE = 2.3 ms/0.76 ms, slice thickness = 0.8 mm, slice number = 14, matrix = 132 \times 192, and flip angle = 5°/20°). Images were sequentially acquired over 80 min with a time interval of 60 seconds for area under the curve (AUC)

calculation. Upon completion of the 10th acquisition, a diluted bolus of Gd-DTPA was IV injected through a catheter at an infusion rate of 6 mL/s. In the second experimental group, three sets of Gd-DTPA-leakage distribution/dynamics were investigated, including (I) before FUS exposure, (II) immediately after FUS exposure, and (III) two hours after FUS exposure. Immediately after conducting FUS-BBB opening, turbo spin echo (TSE) T_2 -weighted images were obtained as a reference to identify the tumor region (repetition time (TR)/echo time (TE) = 2540/41 ms, FOV = 34 \times 40 mm², in-plane resolution = 0.4 \times 0.3 mm², and slice thickness = 0.6 mm).

2.6. MR Analysis of Gd-DTPA Accumulation and Distribution after FUS-BBB Opening. In R_1 -map analysis, a region of interest (ROI) was selected and compared with the non-enhanced contralateral brain to determine the increase in Gd-DTPA concentration caused by BBB opening. AUC maps were then transferred from a series of time-dependent R_1 maps (up to 80 min) to determine pharmacodynamic characteristics of Gd-DTPA for comparison with the dynamics of EB dye permeability. Thus, the total area (AUC) is given by the following equation:

$$AUC_{80 \text{ min}} = \frac{\int Cpt \cdot dt}{V}, \quad (1)$$

where Cpt are vertical segments under the Gd-DTPA concentration curve area and V is total ROI volume.

In experimental group 2, ROIs were selected in the targeted tumor area which was based on the tumor dimensions defined in T_2 images (the same ROI as in the contralateral brain was selected). The distribution and dynamics of Gd-DTPA leakage were evaluated for different tumor sizes including 10 days after implantation (typically <0.05 cm³) and 17 days after implantation (typically >0.05 cm³) and were divided by the tumor dimension. ROI including the entire tumor and the contralateral area were selected. Moreover, in order to evaluate the homogeneity of Gd-DTPA leakage, tumors with dimension >0.05 cm³ were further divided into tumor core (inner half of the area) and tumor peripheral (outer half of the area), based on T_2 images.

2.7. Histology. Albumin-bound EB dye was IV injected as a bolus immediately after sonication. BBB opening was quantified as extravasation of EB. Tumor model animals were sacrificed about 2 h after sonication and MR scanning. Brain samples were serially sectioned (2 μ m thickness) using the same slice direction as in MRI analysis. Representative sections were stained with hematoxylin and eosin (HE). Tumor morphology was histologically evaluated.

3. Results

BBB opening was clearly evidenced by staining with EB dye. A typical image of a normal BBB-opened brain stained with EB dye is shown in Figure 2(b). In addition, a series

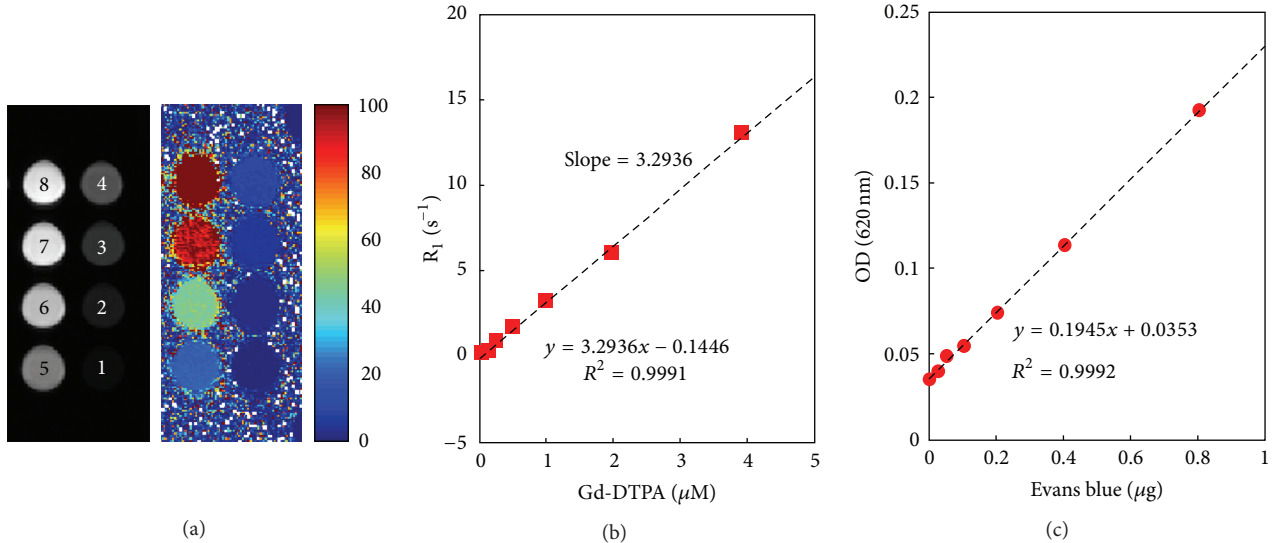


FIGURE 3: (a) T₁ image and corresponding R₁ map for the *in vitro* Gd-DTPA phantom at increasing concentrations (1 and 2: water; 3: 0.12 μM; 4: 0.24 μM; 5: 0.49 μM; 6: 0.97 μM; 7: 1.96 μM; 8: 3.9 μM). (b) Dependence of R₁ on Gd-DTPA concentration; relaxivity was estimated as about 3.2936 s⁻¹ mM⁻¹. (c) Calibration curve of spectrophotometrically determined EB concentration. EB concentrations ranging from 0 to 0.8 μg were tested, resulting in O.D. readings of 0.035 to 0.19 at 620 nm.

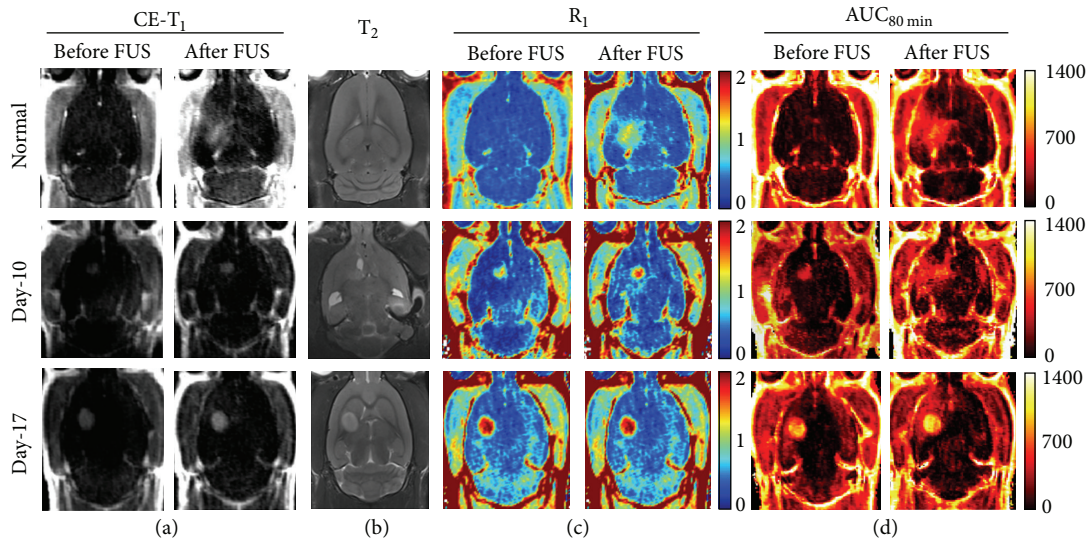


FIGURE 4: Typical MRI for normal animals (upper) as well as animals after 10-day (middle) and 17-day (bottom) tumor implantations. (a) Contrast-enhanced T₁ images before and after FUS exposure. (b) T₂ images (after FUS). (c) R₁ maps before and after FUS exposure. (d) Area under the R₁ curve over 80 minutes (denoted as AUC_{80 min}) before and after FUS exposure.

of R₁ maps obtained at different time points after FUS-BBB opening demonstrated the dynamic change in Gd-DTPA accumulation in a normal brain, with particularly high leakage at the sonication site (Figure 2(c)).

R₁ relaxivity of Gd-DTPA and ELISA measurements of EB dye concentration were calibrated *in vitro*. The detected R₁-signal increased in a highly linear manner with Gd-DTPA concentration (input concentrations of 0, 0.25, 0.5, 1, 2, and 4 μM) as shown by the calibration curve ($r^2 = 0.9991$) (Figure 3(b)). The relaxivity of Gd-DTPA contrast agent was found to be 3.3 at 7 Tesla. The detected ELISA signal also

increased in a highly linear manner with EB concentration (Figure 3(c); $r^2 = 0.9992$). These calibration curves thus allowed precise quantitation of Gd-DTPA and EB deposition in the brain.

FUS-induced BBB opening was verified by CE-MRI. Typical CE-T₁ images, T₂ images, R₁ maps, and AUC maps in normal, 10-day glioma, and 17-day glioma animals are shown in Figure 4. In normal animals, the BBB-opened area was clearly visible in T₁-weighted images. T₂-weighted images did not show any evidence of FUS-induced damage at the target location at pressure amplitudes of 0.4 MPa (Figure 4). In the

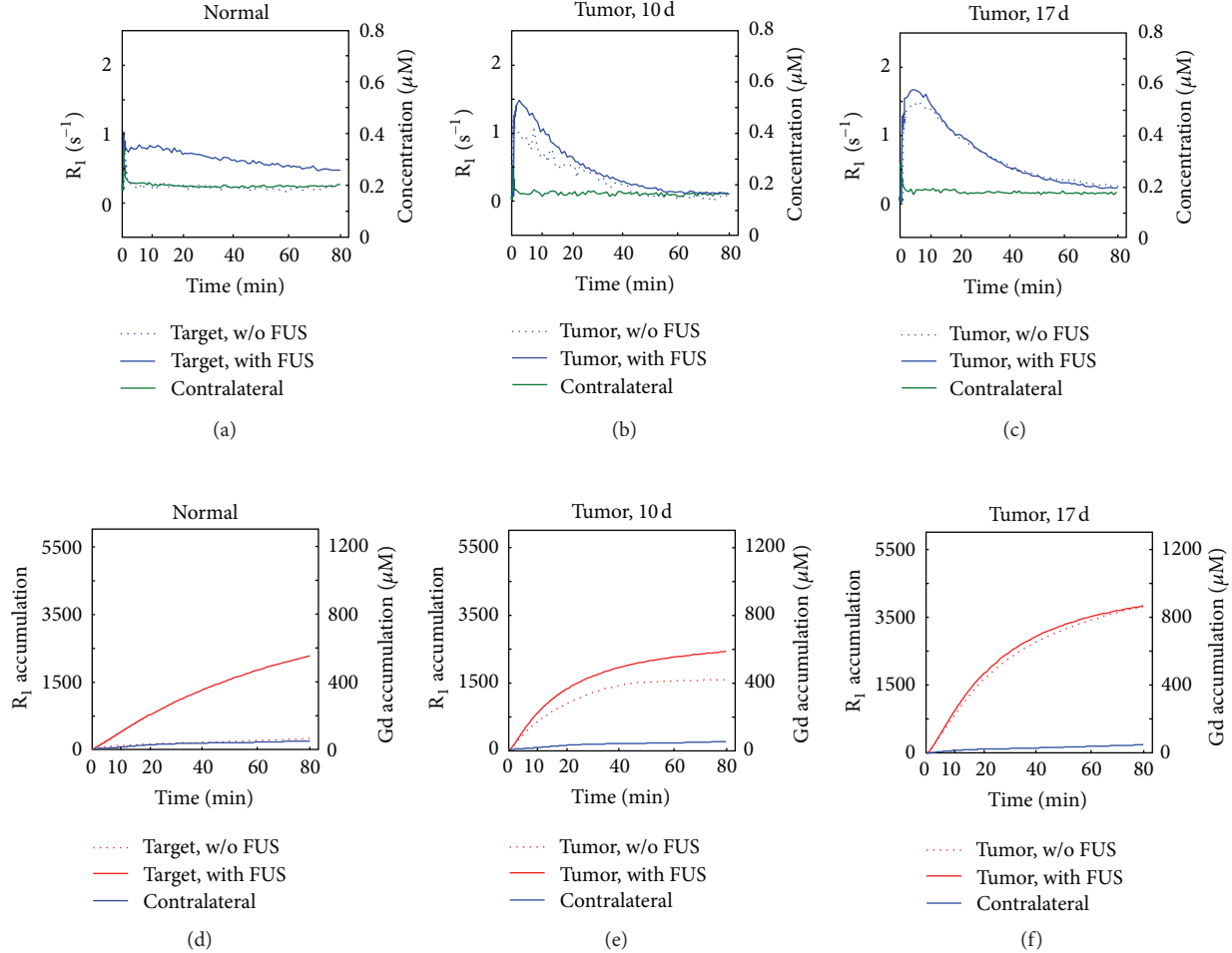


FIGURE 5: (a)–(c) R_1 change as a function of time before and after FUS exposure for normal animals, 10-day and 17-day tumor animals. (d)–(f) The corresponding R_1 accumulation as a function of time over 80 minutes for (a)–(c).

first subgroup of experimental group 1, the R_1 -map signal of the BBB-opening area was increased from 0.1 to about 1.2 by FUS, and AUC maps showed an increase in accumulation of Gd-DTPA deposition from 20 to about 600.

In tumor-bearing animals, the FUS-induced BBB area clearly covered the tumor tissue (Figure 4; small (10-day) or large (17-day) tumors). Sonication resulted in increased Gd-DTPA accumulation in the tumor and in the peripheral BBB-opened area as evidenced by signal enhancement in the R_1 -map images. AUC maps showed maintained high staining intensities after Gd-DTPA injection. In the small (10-day) tumors, FUS resulted in an increase of R_1 signal from 1 to about $1.5 s^{-1}$ and an increase in Gd-DTPA deposition of about 200 (from 400 to 600). However, in large (17-day) tumors, FUS did not lead to a significant change in the R_1 -signal, which increased from 1.9 to $2 s^{-1}$, or the AUC value which increased by only about 50 (from 1000 to 1050).

The kinetics of Gd-DTPA accumulation were evaluated after a single sonication treatment in thirty animals (normal rats: $n = 18$; small-tumor model: $n = 6$; large-tumor model: $n = 6$). An ROI from the BBB-opened area on T_2 -weighted images (target) and the corresponding ROI from

the contralateral brain (contralateral) were used to infer Gd-DTPA concentration from the R_1 signals and the AUC over time in the 10-day tumors (volume $< 0.05 \text{ cm}^3$), 17-day tumors (volume $> 0.05 \text{ cm}^3$), or normal controls after sonication (Figure 5). Figures 5(a)–5(c) showed the comparison of changes in R_1 as a function of time (from 0 to 80 min) for three typical animals. When considering the peak value over the whole scanning process, FUS caused the highest enhancement in R_1 signal of contrast agent in normal tissue (from 0.2 to 0.84; Figure 5(a)). Sonication also led to a large increase in R_1 signal in 10-day tumor, from 0.86 to $1.48 s^{-1}$ (Figure 5(b)). However, the already high permeability of 17-day tumor to Gd-DTPA was not significantly increased by FUS, from 1.49 to $1.62 s^{-1}$ (Figure 5(c)).

The corresponding AUC (accumulation of R_1) as a function of time (from 0 to 80 min) in these three animals is shown in Figures 5(d)–5(f). In the normal animal, total Gd-DTPA accumulation in the BBB-opening area was increased from 44.2 to 552.6 pmol by FUS (Figure 5(d)). Gd-DTPA accumulation in the 10-day tumor increased from 411.7 to 577.5 pmol, compared to only about 73 pmol over time in the contralateral control hemisphere (Figure 5(e)). However,

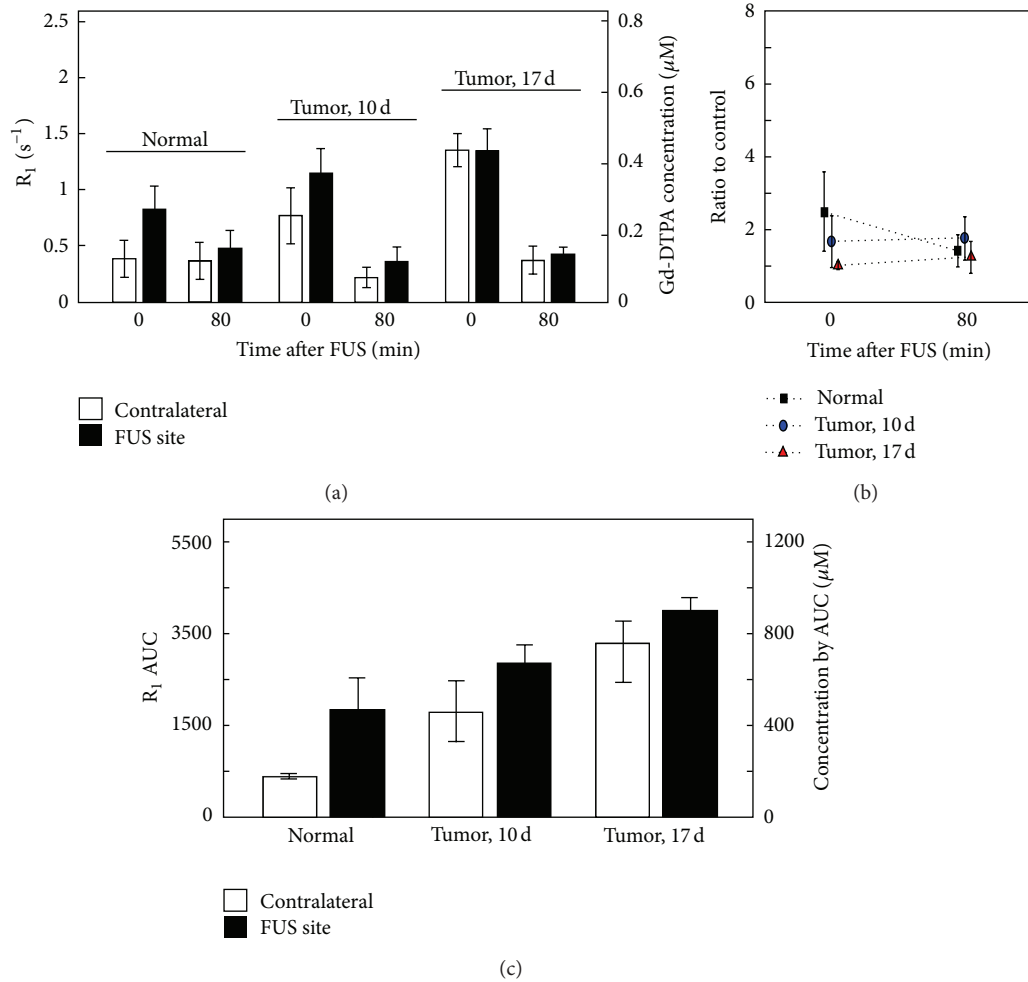


FIGURE 6: (a) Instantaneous R_1 measured immediately or 80 minutes after FUS exposure in normal animals, 10-day and 17-day tumor animals. (b) Ratio of instantaneous R_1 values, immediately and 80 min after FUS. (c) Corresponding R_1 AUC of (a). Images were acquired in time slot II.

Gd-DTPA accumulated to about the same high value with and without FUS (863.8 versus 867.3 pmol) in the 17-day tumor (Figure 5(f)).

Gd-DTPA levels on the FUS-treated and contralateral side were also evaluated at either 10 min or 80 min after a single sonication treatment (Figure 6). The Gd-DTPA signal intensity increased in the BBB-opening area 10 min after sonication as evidenced by an increase in the R_1 signal from $0.3863 s^{-1}$ to $0.8313 s^{-1}$ for control and from $0.77 s^{-1}$ to $1.15 s^{-1}$ for small-tumor animals. However, the contrast agent signals in the FUS-enhanced large tumors were the same as for the contralateral region (about $0.136 s^{-1}$). All R_1 signals in these brain tissues returned to baseline (about $0.428 s^{-1}$) at 80 min after sonication. The ratio of R_1 between the FUS-exposed and control areas went from $2.48 s^{-1}$ at 10 min to $1.4 s^{-1}$ at 80 min in normal tissue and from about 1.8 to $1 s^{-1}$ for the tumor-bearing animals (Figure 6(b)). The AUC at 10 min and 80 min was compared between control and BBB-opened brain regions. At 10 min after sonication, the accumulated Gd-DTPA concentration of the BBB-opened

area increased to $465.99 \mu M$, compared to $667.34 \mu M$ for the small tumor and a limited increase to $896 \mu M$ for the large tumor (Figure 6(c)).

Next we evaluated the correlation between EB leakage (Figure 7(a)) and Gd-DTPA accumulation (estimated by the AUC) in the same region of the brain. We found that the accumulated distribution of Gd-DTPA (i.e., AUC) was highly correlated with the distribution of EB ($r^2 = 0.8897$) (Figure 7(b)). Thus, R_1 -based pharmacodynamic analysis provided a reasonable map of the permeability of the BBB-disrupted region to EB dye over time. EB dye and Gd-DTPA accumulation showed the same tendency of higher overall permeability in tissues of large tumors and less dependence on FUS treatment, as evidenced from the ratios of accumulation between contralateral and FUS-treated regions (Figure 7(c)).

Next, we analyzed Gd-DTPA deposition dynamics in experimental group 2 animals by AUC analysis for three individual time slots: (I) before FUS, (II) immediately after FUS, and (III) 2 hours after FUS. Gd-DTPA concentration

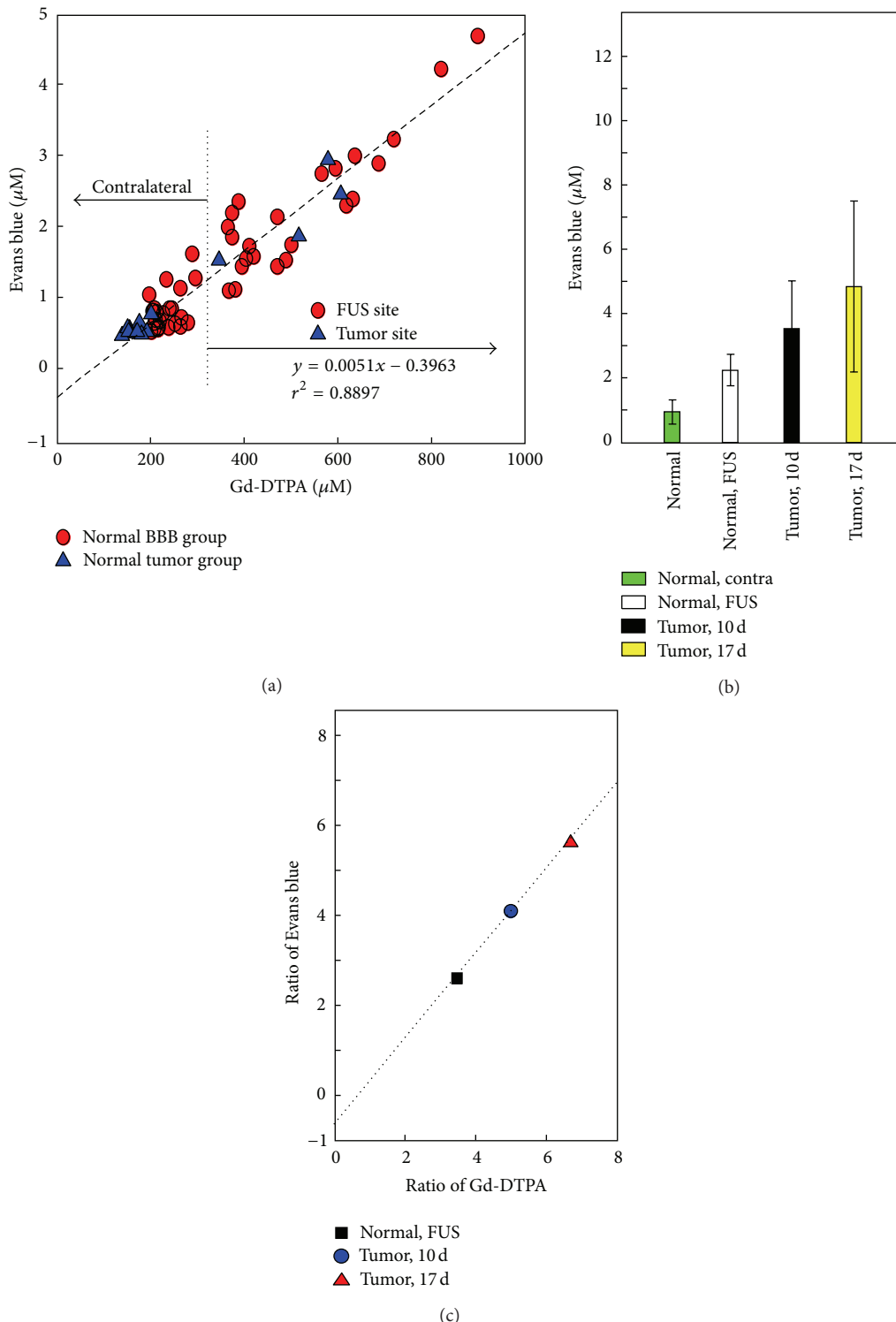


FIGURE 7: (a) Correlation between quantified Evans blue concentration and R_1 -estimated Gd-DTPA concentration in normal (red circle) and tumor (blue triangle) brains. Left arrow: contralateral side and right arrow: with FUS (red circle); normal tumor (blue triangle). (b) Evans blue after FUS exposure in the normal contralateral region, normal FUS targeting region, 10-day tumor region after FUS, and 17-day tumor region after FUS. (c) Correlation of the ratios of FUS: contralateral concentrations of Evans blue and Gd-DTPA in normal and tumor-bearing brains.

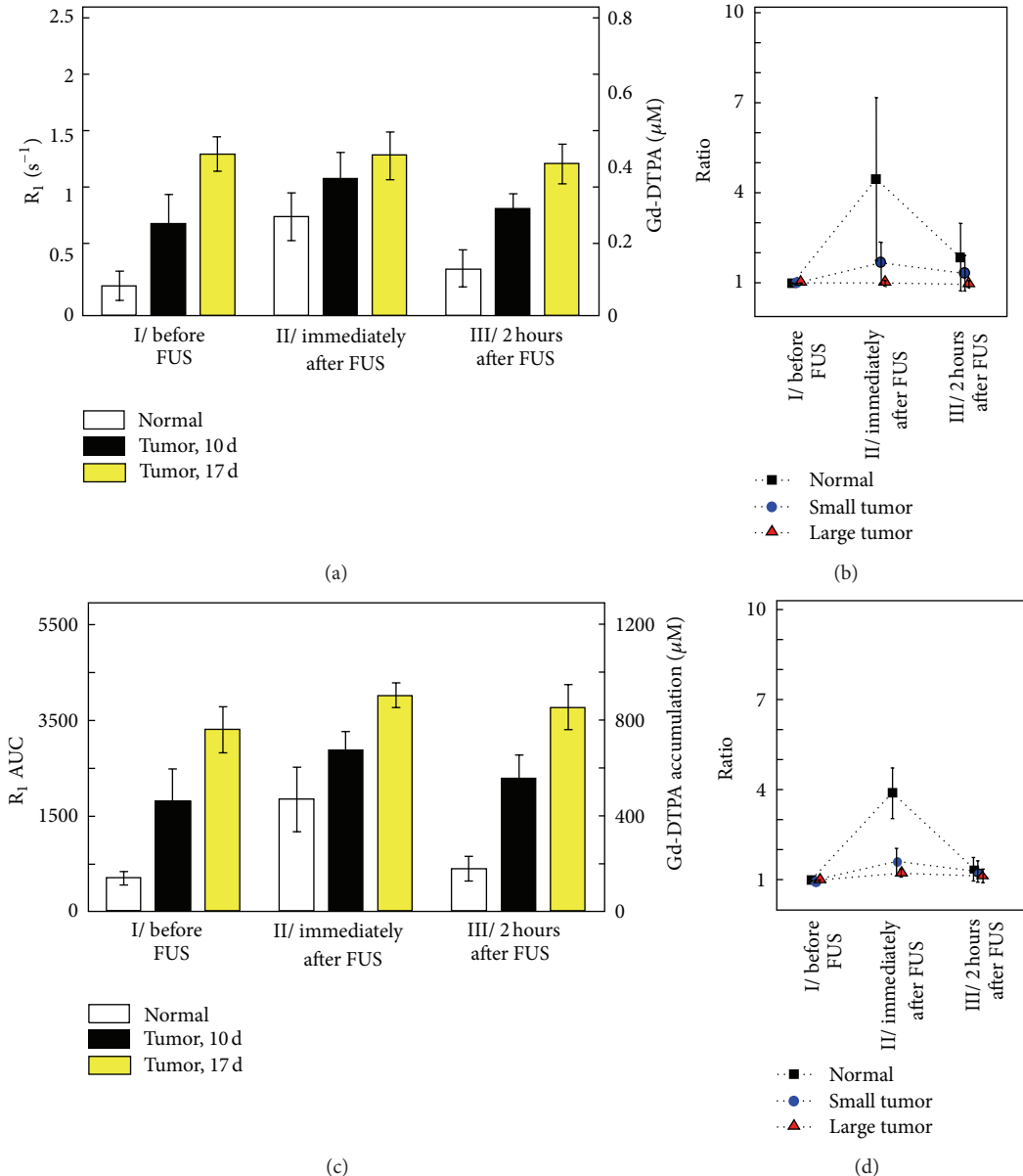


FIGURE 8: (a) Instantaneous R_1 values of the normal animals, 10-day and 17-day tumor animals at MRI acquisition time slots I, II, and III. (b) Ratio of instantaneous R_1 to the value in time slot I. (c) Corresponding R_1 AUC of (a). (d) Ratio of R_1 AUC to the value in time slot I.

and accumulation in the target area presented the same trend at all three time points (Figure 8). As before, we observed a transient peak of R_1 and the AUC in the BBB-opened brain just after sonication (Figures 8(a) and 8(c)). However, the increase in the ratio of R_1 or AUC again differed between the normal and tumor-bearing animals (Figures 8(b) and 8(d)). The ratio was highest in the normal BBB-opening area (R_1 signal 4.4 times than before FUS; AUC: 3.7 times), followed by the small-tumor model (R_1 signal: 1.7 times; AUC: 1.6 times), with no significant change in the large tumor, confirming our previous observations that FUS did not significantly further affect permeability in large tumors. These ratios subsequently decreased at the time point 2 hours after FUS induction, returning to approximately the same

values of DCE-MRI as originally observed before sonication. This result implied that at 2 hours, the BBB-opening area had recovered to the same baseline permeability level to contrast agent as prior to sonication.

HE staining of tumors 10 days after implantation showed even staining without scattered red blood cells in the absence of FUS (Figures 9(a) and 9(b)). Tumor cells were characterized by dense nuclear distribution, and only tiny areas of gliosis infiltrated with chronic inflammatory cells and some hemorrhaging were found (Figures 9(c) and 9(d)). HE staining of tumors 17 days after implantation revealed a number of regions with extensive apoptosis and cavities in the core of the tumor, and hemorrhagic structures with scattered and spreading erythrocytes could be observed

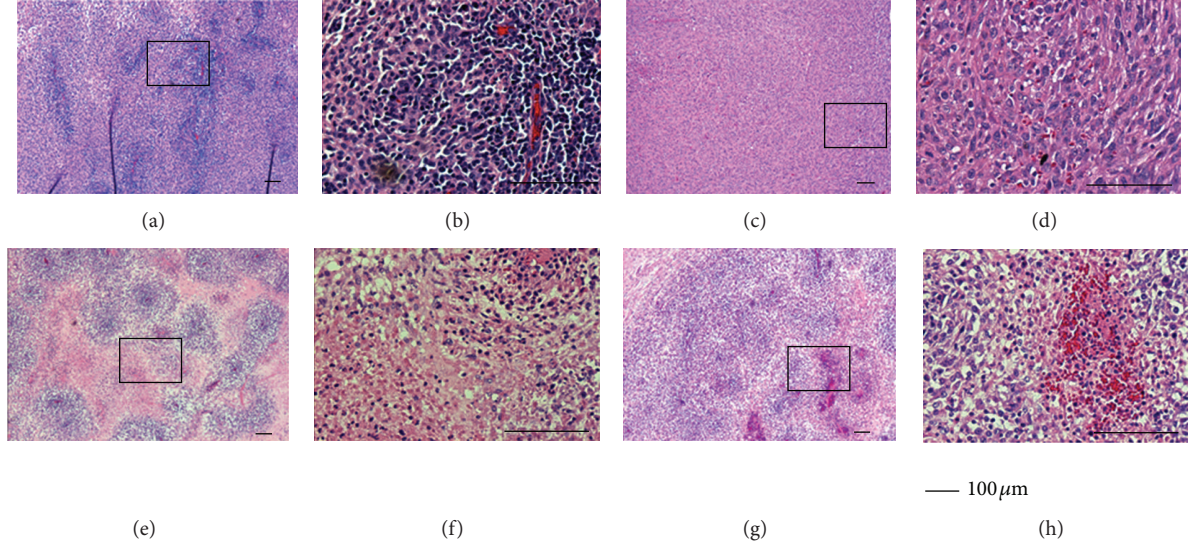


FIGURE 9: HE staining. (a) and (b) Small (10-day) tumor tissue without FUS exposure, 40x and 200x. (c) and (d) Small (10-day) tumor tissue with FUS exposure, 40x and 200x. (e) and (f) Large (17-day) tumor tissue without FUS exposure, 40x and 200x. (g) and (h) Large (17-day) tumor tissue with FUS exposure, 40x and 200x.

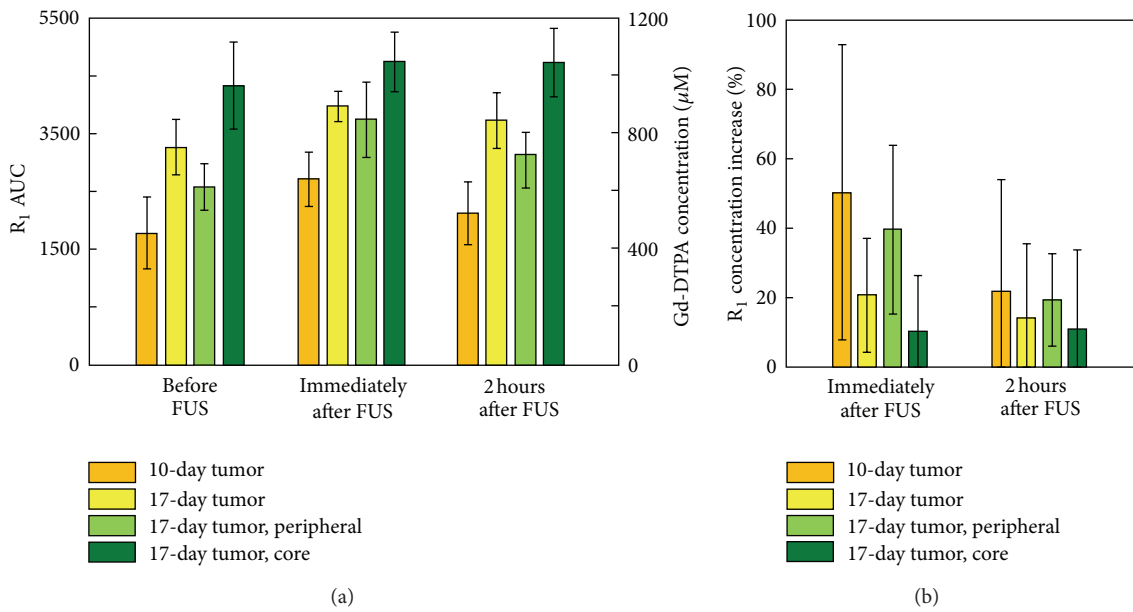


FIGURE 10: (a) R_1 AUC analysis of the core and peripheral subregions of 17-day tumor. (b) R_1 AUC increase relative to time slot I.

around discontinuous vasculature (Figures 9(e) and 9(f)), supporting our findings of high permeability of 17-day tumors based on observation of Gd-DTPA deposition. This structure did not change significantly after sonication (Figures 9(g) and 9(h)) with hemorrhagic regions remaining similar to those in the unexposed tumor.

Previous reports showed that the tumor core consists of a bulky necrotic mass without functional vasculature, whereas the tumor periphery maintains a high degree of vasculature structure [28, 29]. We therefore hypothesized that microbubble-enhanced FUS exposure would have a bigger

effect on enhancing permeability in the peripheral tumor. We further divided the 17-day tumor animals into core and peripheral subregions and then repeated the MRI AUC analysis (Figure 10). We observed that, after FUS exposure, the 17-day peripheral tumor showed a similar trend to the 10-day tumor, which showed a nearly 1.7-fold of instantaneous increase and 50% accumulation increase in Gd-DTPA, and the permeability dropped significantly two hours after FUS exposure to about half (20%), which is similar to 10-day tumor. In contrast, the 17-day tumor core mimicked the behavior of the undivided 17-day tumor, accumulating high

levels of Gd-DTPA both before and after FUS exposure (AUC increase of only 10% after FUS exposure) (Figure 10). This relatively low increase in the AUC persisted when the tumor core was re-evaluated at 2 hours after FUS exposure (9%). These observations suggest that the FUS-BBB opening can provide the most pronounced drug delivery enhancing effect on tumor peripheral or tumors with high-vascularity stage tumors, yet only provides limited effects on bulky and necrotic tumors.

4. Discussion

This study demonstrated the pharmacodynamic characteristics of small-molecule leakage at various stages of tumors after application of microbubble-enhanced FUS to open the BBB. We analyzed two small molecules with similar molecular weights to obtain complimentary data on pharmacodynamic behavior. Gd-DTPA was used to provide contrast in MRI and for semiquantitative verification of biodistribution *in vivo*, and EB dye was used as a measure of drug accumulation after animal sacrifice. These two molecules, which normally do not enter the brain parenchyma from the bloodstream, could potentially be used as surrogate markers for drug delivery. Although the dynamic distribution of Gd-DTPA may differ from that of Evans blue, we demonstrated that the AUC accumulation of Gd-DTPA analyzed by MRI was highly correlated with EB accumulation in the brain ($r^2 = 0.8897$), implying that MRI AUC analysis of Gd-DTPA could predict the concentration of EB accumulating in the brain, and may thus have the potential to predict the pharmacodynamic behavior and biodistribution of other therapeutic agents.

This study employed high-temporal-resolution dynamic CE-MRI that could be utilized for small-molecule *in vivo* distribution and semiquantification, as attempted in previous studies [30, 31]. The unique features provided by dynamic CE-MRI include the capability of rapid evaluation and high spatial resolution, as well as kinetic analysis to evaluate tumor perfusion [30]. Positron emission tomography (PET) has also been used for pharmacological studies in several tumor types [32, 33]. However, potential limitations of PET may include its limited imaging resolution and complexity of radiotracer synthesis. In small tumors, partial volume effects may be significant if the tumor size is less than twice the resolution of the scanner [34]. MRI methods provide the advantage of having good spatial resolution equal to that of corresponding morphologic images. In addition, MRI is minimally invasive and poses little risk to patients. We used voxels of about $0.26 \times 0.26 \times 1\text{ mm}^3$ to construct images sufficient for small-animal analysis. On the other hand, PET relies on radiolabeled molecules that bind to receptors to allow absolute quantification by detection of isotopes. PET may also be limited by its high cost, limited availability of radiotracer, and the need for a cyclotron as well as onsite radiochemistry for radioisotope production [35]. PET involves comprehensive conjugation of radiotracers and specific tailor-made molecules limiting its general use for pharmacodynamic analysis. Although Gd-DTPA cannot be directly conjugated to therapeutic molecules, the

detection of coadministered Gd-DTPA by CE-MRI is highly correlated with targeted molecules, providing an excellent tool for monitoring vasculature and evaluating tissue/tumor permeability at high temporal/spatial resolution, suggesting its continued usefulness for pharmacodynamic analysis of brain drug delivery.

Tumor tissues are known to have high permeability due to the presence of large endothelial cell gaps, incomplete basement membrane, and the relative lack of pericyte or smooth muscle association with endothelial cells [36, 37]. In addition, the network of vasculature in solid tumors is markedly different from the normal hierarchical branching patterns and contains leaky vessel structures. Variations in permeability are also associated with the tumor grade as well as various neoplastic effects that could disrupt the BBB [38]. In this study, we observed that tumors with different levels of progression showed different characteristics of blood-vessel permeability and small-molecule accumulation. We found that the $AUC_{80\text{ min}}$ in small tumors was $452 \pm 122.5\text{ }\mu\text{M}$, whereas in large tumors it reached $754 \pm 48.3\text{ }\mu\text{M}$. Moreover, we confirmed that FUS-BBB opening provided a 50% enhancement of accumulation of Gd-DTPA in small brain tumors and a 40% enhancement at the large tumor periphery, implying that FUS-BBB opening is an effective approach to increase brain-tumor permeability and therefore enhance delivery of therapeutic molecules.

Histological examination by HE staining showed that smaller (10-day) tumors had well-ordered vasculature with fewer abnormal endothelial cell gaps (Figures 9(a) and 9(b)). The blood vessel density in small tumor was lower, resulting in less Gd-DTPA and EB accumulation. In contrast, 17-day tumor tissues contained more large fenestrae (Figures 9(e) and 9(f)), consistent with previous pathological findings that high-grade brain tumors contain neovasculature and apoptotic tumor cells, leading to hyperpermeability [39]. These pathological changes are consistent with the increased Gd-DTPA and EB accumulation that we observed in 17-day tumor tissues before sonication.

Although $AUC_{80\text{ min}}$ correlated well with the pharmacodynamic behavior of another small molecule (EB), Gd-DTPA accumulation can be very different even under the same FUS exposure conditions, for example, varying from 365.2 to 900 μM (Figure 7(b)). These large variations were likely due to differences in skull thickness and angle of incidence between the FUS beam and the skull surface among the animals [40], and the presence of standing waves produced in the skull cavity that alter the peak pressure at the target position and thus the level of BBB opening [41]. Since FUS-BBB opening may vary substantially, it is essential to perform an AUC analysis during CE-MRI to monitor small-molecule delivery into the brain for individual subjects and targets.

5. Conclusion

In this study, we characterized the dynamics of BBB opening in normal and tumor tissues using DCE-MRI with Gd-DTPA contrast agent, and related them to the concentrations of Evans Blue determined from tissues after sacrifice. The

concentrations of the surrogate tracer (Gd-DTPA) and EB dye showed a strong linear correlation. With this dynamic information of tumor permeability, the pharmacodynamic model can be modified to eventually take into account parameters that affect drug delivery over time. Tumor peripheral or high-vascular tumor may have the most significant benefit on blood-brain or blood-tumor permeability increase, which gives critical information when intending to apply FUS for brain drug enhanced delivery. We hope to use such pharmacodynamic predictions along with FUS-induced BBB opening to develop a method for image-guided drug delivery that can estimate the amount of drug that will be delivered to tissues at each time point.

Conflict of Interests

The authors declare that there is no conflict of interests.

Acknowledgments

The authors thank the Molecular Imaging Center, Chang Gung Memorial Hospital. This work was supported by the National Science Council, Taiwan (Grant nos. 100-2321-B-182-010, 100-2120-M-182A-001, and 101-2221-E-182-002-MY3).

References

- [1] K. Hynynen, N. McDannold, N. Vakhodtseva, and F. A. Jolesz, "Noninvasive MR imaging-guided focal opening of the blood-brain barrier in rabbits," *Radiology*, vol. 220, no. 3, pp. 640–646, 2001.
- [2] K. Hynynen, N. McDannold, N. A. Sheikov, F. A. Jolesz, and N. Vakhodtseva, "Local and reversible blood-brain barrier disruption by noninvasive focused ultrasound at frequencies suitable for trans-skull sonifications," *NeuroImage*, vol. 24, no. 1, pp. 12–20, 2005.
- [3] K. Hynynen, N. McDannold, N. Vakhodtseva et al., "Focal disruption of the blood-brain barrier due to 260-kHz ultrasound bursts: a method for molecular imaging and targeted drug delivery," *Journal of Neurosurgery*, vol. 105, no. 3, pp. 445–454, 2006.
- [4] M. Kinoshita, N. McDannold, F. A. Jolesz, and K. Hynynen, "Targeted delivery of antibodies through the blood-brain barrier by MRI-guided focused ultrasound," *Biochemical and Biophysical Research Communications*, vol. 340, no. 4, pp. 1085–1090, 2006.
- [5] N. McDannold, N. Vakhodtseva, and K. Hynynen, "Effects of acoustic parameters and ultrasound contrast agent dose on focused-ultrasound induced blood-brain barrier disruption," *Ultrasound in Medicine and Biology*, vol. 34, no. 6, pp. 930–937, 2008.
- [6] H. L. Liu, Y. Y. Wai, W. S. Chen et al., "Hemorrhage detection during focused-ultrasound induced blood-brain-barrier opening by using susceptibility-weighted magnetic resonance imaging," *Ultrasound in Medicine and Biology*, vol. 34, no. 4, pp. 598–606, 2008.
- [7] H. L. Liu, P. H. Hsu, P. N. Chu et al., "Magnetic resonance imaging enhanced by superparamagnetic iron oxide particles: usefulness for distinguishing between focused ultrasound-induced blood-brain barrier disruption and brain hemorrhage," *Journal of Magnetic Resonance Imaging*, vol. 29, no. 1, pp. 31–38, 2009.
- [8] M. Kinoshita, N. McDannold, F. A. Jolesz, and K. Hynynen, "Noninvasive localized delivery of Herceptin to the mouse brain by MRI-guided focused ultrasound-induced blood-brain barrier disruption," *Proceedings of the National Academy of Sciences of the United States of America*, vol. 103, no. 31, pp. 11719–11723, 2006.
- [9] L. H. Treat, N. McDannold, N. Vakhodtseva, Y. Zhang, K. Tam, and K. Hynynen, "Targeted delivery of doxorubicin to the rat brain at therapeutic levels using MRI-guided focused ultrasound," *International Journal of Cancer*, vol. 121, no. 4, pp. 901–907, 2007.
- [10] J. Mei, Y. Cheng, Y. Song et al., "Experimental study on targeted methotrexate delivery to the rabbit brain via magnetic resonance imaging-guided focused ultrasound," *Journal of Ultrasound in Medicine*, vol. 28, no. 7, pp. 871–880, 2009.
- [11] H. L. Liu, M. Y. Hua, P. Y. Chen et al., "Blood-brain barrier disruption with focused ultrasound enhances delivery of chemotherapeutic drugs for glioblastoma treatment," *Radiology*, vol. 255, no. 2, pp. 415–425, 2010.
- [12] W. M. Pardridge, "The blood-brain barrier: bottleneck in brain drug development," *NeuroRx*, vol. 2, no. 1, pp. 3–14, 2005.
- [13] A. Jemal, R. Siegel, E. Ward et al., "Cancer statistics, 2006," *CA: A Cancer Journal for Clinicians*, vol. 56, no. 2, pp. 106–130, 2006.
- [14] S. A. Grossman and J. F. Batara, "Current management of glioblastoma multiforme," *Seminars in Oncology*, vol. 31, no. 5, pp. 635–644, 2004.
- [15] L. H. Treat, N. McDannold, Y. Zhang, N. Vakhodtseva, and K. Hynynen, "Improved anti-tumor effect of liposomal doxorubicin after targeted blood-brain barrier disruption by MRI-guided focused ultrasound in rat glioma," *Ultrasound in Medicine and Biology*, vol. 38, no. 10, pp. 1716–1725, 2012.
- [16] H. L. Liu, M. Y. Hua, H. W. Yang et al., "Magnetic resonance monitoring of focused ultrasound/magnetic nanoparticle targeting delivery of therapeutic agents to the brain," *Proceedings of the National Academy of Sciences of the United States of America*, vol. 107, no. 34, pp. 15205–15210, 2010.
- [17] K. Liu, G. Wen, X. F. Lv et al., "MR imaging of cerebral extraventricular neurocytoma: a report of 9 cases," *The American Journal of Neuroradiology*, 2012.
- [18] N. McDannold, N. Vakhodtseva, and K. Hynynen, "Blood-brain barrier disruption induced by focused ultrasound and circulating preformed microbubbles appears to be characterized by the mechanical index," *Ultrasound in Medicine and Biology*, vol. 34, no. 5, pp. 834–840, 2008.
- [19] N. Vakhodtseva, N. McDannold, and K. Hynynen, "Progress and problems in the application of focused ultrasound for blood-brain barrier disruption," *Ultrasonics*, vol. 48, no. 4, pp. 279–296, 2008.
- [20] F. Y. Yang, W. M. Fu, W. S. Chen, W. L. Yeh, and W. L. Lin, "Quantitative evaluation of the use of microbubbles with transcranial focused ultrasound on blood-brain-barrier disruption," *Ultrasonics Sonochemistry*, vol. 15, no. 4, pp. 636–643, 2008.
- [21] F. Y. Yang, W. M. Fu, R. S. Yang, H. C. Liou, K. H. Kang, and W. L. Lin, "Quantitative evaluation of focused ultrasound with a contrast agent on blood-brain barrier disruption," *Ultrasound in Medicine and Biology*, vol. 33, no. 9, pp. 1421–1427, 2007.
- [22] J. J. Choi, J. A. Feshitan, B. Baseri et al., "Microbubble-size dependence of focused ultrasound-induced blood-brain barrier

- opening in mice *in vivo*,” *IEEE Transactions on Biomedical Engineering*, vol. 57, no. 1, pp. 145–154, 2010.
- [23] R. Chopra, N. Vykhotseva, and K. Hynnen, “Influence of exposure time and pressure amplitude on blood-brain-barrier opening using transcranial ultrasound exposures,” *ACS Chemical Neuroscience*, vol. 1, no. 5, pp. 391–398, 2010.
- [24] J. Park, Y. Zhang, N. Vykhotseva, F. A. Jolesz, and N. J. McDannold, “The kinetics of blood brain barrier permeability and targeted doxorubicin delivery into brain induced by focused ultrasound,” *Journal of Controlled Release*, vol. 162, no. 1, pp. 134–142, 2012.
- [25] P. S. Tofts and A. G. Kermode, “Measurement of the blood-brain barrier permeability and leakage space using dynamic MR imaging. 1. Fundamental concepts,” *Magnetic Resonance in Medicine*, vol. 17, no. 2, pp. 357–367, 1991.
- [26] F. Vlachos, Y. S. Tung, and E. Konofagou, “Permeability dependence study of the focused ultrasound-induced blood-brain barrier opening at distinct pressures and microbubble diameters using DCE-MRI,” *Magnetic Resonance in Medicine*, vol. 66, no. 3, pp. 821–830, 2011.
- [27] I. M. Noebauer-Huhmann, P. Szomolanyi, V. Juras, O. Kraff, M. E. Ladd, and S. Trattnig, “Gadolinium-based magnetic resonance contrast agents at 7 tesla: *in vitro* T1 relaxivities in human blood plasma,” *Investigative Radiology*, vol. 45, no. 9, pp. 554–558, 2010.
- [28] E. A. Neuwelt, P. A. Barnett, C. I. McCormick, L. G. Remsen, R. A. Kroll, and G. Sexton, “Differential permeability of a human brain tumor xenograft in the nude rat: impact of tumor size and method of administration on optimizing delivery of biologically diverse agents,” *Clinical Cancer Research*, vol. 4, no. 6, pp. 1549–1555, 1998.
- [29] H. Sarin, A. S. Kanevsky, H. Wu et al., “Effective transvascular delivery of nanoparticles across the blood-brain tumor barrier into malignant glioma cells,” *Journal of Translational Medicine*, vol. 6, article 80, 2008.
- [30] A. R. Padhani and J. E. Husband, “Dynamic contrast-enhanced MRI studies in oncology with an emphasis on quantification, validation and human studies,” *Clinical Radiology*, vol. 56, no. 8, pp. 607–620, 2001.
- [31] P. S. Tofts, G. Brix, D. L. Buckley et al., “Estimating kinetic parameters from dynamic contrast-enhanced T(1)-weighted MRI of a diffusible tracer: standardized quantities and symbols,” *Journal of Magnetic Resonance Imaging*, vol. 10, no. 3, pp. 223–232, 1999.
- [32] H. Olsson, C. Halldin, C. G. Swahn, and L. Farde, “Quantification of [¹¹C]FLB 457 binding to extrastriatal dopamine receptors in the human brain,” *Journal of Cerebral Blood Flow and Metabolism*, vol. 19, no. 10, pp. 1164–1173, 1999.
- [33] K. W. Kang, D. S. Lee, J. H. Cho et al., “Quantification of F-18 FDG PET images in temporal lobe epilepsy patients using probabilistic brain atlas,” *NeuroImage*, vol. 14, no. 1, part 1, pp. 1–6, 2001.
- [34] S. L. Bacharach, S. K. Libutti, and J. A. Carrasquillo, “Measuring tumor blood flow with H₂¹⁵O: practical considerations,” *Nuclear Medicine and Biology*, vol. 27, no. 7, pp. 671–676, 2000.
- [35] M. S. Alavijeh and A. M. Palmer, “Measurement of the pharmacokinetics and pharmacodynamics of neuroactive compounds,” *Neurobiology of Disease*, vol. 37, no. 1, pp. 38–47, 2010.
- [36] H. F. Dvorak, L. F. Brown, M. Detmar, and A. M. Dvorak, “Vascular permeability factor/vascular endothelial growth factor, microvascular hyperpermeability, and angiogenesis,” *The American Journal of Pathology*, vol. 146, no. 5, pp. 1029–1039, 1995.
- [37] L. E. Benjamin, D. Golijanin, A. Itin, D. Pode, and E. Keshet, “Selective ablation of immature blood vessels in established human tumors follows vascular endothelial growth factor withdrawal,” *Journal of Clinical Investigation*, vol. 103, no. 2, pp. 159–165, 1999.
- [38] J. S. Taylor, P. S. Tofts, R. Port et al., “MR imaging of tumor microcirculation: promise for the new millennium,” *Journal of Magnetic Resonance Imaging*, vol. 10, no. 6, pp. 903–907, 1999.
- [39] L. F. Brown, K. T. Yeo, B. Berse et al., “Expression of vascular permeability factor (vascular endothelial growth factor) by epidermal keratinocytes during wound healing,” *Journal of Experimental Medicine*, vol. 176, no. 5, pp. 1375–1379, 1992.
- [40] M. A. O'Reilly, A. Muller, and K. Hynnen, “Ultrasound insertion loss of rat parietal bone appears to be proportional to animal mass at submegahertz frequencies,” *Ultrasound in Medicine and Biology*, vol. 37, no. 11, pp. 1930–1937, 2011.
- [41] M. A. O'Reilly, Y. Huang, and K. Hynnen, “The impact of standing wave effects on transcranial focused ultrasound disruption of the blood-brain barrier in a rat model,” *Physics in Medicine and Biology*, vol. 55, no. 18, pp. 5251–5267, 2010.

Research Article

Significance of Coronary Calcification for Prediction of Coronary Artery Disease and Cardiac Events Based on 64-Slice Coronary Computed Tomography Angiography

Yuan-Chang Liu,¹ Zhonghua Sun,² Pei-Kwei Tsay,³ Tiffany Chan,⁴ I-Chang Hsieh,⁵ Chun-Chi Chen,⁵ Ming-Shien Wen,⁵ and Yung-Liang Wan¹

¹ Department of Medical Imaging and Intervention, Chang Gung Memorial Hospital at Linkou, Healthy Aging Research Center, College of Medicine, Chang Gung University, Taoyuan 333, Taiwan

² Discipline of Medical Imaging, Department of Imaging and Applied Physics, Curtin University, Perth, WA 6845, Australia

³ Department of Public Health and Center of Biostatistics, College of Medicine, Chang Gung University, Taoyuan 333, Taiwan

⁴ Michael G. DeGroote School of Medicine, McMaster University, Hamilton, ON, Canada L8S 4L8

⁵ Second Section of Cardiology, Department of Internal Medicine, Chang Gung Memorial Hospital at Linkou, College of Medicine, Chang Gung University, Taoyuan 333, Taiwan

Correspondence should be addressed to Yung-Liang Wan; ylw0518@adm.cgmh.org.tw

Received 3 January 2013; Accepted 4 February 2013

Academic Editor: Fan-Lin Kong

Copyright © 2013 Yuan-Chang Liu et al. This is an open access article distributed under the Creative Commons Attribution License, which permits unrestricted use, distribution, and reproduction in any medium, provided the original work is properly cited.

This work aims to validate the clinical significance of coronary artery calcium score (CACS) in predicting coronary artery disease (CAD) and cardiac events in 100 symptomatic patients (aged 37–87 years, mean 62.5, 81 males) that were followed up for a mean of 5 years. Our results showed that patients with CAD and cardiac events had significantly higher CACS than those without CAD and cardiac events, respectively. The corresponding data were 1450.42 ± 3471.24 versus 130 ± 188.29 ($P < 0.001$) for CAD, and 1558.67 ± 513.29 versus 400.46 ± 104.47 ($P = 0.031$) for cardiac events. Of 72 patients with CAD, cardiac events were found in 56 (77.7%) patients. The prevalence of cardiac events in our cohort was 13.3% for calcium score 0, 50% for score 11–100, 56% for score 101–400, 68.7% for score 401–1,000, and 75.0% for score >1000. Increased CACS (>100) was also associated with an increased frequency of multi-vessel disease. Nonetheless, 3 (20%) out of 15 patients with zero CACS had single-vessel disease. Significant correlation ($P < 0.001$) was observed between CACS and CAD on a vessel-based analysis for coronary arteries. It is concluded that CACS is significantly correlated with CAD and cardiac events.

1. Introduction

The pathogenesis of coronary artery disease (CAD) is a long-term atherosclerotic process that eventually leads to significant stenosis (decrease of lumen diameter by >50%) of the coronary arteries. With reports demonstrating the initial presentation of CAD being acute myocardial infarction or sudden cardiac death in 50% of patients [1], increasing efforts have been made to establish risk factors that can assess patient risk for future coronary events. Unfortunately, the success of conventional risk factors, such as the Framingham Risk Score, clinical examination, and stress testing, have been limited

in their ability to predict the occurrence of CAD, especially among patients within the intermediate risk group [2].

Coronary artery calcium score (CACS) has been regarded as a potential tool to improve risk stratification and predict cardiac events. It has been recognized as a surrogate marker for atherosclerotic plaque burden and holds the advantages of directly visualizing and precisely locating the plaques using computed tomography (CT) [3, 4]. Using Agatston calcium scoring [5], CACS can also be quantified, allowing for a direct individual assessment of each patient, unlike conventional risk factors that only provide a statistical probability for patients developing CAD. A growing number of reports

have emerged supporting the vital use of CACS in the assessment of cardiac event risk stratification [3, 6]. Conventional coronary angiography (CCA) is the gold standard in diagnosing CAD due to its superior spatial and temporal resolution, thus enabling accurate assessment of the degree of coronary stenosis. However, this procedure remains invasive, expensive, and inconvenient for patients. CACS, on the other hand, is most commonly quantified using CT, which is widely used in routine clinical practice as a noninvasive technique.

The vast majority of studies describing the prognostic value of coronary calcification were mainly done in the Western countries [7–10]. Related studies reported from Asian country are relatively scarce [11, 12]. The healthcare system, populations, and disease patterns in Asia differ from Western countries [13]. Prevalence of coronary calcification is different in Caucasian, Chinese, Hispanic, and African populations by figures of 70.4%, 59.6%, 56.5%, and 52.1%, respectively. Compared with Caucasians, the relative risk of death was 2.97 in Africans, 1.58 in Hispanics, and 0.85 in Chinese [2]. In this report from an Asian country, we aim to validate the relationship between CACS, CAD, and cardiac events by using 64-multislice computed tomography (64-MSCT) with CCA as the gold standard.

2. Materials and Methods

2.1. Patients. Medical records of CCA and CACS over 2 years (2006–2008) from Chang Gung Memorial Hospital in Taiwan were retrospectively reviewed of 100 symptomatic patients suggestive of CAD. These symptomatic patients included 81 men, with ages ranging from 37 to 87 (mean 62.5) years. The main symptoms prior to CCA and 64-MSCT testing included chest tightness ($n = 57$), chest pain ($n = 44$), radiating pain ($n = 26$), dyspnea ($n = 38$), and cold sweats ($n = 25$). Risk factors for CAD that were apparent among the patient population included hypertension ($n = 61$), hypercholesterolemia ($n = 27$), hypertriglyceridemia ($n = 36$), smoking history ($n = 14$), diabetes mellitus ($n = 22$), and obesity or overweight ($n = 33$). All patients underwent CCA and MSCT for CACS. The interval between the testing of CCA and 64-MSCT ranged from 0 to 89 (mean 9.16 ± 16.82) days, where the interval was less than two weeks in 79% of all cases. For assessing cardiac events after cardiac CT, 98 patients could be followed up for a mean of 5 years (range 46.7–72.9 months). Each subject was recorded to have at least one cardiac event, by definition as occurrence of either unstable angina requiring revascularization or cardiac death (caused by acute myocardial infarction, ventricular arrhythmias, or refractory heart failure). The institute review board approved the study, and written informed consent was obtained from all patients undergoing CCA and CT. Patients were excluded if they had contrast medium allergy, impaired renal function, history of coronary bypass surgery, and arrhythmia.

2.2. Conventional Coronary Angiography (CCA). CCA was referred to all patients with suspected CAD, as described by their symptoms, risk factors, and experiencing at least one

cardiac event. CCA was done accordingly to the standard Seldinger's technique on an angiographic machine (Integris BH3000, Philips, Eindhoven, The Netherlands) by femoral approach. Cardiologists who had no prior knowledge of MSCT findings quantitatively analyzed the severity of coronary stenosis. The minimal lumen diameter was measured in projections showing the most severe narrowing. The degree of stenosis was classified into four categories: (1) no stenosis, (2) minimal or mild stenosis ($\leq 50\%$), (3) moderate stenosis (50%–70%), and (4) severe stenosis ($> 70\%$). CAD was defined when lumen diameter reduction was greater than 50% (moderate or severe stenosis).

2.3. Cardiac CT Imaging Protocol. All CT scans were performed on a 64-slice scanner with a 0.4 s rotation time (Aquilion Multi-64-slice system, Toshiba Medical Systems). Nonenhanced CT scan for calcium scoring was performed from the level of tracheal bifurcation to the diaphragm using the following parameters: 120 KVp, 300 mA, 0.25 s, slice thickness of 3 mm, and intervals of 3 mm. The calcium scores of each area at each vessel were calculated at an offline commercially available workstation with dedicated software (Software Vitrea 2 V3.9.0.1, MN, USA) and the scores were quantified by the scoring algorithm proposed by Agatston et al. [5], and calcium scores were divided into the following categories: 0, 1–10, 11–100, 101–400, 401–1000, and ≥ 1000 .

2.4. Statistical Analysis. Continuous variables were expressed as mean and standard deviations. For both patient-based and vessel-based analyses, Kruskal-Wallis test was used to analyze whether the CACS were related to the degree of coronary artery stenosis. Mann-Whitney U test was used to investigate the correlation between the CACS and the presence of CAD. Two-sample independent *t*-test was used to analyze the correlation between CACS and cardiac events. Chi-square test was used to assess the correlation between the cardiac events and categorical variables (age, gender, risk factors including hypertension which was defined as blood pressure $> 130/90$ mm Hg, diabetes mellitus, smoking, body mass index, and hypercholesterolemia). Event-free survival curves were constructed using the Kaplan-Meier method to account for censored survival times and compared with the log-rank test. A *P* value of less than 0.05 was considered statistically significant.

3. Results

3.1. Significant Correlation between CACS and CAD on a Patient Basis. Of 100 symptomatic patients, CCA revealed CAD (stenosis $> 50\%$ in diameter) in 72 patients, while the remaining 28 patients had no CAD (stenosis $\leq 50\%$) (Table 1). Among the patients diagnosed with CAD, 57 had severe stenosis and 15 had moderate stenosis. On the other hand, 9 patients had minimal or mild stenosis and 19 patients had no stenosis. Our findings indicated that: (1) there was a significant increase in mean calcification with increasing severity in stenosis, (2) the variability of calcium scoring was

TABLE 1: The correlation between calcium scoring and degree of stenosis, coronary artery disease (CAD) and cardiac events.

Calcium scoring	0	1–10	11–100	101–400	401–1000	≥ 1001	
Number of cases	15	0	16	25	16	28	
Cardiac events ⁺ ($n = 56$)	2 (13.3%)	0	8 (50%)	14 (56%)	11 (68.7%)	21 (75%)	
Degree of stenosis ($n = 100$)							Mean \pm SD
0 = no ($n = 19$)	10 (66.7%)	0	4 (25%)	3 (16%)	2 (12.5%)	0	$87.32 \pm 156.52^*$
1 = minimal or mild ($n = 9$)	2 (13.3%)	0	2 (12.5%)	3 (12%)	2 (12.5%)	0	$220.11 \pm 225.99^*$
2 = moderate ($n = 15$)	1 (6.7%)	0	1 (6.3%)	4 (12%)	3 (18.8%)	6 (21.4%)	$1143.87 \pm 1284.63^*$
3 = severe ($n = 57$)	2 (13.3%)	0	9 (56.2%)	15 (60%)	9 (56.2%)	22 (78.6%)	$1531.09 \pm 3851.32^*$
No CAD = 0 + 1 ($n = 28$)	12	0	6	6	4	0	$130 \pm 188.29^*$
CAD = 2 + 3 ($n = 72$)	3	0	10	19	12	28	$1450.417 \pm 3471.24^*$
Coronary artery disease ($n = 72$)							
One vessel ($n = 33$)	3 (100%)	0	10 (100%)	8 (42.1%)	6 (50%)	6 (21.4%)	
Two vessels ($n = 26$)	0	0	0	8 (42.1%)	3 (25%)	15 (53.6%)	
Three vessels ($n = 13$)	0	0	0	3 (15.8%)	3 (25%)	7 (25%)	

*Statistically significant ($P < 0.001$).

⁺Followup for cardiac events was successful in 98 of 100 patients.

TABLE 2: Calcium score in vessel-based distribution of coronary artery stenosis or coronary artery disease (CAD).

Degree of stenosis	RCA ($n = 100$)		LM ($n = 100$)		LAD ($n = 100$)		LCX ($n = 100$)	
	<i>n</i>	Mean \pm SD	<i>n</i>	Mean \pm SD	<i>n</i>	Mean \pm SD	<i>n</i>	Mean \pm SD
0 = no	51	$116.53 \pm 303.26^*$	81	52.38 ± 121.98	37	$162.57 \pm 394.78^*$	59	$78.47 \pm 196.89^*$
1 = minimal or mild	11	$216 \pm 242.06^*$	6	137.50 ± 135.44	14	$214.07 \pm 270.84^*$	10	$133.20 \pm 246.96^*$
2 = moderate	13	$289 \pm 405.06^*$	6	135.71 ± 217.82	15	$673.67 \pm 270.84^*$	8	$113.38 \pm 104.17^*$
3 = severe	25	$1344.52 \pm 3637.06^*$	7	186.83 ± 188.72	34	$361.06 \pm 415.86^*$	23	$475.09 \pm 1011.95^*$
No CAD = 269	62	$134.18 \pm 297.28^*$	87	58.25 ± 124.86	51	$176.71 \pm 365.0^*$	69	$86.41 \pm 205.9^*$
CAD = 131	38	$1017.63 \pm 3039.3^*$	13	159.31 ± 206.48	49	$456.76 \pm 515.4^*$	31	$381.74 \pm 887.4^*$

RCA: right coronary artery, LM: left main coronary artery, LAD: left anterior descending artery, and LCX: left circumflex artery.

*Statistically significant ($P < 0.001$).

high within each group, and (3) the overall calcium score in patients with CAD was significantly higher than those without CAD (1450.42 ± 3471.24 and 130 ± 188.29 , resp.; $P < 0.001$) (Table 1). This suggests that patients with extensive coronary calcification have a higher probability of moderate stenosis and, thus, are more likely to have CAD. Patients with a calcium score of 0, 11–100, 101–400, 401–1000, and >1000 had a 20%, 62.5%, 76%, 75%, and 100% prevalence of CAD, respectively (Table 1). A significant correlation was confirmed between the degree of stenosis and calcium score ($P < 0.001$) (Table 1).

3.2. Significant Correlation between CACS and CAD on a Vessel Basis. Among the 100 patients, a total of 400 vessels were analyzed in which CAD (severe or moderate stenosis) was found in 131 vessels, and no CAD was found in the remaining 269 vessels (Table 2). Of the 131 vessels with significant stenosis, 38 were in the right coronary artery (RCA) (29%), 13 were in the left main artery (LM) (9.9%), 49 were in the left anterior descending (LAD) (37.4%), and 31 were in the left circumflex artery (LCX) (23.7%). As expected, CACS was significantly greater in patients with CAD than those without CAD, with the corresponding CACS being

1017.63 ± 3039.32 and 134.18 ± 297.28 , respectively, in the RCA ($P < 0.001$), 456.76 ± 515.48 and 176.71 ± 365.09 , respectively in the LAD ($P < 0.001$), and 381.74 ± 887.48 and 86.41 ± 205.94 , respectively, in the LCX ($P < 0.001$). CACS was lower in the LM compared to all other blood vessel in both CAD and non-CAD patient groups. Also, marginal significant findings between the CACS and patients with and without CAD were noticed in the LM (159.31 ± 206.48 and 58.25 ± 124.86 , resp.; $P = 0.055$). Our results revealed a positive correlation between greater calcium score and the frequency of multivessel disease (Table 1). Specifically, all patients with multivessel disease (CAD in two or three arteries) had a calcium score that was at least greater than 100 and patients with CACS > 1000 had a 100% incidence of CAD ($P < 0.001$) (Figure 1).

The sensitivity, specificity, positive predictive value (PPV), negative predictive value (NPV), and accuracy of CACS at different score levels are analyzed in Table 3. Using CCA as the gold standard, in patient-based analysis, CACS of 11–100 yielded the highest sensitivity (95.8%), NPV (80%), and accuracy (80%). CACS of over 1000 revealed the greatest specificity (100%) and PPV (100%). For each coronary artery, CACS of 1–10 yielded the highest sensitivity (91.6%) and NPV

TABLE 3: Sensitivity, specificity, positive predictive value (PPV), negative predictive value (NPV), and accuracy of calcium scoring in assessing coronary artery disease under patient-based (PB) and vessel-based (VB) analyses.

Calcium scoring	0		1–10		11–100		101–400		401–1000		≥1001	
	PB	VB	PB	VB	PB	VB	PB	VB	PB	VB	PB	VB
Sensitivity	100%	100%	Nil	91.6%	95.8%	86.3%	81.7%	61.1%	56.3%	33.6%	39.4%	11.5%
Specificity	0%	0%	Nil	46.1%	41.4%	53.2%	62.1%	77.3%	86.2%	91.8%	100%	98.9%
PPV	32.8%	71%	Nil	45.3%	80%	47.3%	84.1%	56.7%	90.9%	66.7%	100%	83.3%
NPV	Nil	Nil	Nil	91.9%	80%	88.8%	58.1%	80.3%	44.6%	74%	40.3%	69.6%
Accuracy	32.8%	71%	Nil	61%	80%	64%	76%	72%	65%	72.8%	57%	70.3%

Nil: no patients in respective group.

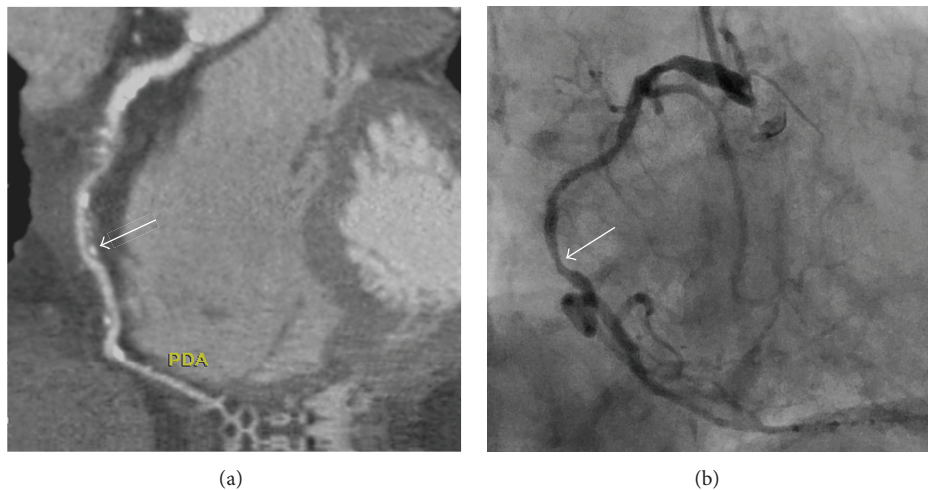


FIGURE 1: A 86-year-old female with two-vessel coronary artery disease, total calcium score was 1278. The calcium score was 325 over the right coronary artery (RCA). (a) A computed tomographic angiogram shows mixed plaques over the middle third of RCA with 54% stenosis (white arrow). (b) Conventional coronary arteriogram confirms the moderate stenosis over the proximal as well as middle (arrow) third of RCA.

(91.9%), and CACS of >1000 revealed the highest specificity (98.9%) and PPV (83.3%). The greatest accuracy (72.8%) was obtained with CACS of 401–1000.

3.3. Zero CACS Scoring Cannot Exclude the Presence of CAD. A total of 15 patients did not have coronary calcification, with 3 (20%) of them having CAD (Table 1), indicating that the complete absence of coronary calcium did not exclude the presence of CAD. Following the analysis of the 3 patients with zero CACS, all were found to have single-vessel CAD primarily involving the LAD (Table 1). All three patients were confirmed to have soft plaques on CT angiograms (Figures 2(a) and 3(a)). One patient had moderate stenosis and 2 had severe stenosis confirmed by CCA (Figures 2(b) and 3(b)).

3.4. A Significant Correlation between CACS and Cardiac Events. Of 98 patients with a mean followup of 5 years, cardiac events occurred in 56 (57.1%) patients which were all associated with CAD. These cardiac events included two cardiac deaths (no revascularization) and 54 revascularization (Table 1) including 3 subsequent cardiac deaths. Of 72

patients with CAD, cardiac events were encountered in 56 (77.7%) subjects. Patients with cardiac events had statistically significant higher CACS than those without cardiac events: 1558.67 ± 513.29 versus 400.46 ± 104.47 ($P = 0.031$). Cardiac events were not significantly related to patient age ($P = 0.576$), gender ($P = 0.775$), hypertension ($P = 0.800$), body mass index ($P = 0.815$), smoking ($P = 1.000$), and hypercholesterolemia ($P = 0.410$) but closely related to diabetes mellitus ($P = 0.021$).

Figure 4 shows significant association of coronary stenosis with major adverse cardiac events. The cumulative event-free subjects curves according to calcium score categories are reported in Figure 5. As shown in these two figures, significant associations were found between the degree of coronary stenosis and calcium scores and the occurrence of cardiac events.

4. Discussion

The strength of our study is that it provides prognostic information of CACS for cardiac events based on a mean followup of 5 years. We also identify the clinical value of

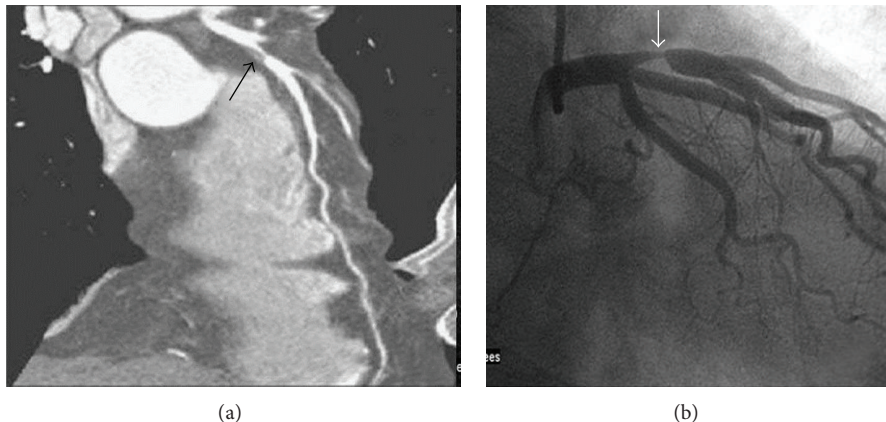


FIGURE 2: A 53-year-old male with zero calcium score. (a) A computed tomographic angiogram shows a soft plaque at the left anterior descending artery (LAD) (black arrow) with severe stenosis. (b) Conventional coronary arteriogram confirms the severe stenosis over the proximal third of the LAD (white arrow).

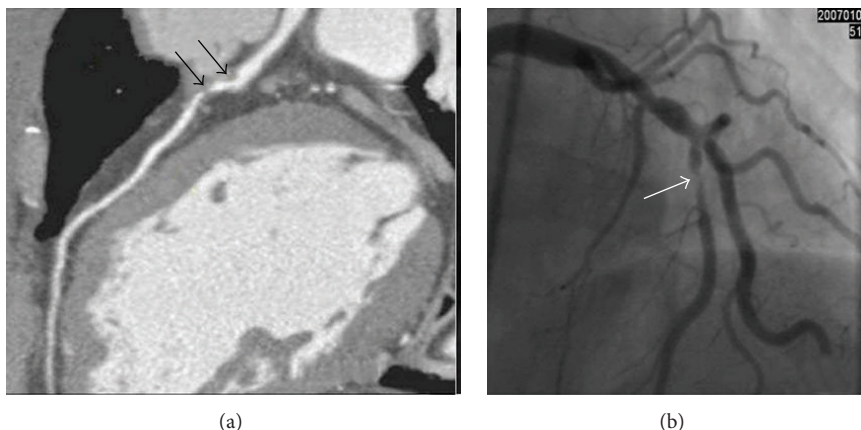


FIGURE 3: A 66-year-old male with zero calcium score. (a) A computed tomographic angiogram shows soft plaques (black arrows) at the left anterior descending artery (LAD) with severe stenosis. (b) Conventional coronary arteriogram confirms the severe stenosis of the LAD (white arrow).

using CACS for determining the presence and degree of CAD, although a zero CACS cannot exclude the presence of CAD.

Up to 50% of CAD patients initially suffer from acute myocardial infarction (AMI) or sudden death [1], and the severity of these hard cardiac events has prompted a greater emphasis on preventative care. Thus, scoring tools that consider demographic and clinical characteristics are used to stratify patients into low-, intermediate-, and high-risk for developing CAD. In addition to the Framingham Risk Score (FRS) that uses a multivariable statistical model to predict a patient's 10-year risk for future cardiovascular events, other tools include clinical examinations, stress testing, C-reactive protein, and family history of CAD. Nonetheless, such prediction models for CAD have limitations [13]. Akosah et al. [14] conducted a survey consisting of a group of 222 asymptomatic patients who suffered from their first AMI and found that 75% of them would not have been considered for therapy according to conventional risk factors. Other studies have

shown that testing can only predict 60–65% of cardiovascular events, leaving up to one-third of patients suffering from a hard cardiac event in the absence of these risk factors [15]. Such shortcomings lie in that conventional risk factors only provide a statistical probability of patients developing CAD, rather than a direct individual assessment [16]. Patients in the intermediate risk group are especially affected, as they are left untreated due to cost inefficiency and their asymptomatic condition results in poor compliance to lifestyle change [2].

The prognostic value of CACS over clinical and laboratory data has been previously studied in a large cohort of patients [12, 16, 17]. These studies showed that an excellent survival was achieved in patients with a zero CACS, but increased cardiac events were closely associated with higher CACS (<400). This is confirmed in our study as we found the similar probability of 5-year cardiac events, which was 75% for CACS >1000 and 13.3% for CACS = 0. The occurrence of cardiac events for the patients with a zero CACS is significantly higher than that reported by Hou and others

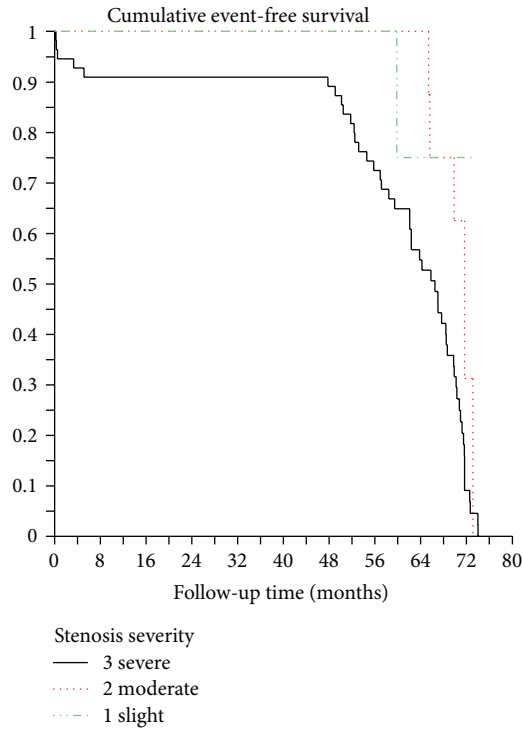


FIGURE 4: Cumulative event-free survival curves by Kaplan-Meier analysis according to the degree of coronary stenosis.

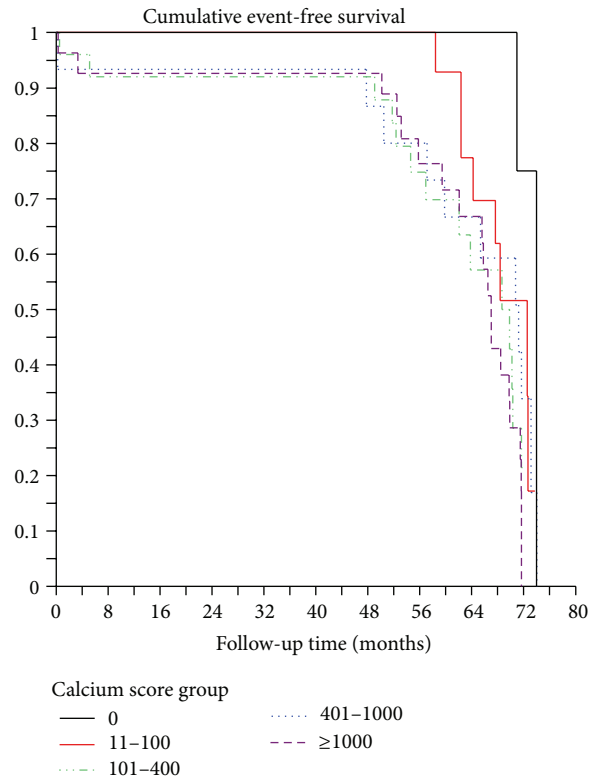


FIGURE 5: Cumulative event-free survival curves by Kaplan-Meier analysis according to the categories of coronary artery calcium score.

[12, 16, 17]. This could be caused by the small sample size in our study. We also found the correlation of severity of CAD with adverse cardiac events, with severe coronary stenosis leading to 86% cardiac events, and only 11.1% for patients with mild degree of coronary stenosis. This indicates incremental prognostic value of adding coronary stenosis to CACS over clinical risk factors.

A growing number of reports have emerged supporting the use of CACS as a diagnostic tool for asymptomatic patients at intermediate risk for CAD and the diagnosis of CAD in symptomatic patients [18, 19]. A study by Raggi et al. [19] concluded that there was a greater incidence of hard cardiac events (AMI and sudden death) in asymptomatic patients who had calcium scores greater than the 75th percentile when compared with their age- and sex-matched controls. Another study reported the odds ratio of hard cardiac events in asymptomatic patients with Agatston CACS scores <100, 100–400, and >400 to be 2.1, 4.2, and 7.2, respectively [20]. Among symptomatic patients, Georgiou et al. [7] reported that calcium score values were significantly related to occurrence of hard cardiac events ($P < 0.001$) and all cardiovascular events ($P < 0.001$), whereby patients with CACS in the upper third and fourth quartiles (greater than the 75th percentile) were 13.2 times more likely to suffer from an event than those with zero or low scores (0 to 25th percentile). Furthermore, Detrano et al. [9] have reported that coronary calcium score is a strong predictor of incident coronary heart disease events (MI, death due to CAD) among four racial groups (Caucasian, African, Hispanic, and Chinese) in the United States. In that study, the

risk of coronary events associated with increasing CACS had a hazard ratio (95% CI) of 1.00 for nondetectable calcium. For CACS of 1–100, 101–300, >300, the hazard ratio was 3.89 (1.71–8.79), 7.08 (3.05–16.47), and 6.84 (2.93–15.99), respectively. Chinese people had a hazard ratio (95% CI) for the risk of coronary heart disease with CACS of 1.25 ($P = 0.11$) compared to the Caucasian people who had a hazard ratio of 1.17 ($P < 0.005$). Our findings are in line with these studies confirming the prognostic value of CACS in a group of symptomatic patients.

According to a report by Budoff et al. [21], when compared with individuals without calcium as a hazard ratio of 1, a calcium score between 1 and 100 was associated with a “hazard ratio” for major coronary events of 3.9, a score between 101 and 300 with a “hazard ratio” of 7.1, and a score of more than 300 with a “hazard ratio” of 6.8. In this study, the prevalence of cardiac events was 13.3% for calcium score 0, 50% for score 11–100, 56% for score 101–400, 68.7% for score 401–1,000, and 75% for score >1000. The mean of CACS in our cohort with cardiac events (1559) was 3.9 times higher than that of cohort without cardiac event (400). In addition to higher CACS, the study also revealed significant correlation ($P = 0.021$) between the diabetes mellitus and cardiac events. It has been reported that type 2 diabetics with a CACS > 100 are expected to have an increased frequency of ischemia in myocardial perfusion imaging; the risk of all-cause mortality was higher in diabetics than in nondiabetics for any degree of CS [22]. All our patients with a CACS above 1000 had CAD,

calcium score higher than 1000 is associated with increased specificity (100%) but decreased sensitivity (39.4%). Larger angiographic studies using electron beam tomography and electron beam computed tomography have reported similar findings [22, 23].

A previous study by Budoff et al. [24] investigated the distribution of calcification within the major coronary arteries to determine the severity and extent of angiographic disease. In another algorithmic model, Schmermund et al. [25] utilized calcium scoring to distinguish patients with or without 3-vessel and/or left main CAD. While recent studies have found a moderate correlation between CACS and the incidence of atherosclerotic disease on vessel-based analysis ($r = 0.521$) [11], our study reveals more comprehensive findings. We demonstrate (1) a statistically significant correlation between the degree of stenosis and calcium score in the RCA, LAD, and LCX ($P < 0.001$) and (2) a significantly higher CACS in patients with CAD than those without CAD in the three aforementioned coronary arteries ($P < 0.001$). Only the LM revealed nonsignificant correlation with respect to CACS and the presence of CAD, although the relationship between stenosis and calcium scoring was close to significance ($P = 0.055$). This finding may be a result of the left main artery bifurcating into the LAD and LCX, and any calcification near this junction could be assigned to varying branches. Such difficulty in assigning calcifications to a single artery could obscure the reported CACS in different blood vessels.

Although the presence of coronary artery calcium is associated with a greater risk of cardiovascular events, its ability to predict future coronary events is not absolute. A zero calcium score only reflects the absence of atherosclerotic lesions with calcified plaques greater than 1 mm in diameter, leaving noncalcified and lipid-laden “vulnerable” plaques to be present in the absence of CACS [26]. Furthermore, any identified calcification only reflects approximately 20% of the total atherosclerotic plaque burden, overlooking any soft plaques that may cause CAD [27]. Nonetheless, the absence of CAC is associated with a very low probability of significant stenosis and future cardiovascular events.

A systematic review of 49 studies revealed that the frequency of cardiovascular event among patients with zero CACS was 0.56% in asymptomatic and 1.8% in symptomatic patients [28]. This review also found CACS to have a negative predictive value as high as 99% for ruling out acute coronary syndrome [29]. Similarly, another series reported that obstructive CAD was found in 7% of patients with zero CACS and in 17% of patients with low CACS (1–100) [30].

In our study, on a per-patient basis, 20% of patients (3 out of 15) with zero CACS had single-vessel CAD. Further analysis revealed that these patients had soft plaques, which was the cause of severe stenosis at the proximal LAD. This percentage is greater than what has been previously reported because the present study population was limited in size and focused on symptomatic patients, resulting in a greater pretest probability. To address the conflict of the prognostic value of a zero calcium score, future studies investigating patient populations of varying pretest probability

for CAD and clinically relevant end points (rather than an angiographic end point) are needed. Thus, despite CACS' predictive power, the occurrence of cardiac events in patients with negative calcium scores suggests that CACS should not be used as a single-decision diagnostic parameter for CAD.

There are several limitations in our study. First, CACS cannot be used to assess noncalcified soft plaques or calcified plaques that are less than 130 HU in density. Noncalcified plaques with density less than 30 HU and positive remodeling are significant predictors of acute coronary syndrome [31]. Second, the patient number of 100 is relatively small in our cohort; however, this was compensated by statistical analysis. Our patients with CAD and cardiac events had significantly higher calcium score than those without CAD ($P < 0.001$) and cardiac events ($P = 0.031$), respectively.

Third, our study included symptomatic patients who underwent clinically relevant 64-MSCT and subsequent CCA. We acknowledge the subsequent selection and verification biases that could have led to the positive correlation between CACS and angiography findings. Ideally, this bias could have been avoided by randomly assigning patients that had undergone 64-MSCT CACS for verification of CAD through conventional angiography, regardless of clinical signs or symptoms. However, it would be unethical to ask asymptomatic patients to undergo unnecessary CCA due to its invasive nature. Furthermore, since our study only focuses on symptomatic patients, our data can only suggest a similar relationship between CACS and CAD to exist in asymptomatic patients. The study also does not assess if any subjects belonged to the intermediate risk group. Future studies would benefit from investigating the correlation among CACS, CAD, and clinical or Framingham's risks factors in each patient.

In conclusion, this study further confirms the significant relationship between the CACS and the prevalence of cardiac events and the presence of CAD on a vessel-based in addition to a patient-basis analysis. The prevalence of cardiac events was significantly increased with an increase of CACS. Increased CACS (>100) was also associated with an increased frequency of multivessel disease and patients with CACS > 1000 had a 100% incidence of CAD. Although our data supports calcium screening as an additional filter before coronary angiography in symptomatic patients, a zero CACS could not exclude the presence of significant CAD.

Conflict of Interests

All authors assert that there is no conflict of interests (both personal and institutional) regarding specific financial interests that are relevant to the work conducted or reported in this paper.

Acknowledgment

The study was supported in part by a Research Grant from the National Science Council, No. NSC 95-2314-B-182A-131-MY2.

References

- [1] W. B. Kannel and A. Schatzkin, "Sudden death: lessons from subsets in population studies," *Journal of the American College of Cardiology*, vol. 5, no. 6, supplement 1, pp. 141B–149B, 1985.
- [2] M. J. Budoff and K. M. Gul, "Expert review on coronary calcium," *Vascular Health and Risk Management*, vol. 4, no. 2, pp. 315–324, 2008.
- [3] C. C. Chen, C. C. Chen, I. C. Hsieh et al., "The effect of calcium score on the diagnostic accuracy of coronary computed tomography angiography," *International Journal of Cardiovascular Imaging*, vol. 27, supplement 1, pp. 37–42, 2011.
- [4] M. J. Budoff, S. Achenbach, R. S. Blumenthal et al., "Assessment of coronary artery disease by cardiac computed tomography: a scientific statement from the American Heart Association Committee on Cardiovascular Imaging and Intervention, Council on Cardiovascular Radiology and Intervention, and Committee on Cardiac Imaging, Council on Clinical Cardiology," *Circulation*, vol. 114, no. 16, pp. 1761–1791, 2006.
- [5] A. S. Agatston, W. R. Janowitz, F. J. Hildner, N. R. Zusmer, M. Viamonte, and R. Detrano, "Quantification of coronary artery calcium using ultrafast computed tomography," *Journal of the American College of Cardiology*, vol. 15, no. 4, pp. 827–832, 1990.
- [6] P. Greenland, L. LaBree, S. P. Azen, T. M. Doherty, and R. C. Detrano, "Coronary artery calcium score combined with Framingham score for risk prediction in asymptomatic individuals," *The Journal of the American Medical Association*, vol. 291, no. 2, pp. 210–215, 2004.
- [7] D. Georgiou, M. J. Budoff, E. Kaufer, J. M. Kennedy, B. Lu, and B. H. Brundage, "Screening patients with chest pain in the emergency department using electron beam tomography: a follow-up study," *Journal of the American College of Cardiology*, vol. 38, no. 1, pp. 105–110, 2001.
- [8] G. Pundziute, J. D. Schuijf, J. W. Jukema et al., "Prognostic value of multislice computed tomography coronary angiography in patients with known or suspected coronary artery disease," *Journal of the American College of Cardiology*, vol. 49, no. 1, pp. 62–70, 2007.
- [9] R. Detrano, A. D. Guerci, J. J. Carr et al., "Coronary calcium as a predictor of coronary events in four racial or ethnic groups," *The New England Journal of Medicine*, vol. 358, no. 13, pp. 1336–1345, 2008.
- [10] M. Hadamitzky, R. Distler, T. Meyer et al., "Prognostic value of coronary computed tomographic angiography in comparison with calcium scoring and clinical risk scores," *Circulation*, vol. 4, no. 1, pp. 16–23, 2011.
- [11] E. S. Ma, Z. G. Yang, Y. Li, Z. H. Dong, L. Zhang, and L. L. Qian, "Correlation of calcium measurement with low dose 64-slice CT and angiographic stenosis in patients with suspected coronary artery disease," *International Journal of Cardiology*, vol. 140, no. 2, pp. 249–252, 2010.
- [12] Z. H. Hou, B. Lu, Y. Gao et al., "Prognostic value of coronary CT angiography and calcium score for major adverse cardiac events in outpatients," *JACC: Cardiovasc Imaging*, vol. 5, no. 10, pp. 990–999, 2012.
- [13] I. C. Tsai, B. W. Choi, C. Chan et al., "ASCI 2010 appropriateness criteria for cardiac computed tomography: a report of the Asian Society of Cardiovascular Imaging cardiac computed tomography and cardiac magnetic resonance imaging guideline Working Group," *International Journal of Cardiovascular Imaging*, vol. 26, no. 1, pp. 1–15, 2010.
- [14] K. O. Akosah, A. Schaper, C. Cogbill, and P. Schoenfeld, "Preventing myocardial infarction in the young adult in the first place: how do the national cholesterol education panel III guidelines perform?" *Journal of the American College of Cardiology*, vol. 41, no. 9, pp. 1475–1479, 2003.
- [15] P. Raggi, "Coronary-calcium screening to improve risk stratification in primary prevention," *The Journal of the Louisiana State Medical Society*, vol. 154, no. 6, pp. 314–318, 2002.
- [16] S. Möhlenkamp, N. Lehmann, P. Greenland et al., "coronary artery calcium score improves cardiovascular risk prediction in persons without indication for statin therapy," *Atherosclerosis*, vol. 215, pp. 229–236, 2011.
- [17] S. Möhlenkamp, N. Lehmann, S. Moebus et al., "quantification of coronary atherosclerosis and inflammation to predict coronary events and all-cause mortality," *American College of Cardiology Foundation*, vol. 57, pp. 1455–1464, 2011.
- [18] S. Achenbach and P. Raggi, "Imaging of coronary atherosclerosis by computed tomography," *European Heart Journal*, vol. 31, no. 12, pp. 1442–1448, 2010.
- [19] P. Raggi, T. Q. Callister, B. Cooil et al., "Identification of patients at increased risk of first unheralded acute myocardial infarction by electron-beam computed tomography," *Circulation*, vol. 101, no. 8, pp. 850–855, 2000.
- [20] M. J. Pletcher, J. A. Tice, M. Pignone, and W. S. Browner, "Using the coronary artery calcium score to predict coronary heart disease events: a systematic review and meta-analysis," *Archives of Internal Medicine*, vol. 164, no. 12, pp. 1285–1292, 2004.
- [21] M. J. Budoff, R. L. McClelland, K. Nasir et al., "Cardiovascular events with absent or minimal coronary calcification: the Multi-Ethnic Study of Atherosclerosis (MESA)," *American Heart Journal*, vol. 158, no. 4, pp. 554–561, 2009.
- [22] R. Haberl, A. Becker, A. Leber et al., "Correlation of coronary calcification and angiographically documented stenoses in patients with suspected coronary artery disease: results of 1,764 patients," *Journal of the American College of Cardiology*, vol. 37, no. 2, pp. 451–457, 2001.
- [23] D. V. Anand, E. Lim, D. Hopkins et al., "Risk stratification in uncomplicated type 2 diabetes: prospective evaluation of the combined use of coronary artery calcium imaging and selective myocardial perfusion scintigraphy," *European Heart Journal*, vol. 27, no. 6, pp. 713–721, 2006.
- [24] M. J. Budoff, G. A. Diamond, P. Raggi et al., "Continuous probabilistic prediction of angiographically significant coronary artery disease using electron beam tomography," *Circulation*, vol. 105, no. 15, pp. 1791–1796, 2002.
- [25] A. Schermund, K. R. Bailey, J. A. Rumberger, J. E. Reed, P. F. Sheedy, and R. S. Schwartz, "An algorithm for noninvasive identification of angiographic three-vessel and/or left main coronary artery disease in symptomatic patients on the basis of cardiac risk and electron-beam computed tomographic calcium scores," *Journal of the American College of Cardiology*, vol. 33, no. 2, pp. 444–452, 1999.
- [26] L. Wexler, B. Brundage, J. Crouse et al., "Coronary artery calcification: pathophysiology, epidemiology, imaging methods, and clinical implications. A statement for health professionals from the American Heart Association," *Circulation*, vol. 94, no. 5, pp. 1175–1192, 1996.
- [27] J. A. Rumberger, D. B. Simons, L. A. Fitzpatrick, P. F. Sheedy, and R. S. Schwartz, "Coronary artery calcium area by electron-beam computed tomography and coronary atherosclerotic plaque area: a histopathologic correlative study," *Circulation*, vol. 92, no. 8, pp. 2157–2162, 1995.

- [28] A. Sarwar, L. J. Shaw, M. D. Shapiro et al., "Diagnostic and prognostic value of absence of coronary artery calcification," *JACC: Cardiovascular Imaging*, vol. 2, no. 6, pp. 675–688, 2009.
- [29] R. Rubinshtain, T. Gaspar, D. A. Halon, J. Goldstein, N. Peled, and B. S. Lewis, "Prevalence and extent of obstructive coronary artery disease in patients with zero or low calcium score undergoing 64-slice cardiac multidetector computed tomography for evaluation of a chest pain syndrome," *American Journal of Cardiology*, vol. 99, no. 4, pp. 472–475, 2007.
- [30] S. Motoyama, M. Sarai, H. Harigaya et al., "Computed tomographic angiography characteristics of atherosclerotic plaques subsequently resulting in acute coronary syndrome," *Journal of the American College of Cardiology*, vol. 54, no. 1, pp. 49–57, 2009.
- [31] J. Abdulla, K. S. Pedersen, M. Budoff, and K. F. Kofoed, "Influence of coronary calcification on the diagnostic accuracy of 64-slice computed tomography coronary angiography: a systematic review and meta-analysis," *The International Journal of Cardiovascular Imaging*, vol. 28, pp. 943–953, 2011.